

**Nickel-mediated bond activation of small alkanes  
and of molecular oxygen –  
Ligand effects and the role of the metal's formal  
oxidation state**

vorgelegt von  
Diplom-Chemikerin Maria Schlangen  
aus Meppen

Von der Fakultät II – Mathematik und Naturwissenschaften  
der Technischen Universität Berlin  
zur Erlangung des akademischen Grades  
Doktor der Naturwissenschaften  
Dr. rer. nat.

genehmigte Dissertation

Promotionsausschuss:

Vorsitzender: Prof. Dr. Andreas Grohmann

Berichter: Prof. Dr. Drs. h. c. Helmut Schwarz

Berichter: Dr. habil. Detlef Schröder

Tag der wissenschaftlichen Aussprache: 16.10.2008

Berlin 2008

D 83



Für meine Eltern





## Acknowledgement

Most of all, I would like to thank Prof. Dr. Drs. h.c. Helmut Schwarz to allow me the greatest scientific latitude one can think of and his unique support and assistance at the same time. Sincere thanks for his trust in my work and many inspiring discussions. I am very grateful for the excellent instrumental equipment and the knowledge transfer provided by invited lecturers and participation in conferences. All what I learned during the last years is invaluable for me.

I would like to express my gratitude to Dr. Thomas Weiske for his dedicated care and very helpful practice of the mass spectrometers including computer administration. Though mainly from far away, special thanks go to Dr. habil. Detlef Schröder for his superior support in all kind of questions from so many fields in chemistry. I am also much obliged to him for acting as the second examiner. Further, I wish to thank Prof. Dr. Christoph van Wüllen for teaching me the way of thinking in terms of quantum chemistry with both patience and ambition. Moreover, I am grateful to Prof. Dr. Andreas Grohmann for chairing the scientific discussion of the oral PhD examination.

In addition, I am indebted to Waltraud Zummack for the cordial teamwork and the synthesis of isotopically labeled compounds. Furthermore, I have to thank Prof. Dr. Peter Roesky for the preparation of the catalyst required for the synthesis of [*all-cis*-1,2,3,4,5,6- $D_6$ ]-cyclohexane. I would like to thank Dr. Xinhao Zhang who, in a fruitful collaboration, carried out the calculations related to  $O_2$  activation.

Many thanks also to Francesca Novara for the pleasant daily teamwork and for her interest in my work. Moreover, I appreciate the probing questions of Burkhard Butschke which often caused me to reconsider my own arguments. Finally, I thank Sandra Feyel and Héloïse Soldi-Lose for several moments of exhilaration.



## Zusammenfassung

Den Gegenstand der vorliegenden Arbeit stellen Studien zur Nickel-vermittelten Bindungsaktivierung von kleinen Alkanen und molekularem Sauerstoff dar, die mit Hilfe von massenspektrometrischen Methoden untersucht wurden. Die Erzeugung der Nickel-haltigen Kationen erfolgte mittels einer Clusterquelle nach Smalley bei der Fourier-Transform Ion-Cyclotron Resonance (FT-ICR) Methode und durch Elektrospray-Ionisierung (ESI) bei der Tandem-Massenspektrometrie mit linearen Quadrupolen.

Im Gegensatz zu den relativ unreaktiven  $3d$ -Metallclustern  $M_2^+$  gegenüber Alkanen zeichnen sich Nickel-haltige, heteronukleare Dimere  $NiM^+$  wie homonukleares  $Ni_2^+$  im allgemeinen durch eine relativ hohe Reaktivität aus, insbesondere in Kombination mit einem der späten  $3d$ -Metalle oder auch mit Aluminium. Eine Ausnahme ist das quasi-inerte  $NiFe^+$ , für das so gut wie keine Bindungsaktivierung beobachtet wird, während eine effiziente Dehydrierung - einschließlich von Ethan - durch  $Ni_2^+$ ,  $NiCu^+$  und  $NiAl^+$  erfolgt.

Die Reaktivität von einkernigen  $Ni^I$ -Komplexen  $NiL^+$  mit neutralen closed-shell Liganden  $L$  wie  $CO$  oder  $H_2O$  ist im Vergleich zu der von nacktem  $Ni^+$  stark herabgesetzt, während sich  $Ni^{II}$ -Komplexe  $NiX^+$  mit anionischen Liganden  $X^-$  als viel reaktiver gegenüber Alkanen erweisen ( $X = H, F, Cl, Br, I, OH, OCH_3$ ). Formal gleiche Prozesse wie die Methanaktivierung durch  $NiH^+$  und  $NiF^+$  zeigen bei genauerer Betrachtung der Reaktionsmechanismen eindeutige Unterschiede sowohl untereinander als auch im Vergleich zu den scheinbar verwandten Metallhydriden  $PdH^+$  und  $PtH^+$  der zweiten und dritten Übergangsmetallreihe. In den untersuchten Reaktionen von  $NiX^+$  ( $X = F, Cl, Br, I$ ) mit Ethan, Propan und  $n$ -Butan führt zum einen die Variation des Halogenid-Liganden als auch die Wahl des Substrates zu einer systematischen Veränderung der Reaktionskanäle.

Basierend auf Markierungsexperimenten und quantenmechanischen Untersuchungen gibt es Hinweise, dass unterschiedliche Strukturisomere der Zusammensetzung  $[Ni, C, H_3, O]^+$  mittels ESI in der Gasphase erzeugt werden. Dies findet man auch für den Wasser-Komplex  $Ni(H_2O)^+$ , der gleichzeitig mit dem formalen  $Ni^{III}$ -Komplex  $Ni(H)(OH)^+$  generiert wird. Markierungsexperimente zeigen, dass die Erzeugung dieser beiden Komplexe unabhängig voneinander erfolgt. Die Genese und die Existenz wie auch die strukturellen Charakteristika und ungewöhnlichen Reaktivitätseigenschaften von  $Ni(H)(OH)^+$  in der Gasphase werden zum ersten Mal beschrieben. Wie erwartet, wird für den  $Ni^I$ -Komplex  $Ni(H_2O)^+$  mit intaktem Wasser-Liganden keine Reaktivität gegenüber z.B.  $CH_4$  oder  $O_2$  beobachtet; hochvalentes  $Ni(H)(OH)^+$  hingegen zeigt eine sehr hohe Reaktivität und aktiviert sowohl C-H-Bindungen in Methan als auch molekularen Sauerstoff.



## Abstract

Reactivity studies on the nickel-mediated bond activation of small alkanes have been investigated by means of Fourier-transform ion-cyclotron resonance (FT-ICR) and tandem mass spectrometry with linear quadrupoles. In the former method, the ions are generated by a Smalley-type cluster-ion source and for the latter, an electrospray-ionization (ESI) source was used for ion formation.

In contrast to the  $3d$  transition-metal dimers  $M_2^+$ , which exhibit a relatively low reactivity towards small alkanes, the pronounced reactivity of  $Ni_2^+$  and nickel-containing dimers  $NiM^+$  in general is remarkable, especially when combined with a late  $3d$  transition metal or with aluminum. An exception is  $NiFe^+$ ; almost no indication of bond activation of methane, ethane, propane, butane, or cyclohexane is observed, whereas efficient dehydrogenation of ethane takes place for  $NiM^+$  ( $M=Ni, Cu$ , and  $Al$ ).

Mononuclear  $Ni^I$  complexes  $NiL^+$  with neutral, closed-shell ligands  $L$  like  $CO$  or  $H_2O$  are relatively inert towards alkanes compared to atomic  $Ni^+$ , whereas  $Ni^{II}$  complexes  $NiX^+$  with an anionic ligand  $X^-$  are much more reactive. With respect to the actual reaction mechanism, the formally similar bond activations of methane by  $NiH^+$  and  $NiF^+$  prove to be different from each other as well as from the related  $PdH^+$  and  $PtH^+$  couples of the second- and third-row transition metals. In the reactions of the respective halide complexes  $NiX^+$  ( $X=F, Cl, Br, I$ ) with ethane, propane, and  $n$ -butane, a systematic shift is observed by changing the nature of both the ligand  $X$  and the substrate  $RH$ .

Based on labeling and computational studies, more than one structural isomer of  $[Ni, O, C, H_3]^+$  are generated in the gas phase by ESI. The same holds true for the nickel-water complex  $Ni(H_2O)^+$  and the formal  $Ni^{III}$  complex  $Ni(H)(OH)^+$  which are formed independently in the electrospray-ion source. The unprecedented genesis and existence of the latter complex as well as its exceptional reactivity and structural characteristics in the gas phase are reported for the first time. The expected low reactivity of the formal  $Ni^I$  complex  $Ni(H_2O)^+$  with *e. g.*  $CH_4$  or  $O_2$  contrast the high reactivity of  $Ni(H)(OH)^+$  being capable of activating C–H bonds of methane as well as molecular oxygen.



# Contents

Introduction	1
I Methods	9
1 Experiment	11
1.1 Fourier-transform ion-cyclotron resonance mass spectrometry (FT-ICR)	11
1.1.1 Motions of ions in the ICR cell	12
1.1.2 Ion excitation, detection, and isolation	13
1.1.3 Instrumental Setup	15
1.2 Electrospray-ionization mass spectrometry (ESI-MS)	16
1.2.1 Formation of gas-phase ions from solution	16
1.2.2 Instrumental Setup	19
1.2.3 Operation modes	20
2 Theoretical description of gas-phase reactions	23
2.1 Unimolecular dissociation	23
2.2 Ion-molecule reactions	25
2.3 Labeling experiments and kinetic isotope effects	27
3 Quantum-chemical methods	29
3.1 Density functional theory	33
3.1.1 DFT functionals	34
3.2 Computational details	35
II Reactivity of nickel dimers $\text{NiM}^+$ and of related cluster cations	37
4 Reactivity of homo- and heteronuclear $3d$ metal dimers $\text{M}_2^+$ and $\text{MM}'^+$	39
4.1 Reactions with cyclohexane	39
4.2 Reactions with ethane, propane, and $n$ -butane	46
III Reactivity of mononuclear nickel complexes	49

5	Reactivity of Ni <sup>I</sup> complexes NiL <sup>+</sup> (L = CO and H <sub>2</sub> O)	51
6	Reactivity of Ni <sup>II</sup> complexes	55
6.1	Reactivity of NiH <sup>+</sup> and Ni(H)(L) <sup>+</sup> (L = CO and H <sub>2</sub> O)	55
6.1.1	Reactions with methane	55
6.1.2	Thermal activation of methane by group 10 metal hydrides MH <sup>+</sup>	58
6.1.3	Excursion: $\sigma$ -bond metathesis <i>vs</i> oxidative addition	62
6.1.4	Reactions with ethane, propane, and <i>n</i> -butane	65
6.2	Reactivity of nickel-halide complexes NiX <sup>+</sup>	72
6.3	Reactivity of Ni(OH) <sup>+</sup> and [Ni,C,H <sub>3</sub> ,O] <sup>+</sup>	87
6.3.1	Reactions with ethane	89
6.3.2	Reactions with propane and <i>n</i> -butane	104
7	Reactivity of the Ni <sup>III</sup> complex Ni(H)(OH) <sup>+</sup>	109
7.1	Structure and formation of Ni(H)(OH) <sup>+</sup>	109
7.2	Activation of methane	112
7.3	Activation of molecular oxygen	115
8	Conclusions and outlook	125
	Appendix	129
A.1	Reactions of nickel dimers NiM' <sup>+</sup> with background oxygen	131
A.2	Determination of branching ratios	131
A.3	Solutions used for ESI	133
A.4	Synthesis of [ <i>all-cis</i> -1,2,3,4,5,6-D <sub>6</sub> ]-cyclohexane	134
A.5	Relevant bond length of B3LYP-calculated geometries	135
A.6	ESI source spectra of Fe, Co, and Ni halides	144
	References	145
	Publication list	161
	Curriculum Vitae	163



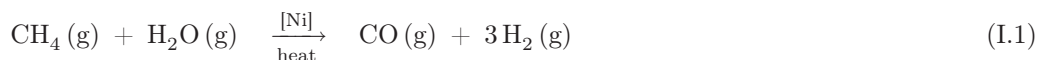
Parts of this work have been published in:

1. "Pronounced ligand effects and the role of formal oxidation states in the nickel-mediated thermal activation of methane", M. Schlangen, D. Schröder, H. Schwarz, *Angew. Chem.* **2007**, *119*, 1667; *Angew. Chem. Int. Ed.* **2007**, *46*, 1641.
2. "Specific processes and scrambling in the dehydrogenation of ethane and the degenerate hydrogen exchange in the gas-phase ion chemistry of the  $[\text{Ni,C,H}_3,\text{O}]^+/\text{C}_2\text{H}_6$  couple", M. Schlangen, D. Schröder, H. Schwarz, *Helv. Chim. Acta* **2007**, *90*, 847.
3. "Thermal activation of methane by 'bare' group 10 metal-hydride cations  $\text{MH}^+$  (M = Ni, Pd, and Pt): The same and not the same", M. Schlangen, H. Schwarz, *Angew. Chem.* **2007**, *119*, 5771; *Angew. Chem. Int. Ed.* **2007**, *46*, 5614.
4. "Ligand and substrate effects in the gas-phase reactions of  $\text{NiX}^+/\text{RH}$  couples (X = F, Cl, Br, I; R =  $\text{CH}_3$ ,  $\text{C}_2\text{H}_5$ ,  $\text{C}_3\text{H}_7$ ,  $n\text{-C}_4\text{H}_9$ )", M. Schlangen, D. Schröder, H. Schwarz, *Chem. Eur. J.* **2007**, *13*, 6810.
5. "Insertion of molecular oxygen in transition-metal hydride bonds, oxygen-bond activation, and unimolecular dissociation of metal-hydroperoxide intermediates", M. Schlangen, H. Schwarz, *Helv. Chim. Acta* **2008**, *91*, 379.

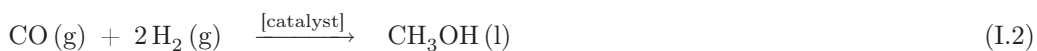


## Introduction

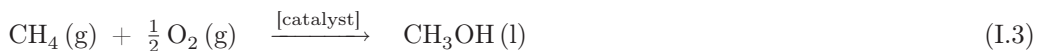
In consideration of increasingly depleted resources of fossil fuel and at the same time steadily increasing world energy demands due to appreciated progress of China, India, and other developing countries, new technology-based solutions are necessary for the 21st century to allow for an ecologically benign energy supply. Although it is important to consider a switch to long-term future alternatives such as the proposed hydrogen-based economy or nuclear fusion [1], it is critical to develop greener technologies for fossil fuel-based processes that will continue to be important in the next decade. One of the great challenges is the direct, selective oxidation of methane (reaction I.3) and higher alkanes to the corresponding alcohols.



$$\Delta_{\text{r}}H^\circ = 206 \text{ kJ mol}^{-1}$$



$$\Delta_{\text{r}}H^\circ = -91 \text{ kJ mol}^{-1}$$



$$\Delta_{\text{r}}H^\circ = -129 \text{ kJ mol}^{-1}$$

Although there are now several catalytic systems known that directly convert methane to methanol [2-9], they are not used commercially due to the high production cost. Today, methanol is almost exclusively produced from syn-gas (reaction I.2) which is a mixture of hydrogen, carbon monoxide, and  $\text{CO}_2$ . Syn-gas is mainly produced by methane steam-reforming in which methane is reacted in a highly endothermic reaction with steam over a catalyst (reaction I.1) typically based on nickel, at high temperatures. Alternative routes for the direct and selective oxidation of alkanes at lower temperatures require the development of high-performance catalysts that profits from a detailed insight into the particular role of the electronic structures of the transition metal in the elementary steps involved in these reactions.

The catalytic activity of nickel was discovered already in 1902 by Sabatier (Nobel prize in 1912) and Senderens in the methanation reaction [10], *i. e.* the reversal of Equation I.1. The catalytic reduction of carbon monoxide by molecular hydrogen is also of importance in Fischer-Tropsch synthesis [11, 12] in which a mixture of CO and H<sub>2</sub> is converted into liquid hydrocarbons. Furthermore, nickel proved to be also an active catalyst in the pioneering work of olefin-polymerization catalysis<sup>1</sup> [14–16] as well as cyclooligomerization, cycloadditions, and coupling reactions<sup>2</sup> [19–23]. Though nickel was later often displaced by other transition-metal catalysts, *e. g.* iron was mainly used in the Fischer-Tropsch synthesis [24–27] and palladium is considered as the metal of choice in cross-coupling reactions [28, 29], several recent reviews on nickel chemistry in the recent years reflect a regrowing interest in nickel catalysis [16, 30]. Nickel is also very important in biocatalysis; here, however, it has been overlooked for a long time due to inadequate analytical methods required for nickel.<sup>3</sup> Meanwhile, more sophisticated chemical analysis *e. g.* electron-spin resonance spectroscopy of <sup>61</sup>Ni-enriched material as well as atom-absorption and atom-emission spectroscopy allowed for the detection of several nickel-containing enzymes. The investigation of the associated catalytic transformations is a rapidly growing field of research in chemistry and biology [32].

Because surface defects often constitute the active sites for chemical reactions in heterogeneous catalysis, support-free transition-metal clusters may serve as a model to study the intrinsic properties of the catalysts. As demonstrated earlier, gas-phase experiment provide a powerful experimental approach to assess the inherent reactivities of the cluster ions under well-defined conditions without being obscured by ill-defined solvation, aggregation, counter ions, and other effects [33–36]. In the first part of this work, the reactivities of homonuclear transition-metal dimers M<sub>2</sub><sup>+</sup> towards small alkanes and the influence of the neighbor atom M in nickel-containing dimers NiM<sup>+</sup> have been investigated. The variation of surface textures and the combination of different transition metals are, amongst others, possible means to enhance the performance and to enlarge the number of given catalytic systems. For example, synergistic effects of different transition metals proved to bring about efficient C–N coupling reactions in gas-phase experiments with bimetallic cluster cations not being achieved by the homonuclear analogues [37–40].

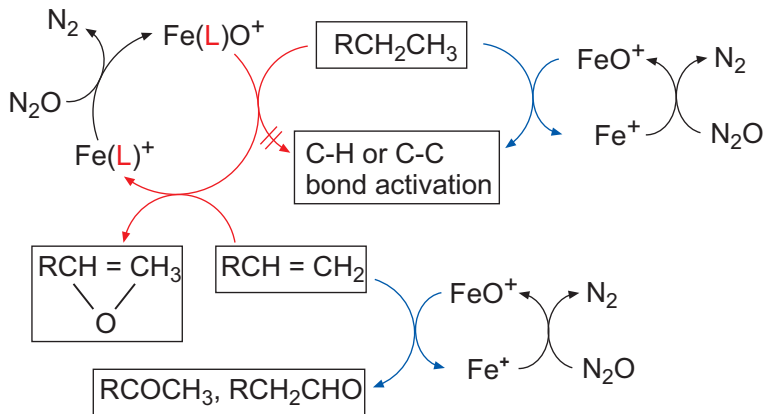
Whereas homo- and heteronuclear clusters are considered to be proper model systems to study the processes in heterogeneous catalysis on a molecular level, ligand effects constitute the counterpart for probing mononuclear, homogeneous catalysts. Reactivity studies of naked and ligated transition-metal ions in the gas phase, and in particular aspects related

<sup>1</sup> The “nickel effect”, discovered by Ziegler et al. [13] represents the starting point for the development of the Ziegler polymerization catalysts.

<sup>2</sup> Nickel-catalyzed reactions of Grignard reagents with alkenyl and aryl halides [17, 18] are often regarded as the genesis of modern cross-coupling reactions.

<sup>3</sup> Ni<sup>II</sup> complexes with physiologically relevant ligands are neither characteristic in light absorption nor they are easily accessible by Mössbauer spectroscopy. Further, nickel is often only one of several inorganic components of the enzymes [31].

to the ongoing challenge of selective activation of inert C–H and C–C bonds, have gained quite some attention in the past decades [33, 34, 36, 40–49]. Perhaps the most striking ligand effects are observed in the gas-phase reactions of 3d transition metals [50, 51]. Thus, thermalized ground-state reactions of 3d monoatomic cations do not activate methane [4, 42, 50–55], but some of the corresponding binary metal oxides exhibit remarkable reactivity [45, 56, 57]; for example,  $\text{Mn}^+$  is the last reactive 3d transition-metal cation toward alkanes, whereas  $\text{MnO}^+$  is the most reactive one [58–60].<sup>4</sup>



Scheme I.1

Clearly, coordination of a metal by a covalently bound ligand X affects considerably the electronic structure and can thus be used to control to some extent the efficiency and nature of the chemical transformations. However, “all-or-nothing” effects can also be induced by the ligation of neutral closed-shell ligands. For example, “naked”  $\text{FeO}^+$  behaves as a powerful reagent for the activation of C–H and C–C bonds [45] and also effects product isomerization during the course of an oxidation, *e. g.*, olefin  $\rightarrow$  epoxide  $\rightarrow$  aldehyde, whereas the mono-ligated species  $\text{Fe(L)O}^+$  (L = benzene, pyridine) are entirely unreactive toward bond activation of alkanes [61]. In contrast, oxygen-atom transfer from  $\text{Fe(L)O}^+$  to olefins (see Scheme I.1) occurs at the collision rate with less than 10 % formation of by-products, and - based on circumstantial evidence - formation of epoxides rather than ketones or aldehyds takes place. As the  $\text{Fe(L)O}^+$  catalyst itself can be conveniently regenerated by treating  $\text{FeL}^+$  with  $\text{N}_2\text{O}$ , with an efficiency ranging from 40–86 % depending on L, a catalytic cycle closes [36].

This example demonstrates that appropriately chosen ligands can enhance the selectivity of a reagent at the expense of reactivity [61]. Interesting ligand effects have also been

<sup>4</sup> Theoretical studies (Ref. [59]) predict  $\text{CuO}^+$  to be even more reactive than  $\text{MnO}^+$ ; however, this conjecture has not yet been probed experimentally because gaseous  $\text{CuO}^+$  cannot be made in amounts sufficient for reactivity studies (Ref. [60]).

observed in the  $\text{H}^-/\text{D}^-$  transfer from the methyl group of labeled  $N,N$ -dimethylaniline to  $\text{Fe}(\text{L})\text{O}^+$  ( $\text{L} = \text{C}_6\text{H}_6$ ,  $\text{C}_6\text{H}_5\text{CN}$ ) such that the magnitude of the kinetic isotope effect (KIE) could be varied by tuning the electronic properties of the ligand  $\text{L}$  [62]. In this work, the effect on the reactivity of nickel cations upon ligation of neutral closed-shell ligands has been investigated in the reactions of  $\text{NiL}^+$  (Chapter 5) and  $\text{Ni}(\text{H})(\text{L})^+$  (Chapter 6.1) ( $\text{L} = \text{CO}$  and  $\text{H}_2\text{O}$ ) with small alkanes.

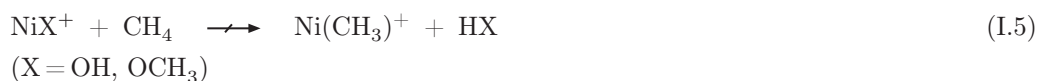
An extraordinary ligand effect was also reported for diatomic  $\text{MH}^+$  ions ( $\text{M} = \text{Fe}$ ,  $\text{Co}$ ,  $\text{Ni}$ ) (reaction I.4,  $\text{M} = \text{Fe}$ ,  $\text{Co}$ ,  $\text{Ni}$ ) [63, 64]: Whereas the naked metal ions  $\text{M}^+$  do not bring about thermal C–H bond cleavage,  $\text{NiH}^+$  activates methane at temperatures as low as 80 K,  $\text{CoH}^+$  reacts at room temperature, and for  $\text{FeH}^+$  temperatures above 600 K are required for the  $\text{H}/\text{CH}_3$  ligand exchange, which is exothermic for all three metal hydrides [65].



Computational studies revealed that the different activation parameters reflect the differences in the energy separations between the  $3d^{n-1}4^1$  and the  $3d^n$  states for  $\text{Fe}^+$ ,  $\text{Co}^+$ , and  $\text{Ni}^+$ ; the preference for the  $3d^n$  state increases from  $\text{Fe}^+$  to  $\text{Ni}^+$ . In contrast to the second-row metals which preferably bind to hydrogen with the  $4d$  rather than the  $5s$  electrons, the first-row metals tend to bind predominantly with their  $4s$  orbital instead of the  $3d$  orbitals [66–68]. Thus, the best bonds to hydrogen are obtained by using the high-spin  $4s3d^{n-1}$  state which corresponds to the ground state of  $\text{Fe}$  and to excited states of  $\text{Co}$  and  $\text{Ni}$ , being most disfavored for nickel. As a result, the ground states of the hydrides  $\text{MH}^+$  ( $\text{M} = \text{Fe}$ ,  $\text{Co}$ ,  $\text{Ni}$ ) are the high-spin states, but the separation to the corresponding low-spin states decreases from iron to nickel. In contrast, the low-spin state is favored for the transition structure of the ligand switch according to reaction I.4 since the electronic repulsion between the  $d$  orbitals of the metal and the dative  $\sigma\text{-C-H}$  bond of methane is reduced for the low-spin state. This energy profile results in a two-state reactivity (TSR) scenario (“two-state-reactivity” concept) [69–72] in which transitions from one potential-energy surface (PES) to the other take place during the course of the reaction at both the entrance and the exit channels [65]. The crossings are lower in energy with decreasing separation of the high- and low-spin states of the cations, *i. e.* in going from  $\text{Fe}^+$  to  $\text{Ni}^+$ .

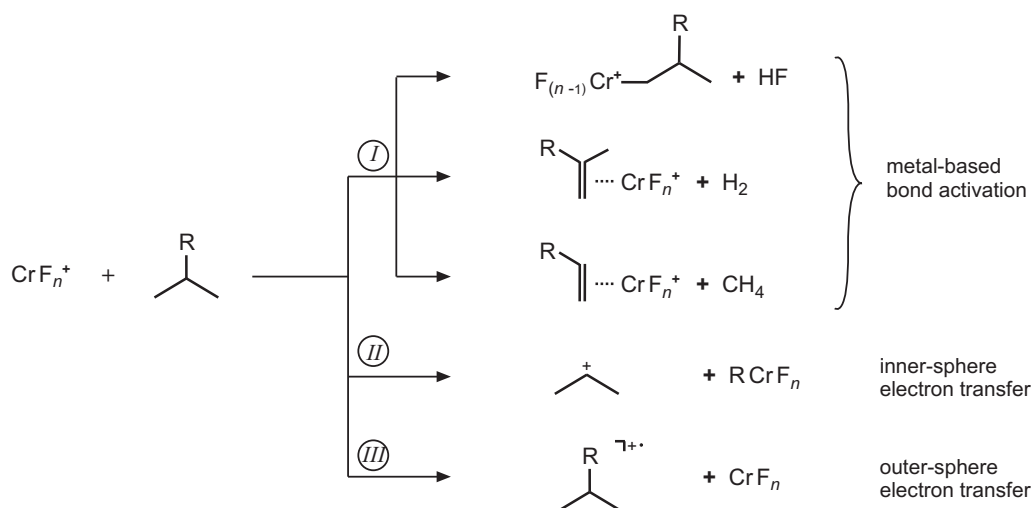
Exothermicity is not a sufficient criterion to allow for the occurrence of reaction I.4, because, for several systems with  $\text{M}^+-\text{X}$  bonds weaker than the  $\text{M}^+-\text{CH}_3$  bond, thermal activation of  $\text{CH}_4$  does not take place, and the  $\text{Ni}^{\text{II}}$  complexes described in reaction I.5 may serve as useful examples. For the  $\text{NiX}^+$  cations with  $\text{X} = \text{OH}$  and  $\text{OCH}_3$ , the  $\text{X}/\text{CH}_3$  ligand exchanges are exothermic [73, 74]; their non-occurrence points to the existence of kinetic barriers (see also [75]).

Higher alkanes are generally much more reactive than methane - which is most inert



of all hydrocarbons - for both the bare and the ligated 3*d* and 4*d* transition-metal cations [33, 42, 44, 46, 50]. Whereas being unreactive towards methane, NiX<sup>+</sup> ions (X = OH, OCH<sub>3</sub>) give rise to a rich gas-phase ion chemistry as described in Chapter 6.3 involving various types of C–H and C–C bond activation when reacted with alkanes C<sub>n</sub>H<sub>2n+2</sub> (*n* = 2–4).

The effect of halide ligands on the reactivity of 3*d* transition-metal cations has been investigated in several studies. For example, the observation that ground-state atomic Cr<sup>+</sup> does not display any reactivity toward saturated hydrocarbons [76] is striking, whereas the diatomic CrCl<sup>+</sup> reacts with alkanes larger than propane; in turn bare Fe<sup>+</sup> activates small alkanes, whereas FeCl<sup>+</sup> does not [77]. Further, it is not really surprising that not only the nature of the ligand X controls the outcome of a given ion-molecule reaction, as for example demonstrated in a systematic investigation of FeX<sup>+</sup> cations (L = H, CH<sub>3</sub>, C<sub>3</sub>H<sub>5</sub>, NH<sub>2</sub>, OH, F, Cl, Br, I) with acetone [78]; also the number of ligands as well as the substrate itself matter, and the generic reactions of CrF<sup>+</sup>/alkane complexes depicted in Scheme I.2 may serve as an illustrative example. Here, with both increasing oxidation state of chromium, that is, the number *n* of fluorine attached to it, and increasing size of the alkane, the branching ratio of the possible reaction pathway shifts from homolytic C–H and C–C bond activation (path (I)) to hydride and methanide-ion transfer (path (II)) to yield carbocations, and finally to electron transfer (path (III)) generating hydrocarbon cation radicals [79].



Scheme I.2

In Chapter 6.2, gas-phase experiments of various  $\text{NiX}^+/\text{RH}$  couples ( $\text{X} = \text{F}, \text{Cl}, \text{Br}, \text{I}$ ;  $\text{R} = \text{CH}_3, \text{C}_2\text{H}_5, \text{C}_3\text{H}_7, n\text{-C}_4\text{H}_9$ ) are described which are generated and studied under the conditions of ESI mass spectrometry. It will be shown that the richness of reactions previously observed by varying the formal oxidation state of the transition metal, as for example in  $\text{CrF}_n^+$ , can to some extent also be achieved by systematically changing the nature of the ligand  $\text{X}$  in diatomic  $\text{NiX}^+$ .

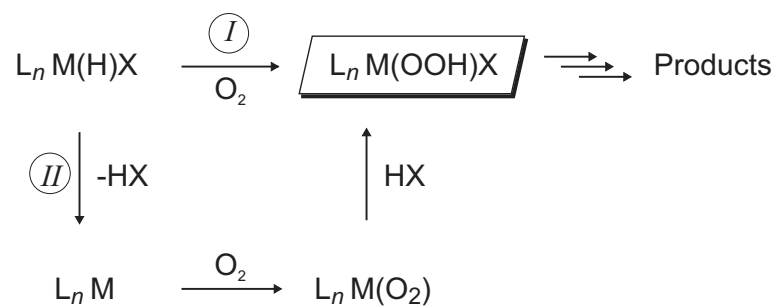
To discuss the formal oxidation state of nickel, let us return to the direct conversion of methane to methanol, reaction I.3. Practical and principal problems associated with, *e.g.* overoxidation of the starting material (“combustion”) or with spin constraints complicate these, typically spin-forbidden processes for which molecular oxygen constitutes the quintessential terminal oxidant because the reagent is available at virtually no cost and produces no environmentally hazardous by-products [80, 81].

In the gas phase, bare transition-metal monoxide cations  $\text{MO}^+$  are known to accomplish direct methane hydroxylation, among them  $\text{NiO}^+$  with nickel in the formal oxidation state +3 forming methanol efficiently from methane with a branching ratio (BR) of 100 % [59, 82, 83]. Under the conditions of ESI, a formal  $\text{Ni}^{\text{III}}$  complex  $\text{Ni}(\text{H})(\text{OH})^+$  can be generated, a structural isomer of the nickel-water complex, whose unprecedented reactivity towards methane and molecular oxygen is presented in Chapter 7.

Nature solved the specific activation of alkanes to alcohols by developing powerful metalloenzymes (*e.g.* oxidases) [84, 85], and for *in vitro* experiments numerous efficient catalytic systems, often based on palladium complexes, are now available [86]. As to the mechanism(s) of metal-mediated oxidations by molecular oxygen, several variants have been proposed [86], and of particular interest is the direct insertion of triplet oxygen into a (singlet) palladium(II)-hydride bond to generate a palladium(II)-hydroperoxide species (Scheme I.3:  $\text{M} = \text{Pd}$ ; path (I)) [87]. While the formation of genuine palladium(II)-hydroperoxides has been demonstrated experimentally to occur [88, 89], it has been difficult to mechanistically unambiguously characterize how  $\text{O}_2$  interacts with the palladium center, *e.g.* via path (I) or via reductive elimination of  $\text{HX}$  followed by  $\text{O}_2$  and  $\text{HX}$  uptakes (path (II)) [90]. Experimental evidence for the latter pathway with a N-heterocyclic palladium-carbene complex has been provided recently [91]. Computational studies suggest that, depending on the nature of the ligand  $\text{L}$  and the counterion  $\text{X}$ , in addition to Scheme I.3 quite a few mechanistic alternatives are conceivable, and the investigations of structurally more simple model complexes were recommended [92–97]. Further, for the oxidation of other late transition-metal hydrides different mechanisms, *e.g.* radical chain autoxidation, seem to exist, and examples which have been looked at include hydride complexes of  $\text{Rh}$ ,  $\text{Pt}$ ,  $\text{Co}$  and  $\text{Ir}$  [98–107]; however, neither the lighter congener of palladium and platinum, *i.e.* nickel-hydride derivatives nor iron-based compounds, have been examined.

In the context of gas-phase oxygen-activation studies aimed at uncovering intrinsic mech-





Scheme I.3

anistic features of this important class of processes numerous ionic systems have been investigated [108–122], and with regard to the above described mechanistic puzzles of metal hydride/O<sub>2</sub> couples, we have decided to explore the thermal reactions of molecular oxygen also with the transition-metal hydride cations M(H)(OH)<sup>+</sup> in the gas phase; the results are presented in Chapter 7.3. These formal M<sup>III</sup> cations were chosen for the quite extraordinary reactivity of Ni(H)(OH)<sup>+</sup> towards methane, Chapter 7.2.



## Part I

### Methods



# 1 Experiment

Two different mass-spectrometry based methods have been used for the experiments. First, Fourier-transform ion-cyclotron resonance mass spectrometry (FT-ICR MS) was applied to investigate the reactivity of transition-metal dimers  $MM'^+$  (see part II). The FT-ICR mass-spectrometry method provides advantageous features like an extremely high resolution power and the opportunity to perform  $MS^n$  experiments. Additionally, the Berlin Bruker Spectrospin CMS-47XFT-ICR mass spectrometer [123, 124] is equipped with an external cluster-ion source of the Smalley type [125] developed by the group of Niedner-Schatteburg [126] which offers the formation of charged transition-metal clusters for reactivity studies in the gas phase. The second instrument utilized is a linear quadrupole mass spectrometer which is furnished with an ESI source. This method of ion formation offers a tremendous extension of the type of ions for investigations as it enables the formation of transition-metal complexes with a vast variety in terms of the nature and numbers of ligands. By this means, several cationic nickel complexes have been generated in the gas phase and studied with respect to their structural properties and reactivity.

## 1.1 Fourier-transform ion-cyclotron resonance mass spectrometry (FT-ICR)

The introduction of FT-ICR in 1974 circumvented the disadvantage of the previously used ICR method. While in the latter all frequencies are scanned successively, in FT-ICR a broadband radio-frequency (RF) pulse is used to excite all ions simultaneously for subsequent detection of the trapped ions. The detection is based on the measurement of image currents in the detector plates. The transient free induction decay (FID) is recorded and converted from the time domain to the frequency domain by means of Fourier transformation, *i. e.* the complex FID caused by the superposition of many frequencies of the RF pulse is deconvoluted to reveal the single contributing frequencies. Because frequencies can be measured with high accuracy, FT-ICR mass spectrometry offers an inherently high resolution and thus high mass accuracy. Additionally, the ion detection is non destructive, *i. e.* the ions are not lost upon detection giving the opportunity to perform  $MS^n$  experiments. The basic principles of the ICR processes and the details of the instrumental setup of the Bruker Spectrospin CMS-47XFT-ICR mass spectrometer are described in the following sections.

## 1.1.1 Motions of ions in the ICR cell

An ion moving in a magnetic field  $\vec{B}$  is exposed to the Lorentz force  $F_L$  perpendicular to the direction of the ion motion and to the magnetic field. If the Lorentz force  $F_L$  equals the centrifugal force  $F_C$ , the relation between the magnetic field and the properties of the ion, *i. e.* the charge  $q$ , the mass  $m$ , and the velocity  $v_{xy}$  of the ion moving in the  $x$ - $y$  plane on a radius  $r$ , is given in Equation 1.1:

$$F_L = F_C \Leftrightarrow q \cdot v_{xy} \cdot B = \frac{m \cdot v_{xy}^2}{r} \quad (1.1)$$

Equation 1.1 can be modified, if  $v_{xy}$  is expressed in terms of the angular velocity  $\omega$  about the  $z$ -axis:

$$\omega = \frac{q \cdot B}{m} \quad (1.2)$$

resulting in a term for the ion-cyclotron frequency  $\omega_c$  (given in Hz):

$$\omega_c = \frac{9.648528 \cdot 10^7 \cdot B}{m/z} \quad (1.3)$$

( $B$  in tesla,  $m$  in u, and  $z$  multiples of elementary charge)

Equation 1.3 is the so called cyclotron equation that implies that the determination of a mass-to-charge ratio  $m/z$  of ions is independent from their velocity and the radius  $r$ .

Additionally to the Lorentz force  $F_L$ , the ions in the cell are exposed to a force due to the electrostatic potential  $U_{trap}$  of the trapping electrodes (Equation 1.4, see also Figure 1.3 on page 15) which prevent the ions to escape the ICR cell along the  $z$ -axis.

$$F = q \cdot \phi = q \cdot U_{trap} \cdot \left( \gamma + \frac{\alpha \cdot (2 \cdot z^2 - r^2)}{a^2} \right) \quad (1.4)$$

The parameters  $\gamma$ ,  $\alpha$ , and  $a$  are defined by the geometry of the ICR cell (for cyclinder-shaped cells such as in the Bruker Spectrospin CMS-47XFT-ICR mass spectrometer the values are:  $\gamma = 0.2787$ ,  $\alpha = 2.8404$ , and  $a = \text{cell length}$ ) and are the same for each ion. The additional force has an effect on the cyclotron resonance:

$$m \cdot \omega^2 \cdot r = q \cdot B \cdot \omega \cdot r - \frac{q \cdot U_{trap} \cdot \alpha \cdot r}{a^2} \quad (1.5)$$

The solution of Equation 1.5, quadratic in  $\omega$ , results in terms for the disturbed cyclotron

frequency  $\omega_+$  and the so called magnetron frequency  $\omega_-$ :

$$\omega_+ = \frac{\omega_c}{2} + \left( \left( \frac{\omega_c}{2} \right)^2 - \frac{\omega_z^2}{2} \right) \quad (1.6)$$

$$\omega_- = \frac{\omega_c}{2} - \left( \left( \frac{\omega_c}{2} \right)^2 - \frac{\omega_z^2}{2} \right) \quad (1.7)$$

These terms are expressed by the undisturbed cyclotron frequency  $\omega_c$  that is observed in the absence of the trapping potential and the trapping oscillation frequency  $\omega_z$ :

$$\omega_z = \sqrt{\frac{2 \cdot q \cdot U_{trap} \cdot \alpha}{m \cdot a^2}} \quad (1.8)$$

The movements of the ions in the ion-cyclotron resonance (ICR) cell is a superposition of  $\omega_-$ ,  $\omega_+$ , and  $\omega_z$ , which directions and dimensions are separately shown in Figure 1.1. As indicated, the cyclotron frequency  $\omega_+$  is usually much larger than the magnetron and trapping frequencies  $\omega_-$  and  $\omega_z$ . Thus, only the disturbed cyclotron frequency  $\omega_+$  matters for excitation and detection of the ions while  $\omega_-$  and  $\omega_z$  are generally not detected.

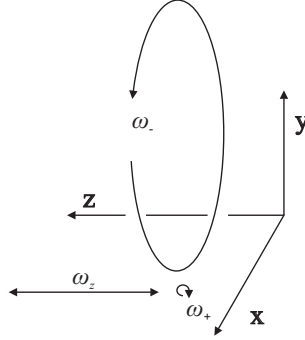


Figure 1.1 – Ion motion and frequencies in the ICR cell. The magnetic field parallels the z-axis. See also Figure 1.3.

### 1.1.2 Ion excitation, detection, and isolation

The orbital ion motion in an ICR described in the last section does not by itself generate an observable electrical signal at the detector plates of the ICR cell, because due to different injection time into the cell, ions with the same frequency and radius do not have the same phase, *i. e.* they occupy the total orbit rather than only a small sector of it. Thus, the net difference in detected charges between the detector plates is zero. Furthermore, the radius

of ions moving at room temperature are usually too small to induce a detectable signal, even if they had the same phase. To allow for the detection of the FID, an RF electric field between the excitation plates of the cell forms coherent ion packages composing of ions of the same  $m/z$  value pushed to a larger orbital radius (Figure 1.2).

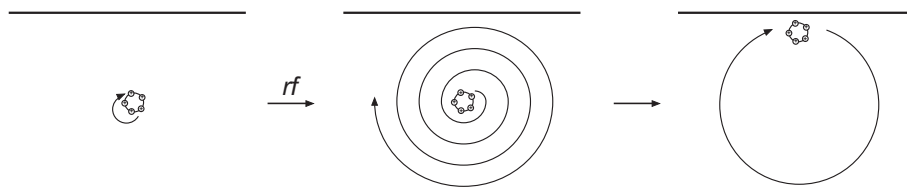


Figure 1.2 – Excitation by a pair of RF electrodes providing an alternating electric field at the ion cyclotron frequency

In addition to ion detection, ion excitation can also be applied for ion isolation by exciting the unwanted ions to orbitals larger than the radius of the ICR cell and thus giving rise to an ejection of all but the wanted ion from the cell. Several excitation modes have been developed. The Bruker Spectrospin CMS-47XFT-ICR mass spectrometer is equipped with the FERETS (“front end resolution enhancement by using tailored frequency sweeps”) technique [127], which provides the removal of unwanted ions by a combination of broad-band and single-ion ejections. Since the ideally rectangular shape of the excitation pulses deviate in reality to higher and lower frequency tailing, the ion of interest might be excited by off-resonant frequencies. The deactivation of kinetically excited ions is achieved by sufficient collisions with argon that is pulsed into the ICR cell after mass selection.

Like for ion excitation, two different acquisition modes exist for ion detection. The broad-band mode has been applied to monitor the progress of a reaction by recording the intensities of the parent and the product ions with possibly large  $m/z$  distances simultaneously (and thus a larger mass window) against the reaction time at a constant pressure. This is a prerequisite for the determination of the reaction rate. The second mode scans a much smaller mass range and allows for longer detection times and consequently for higher mass resolution. This mode was used either to confirm the ions’ elemental compositions or to assess the relative intensities for ions which possess the same nominal mass and thus cannot be distinguished in the broad-band mode. The last point is often beneficial in labeling studies, in which for example the separation between two hydrogen atoms ( $m/z$  2.01566) and one deuterium atom ( $m/z$  2.01410) might be crucial to know for the understanding and elucidation of reaction mechanisms.



## 1.1.3 Instrumental Setup

The three main functions of the Bruker Spectrospin CMS-47XFT-ICR mass spectrometer [123, 124], *i. e.* ion generation, ion transfer, and ion storage, are achieved by the three parts of the instruments, namely, the ion source, ion optics, and the ICR cell (Figure 1.3).

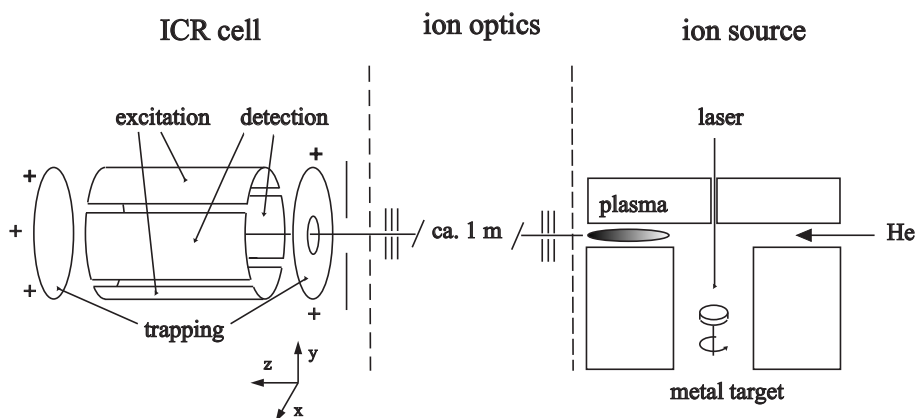


Figure 1.3 – ICR scheme

For the metal-ion generation, the fundamental of a pulsed Nd:YAG laser (Spectron Systems,  $\lambda = 1064 \text{ nm}$ , repetition rate  $5 \text{ Hz}$ ) is focused on a rotating metal target. From the generated hot metal plasma, neutral and ionic metal clusters are formed by a helium pulse that absorbs the excess energy released upon particle aggregation. The clusters are further cooled down by supersonic expansion before entering the ion optics. The latter comprises a system of electrostatic potentials and lenses by which the atomic and cluster ions are transferred to the ICR cell whereas neutral components are removed by differential pumping. The pressure in the downstream source region is about  $10^{-6} \text{ mbar}$ , whereas a high vacuum of  $1\text{--}2 \cdot 10^{-9} \text{ mbar}$  is reached in the ICR cell. The latter is located in the field of a superconducting magnet (Oxford Instruments, max. field strength  $7.05 \text{ T}$ ). After the transfer into the cell, the isolated ions can be exposed to the neutral substrates which are introduced into the cell by leak valves at stationary pressures of about  $10^{-8}$  to  $10^{-7} \text{ mbar}$ ; the pressure is measured by a calibrated ion gauge (BALZERS IMG070). Ligated species can be formed and investigated via  $\text{MS}^n$  sequences of mass selection, neutralization, and re-isolation by pulsing the proper neutral compound via one or two pulsed valves into the cell. The instrument and the data analysis is controlled by a Bruker Aspect 3000 mini computer.

## 1.2 Electrospray-ionization mass spectrometry (ESI-MS)

ESI-MS allows the “soft” transfer of ions from the liquid phase into the state of an isolated gas-phase ion which can be investigated subsequently in the mass spectrometer. The analyte is dissolved at very low concentration, typically  $10^{-6}$ - $10^{-3}$  M, in a volatile solvent. The ESI process starts with the formation of charged droplets at atmospheric pressure. The behavior of a droplet with a net electric charge that loses its solvent molecules via evaporation had been studied already in 1882 by Lord Rayleigh [128]. Due to the shrinking of the droplet, the charge density on its surface is continuously increased until the Rayleigh limit is reached. At this point, Coulomb repulsion overcomes surface tension leading to a disintegration of the droplets to smaller sub-units (for details of the shrinking process, see section 1.2.1). This Rayleigh instability has been observed by Zeleny thirty five years later [129]. He passed a stream of conducting volatile liquid through a small-bore thin-walled tube or needle maintained at a high potential relative to an opposing encounter electrode and observed the break-up of charged droplets as the solvent evaporated. Repeating sequences of droplet shrinking and subsequent disintegration lead eventually to the formation of isolated ions in the gas phase. This phenomenon is utilized in electrohydrodynamic ionization (EHI) [130, 131] as well as in ESI. In contrast to EHI, the electrostatic sprayer in ESI is performed at atmospheric pressure providing sufficient energy by the surrounding gas to vaporize volatile solvent without freezing the aerosol droplets. Thus, ESI is not limited to low-volatility solvents as EHI is. This advantage was recognized by Dole et al. in 1968 and exploited in his experiments with electrosprayed polystyrene solutions [132]. Additionally, the collisions of the ions with molecules of the ambient gas reduce their initially high kinetic energies to those of the neutral gas molecules, thereby avoiding the need for mass analyzers capable of recording high energy ions, for example, magnetic sector instruments. However, even the most expensive magnetic sector instruments, then available, were unable to analyze singly charged ions with masses larger than about ten-thousand Daltons like the high molecular weight polystyrene used in Dole’s group. The introduction of ESI to mass spectrometry was finally realized by Fenn (Nobel prize in 2002) and co-workers who coupled an ESI ion source to a quadrupole mass spectrometer. Thus, the detection of analytes with molecular weights of 100-2000 u are possible. Nowadays, beside matrix-assisted laser-desorption ionization (MALDI), ESI is the most commonly employed ionization method especially for biological applications of mass spectrometry.

### 1.2.1 Formation of gas-phase ions from solution

**Formation of charged droplets.** — In ESI-MS, a dilute solution of analyte is pumped through a capillary at a very low flow rate of 0.1 up to  $10\ \mu\text{l min}^{-1}$ . The capillary is held at either positive or negative electric potential of 2-5 kV with reference to a counter elec-

trode (skimmer); the latter constitutes the entrance to the high vacuum region of the mass analyzer. At the tip of the capillary, the liquid is exposed to an electric field which causes charge separation in the liquid and finally forms a Taylor cone (Figure 1.4) [133]. At a critical electric field strength a thin jet emerges from the cone towards the skimmer. In the so called cone-jet mode at low voltages applied, only an extension of the cone is truncated into a series of uniform droplets. With a further increase in potential, several jets are formed and identified as the multi-jet mode. This mode is unstable and thus not used for analytical purposes.

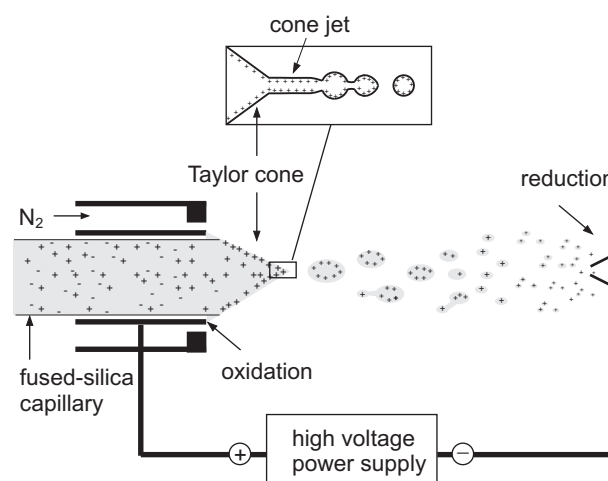


Figure 1.4 – Formation of the Taylor cone and redox processes in the ion source applying a positive ion mode

In the positive (negative) ion mode of ESI, the dominant chemical reaction at the metallic contact to the solution corresponds to oxidation (reduction) (Figure 1.4) [134]. The equivalents of electrochemical reactants consumed and electrochemical products formed in these reactions are exactly equal to the amount of charge separation that occurs at the capillary tip. This charge in turn equals exactly the amount of charge of the produced droplets and is denoted as excess charge to distinguish it from the cations and anions in the solution. The latter ions are both neutralized by the corresponding counterions and do not result in gas phase ions [135, 136].

The droplets are driven away from each other due to their charge by Coulomb repulsion, thus forming a fine spray of charged droplets (electrospray). The degree of dispersing the liquid into an aerosol depends on the flow rate of the solution and the spray voltage applied to the capillary [137]. Flow rates higher than  $10 \mu\text{l min}^{-1}$  do not produce the desired fog

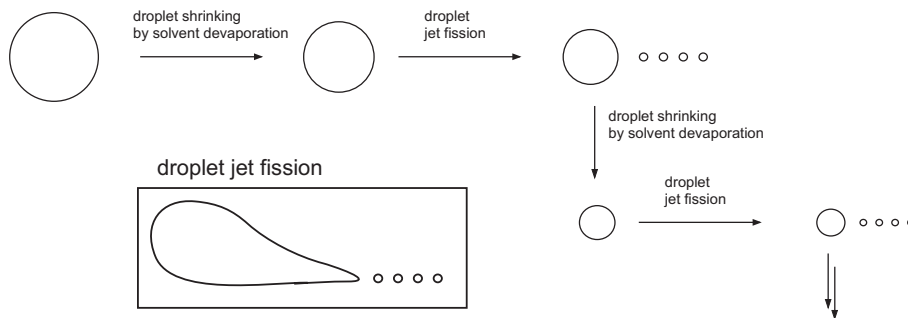


Figure 1.5 – Shrinking of the droplets by evaporation of the solvent and disintegration by Coulomb fission

but rather a stream of larger droplets. An increased voltage permits the nebulization of these droplets but initiates at the same time a corona discharge that substantially lowers the sensitivity for samples ionized in solution. Therefore, several sprayer modifications have been developed to improve the spray conditions. The design most widely used is the pneumatically assisted ESI interface [137–139] which is also applied in the experiments of this work. The electron-scavenging gas ( $N_2$ ) blows coaxially around the spray capillary and serves for the nebulizing of the liquid stream. The combination of pneumatic nebulization and an electric field tolerates higher flow rates and reduces the influence of the surface tension of the solvent used.

**Shrinking and disintegration of the charged droplets.** – Assisted by the nebulizing gas, solvent molecules are rapidly evaporated from the newborn droplets and consequently the charge density of its surface continuously increases. As mentioned above, disintegration of the droplet into smaller sub-units takes place at the Rayleigh limit, *i.e.* as soon as electrostatic repulsion exceeds the force of surface tension. This process does not proceed in a Coulomb explosion that will generate a cluster of droplets with approximately equal size as it has been assumed before. Instead, the flying droplets undergo deformation and eject a series of much smaller microdroplets from an elongated end (Coulomb fission, Figure 1.5). Thus, the flying droplets are not spherical and exhibit an inhomogeneous charge density which is significantly increased at the region of sharper curvature. Because the small microdroplets are split up from this dense-charge region, they carry only 1-2 % of the mass of the parent droplet but about 10-18 % of the parent’s charge [140, 141].

**Formation of gas-phase ions from small, highly charged droplets.** – Two mechanisms have been proposed for the formation of a gas phase ion from the small charged droplets of the electrospray. The older charged-residue model of Dole [132] was adopted for neutral macromolecules and has later been extended by Röllgen and co-workers for ions [142]. According to this model, a cascade of Coulomb fissions after evaporation of neutral solvent molecules leads to the formation of microdroplets enclosing only one molecule of the analyte. Subsequent evaporation from this ultimate droplet accompanied by charge transfer to the analyte produces a free gas-phase ion. In contrast, in the ion-evaporation model [143, 144] of Iribane and Thomson, the gas-phase ion is not formed via smaller and smaller droplet generation, but derives directly from a multiple charged microdroplet due to a field strength that is below the one necessary for Coulomb fission, but is large enough to bring about evaporation of partially solvated ions, *i. e.* ion emission becomes possible in competition with solvent evaporation.

### 1.2.2 Instrumental Setup

The ESI-MS experiments were carried out on a commercial VG BioQ mass spectrometer. The formation of gas-phase ions from solution starts from forcing the dilute sample solution filled in a Hamilton microlitre syringe by a infusion pump through a fused-silica capillary at typical flow rates of  $2\text{--}3\ \mu\text{l min}^{-1}$ . In general, many volatile, polar solvent are suitable for ESI; however, in the experiments of this work, pure water or methanol, or a mixture of both, were used as solvents. The capillary is part of the coaxial probe of the VG-BioQ and allows the simultaneous influx of sample, drying and nebulizer gas ( $\text{N}_2$ ).

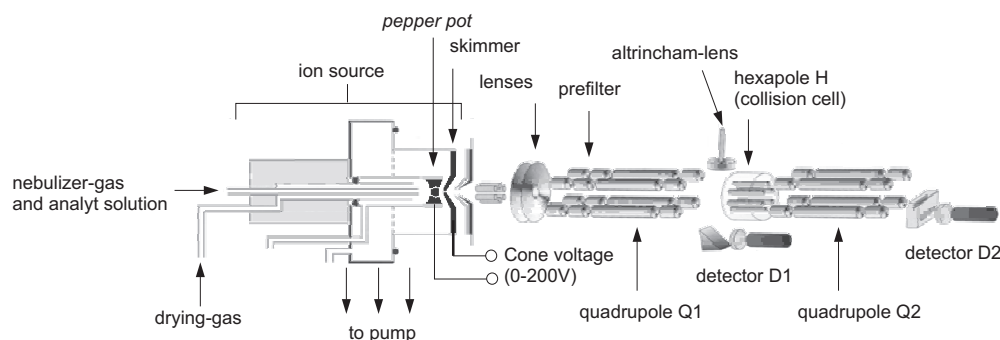


Figure 1.6 – Schematic setup of the VG-BioQ

After the transfer of the ions to the mass analyzer by the ion optics and the passage of two

prefilters, they are entering the triple-quadrupole mass spectrometer with QHQ configuration (Q: quadrupole, H: hexapole) which consists of a scanning quadrupole Q1 analyzer for separating the original precursor ion(s), an unscanned RF hexapole that serves as a collision cell to fragment the ions by collision with a noble gas or a neutral reactant molecule, and a scanning quadrupole Q2 that can separate the corresponding fragment and product ions formed in the hexapole (Figure 1.6). Depending on the operation MS mode (see below), the ions are either deflected from their linear path after their passage through Q1 by an altrincham lens and detected by detector D1 or they move forward into the hexapole collision cell. As mentioned, the hexapole is a pure RF unit without any mass-filter abilities but allows to refocus the ion beam scattered by collisions with collision gas or reactant present in the cell. After mass analysis<sup>5</sup> in Q2 the ions can be detected by detector D2. D1 and D2 exist of a Dynolite TM detector system incorporating a low-noise photomultiplier with a typical amplification factor of  $10^5$ .

High vacuum conditions are achieved by an oil diffusion pump and the pressure is controlled by active Penning and Pirani vacuum gauges. The instrument as well as data acquisition and processing is controlled by the software package MassLynx NT.

### 1.2.3 Operation modes

The degree of solvation as well as fragmentation of the gas-phase ions before entering the high vacuum region of the mass analyzer can be tuned by the potential between the nozzle and the skimmer (cone voltage); in the experiments, typical cone voltages varied from 40 to 80 V. The generation of fragment ions for further tandem MS provides a pseudo MS<sup>3</sup> operation (in a real MS<sup>3</sup> experiment, the ion is mass selected prior to the first CID stage). After entering the mass spectrometer, the ions can be exposed and analyzed either by scanning only the first analyzer Q1 or by the combined use of the two mass analyzers Q1 and Q2. The first scan mode provides an overview of the ions generated in the ion source and is hence referred to as source spectra. Further scanning techniques, making use of both mass analyzers, are:

- a) Daughter-ion scan: The daughter-ion mode is mostly used in this work and allows for reactivity studies of mass-selected ions with neutral reactants. This is done by fixing the first quadrupole to the mass of the wanted ion which then is exposed to the neutral substrate in the hexapole. Finally, the resulting product ions are scanned in Q2. The same mode of operation is also used in the CID experiments. Here, a noble gas instead of a reactant is leaked in the hexapole as collision gas. The collision energy  $E_{\text{lab}}$  and thus the degree of fragmentation can be tuned by applying various acceleration voltages at the hexapole in the order of 0-250V.

---

<sup>5</sup> In contrast to the ICR, it is not the resolution  $R = \frac{m}{\Delta m}$  but  $\Delta m$  that is constant for quadrupoles with  $\Delta m = 1$ , *i. e.* quadrupoles provide a so called unit mass resolution [145].

- b) Parent-ion scan: In the parent-ion mode, the quadrupole analyzers operate in the reversed mode as compared to the daughter-ion mode, *i. e.* the second quadrupole is set to a defined  $m/z$  value; passing through Q2 is only possible for an ion with this mass to charge ratio while its possible precursor ions are scanned by the first analyzer Q1. This mode of operation was used, for example, to uncover the different formation of two structural isomers of the ion with the formal composition  $[\text{Ni}, \text{H}_2, \text{O}]$  (see Chapter 7.1).
- c) Neutral-loss/-gain scan: In this mode of operation, the two analyzers Q1 and Q2 are used synchronously. While an ion with  $m/z = m$  is scanned in Q1, only ions with  $m/z = m + \Delta m$  pass the second analyzer and reach the detector ( $\Delta m$  is equal to neutral loss or neutral gain, respectively). Thus, only ions which undergo the same neutral loss (gain) in the hexapole-collision cell meet the demands to pass both analyzers. Neutral-loss and neutral-gain scans are convenient methods in studying drug metabolism, for example, to scrutinize the sample for ion classes which show a common fragmentation. More important in the context of the present work is the application of neutral-loss/gain scans for reactivity screening. For example, if the hexapole collision cell is filled with methane, all ions in the cell which bring about dehydrogenation of methane are monitored in a neutral-gain spectrum with  $\Delta m = +14$ . Furthermore, a gas-phase reaction in the hexapole can only be assigned to an ion which incorporates a transition metal with a characteristic isotopic pattern if the signals for each isotopomeric ion are echoed in the corresponding neutral-loss/gain spectrum.





## 2 Theoretical description of gas-phase reactions

In the present work, mass spectrometry was not used as it is mostly employed, *i. e.* for analytical purposes, but rather to examine ion-molecule reactions as well as fragmentation pathways of selected ions, that is in short: to study the chemistry of isolated ions. Several theories have been developed to describe these processes in the gas phase which shall not be reproduced here in detail; only the implications are addressed in the following sections which are helpful to interpret the experimental data.

### 2.1 Unimolecular dissociation

Since the information given by the mass-to-charge ratio are related only to the composition but not to the structure of the reactant and product ions, further experiments are helpful and fortunately available to elucidate structural properties of transition-metal complexes in the gas phase, *e. g.* ligand-exchange reactions with labeled compounds or collision-induced dissociation (CID) experiments; details of the latter are described in the following.

Reactions in the mass spectrometer take place at a pressure of  $10^{-4}$  mbar or below which are considered to correspond to single collision conditions.<sup>6</sup> In contrast to condensed phase chemistry, the reactants in the gas phase can consequently not release their excess energy absorbed for example in a CID experiment. In the quasi-eliqubrium theory (QET) as well as in the Rice-Ramsperger-Marcus-Kassel theory (RRKM theory), the collision is the starting point of a new time scale of the ensuing processes which occur under the following assumptions:

- a) Radiationless transitions: Energy release by radiation is neglected which is justified for small ions [148].<sup>7</sup>
- b) Ergodicity: The ions are regarded as micro-canonical ensembles, *i. e.* they are described as isolated systems in which the energy is randomly distributed over all degrees of

---

<sup>6</sup> According to Holmes [146], single collision conditions are determined by the portion of ions lost by the total number of collisions which lead to fragmentation, scattering, charge exchange (neutralization), charge inversion or stripping. At a pressure of about  $6 \cdot 10^{-2}$  mbar, the collision probability for single or double collisions is 10 % assuming a path of 1 cm and a collision cross section of the ion of  $5 \cdot 10^{-16}$  cm<sup>2</sup>, which correspond to 95 % to single collisions and to 5 % to double collisions (see also [147]). The probability for more than two successive collisions are equal to zero at the conditions given.

<sup>7</sup> For an example in which this assumption is not warranted, see [149].

freedom.<sup>8</sup> The time between the collision and the fragmentation is sufficient for the statistical energy distribution.

Ion dissociation occurs, if the minimum energy is concentrated in the reaction coordinate; this energy value corresponds to the activation energy  $E_a$  for fragmentation. According to QET and RRKM theory, the rate constant  $k_{(E)}$  for dissociation is proportional to the probability that at least the amount of  $E_a$  out of the randomly distributed energy is cumulated in the reaction coordinate.

Often there exist multiple fragmentation pathways of an ion leading to different  $k_{(E)}$  functions. Two different types of fragmentation can be distinguished which are connected with either a rearrangement fragmentation or a homolytic bond cleavage running through a tight or a loose transition structure, respectively. The rearrangement demands usually less activation energy, because the energy for the bond rupture is compensated by the energy gained due to the formation of new bonds. Then, the neutral fragment is expelled in a second step. Such a reaction depends on having the proper alignment for the rearrangement at the same time when sufficient energy is put into the bond to be cleaved. For a simple bond cleavage instead, there is no need for a specific orientation of the molecule while the cleavage proceeds. Here, the dissociation only requires enough energy in the respective bond. The  $k_{(E)}$  functions of the same type run often parallel, whereas  $k_{(E)}$  functions of different types cross over at an intermediate internal energy (Figure 2.1). This distinct behavior is exemplified in the fragmentation patterns of  $[\text{Ni,C,H}_3,\text{O}]^+$  in CID experiments which have been carried out to give information about which structural isomer is responsible for the puzzling reactions with ethane (see Chapter 6.3.1) and to compare the PES of this complex with related transition-metal complexes [112, 150, 151].

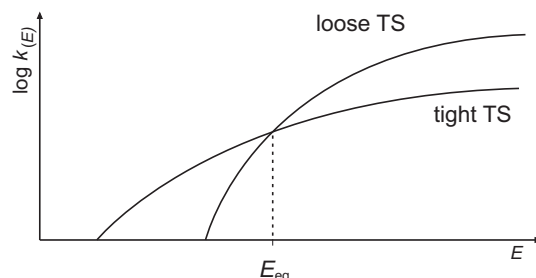


Figure 2.1 – The onset and slope of the rate constant against the internal energy depend on the mode of dissociation, *i. e.* rearrangement fragmentation or homolytic bond cleavage.

To a first approximation, the energy dependence of the CID fragments can be described

<sup>8</sup> A micro-canonical ensemble possesses constant energy, a constant volume, and a constant number of particles. In QET and RRKM theory, the statistical distribution over the degrees of freedom substitutes the equilibration between particles.

by the sigmoid functions given in Equation 2.1; for the parent ion M, the relation is given by Equation 2.2.

$$I_i(E_{\text{CM}}) = \frac{BR_i}{1 + e^{(E_{1/2} - E_{\text{CM}}) \cdot b_i}} \quad (2.1)$$

$$I_M(E_{\text{CM}}) = 1 - \sum \frac{BR_i}{1 + e^{(E_{1/2} - E_{\text{CM}}) \cdot b_i}} \quad (2.2)$$

Here,  $b$  (in  $\text{eV}^{-1}$ ) describes the rise of the sigmoid curve and thus the phenomenological energy dependence,  $BR_i$  stands for the branching ratio of a particular product ion ( $\sum BR_i = 1$ ),  $E_{1/2}$  is the energy at which the sigmoid function has reached half of its maximum, and  $E_{\text{CM}}$  is the collision energy in the center-of-mass frame (Equation 2.3),

$$E_{\text{CM}} = \frac{z \cdot m_T}{m_T + m_I} \cdot E_{\text{lab}} \quad (2.3)$$

where  $z$  is the ion's charge,  $m_T$  and  $m_I$  stand for the masses of the collision gas and the ion, respectively.

## 2.2 Ion-molecule reactions

As for unimolecular dissociations also for ion-molecule reactions several theories have been developed. Already in 1905, Langevin introduced an expression for the collision rate  $k_L$ , based on the kinetic theory of gases, to quantify the collisions between an ion with the charge  $q$  and a neutral molecule with the polarizability  $\alpha$  (Equation 2.4), that together possess the reduced mass  $m_r$  [152].

$$k_L = 2\pi q \sqrt{\frac{\alpha}{m_r}} \quad (2.4)$$

The Langevin theory has later been improved to the average-dipole orientation (ADO) theory, developed by Su and Bowers [153], by taking the dipole moment of the neutral reactant into account. Beside  $\alpha, m_r$ , and  $q$ ,  $k_{\text{ADO}}$  is also a function of the dipole moment  $\mu_D$  and the temperature  $T$ . Considering the conservation of angular momentum, further refinements have been achieved in the capture theory with the collision rate  $k_{\text{cap}}$  presented by Su and Chesnavich [154, 155]. The differences of the collision rates  $k_L$ ,  $k_{\text{ADO}}$ , and  $k_{\text{cap}}$  depend on the permanent dipole moment  $\mu_D$ ; since  $\mu_D$  is zero for all substrates used in the ICR experiments of the present work (methane, ethane, propane, *n*-butane, and cyclohexane), all theories yield the same value for the collision rate, *i. e.*  $k_L = k_{\text{ADO}} = k_{\text{cap}}$ .

The collision rate provides a value for the maximum reaction rate constant and consequently serves as a reference to the rate constant  $k$ . The relation of reaction rate and collision rate yields the efficiency  $\phi$  of a reaction which represents the percentage of collisions resulting in a reaction (including adduct formation); the remaining part of the collisions leads to re-dissociation of the encounter complex into the reactants.

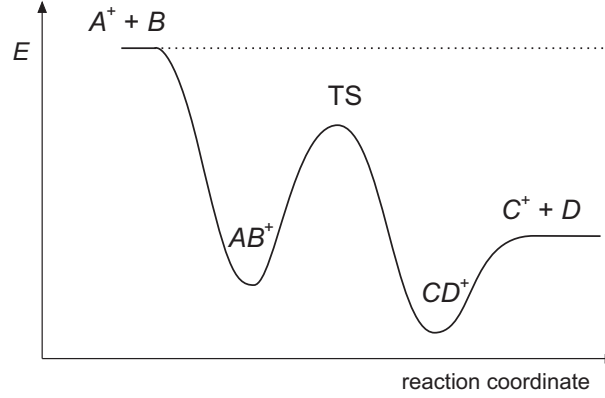


Figure 2.2 – Double minimum potential of an ion-molecule reaction.

In general, the formation of the encounter complex  $AB^+$  between an ion  $A^+$  and a neutral molecule  $B$  in the gas phase is exothermic. Whether a subsequent reaction takes place or not depends on the relative energies of the transition structure TS and the products with respect to the entrance channel, *i. e.* separated  $A^+$  and  $B$  (Figure 2.2). Clearly, if no reaction is observed, either the transition structure or the exit channel is higher in energy in comparison to the educts. Furthermore, the lower the energy of both, the higher is the efficiency.

Because neutral molecules  $B$  are continuously leaked into the reaction cell at a constant pressure and since its amount largely exceeds the number of ions  $A^+$ , the reaction rate can be determined according to a pseudo first-order reaction in the intensity  $[A^+]$  (Equation 2.5).

$$\frac{d[A^+]}{dt} = -k[B][A^+] \cong -k_{\text{exp}}[A^+] \quad (2.5)$$

$$\Leftrightarrow \ln[A^+] = -k_{\text{exp}} \cdot t \quad (2.6)$$

Recording the temporal decline of the reactant-ion intensity at a constant pressure, the experimentally observed reaction-rate constant  $k_{\text{exp}}$  is given by the slope of  $\ln[A^+]$  against the reaction time  $t$  according to Equation 2.6. For the calculation of the absolute rate constant  $k$  the knowledge of  $[B]$  is required which depends not only on the pressure but also

on the relative ion-gauge sensitivity  $R$  towards  $B$  [156, 157] and the calibration factor  $F$ ; the latter has to be determined routinely by calibrating the ion gauge. Since the determination of the absolute pressure by the ion gauge is of limited accuracy [156, 157], the uncertainties associated with  $k$  amount to 30 % [158].

For the reactions investigated in the ESI experiments, only relative but not absolute rate constants  $k_{\text{rel}}$  are obtained by measuring reactant- and product-ion intensities at varied pressures, since the exact time needed for an ion to pass the reaction cell (*i. e.* hexapole) of the VG BioQ mass spectrometer is not known. As a measure of the effects of  $L$  and  $X$  ( $L$  = neutral, closed-shell ligand;  $X$  = covalently bonded, open-shell ligand) as well as the substrates  $RH$  on the reactivity of the various  $NiL^+/RH$  and  $NiX^+/RH$  couples, the overall reaction rates  $k_{\text{rel}}$  presented in this Thesis and obtained by measurements at the VG BioQ, are given relative to the most reactive system, that is,  $NiBr^+/C_3H_8$  with  $k_{\text{rel}} = 100$ , unless noted otherwise.

## 2.3 Labeling experiments and kinetic isotope effects

Isotopic labeling at a specific position offers valuable information about the regioselectivity of bond activation, and labeled studies are widely used to elucidate reaction mechanisms in the gas phase as well as in condensed media. Furthermore, the isotopic substitution might cause a change in the reaction-rate constant. When measuring isotope effects for reactions involving a substitution of hydrogen by deuterium, the kinetic isotope effect (KIE) is expressed as  $k_H/k_D$ . The measurement of isotope effects thus requires to run two kinetic analysis or to design a proper competition experiment; this alternatives are referred to intermolecular *vs* intramolecular isotope effects, respectively.

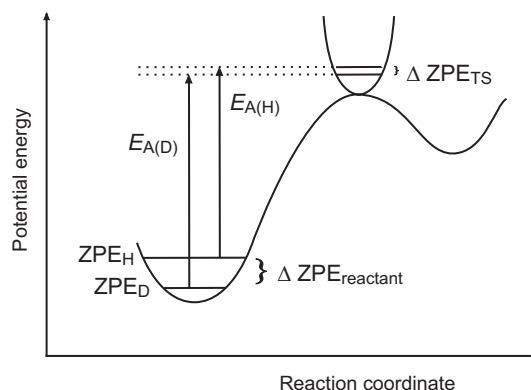
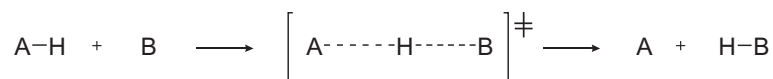


Figure 2.3 – Reaction coordinate of labeled and unlabeled compounds. The difference between  $E_{A(H)}$  and  $E_{A(D)}$  are one of the reasons for kinetic isotope effects.

Due to different reduced masses  $\mu$ , the zero-point energy (ZPE) of a deuterated compound ( $\text{ZPE}_\text{D}$ ) and of the respective unlabeled molecule ( $\text{ZPE}_\text{H}$ ) are different (Figure 2.3). Furthermore, the ZPEs alter in the course of a reaction from the reactant to the transition structure resulting in a difference between  $\Delta\text{ZPE}_\text{TS}$  and  $\Delta\text{ZPE}_\text{reactant}$ . Consequently, the activation energies  $E_{\text{A(H)}}$  and  $E_{\text{A(D)}}$  of the labeled and unlabeled compound are shifted thus causing a KIE. The vibrational modes that have the largest force constants and those that undergo the largest changes have the greatest influence on the isotope effect.

$$\text{ZPE} = \frac{1}{2} \cdot h \cdot \nu = \frac{h}{4\pi} \sqrt{\frac{f}{\mu}} \quad (2.7)$$

The value of a KIE depends on the difference  $\Delta\text{ZPE}_\text{reactant}$  and reaches its maximum if the vibrational energy of the transition structure is the same for both isotopomers, *i. e.*  $\Delta\text{ZPE}_\text{TS} = 0$ . The vibration mode that defines the reaction coordinate of a bond breaking is transferred into a translational degree of freedom in the associated transition structure [159] and thus does not affect its vibrational energy. However, vibration modes developed at the transition structure that have no analog in the reactant may render  $\Delta\text{ZPE}_\text{TS}$  to non-zero and thus diminish the KIE. In this respect, the symmetric stretching vibration is of highest importance, Scheme 2.1.



Scheme 2.1

$\Delta\text{ZPE}_\text{TS}$  is the largest, if the extent of *e. g.* hydrogen-atom transfer in the transition structure is either very low or very pronounced; a more symmetric transition structure results in smaller  $\Delta\text{ZPE}_\text{TS}$  and thus in a larger KIE since in this case the movement of the H(D) atom has a minor effect on the vibrational energy.

Isotopic substitution at a bond that is not being broken can also influence the ZPE. This kind of KIE has been coined secondary KIE and originate mainly from a change in hybridization but can also be traced back to hyperconjugation or steric effects. For rehybridization, for example, bending modes experience the largest changes; the appropriate force constants are higher for a  $\text{C}(sp^3)\text{-H}$  bond compared to  $\text{C}(sp^2)\text{-H}$ . Thus, a rehybridization from  $sp^3$  to  $sp^2$  diminishes  $\Delta\text{ZPE}_\text{TS}$  relative to  $\Delta\text{ZPE}_\text{reactant}$  and consequently causes a *normal* KIE, *i. e.*  $k_\text{H}/k_\text{D} > 1$ , whereas a rearrangement from  $sp^2$  to  $sp^3$  leads to  $\Delta\text{ZPE}_\text{TS} > \Delta\text{ZPE}_\text{reactant}$  and thus induces an *inverse* KIE with  $k_\text{H}/k_\text{D} < 1$ .

### 3 Quantum-chemical methods

The knowledge of the geometry of the reactants, intermediates, transition structures, and products and their associated relative energies, obtained by quantum-chemical calculations, provides valuable information about the mechanism of a chemical reaction [160–162]. Furthermore, insight in the electronic structure allows the assignment of a reaction proceeding solely on the ground state PES or crossing from one spin state to another according to the TSR concept. The reactions of  $\text{NiH}^+$ ,  $\text{PdH}^+$ , and  $\text{PtH}^+$ , for example, cannot be distinguished mechanistically by experiment; however, as revealed by theory, the mechanistic details are different for all three cations (see Chapter 6.1.2).

Each operator in quantum mechanics is associated with an observable in classical mechanics; the Hamilton operator  $\hat{H}$  (Equation 3.1) belongs to the total energy of the system [163].

$$\hat{H} = - \underbrace{\sum_n \frac{p_n^2}{2M_n}}_{T_n} - \underbrace{\sum_i \frac{p_i^2}{2m}}_{T_e} + \underbrace{\frac{1}{2} \sum_{nn'} \frac{Z_n Z_{n'} e^2}{|R_n - R_{n'}|}}_{V_{nn'}} + \underbrace{\frac{1}{2} \sum_{ij} \frac{e^2}{|r_i - r_j|}}_{V_{ee}} - \underbrace{\sum_{in} \frac{Z_n e^2}{|R_n - r_i|}}_{V_{ne}} \quad (3.1)$$

Here,  $R_n$  and  $p_n$ ,  $r_i$ , and  $p_i$  represent the positions and momenta of the nuclei and the electron, respectively.  $Z_n$  and  $M_n$  are the atomic number and the mass of nucleus  $n$ , and  $m$  stand for the electron mass. The kinetic-energy terms of the nuclei and the electrons are denoted as  $T_n$  and  $T_e$ , respectively; the Coulomb-interaction terms are described by  $V_{nn'}$ ,  $V_{ee}$ , and  $V_{ne}$  (core-core, electron-electron, and core-electron, respectively).

The associated non-relativistic, time-dependent Schrödinger equation (Equation 3.2) plays a central role in computational chemistry for the properties of molecules which - in principle - are all known by solving the Schrödinger equation for the total wave function  $|\Psi(x, R, t)\rangle$  depending on the spatial and spin coordinates  $x$  of the electrons, the spatial coordinates  $R$  of the nuclei, and the time  $t$ . However, an analytic solution is only possible for one-electron systems and although a numerical solution could be obtained also for many-body systems, it is impossible in practice; thus, approximations have to be employed.

$$i\hbar \frac{\partial}{\partial t} |\Psi(x, R, t)\rangle = \hat{H} |\Psi(x, R, t)\rangle \quad (3.2)$$

The first assumption is the time-independency of  $\hat{H}$ ; this is appropriate as long as the system does not experience any time-dependent external forces. It allows for the application of the separation ansatz (Equation 3.3) on the time-dependent Schrödinger equation (Equation 3.2) and yields the time-independent Schrödinger equation (Equation 3.4).

$$\Psi(x, R, t) = f(t) \cdot \psi(x, R) \quad (3.3)$$

$$\hat{H} | \psi(x, R) \rangle = E | \psi(x, R) \rangle \quad (3.4)$$

The second and more significant restriction, the Born-Oppenheimer approximation, permits the separation of the electron movements from the nuclei motion; thus, the total wave function can be factorized again in two wave functions ( $\xi(R)$  for the nuclei and  $\phi(x; R)$  specifying the electrons, Equation 3.5). In 1923, Born and Oppenheimer noted that nuclei are much heavier than electrons and move on a time scale which is about two orders of magnitude longer than that of the electrons. It is therefore sensible to regard the nuclei as fixed as far as the electronic part of the problem is concerned. Hence, the nuclear kinetic energy  $T_n$  is reduced to zero and the core-core potential  $V_{nn}$  is constant for a given geometry. Accordingly,  $T_n$  in the electronic Schrödinger equation (Equation 3.6) is omitted from the total Hamiltonian  $\hat{H}$  yielding the remaining electronic Hamiltonian  $\hat{H}_{el}$ , in which the nuclear positions  $R$  enter as parameters. Presuming that the electrons respond instantaneously to the nuclear motion, the variation of the nuclear positions maps out a multi-dimensional ground-state PES.

$$\psi(x, R) = \phi(x; R) \cdot \xi(R) \quad (3.5)$$

$$\begin{aligned} \hat{H}_{el}\phi(x; R) &= - \underbrace{\sum_i \frac{p_i^2}{2m}}_{T_e} + \underbrace{\frac{1}{2} \sum_{nn'} \frac{Z_n Z_{n'} e^2}{|R_n - R_{n'}|}}_{V_{nn'}=const.} + \underbrace{\frac{1}{2} \sum_{ij} \frac{e^2}{|r_i - r_j|}}_{V_{ee}} - \underbrace{\sum_{in} \frac{Z_n e^2}{|R_n - r_i|}}_{V_{ne}} \\ &= E_{el}\phi(r_i; R_n) \end{aligned} \quad (3.6)$$

Continuing with the electronic Schrödinger equation, further approximations are inevitable to describe the electron-electron interaction  $V_{ee}$  (Equation 3.6) depending on the coordinates of all the electrons. To tackle the mutual impact of the electrons, the independent-particle approximation is introduced, in which the interaction of each electron with all the others is



treated in an average way. This is done by splitting the wave function for  $N$  electrons into  $N$  one-electron wave functions (Equation 3.7).

$$\psi(x_1, x_2, \dots, x_N) = \chi_1(x_1) \chi_2(x_2) \dots \chi_N(x_N) \quad (3.7)$$

The one-electron wave functions  $\chi_i(x_i)$  in Equation 3.7 are composed of the space function  $\psi_i(r_i)$  and either spin function  $\alpha(i)$  or  $\beta(i)$ . They are described in terms of Slater determinants (Equation 3.8), to account for the Pauli principle, *i. e.* to ensure the wave function to be antisymmetric upon permutation of two electrons.

$$\psi_{HF}(x_1, x_2, \dots, x_N) = \sqrt{\frac{1}{N!}} \begin{vmatrix} \chi_1(x_1) & \cdots & \chi_N(x_1) \\ \vdots & \ddots & \vdots \\ \chi_1(x_N) & \cdots & \chi_N(x_N) \end{vmatrix} \quad (3.8)$$

The set of spin orbitals that gives the best description of the system in its ground state is obtained by application of the variational principle to the Slater determinant, which leads to the pseudo-Eigenwert problem given in Equation 3.9.

$$\hat{F}(r_1) | \chi_i(x_1) \rangle = \epsilon_i | \chi_i(x_1) \rangle \quad (3.9)$$

Here, the Fock-operator  $\hat{F}$  corresponds to the orbital energy  $\epsilon_i$  of spin orbital  $i$ . It consist of a one-electron operator  $\hat{h}$  (kinetic energy of the electron and electron-nuclei interaction) and the sum of two-electron operators: the Coulomb operator  $\hat{J}$  and the exchange operator  $\hat{K}$  (Equation 3.10). The first one describes the classical interaction of electron 1 with the averaged potential of electron 2. The effect of the second operator  $\hat{K}$  is called exchange interaction between the two electrons for which no analogon in classical mechanics exists. The corresponding exchange integral is unequal to zero only for electrons 1 and 2 possessing the same spin functions. Because  $\hat{J}$  and  $\hat{K}$  depend on the solutions of Equation 3.9, *i. e.* the spin orbitals  $\chi_i$ , the latter are only obtainable by iteratively optimization of trial orbitals

until a self-consistent solution (self-consistent field (SCF)) is reached.

$$\hat{f} = \underbrace{\frac{p_1^2}{2m} - \frac{Z_n e^2}{|R_n - r_1|}}_{\hat{h}} + \underbrace{\sum_j \int \chi_j(2)^* \chi_j(2) \frac{1}{|r_1 - r_2|} dr_2}_{\hat{j}} - \underbrace{\sum_j \left[ \int \chi_j(2)^* \chi_i(2) \frac{1}{|r_1 - r_2|} dr_2 \right] \chi_j}_{\hat{K}} \quad (3.10)$$

The Coulomb and exchange integrals include the interactions of one electron with all the others. Thus, the system's total energy  $E_{HF}$  (Hartree-Fock energy) is not the sum of the energies  $\epsilon_i$  of the occupied orbitals since the contribution of the electron-electron interaction is too high by a factor of 2. This taken into account in the expression for  $E_{HF}$  (Equation 3.11).

$$\begin{aligned} E_{HF} &= \sum_i \langle \chi_i | \hat{f} | \chi_i \rangle \\ &= \sum_i \langle \chi_i | h | \chi_i \rangle + \frac{1}{2} \sum_i \sum_j (ii | jj) - (ij | ji) \end{aligned} \quad (3.11)$$

with the

$$\begin{aligned} \text{one electron integrals} \quad & \langle \chi_i | \hat{h} | \chi_i \rangle = \int \chi_i^*(1) \hat{h} \chi_i(1) dr_1 \\ \text{Coulomb integrals} \quad & (ii | jj) = \int \chi_i^*(1) \chi_i(1) \frac{1}{|r_1 - r_2|} \chi_j^*(2) \chi_j(2) dr_1 dr_2 \\ \text{exchange integrals} \quad & (ij | ji) = \int \chi_i^*(1) \chi_j(1) \frac{1}{|r_1 - r_2|} \chi_j^*(2) \chi_i(2) dr_1 dr_2 \end{aligned}$$

The difference between the exact energy and  $E_{HF}$  is the so called correlation energy which is subdivided into dynamic and non-dynamic correlation energy. Dynamic correlation means the neglect of the instantaneous interaction of electrons due to the average treatment of the interaction of electron  $i$  with the other  $N - i$  electrons of the system. The non-dynamic correlation accounts for the strong mixing of low-lying excited or nearly degenerate states, and this term is especially pronounced in open-shell systems.

### 3.1 Density functional theory

The basis of density-functional theory (DFT) can be traced back to the Hohenberg-Kohn theorem which states the existence of a functional that assigns a given density function to a corresponding energy value [164] (see also [162]). Thus, not the wave function itself but the square of the wave function  $\chi_i^2$  is the decisive parameter which is interpreted as the probability density  $\rho(i)$  associated with the position of the electron  $i$ . However, no formalism for the derivation of the corresponding functionals of the electron density is provided; furthermore, explicit expressions do not exist for all of the terms that contribute to the total energy. To begin with, only the Coulomb term for the electron-nuclear attraction,  $V_{ne}$ , is exactly given by  $\rho$ :

$$V_{ne}(1) = \left\langle \chi_i(1) \left| \sum_n \frac{Z_n e^2}{|R_n - r_1|} \right| \chi_i(1) \right\rangle = - \sum_n \int \frac{Z_n e^2}{|R_n - r_1|} \rho(1) dr_1 \quad (3.12)$$

The electron-electron interaction  $V_{ee}$  and the kinetic energy  $T_e$  of the electrons instead are not defined by the electron density. For the former, only the Coulomb and not the exchange term is specified (Equation 3.13), and for the latter exists no explicit expression as a function of  $\rho(i)$ .

$$V_{ee}(1) = \underbrace{\frac{1}{2} \int \frac{\rho(1)\rho(2)}{|r_{12}|} dr_1 dr_2}_{\text{Coulomb term}} + \text{“remainder”} \quad (3.13)$$

To yield a relation between  $T_e$  and  $\rho(i)$ , the Kohn-Sham-Method is applied, *i. e.* the orbitals with the lowest kinetic energy of the electron – like in the SCF method – are optimized which then reproduce a related electron density (Equation 3.14). The difference between the exact kinetic energy  $T_e$  and the one obtained in the Kohn-Sham-method ( $T_{KS}$ , Equation 3.14) is combined with the “remainder” in Equation 3.13 in the so called exchange-correlation energy  $E_{XC}(\rho)$ . It represents one of the density functionals for the total DFT energy  $E(\rho)$  expressed in terms of  $\rho$  (Equation 3.15) with  $V_{ne}$  and the Coulomb term merged to  $U(\rho)$ .

$$T_{KS}(\rho) = \sum_i \left\langle \chi_i \left| \frac{p_i^2}{2m} \right| \chi_i \right\rangle \quad (3.14)$$

$$E(\rho) = T_{KS}(\rho) + U(\rho) + E_{XC} \quad (3.15)$$

The terms in Equation 3.15 are incorporated in the Kohn-Sham operator  $\hat{F}_{KS}$  which yields the Kohn-Sham molecular orbital by the iterative solution of the Kohn-Sham equations Equation 3.16.

$$\left[ \frac{p_1^2}{2m} + \sum_n \frac{Z_n e^2}{|R_n - r_1|} + \int \frac{\rho(2)}{|r_{12}|} dr_2 + V_{XC} \right] \chi_i = \epsilon_{KS} \chi_i \quad (3.16)$$

### 3.1.1 DFT functionals

The result obtained by Equation 3.16 is still exact, because so far no approximations have been used. However, as mentioned before, an explicit expression for  $E_{XC}$  by the electron density is not known. In order to find adequate approximations, several functionals have been developed. A simple approximation is the local density approximation (LDA) based on the homogeneous electron gas which assumes that the electron density in a system is either constant or varies only slowly with position (Equation 3.17).

$$E_{XC}^{LDA}[\rho] = \int \rho(r) \epsilon_{XC}[\rho(r)] dr \quad (3.17)$$

From the many expressions developed for the  $\rho$ -dependency of  $\epsilon_{XC}$ , that of Vosko, Wilk, and Nusair has gained quite some importance [165]. However, this approximation of a constant electron density might be appropriate for the description of bulk metal systems, it does not meet the requirements given in a molecule, where the density is strongly inhomogeneous. The resulting overbinding, for example, is a well-known problem because the lower the surface the lower is the energy in LDA, thus favoring bound molecules in comparison to the separated fragments. In order to resolve this handicap, the so-called non-local corrections were introduced taking into account the gradient of the electron density. Well-known non-local corrections have been developed by Becke [166] and Perdew [167, 168] which are often used in combination as BP functionals, *e. g.* the BP86 functional which is composed of an exchange functional  $E_X$  of Becke and a functional for correlation  $E_C$  of Perdew. Also established are non-local functionals introduced by Lee, Yang, and Parr (LYP) [169].

*Hybrid functionals.*— While in HF based methods no correlation interactions are taken into account, the approximation for the exchange-correlation functional  $E_{XC}$  in DFT already

includes correlation contributions. In contrast, the exchange interaction is exact in HF methods and accordingly less accurate in DFT. The incorporation of the proper exchange interaction from HF methods into the DFT formalism can thus improve the accuracy. This is achieved in hybrid methods like B3LYP and B3LYP (Equations 3.18) and 3.19 in which weight factors for the exact exchange  $E_X^{SCF}$  in Equations 3.18 and 3.19 are determined semi-empirically by fitting parameters to experimental heats of formations. Despite the approximations used in these calculations, the hybrid methods often yield surprisingly good results. Particularly, the B3LYP method is a powerful tool for the derivation of geometries and it has proven to be very useful in the performance of cost-efficient calculations on many molecular systems; however, in some cases it was found that B3LYP tends to overestimate bond energies quite substantially. Further, the self-interaction error in local DFT, *i. e.* the unphysical interaction of an electron with itself, can lead to an underestimation of barrier heights [170–172].

$$E_{B3LYP} = 0.5E_X^{LDA} + 0.5E_X^{SCF} + 0.5E_X^B + 0.5E_C^{LDA} \quad (3.18)$$

$$E_{B3LYP} = 0.8E_X^{LDA} + 0.2E_X^{SCF} + 0.72E_X^B + 0.81E_C^{LYP} + 0.19E_C^{LDA} \quad (3.19)$$

Recently, the M06 suite of complementary functionals have been introduced by Truhlar and co-workers [172, 173] which are adapted to given chemical aspects, *e. g.* transition-metal bonding, non-covalent interactions, electronic excitation energies etc.. However, the B3LYP functional is applied for comparison throughout for the chemical questions addressed in the present work; the use of B3LYP for a *qualitative* interpretation of reactions observed (or not observed) experimentally is regarded as more than justified.

### 3.2 Computational details

In the computational studies, the geometries were optimized at the B3LYP level of theory [169, 174] as implemented in the Gaussian03 programme package [175], using basis sets of approximately triple- $\zeta$  quality. For Ni as well as for H, C, and O atoms, these were the triple- $\zeta$  plus polarization basis sets (TZVP) of Ahlrichs and co-workers [176]. For palladium, the Stuttgart-Dresden scalar-relativistic pseudopotentials (ECP28MWB replacing 28 core electrons) were employed in conjunction with the corresponding (8s,7p,6d)/[6s,5p,3d] basis set describing the  $4s5s4d$  valence shell of Pd [177–179]. The accuracy of this qualitative approach is in the order of  $\pm 20 \text{ kJ mol}^{-1}$  for relative energies of isomers [180] (see also [162]). The nature of the stationary points as minima or saddle points was characterized by (unscaled) frequency analysis, and intrinsic reaction coordinate calculations were performed

to link transition structures with the intermediates [181–183].

## Part II

Reactivity of nickel dimers  $\text{NiM}^+$  and of related cluster  
cations





## 4 Reactivity of homo- and heteronuclear $3d$ metal dimers $M_2^+$ and $MM'^+$

The starting point of the present work are reactivity studies of the cationic nickel dimer  $Ni_2^+$  in the gas phase. The gas-phase reactivities of *atomic* transition-metal ions  $M^+$  have been investigated in detail previously and a large number of gas-phase studies revealed a high reactivity of gaseous first-row metal cations toward alkanes. C–H and/or C–C bond activation of small alkanes, starting from propane, is observed for all  $3d$  metal cations except for  $Cr^+$ ,  $Mn^+$ ,  $Cu^+$ , and  $Zn^+$  [33]. In comparison, most of the  $3d$  dimers  $MM'^+$  are not as reactive as their mononuclear counterparts. For example, while naked  $Co^+$  brings about C–H bond activation of propane, no reaction takes place if  $Co_2^+$  is exposed to propane in the gas phase.  $Ni_2^+$  is an exception, *e. g.* ethene is dehydrogenated by the dimer, but not by  $Ni^+$  [53]. In the following Chapter, the reactivity patterns of  $3d$  metal dimers towards small linear alkanes and cyclohexane are described. The first section deals with the reactions of cyclohexane which have been investigated for each homonuclear  $M_2^+$  with  $M = Ti - Cu$ . In addition, the reactions of the heteronuclear dimers  $NiM^+$  ( $M = Ti, Mn, Fe, Co, Cu$ , and  $Al$ ) with cyclohexane have been examined to determine the influence of  $M$  in  $NiM^+$  on the reactivity, because  $Ni_2^+$  exhibits a very high efficiency in the reactions with cyclohexane. Furthermore, the features of nickel-containing dimers  $NiM^+$  ( $M = Fe, Co$ , and  $Ni$ ) appeared to be also peculiar as noted in another related study [184, 185]. For the same reason, the investigations with linear alkanes are focused mainly on nickel-containing clusters which are described in section 4.2. Because  $CoCu^+$  possesses the same number of electrons as  $Ni_2^+$ , this dimer has also been included in the investigations. It will be shown that the reactivity patterns of the dimers  $NiM^+$  with cyclohexane and linear alkanes vary remarkably with respect to  $M$ .

### 4.1 Reactions with cyclohexane

As already mentioned, most of the atomic  $3d$  transition-metal cations  $M^+$  are capable to bring about bond activation of alkanes. Accordingly, dehydrogenation and elimination of propene are observed in the reaction with cyclohexane for  $Sc^+$ ,  $Ti^+$ ,  $V^+$ ,  $Fe^+$ ,  $Co^+$ , and  $Ni^+$  to different degrees. A detailed mechanistic study [186] of the reactions with [*all-cis*-1,2,3,4,5,6- $D_6$ ]-cyclohexane (**1**) revealed a remarkable face-selective dehydrogenation from one site of the alkane ring only by the early transition-metal cations  $Ti^+$  and  $V^+$ , whereas

$Fe^+$ ,  $Co^+$ , and  $Ni^+$  induce H/D exchange processes involving both faces of the ring. To compare the reactivities of the atomic cations with those of the corresponding dimers, analogous experiments have been performed for the cluster cations  $M_2^+$  ( $M = Ti, V, Cr, Mn, Fe, Co, Ni$ , and  $Cu$ ) as well as for  $NiM^+$  ( $M = Ti, Mn, Fe, Co, Cu, Al$ ) and  $CoCu^+$  for the reasons mentioned above. The results are given in Tables 4.1 and 4.2, respectively.

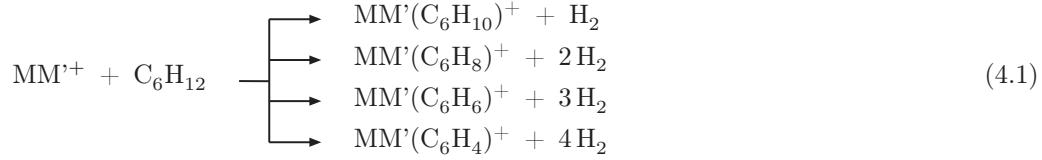


Table 4.1 – Branching ratios<sup>a</sup> of the neutral losses, relative rate constants, and efficiencies in the reactions of mass-selected, homonuclear  $M_2^+$  cations ( $M = Ti, V, Cr, Mn, Fe, Co, Ni, Cu$ ) with cyclohexane.

M	- H <sub>2</sub>	- 2 H <sub>2</sub>	- 3 H <sub>2</sub>	- 4 H <sub>2</sub>	$k_{\text{exp}}^b$	$\phi^c$
Ti		8	90	2	4.2	36
V			100		0.2	2
Cr		100			0.03	0.3
Mn	-	-	-	-	< 0.001	
Fe			100		0.005	0.02
Co	-	-	-	-	< 0.001	
Ni		5	95		9.3	83
Cu	100				2.5	23

<sup>a</sup> Normalized to a sum of 100.

<sup>b</sup> Given in  $10^{-10} \text{ cm}^3 \text{ s}^{-1} \text{ molecule}^{-1}$ .

<sup>c</sup> Given in %.

As found in previous work [185], cationic transition-metal dimers are more inclined to specific C–H bond activation compared to the atomic cations, which accomplish C–H as well as C–C bond activations [33]. For any reaction channel observed with *c*-C<sub>6</sub>H<sub>12</sub> (Tables 4.1 and 4.2), none of the dimeric cations indicate the operation of C–C bond activation; instead, only single or multiple dehydrogenation according to Equation 4.1 take place. Furthermore, relatively *efficient* dehydrogenation is observed only for three of the eight homonuclear clusters investigated, namely for  $Ti_2^+$ ,  $Ni_2^+$ , and  $Cu_2^+$ ; for the remaining dimers  $V_2^+$ ,  $Cr_2^+$ ,  $Mn_2^+$ ,  $Fe_2^+$ , and  $Co_2^+$ , dehydrogenation occurs either only sluggishly ( $V_2^+$ ,  $Cr_2^+$ , and  $Fe_2^+$ ) or does not take place at all ( $Mn_2^+$  and  $Co_2^+$ ). In contrast, heteronuclear dimers of nickel combined with a late transition metal - except for  $NiFe^+$  - *i. e.*  $NiCo^+$  and  $NiCu^+$ , show

Table 4.2 – Branching ratios<sup>a</sup> of the neutral losses, relative rate constants, and efficiencies in the reactions of mass-selected, heteronuclear NiM<sup>+</sup> cations (M = Ti, Mn, Fe, Co, Cu, Al) and of CoCu<sup>+</sup> with cyclohexane.

MM'	- H <sub>2</sub>	- 2 H <sub>2</sub>	- 3 H <sub>2</sub>	$k_{\text{exp}}^b$	$\phi^c$
NiTi		75	25	5.8	51
NiMn	90	4	6	0.9	8
NiFe			100	0.01	0.1
NiCo		13	87	6.9	62
NiCu		20	80	9.3	85
NiAl		65	35	8.8	73
CoCu		26	74	7.1	65

<sup>a</sup> Normalized to a sum of 100.

<sup>b</sup> Given in  $10^{-10} \text{ cm}^3 \text{ s}^{-1} \text{ molecule}^{-1}$ .

<sup>c</sup> Given in %.

almost the same high efficiency towards C–H bond activation of cyclohexane as homonuclear Ni<sub>2</sub><sup>+</sup>. Likewise, also the branching ratios of double *vs* triple dehydrogenation are similar with triple dehydrogenation being the major reaction channel. Interestingly, also CoCu<sup>+</sup> brings about efficient dehydrogenation up to three times (65 % efficiency, BR: 74 % 3 H<sub>2</sub> loss, 26 % 2 H<sub>2</sub> loss, Table 4.2), while for Co<sub>2</sub><sup>+</sup> no reaction is observed, and for Cu<sub>2</sub><sup>+</sup> only single dehydrogenation with a much smaller efficiency as compared to Ni<sub>2</sub><sup>+</sup> takes place (23 % for Cu<sub>2</sub><sup>+</sup> *vs* 83 % for Ni<sub>2</sub><sup>+</sup>, Table 4.1). Apparently, 19 electrons in the valence shell of the 3d dimers are favorable for reactivity. However, the same number of electrons results not in similar reactivity for the combined system of iron and copper compared to NiCo<sup>+</sup> for which efficient bond activation is observed. According to the work of Freiser and co-workers [187], FeCu<sup>+</sup> is unreactive with linear (C<sub>1</sub>–C<sub>6</sub>) and cyclic (C<sub>3</sub>–C<sub>6</sub>) alkanes. What is also remarkable and cannot be elucidated only by gas-phase experiments is the non-reactivity of NiFe<sup>+</sup> in comparison to the highly reactive NiCo<sup>+</sup> and Ni<sub>2</sub><sup>+</sup> cluster cations, or, in other words, it is not clear which factors make the nickel-containing cationic dimers so reactive (which, however, does not hold true for NiFe<sup>+</sup>) whereas Fe<sub>2</sub><sup>+</sup> and Co<sub>2</sub><sup>+</sup> are unreactive.

The combinations of nickel with a 3d metal onward the left side of the periodic table, *i. e.* NiMn<sup>+</sup> and NiTi<sup>+</sup>, lead again to a successive rise of reactivity, which is regained for the latter dimer with 51 % efficiency. However, the main reaction channel for NiTi<sup>+</sup> is double instead of triple dehydrogenation in contrast to Ni<sub>2</sub><sup>+</sup> and Ti<sub>2</sub><sup>+</sup>; for the latter, even fourfold dehydrogenation is observed. Also for NiAl<sup>+</sup>, which features a high efficiency, only single and double dehydrogenation take place.

To shed light on the reaction mechanism, the reactions with [*all-cis*-1,2,3,4,5,6-D<sub>6</sub>]-cyclo-

Table 4.3 – Isotope patterns<sup>a</sup> of double and triple dehydrogenation of [*all-cis*-1,2,3,4,5,6-D<sub>6</sub>]-cyclohexane (**1**) by  $MM'^+$ .

MM'	Ni <sub>2</sub>	Ni <sub>2</sub> <sup>b,c</sup>	NiTi <sup>d</sup>	NiCo <sup>c</sup>	NiCu <sup>c</sup>	NiAl <sup>c</sup>	CoCu <sup>c</sup>	Ti <sub>2</sub> <sup>e,f</sup>
- 2 H <sub>2</sub>	3	3 (8)	43 (45)	3 (4)	3 (7)	24 (27)	10 (10)	
- [H <sub>3</sub> ,D]			4 (6)					
- [H <sub>2</sub> ,D <sub>2</sub> ]	1		8					
- [D <sub>3</sub> ,H]			4 (3)					
- 2 D <sub>2</sub>	8	9 (5)	12 (11)	10 (10)	19 (15)	18 (15)	27 (29)	
- 3 H <sub>2</sub>	52	61 (60)	21 (15)	77 (77)	50 (53)	49 (49)	54 (49)	10 (7)
- [H <sub>5</sub> ,D]			2 (0)					27 (28)
- [H <sub>4</sub> ,D <sub>2</sub> ]	7		4 (2)					32 (37)
- [H <sub>3</sub> ,D <sub>3</sub> ]			0 (3)					20 (21)
- [H <sub>2</sub> ,D <sub>4</sub> ]	6		1 (1)					11 (6)
- [H,D <sub>5</sub> ]			0 (0)					0 (1)
- 3 D <sub>2</sub>	23	27 (27)	1 (6)	10 (9)	28 (25)	9 (9)	9 (12)	0 (0)
$k_1/k_2$		0.11		0.03	0.03	0.36	0.04	
$k_{\text{rad}}/k_2$		1.01		1.43	1.73	0.99	1.77	
KIE		1.21	1.28	1.43	1.11	1.33	1.10	2.58

<sup>a</sup> Given in %.<sup>b</sup> Disregarding the mixed isomers.<sup>c</sup> Modeled numbers according to Scheme 4.1 are given in parenthesis. See text and section 6.1 for details of the modeling.<sup>d</sup> In the modeling (numbers are given in parenthesis), face-specific dehydrogenation from one side of the ring as well as scrambling processes have been considered; the ratios are  $f_{\text{spec}} = 76\%$  and  $f_{\text{scr}} = 24\%$ , respectively. The ratio for double dehydrogenation of one face of the carbon ring combined with single dehydrogenation of the opposite side has been fitted to 0%.<sup>e</sup> Due to the low intensity of the corresponding signals, double and fourfold dehydrogenation have been neglected.<sup>f</sup> Modeled numbers are given in parenthesis; a complete scrambling of all H/D positions of [*all-cis*-1,2,3,4,5,6-D<sub>6</sub>]-cyclohexane with a KIE of 2.58 has been assumed.

hexane proved once more [186] to be very useful.<sup>9</sup> From the data in Table 4.3, it is obvious that face selectivity, as observed for  $Ti^+$ , is not conserved for  $Ti_2^+$ . In sharp contrast, complete scrambling processes occur during the reaction of  $Ti_2^+$  with cyclohexane indicated by the reasonable agreement of modeled values and the experimental branching ratios for triple dehydrogenation (assuming a KIE of 2.58 for each C–H *vs* C–D bond activation, *i. e.* the elimination of 3 H<sub>2</sub> is KIE to the power of six times faster than the loss of 3 D<sub>2</sub>,

<sup>9</sup> For technical aspects of the elaboration of the experimental data, see section A.2 in the Appendix.

Table 4.3).<sup>10</sup> The reactive late 3d metal dimers NiCo<sup>+</sup>, NiCu<sup>+</sup>, and CoCu<sup>+</sup> also exhibit a contrasting behavior in comparison to the corresponding reactive atomic cations Co<sup>+</sup> and Ni<sup>+</sup> (for Cu<sup>+</sup>, no reactivity towards cyclohexane is observed [186]): The dimers are found to react highly specific whereas for the atomic cations H/D equilibration takes place. In the case of Ni<sub>2</sub><sup>+</sup>, dehydrogenation does not proceed exclusively from one side of the ring since [H<sub>2</sub>,D<sub>4</sub>] as well as [H<sub>4</sub>,D<sub>2</sub>] are eliminated; however, scrambling processes entailing an H/D equilibration between the two faces do not happen; instead, stereoselective dehydrogenation of both faces occurs as indicated in the absence of losses with odd numbers of H/D atoms.

Table 4.4 – Isotope patterns<sup>a</sup> of single dehydrogenation of [*all-cis*-1,2,3,4,5,6-D<sub>6</sub>]-cyclohexane (**1**) by MM'<sup>+</sup>.

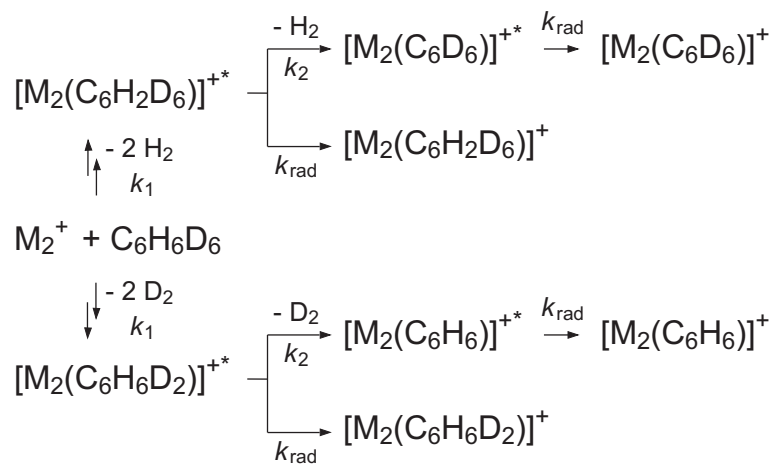
MM'	- H <sub>2</sub>	- HD	- D <sub>2</sub>			
NiMn	79 (79)	3 (3)	18 (18)	$f_{\text{spec}} = 92 \%$	$f_{\text{scr}} = 8 \%$	KIE = 2.11
Cu <sub>2</sub>	64 (63)	31 (31)	5 (6)	$f_{\text{spec}} = 19 \%$	$f_{\text{scr}} = 81 \%$	KIE = 3.27

<sup>a</sup> Given in % (modeled numbers are given in parenthesis). See text and section 6.1 for details.

To model the isotope patterns of double and triple dehydrogenation in the case of Ni<sub>2</sub><sup>+</sup>, NiAl<sup>+</sup>, NiCo<sup>+</sup>, NiCu<sup>+</sup>, and CoCu<sup>+</sup>, a more detailed kinetic scheme had to be considered. For these dimers, the experimental data for double dehydrogenation, given Table 4.3, suggest a higher and, thus, a faster rate for the loss of 2 D<sub>2</sub> *vs* 2 H<sub>2</sub>, and this would imply an *inverse* KIE. As discussed in Chapter 2.3, inverse KIEs are typically found for secondary KIEs and are often caused by a change in hybridization from *sp*<sup>2</sup> to *sp*<sup>3</sup>. In contrast, the hybridization of the carbon atoms changes by dehydrogenation from *sp*<sup>3</sup> to *sp*<sup>2</sup>; thus, the phenomenologically observed higher degree of 2 D<sub>2</sub> *vs* 2 H<sub>2</sub> eliminations is, more likely, not based on an inverse KIE, but on the fact that the expulsion of H<sub>2</sub> from MM'(C<sub>6</sub>H<sub>2</sub>D<sub>6</sub>)<sup>+</sup> (mandatory for face selectivity) proceeds faster than the loss of D<sub>2</sub> from MM'(C<sub>6</sub>H<sub>6</sub>D<sub>2</sub>)<sup>+</sup>. This again is not necessarily caused by an intrinsically high KIE for the third dehydrogenation but is rather a result of an increased lifetime of the rovibrationally excited MM'<sup>+</sup>/D<sub>2</sub>-cyclohexadiene intermediate. Because the third dehydrogenation is hampered by a KIE, the latter induces an isotopically sensitive branching [188, 189] in the competition between dehydrogenation and radiative cooling. This way of reasoning has been taken into account in the modeling of the experimental data according to Scheme 4.1, with  $k_1$  being the combined rate constant for the first and second dehydrogenation,  $k_2$  stands for rate constants of the third dehydrogenation, and  $k_{\text{rad}}$  for the radiative cooling of the MM'<sup>+</sup>/cyclohexadiene intermediate, respectively.

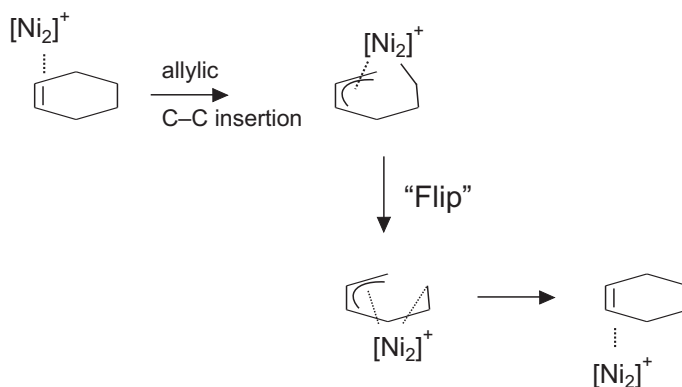
<sup>10</sup> Note that this calculation of the KIE is different from the procedure reported in reference [186] where the KIE accounts to the overall ratio of C–H versus C–D bond activation of [*all-cis*-1,2,3,4,5,6-D<sub>6</sub>]-cyclohexane in all events of multiple dehydrogenation.

The modeled data are given in parenthesis in Table 4.3 and are in relatively good agreement with the experimental data; disregarding the possible role of radiative cooling in the modeling, results in quite large differences between the experimental findings and the modeling data.



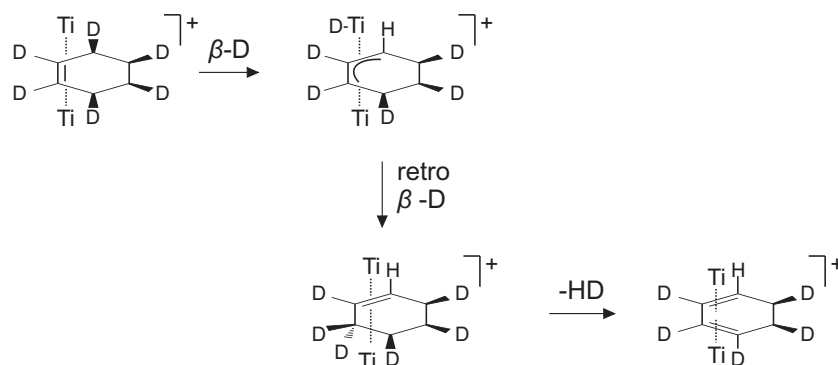
Scheme 4.1

The combination of nickel and titanium in  $\text{NiTi}^+$  gives rise to a mixture of both features of the corresponding homonuclear dimers, *i. e.* scrambling processes take place (*e. g.* loss of  $[\text{H}_3, \text{D}_3]$ ), but due to the large amount of  $3 \text{H}_2$  elimination it is obvious that face selectivity is preserved to some extent. Accordingly, the experimental data can be fitted quite well by taking into account face-selective dehydrogenation as well as scrambling processes with a ratio of  $f_{\text{spec}} = 76\%$  and  $f_{\text{scr}} = 24\%$ , respectively (see footnote *d* of Table 4.3).



Scheme 4.2

To discuss the distinct behavior of the early transition-metal dimer  $\text{Ti}_2^+$  *vs* the late 3d metal clusters let us review briefly the explanation for equilibrium processes of the atomic



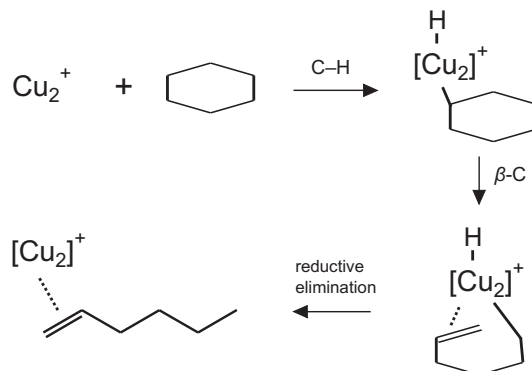
Scheme 4.3

cations [186]. As mentioned, face selectivity is pronounced for the early  $3d$  atomic cations. For  $\text{Sc}^+$ , however, stereoselective dehydrogenation of both sides – indicated by  $[\text{H}_2, \text{D}_4]$  and  $[\text{H}_4, \text{D}_2]$  elimination – is observed, as it is for  $\text{Ni}_2^+$  in this work. This mode of dehydrogenation can be explained by a ring-flipping process in which after the first dehydrogenation the metal changes the coordination site via an allylic C–C bond insertion (Scheme 4.2).

For the complete scrambling processes, observed for the system  $\text{Ti}_2^+/\text{C}_6\text{H}_6\text{D}_6$ , the elimination of odd numbers of H/D atoms are not in line with a ring flip mechanism. Eventually, pathways involving the bond breaking of the metal-metal bond take place, resulting in a sandwich complex  $[\text{Ti-benzene-Ti}]^+$ . This alternative reaction channel might be of importance especially for the dehydrogenation by  $\text{Ti}_2^+$  because it is known for both neutral early  $3d$  metal clusters [190, 191] and for cationic  $\text{V}_4^+$  [192] to form favorably multiple sandwich complexes with benzene in contrast to clusters of late first-row transition metals which rather adopt rice-ball structures [193]. Thus, it is quite conceivable that the metal-metal bond of  $\text{Ti}_2^+$  is broken and the metal atoms are moved to opposite sides of the carbon ring. Assuming a bond breaking of the Ti–Ti bond, the observed H/D equilibration between the two faces can be explained by titanium-mediated H/D migrations as depicted in Scheme 4.3.

The different behavior of  $\text{NiCu}^+$  and  $\text{Cu}_2^+$  is not only indicated in the lower reactivity of the latter dimer, but also evident from the results of the reaction with **1** (Table 4.4): In contrast to the face-selective triple dehydrogenation by  $\text{NiCu}^+$  (Table 4.3), already in the single dehydrogenation by  $\text{Cu}_2^+$ , both faces of the carbon ring are involved. Scrambling processes in the case of single dehydrogenation are neither explainable by a ring-flip mechanisms (Scheme 4.2) nor by the formation of a “sandwich” complex as proposed for  $\text{Ti}_2^+$  (Scheme 4.3). In contrast, a ring-opening process, *i. e.* the isomerization of cyclohexane to *n*-hexene as depicted in Scheme 4.4, might prevent the differentiation between the two faces of the former carbon ring; this process could also be the reason for the small amount of HD elimination by  $\text{NiMn}^+$  and, furthermore, for the elimination of odd numbers of H/D atoms observed in

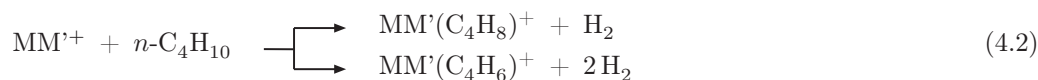
the case of  $Ti_2^+$  and  $NiTi^+$ .



Scheme 4.4

## 4.2 Reactions with ethane, propane, and *n*-butane

The low reactivity of  $NiFe^+$  in comparison to the other nickel dimers is clearly evidenced in the reactions with cyclohexane. All other clusters  $NiM^+$  are similarly reactive towards  $c\text{-C}_6\text{H}_{12}$  with respect to the efficiency and branching ratios. In order to perhaps detect more subtle differences between these cluster cations, experiments with alkanes were performed by employing a set of substrates with decreasing reactivity, namely *n*-butane, propane, ethane, and methane.



Single and double dehydrogenations according to Equation 4.2 are observed in the reaction with *n*-butane and the BRs and efficiencies are given in Table 4.5. For  $NiFe^+$  and  $NiMn^+$ , whose reactivities towards  $c\text{-C}_6\text{H}_{12}$  are close to zero or quite inefficient, respectively (see Table 4.2), no reaction with *n*-butane is observed.

The trend in reactivity with respect to the efficiency and the extent of dehydrogenation found for cyclohexane is the same for *n*-butane with  $NiCu^+$  and  $Ni_2^+$  affording equally high efficient dehydrogenation.  $NiTi^+$  is least reactive, and  $NiCo^+$ ,  $NiAl^+$ , as well as  $CoCu^+$  bear intermediate efficiencies. Also the amount of  $H_2$  elimination from *n*-butane reflects, by and large, the one reported above already for  $c\text{-C}_6\text{H}_{12}$ . For example, the degree of dehydrogenation is the smallest for  $NiTi^+$  in the reaction with cyclohexane (double dehydrogenation) as well as with *n*-butane (single dehydrogenation), whereas in the case of the other cations these substrates are mainly oxidized to benzene and butadiene, respectively.



Table 4.5 – Branching ratios<sup>a</sup> of the neutral losses, relative rate constants, and efficiencies in the reactions of mass-selected MM'<sup>+</sup> with *n*-butane, propane, and ethane.

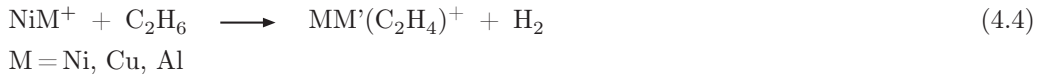
MM'	<i>n</i> -butane				propane			ethane		
	-H <sub>2</sub>	-2H <sub>2</sub>	$k_{\text{exp}}^b$	$\phi^c$	-H <sub>2</sub>	$k_{\text{exp}}^b$	$\phi^c$	-H <sub>2</sub>	$k_{\text{exp}}^b$	$\phi^c$
NiTi	100		1.3	12	-	-				
NiMn	-	-	-							
NiFe	-	-	-							
NiCo	10	90	5.7	53	100	1.2	11	100	0.006	0.06
Ni <sub>2</sub>	37	63	8.3	77	100	6.3	60	100	6.5	64
NiCu	46	54	8.6	80	100	6.6	64	100	6.6	65
NiAl	57	43	7.2	63	100	7.2	66	100	2.4	23
CoCu	100		4.3	40	100	0.9	9	-	-	

<sup>a</sup> Normalized to a sum of 100.<sup>b</sup> Given in 10<sup>-10</sup> cm<sup>3</sup> s<sup>-1</sup> molecule<sup>-1</sup>.<sup>c</sup> Given in %.

In the reaction with propane, the cluster cations still being “in the race” for bond activation are Ni<sub>2</sub><sup>+</sup>, NiCo<sup>+</sup>, NiCu<sup>+</sup>, NiAl<sup>+</sup>, and CoCu<sup>+</sup>; all cations are capable of dehydrogenation of propane according to Equation 4.3.



Interestingly, with respect to the inertness of Co<sub>2</sub><sup>+</sup> and the low reactivity of Cu<sub>2</sub><sup>+</sup> even towards *c*-C<sub>6</sub>H<sub>12</sub>, CoCu<sup>+</sup> is still capable of dehydrogenation of propane, although relatively inefficient compared to the other dimers (Table 4.5). Also for NiCo<sup>+</sup> the efficiency is low in comparison to Ni<sub>2</sub><sup>+</sup>, NiAl<sup>+</sup>, and NiCu<sup>+</sup> which bring about quite efficient dehydrogenation of propane.



Reactivity towards ethane is observed for Ni<sub>2</sub><sup>+</sup>, NiAl<sup>+</sup>, and NiCu<sup>+</sup>; for the dimers CoCu<sup>+</sup> and NiCo<sup>+</sup> which are capable of bond activation of propane, either the reaction rate  $k_{\text{exp}}$  is very small (in the order of 10<sup>-13</sup> cm s<sup>-1</sup> molecule<sup>-1</sup>), *i. e.* the efficiency is close to zero, or no reaction takes place at the detection limit (Table 4.5). In the case of Ni<sub>2</sub><sup>+</sup> and NiCo<sup>+</sup> instead, the efficiency of ethane dehydrogenation is even slightly higher relative to the elimination of H<sub>2</sub> from propane. Also for NiAl<sup>+</sup>, quite efficient dehydrogenation of ethane takes

place, although the efficiency drops from 66 % for the  $NiAl^+/C_3H_8$  couple to 23 % in the  $NiAl^+/C_2H_6$  system (Table 4.5).

Table 4.6 – Isotope patterns<sup>a</sup> for the dehydrogenation of  $CH_3CD_3$  (**2**) by the nickel dimers  $NiM^+$  ( $M = Ni, Cu, Al$ ).

$MM'$	- $H_2$	- HD	- $D_2$			
$Ni_2$	24 (24)	63 (63)	13 (13)	$f_{\text{spec}} = 10 \%$	$f_{\text{scr}} = 90 \%$	KIE = 1.38
$NiCu$	29 (28)	58 (59)	13 (13)	$f_{\text{spec}} = 1 \%$	$f_{\text{scr}} = 99 \%$	KIE = 1.48
$NiAl$		100				

<sup>a</sup> Given in % (modeled numbers are given in parenthesis). For details of the modeling, see text and section 6.1.

The isotope patterns of  $H_2/HD/D_2$  eliminations in the reactions of the dimers with labeled  $CH_3CD_3$  (**2**) have been modeled considering a KIE and, additionally, two parameters  $f_{\text{spec}}$  for the ratio of a specific dehydrogenation according to a 1,2-elimination, and  $f_{\text{scr}}$  for the fraction of the hydrogen-scrambling processes.  $NiCo^+$  and  $NiCu^+$  are similar with respect to the efficiency as well as to the reaction mechanism. For both complexes, the ratio of  $H_2$ , HD, and  $D_2$  losses is in line with almost complete scrambling of H/D atoms preceding dehydrogenation (with a ratio of  $f_{\text{scr}} = 99\%$  for  $NiCu^+$  and  $f_{\text{scr}} = 90\%$  for  $Ni_2^+$ , see Table 4.6). In contrast, the exclusive loss of HD in the reaction of  $NiAl^+$  with **2** indicates a specific 1,2-elimination without any reversible scrambling processes involved (Table 4.6).

Ethane is the smallest alkane that is activated by  $Ni_2^+$ ,  $NiAl^+$ , and  $NiCu^+$ ; for none of these dimeric cluster cations reactions with methane are observed in the gas phase.

## Part III

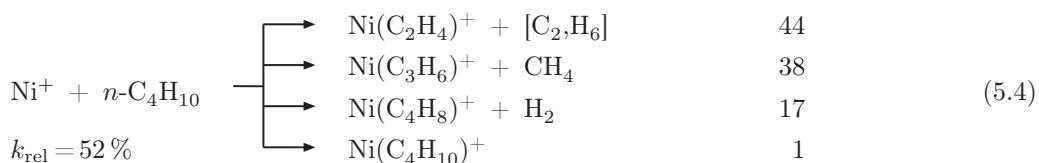
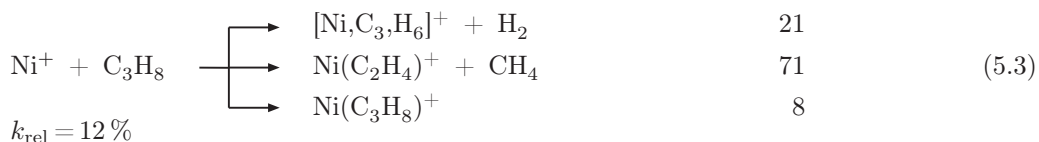
### Reactivity of mononuclear nickel complexes



## 5 Reactivity of Ni<sup>I</sup> complexes NiL<sup>+</sup> (L = CO and H<sub>2</sub>O)

The reactivity studies of NiM<sup>+</sup> towards small alkanes described in Part II of this Thesis reveal a quite varied gas-phase chemistry; depending on M, large difference with respect to reactivity (*e. g.* NiCo<sup>+</sup> *vs* NiFe<sup>+</sup>) as well as to the mechanism of the reaction (*e. g.* Ni<sub>2</sub><sup>+</sup>/C<sub>2</sub>H<sub>6</sub> *vs* NiAl<sup>+</sup>/C<sub>2</sub>H<sub>6</sub>) are observed. While homo- and heteronuclear clusters are considered to be proper model systems to study the processes in heterogeneous catalysis on a molecular level, the knowledge of ligand effects can help to elucidate the intrinsic properties of homogeneous catalysts. Starting with formal nickel(I), the reactivities of a series of cationic Ni<sup>I</sup>, Ni<sup>II</sup>, and Ni<sup>III</sup> complexes are described which have been examined by ESI-MS.

Propane is the smallest alkane that is activated by naked Ni<sup>+</sup>: C–H as well as C–C bond activation is observed according to Equation 5.3 (see also [194, 195]), whereas no reactions are observed with neither ethane nor methane (Equation 5.1 and Equation 5.2).



As mentioned above for the chemistry of iron oxide FeO<sup>+</sup>, the addition of a neutral, closed-shell ligand to naked M<sup>+</sup> affects the electronic structure of the transition-metal center such that its reactivity is strongly influenced even though the formal oxidation state does not change upon ligation. Further, in the reaction of *e. g.* the ligated iron ions FeL<sup>+</sup> (L = H<sub>2</sub>O and CO) with propane, drastic changes in the overall reactivity and selectivity are observed

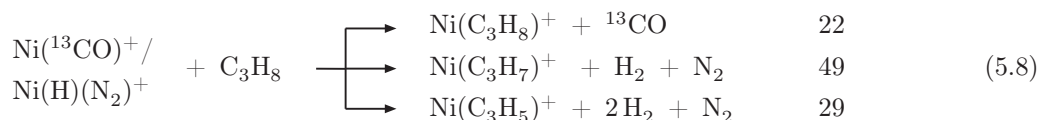
in comparison to naked Fe<sup>+</sup> [51, 195]. While low-spin Fe<sup>+</sup> (<sup>4</sup>F) is much more reactive than high-spin Fe<sup>+</sup> (<sup>6</sup>D), the reactivity of low-spin Fe(CO)<sup>+</sup> (<sup>4</sup>Σ<sup>-</sup>) is drastically decreased at thermal energies compared to high-spin Fe(H<sub>2</sub>O)<sup>+</sup> (<sup>6</sup>A<sub>1</sub>); the latter being similarly reactive as Fe<sup>+</sup> (<sup>6</sup>D). Also, demethanation of propane by Fe(H<sub>2</sub>O)<sup>+</sup> is much more favored in competition with dehydrogenation when compared with ground state Fe<sup>+</sup> [195].



To study the effects of neutral ligands on the reactivity of Ni<sup>+</sup>, reactions of nickel complexes with back-donating CO as well as σ- and (weak) π-donating H<sub>2</sub>O, *i. e.* Ni(CO)<sup>+</sup> and Ni(H<sub>2</sub>O)<sup>+</sup>, towards small linear alkanes up to *n*-butane have been investigated.



$$k_{\text{rel}} = 37\%$$

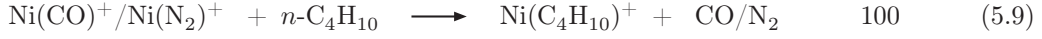


$$k_{\text{rel}} = 43\%$$

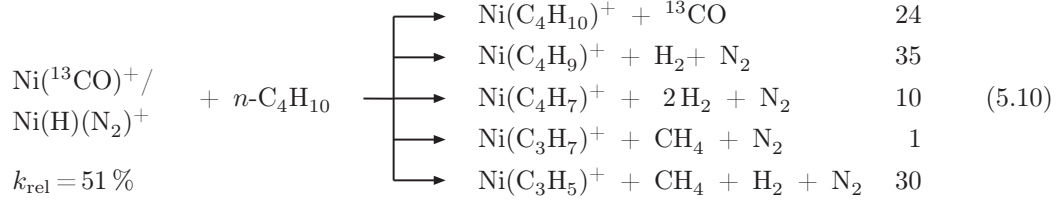
As known from the work of Bowers and co-workers [196], the complex Ni(CO)<sup>+</sup> is formed in the reaction of Ni<sup>+</sup> with acetone under elimination of ethane according to Equation 5.5; thus, Ni(CO)<sup>+</sup> can easily be generated in the ESI source from a solution of a nickel salt in acetone.

However, the investigation of Ni(CO)<sup>+</sup> is hampered by the presence of N<sub>2</sub> as drying gas in the ESI source whereby isobaric Ni(N<sub>2</sub>)<sup>+</sup> is formed. The separation of these isomers can be achieved by using acetone-2-<sup>13</sup>C as solvent; but here, in turn, the signal of Ni(<sup>13</sup>CO)<sup>+</sup> is superimposed by isobaric Ni(H)(N<sub>2</sub>)<sup>+</sup>. Nevertheless, a comparison of both systems Ni(<sup>13</sup>CO)<sup>+</sup>/Ni(H)(N<sub>2</sub>)<sup>+</sup> and Ni(CO)<sup>+</sup>/Ni(N<sub>2</sub>)<sup>+</sup> in their reactions with propane and *n*-butane, Equations 5.7 - 5.10, allows to assign the ligand-exchange reaction to Ni(CO)<sup>+</sup> as the only reaction channel since this signal is observed for both systems Ni(CO)<sup>+</sup>/Ni(N<sub>2</sub>)<sup>+</sup> and Ni(<sup>13</sup>CO)<sup>+</sup>/Ni(H)(N<sub>2</sub>)<sup>+</sup>.<sup>11</sup>

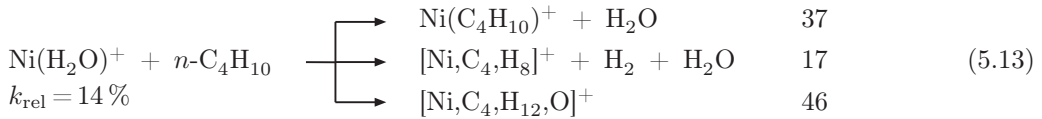
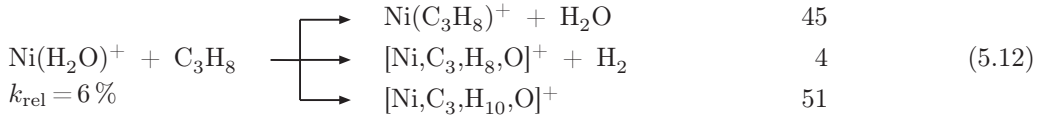
<sup>11</sup> In the reaction with ethane, no common reaction channel is observed for the systems Ni(<sup>13</sup>CO)<sup>+</sup>/Ni(H)(N<sub>2</sub>)<sup>+</sup> and Ni(CO)<sup>+</sup>/Ni(N<sub>2</sub>)<sup>+</sup>, *i. e.* Ni(CO)<sup>+</sup> does not react with ethane, Equation 5.6.



$$k_{\text{rel}} = 37 \%$$



Furthermore, the ligand exchange in the reaction of  $\text{Ni}(\text{C}_4\text{H}_{10})^+/\text{Ni}(\text{H})(\text{N}_2)^+$  with  $\text{C}_3\text{H}_8$  and  $n\text{-C}_4\text{H}_{10}$  is expected to be due to  $\text{Ni}(\text{C}_4\text{H}_{10})^+$  and not to originate from  $\text{Ni}(\text{H})(\text{N}_2)^+$ . The relative efficiency for this reaction channel amounts to 9 % for propane and to 12 % for  $n$ -butane, respectively;<sup>12</sup> due to the isobaric overlap, these data are lower limits for the ligand-exchange reactions  $\text{Ni}(\text{CO})^+ + \text{C}_n\text{H}_{2n+2} \rightarrow \text{Ni}(\text{C}_n\text{H}_{2n+2})^+ + \text{CO}$  ( $n = 3, 4$ ). An upper limit is obtained by the relative rates for the reactions of  $\text{Ni}(\text{CO})^+/\text{Ni}(\text{N}_2)^+$  with  $\text{C}_3\text{H}_8$  and  $n\text{-C}_4\text{H}_{10}$ , because ligand exchange is expected to be much faster for  $\text{Ni}(\text{N}_2)^+$  compared to  $\text{Ni}(\text{CO})^+$  due to the much lower binding energy of the latter complex ( $D_0(\text{Ni}^+ - \text{CO}) = 175 \text{ kJ mol}^{-1}$  [197],  $D_0(\text{Ni}^+ - \text{N}_2) = 111 \text{ kJ mol}^{-1}$  [197]). Here, the relative efficiencies for ligand exchange vary largely from day to day in agreement with a varying composition of isobaric  $\text{Ni}(\text{CO})^+$  and  $\text{Ni}(\text{N}_2)^+$  ions produced in the ESI source; the rates given in Equations 5.7 and 5.9 are the lowest values observed in the various experiments.



None of the  $\text{Ni}^{\text{I}}$  cations is able to activate methane or ethane. As indicated in the reactions with propane and  $n$ -butane, the coordination of  $\text{H}_2\text{O}$  or  $\text{CO}$  to  $\text{Ni}^+$  clearly leads to a

<sup>12</sup> As mentioned before, all rates for the reactions of the nickel complexes presented in the following sections are given relative to the fastest reaction observed ( $\text{NiBr}^+ + \text{C}_3\text{H}_8$ , see also section 6.2).

much lower reactivity in comparison to naked  $\text{Ni}^+$  (Reactions 5.3 and 5.4). The relative efficiencies for the reactions of naked  $\text{Ni}^+$  involving bond activation (regardless of adduct formation) are 11 % and 51 % with propane and *n*-butane, respectively, whereas the relative dehydrogenation rates of  $\text{Ni}(\text{H}_2\text{O})^+$  are < 1 % for propane and only 2 % for *n*-butane; for  $\text{Ni}(\text{CO})^+$ , no indications for bond activation either for propane or *n*-butane are observed. A reduced reactivity due to ligation by a closed-shell ligand has been noted previously in several studies [61, 198, 199]; among the very few notable exceptions of ligand-*enhanced* reactivity there are also complexes bearing carbonyl ligands [200–203].



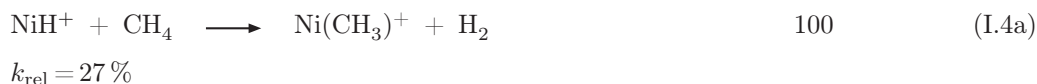
## 6 Reactivity of Ni<sup>II</sup> complexes

As stated above, the coordination of closed-shell ligands L often decreases or even completely suppresses bond-activation reactions. In contrast, open-shell ligands X which form a covalent bond with the metal cation can induce a drastic increase in reactivity of the metal center. Several complexes NiX<sup>+</sup> have been examined and are described in the following sections, starting with the reactivity of cationic hydride complexes NiH<sup>+</sup> and Ni(H)(L)<sup>+</sup> (L = CO and H<sub>2</sub>O) towards methane, ethane, propane and butane.

### 6.1 Reactivity of NiH<sup>+</sup> and Ni(H)(L)<sup>+</sup> (L = CO and H<sub>2</sub>O)

#### 6.1.1 Reactions with methane

In line with earlier findings [63–65], NiH<sup>+</sup> generated by ESI reacts efficiently with methane (Reaction I.4a). As already shown by Zhang and Bowers [65], the Ni-mediated H/CH<sub>3</sub> ligand



exchange constitutes a textbook example for the operation of TSR [43, 49, 70, 72, 204] because crossings between the high-spin and low-spin potential energy surfaces take place at both the entrance and the exit channel. In order to compare the H/CH<sub>3</sub> ligand switch in detail with the related PdH<sup>+</sup>/CH<sub>4</sub> and NiX<sup>+</sup>/CH<sub>4</sub> couples (X = F and OH) which have also been investigated in this work, the energy profile of reaction I.4a has been recalculated (Figure 6.1). In accordance with the work of Zhang and Bowers, a TSR scenario allows the reaction of NiH<sup>+</sup> with methane to take place under thermal conditions, although the relative energy of the relevant transition structure is 4 kJ mol<sup>−1</sup> above the entrance channel of separated NiH<sup>+</sup>/CH<sub>4</sub>. This is somewhat larger in energy compared to the results of Zhang who calculated the transition structure to be -7 kJ mol<sup>−1</sup> below the entrance channel. However, both calculations are in agreement that a favorable pathway is opened up by surface crossing to the low-spin state thus bypassing an energetically rather unfavorable transition structure of triplet TS **3a/4a** associated with a spin-conserving  $\sigma$ -metathesis process on the high-spin ground-state surface. As discussed in the introduction, this TSR scenario is favored by the relatively small energy separation (88 kJ mol<sup>−1</sup> in this work, 80 kJ mol<sup>−1</sup> in the work of Bowers) of the two relevant spin states of NiH<sup>+</sup>, that is, ground-state <sup>3</sup>Δ and

excited  $^1\Sigma^+$ . A comparative discussion of this process with the related systems mentioned will be given in Chapters 6.1.2 and 6.2.

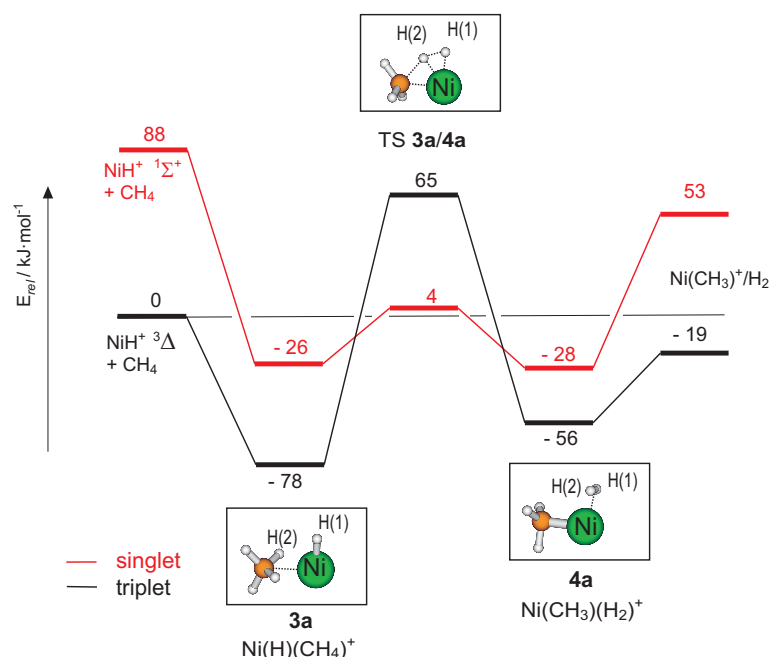


Figure 6.1 – Energy diagram (in  $\text{kJ mol}^{-1}$ ) for the reaction of  $\text{NiH}^+$  and methane. The values are relative to the entrance channel and corrected for zero-point vibrational energies.

In contrast to bare  $\text{Ni}^+$ , the reactivity of the hydride  $\text{NiH}^+$  is not largely influenced when additional “inert” ligands such as CO and  $\text{H}_2\text{O}$  are coordinated to the  $\text{NiH}^+$  core (reactions 6.1 and 6.2); only a slight decrease of the relative rate constants, relative to that for reaction I.4a, is caused by the presence of these ligands. In the case of  $\text{Ni}(\text{H})(\text{CO})^+$ , the product ions consist either of methyl complexes  $\text{Ni}(\text{CH}_3)(\text{CO})^+$  or acyl cations  $\text{Ni}(\text{COCH}_3)^+$ ; the latter can be formed by CO insertion into the newly formed Ni–C bond. Beside cobalt and rhodium, nickel is well known to mediate C–C bond coupling via insertion of CO into the Ni–C bond thus forming aldehydes, ketones, or carboxylic acids [205–209]. The insertion of CO into a Ni–C bond plays also an important role in the synthesis of acetyl-coenzyme A by acetyl-CoA synthases [210–214]. As the quadrupole based mass spectrometer does not allow a distinction between  $\text{Ni}(\text{CH}_3)(\text{CO})^+$  and  $\text{Ni}(\text{COCH}_3)^+$  by further investigations, the connectivities of the product complexes are not clearly assigned. This is also true for the respective product ions observed in the reactions of  $\text{Ni}(\text{H})(\text{CO})^+$  with ethane, propane, and butane (Chapter 6.1.4) in which the corresponding alkanoyl complexes might be formed (Equations 6.11, 6.16, and 6.19).



$$k_{\text{rel}} = 26 \%$$



$$k_{\text{rel}} = 20 \%$$

Detailed modeling of the isotope distributions in isotopic variants of reactions I.4a, 6.1, and 6.2 (Table 6.1) reveals a competition between direct H/ $\text{CH}_3$  ligand switch and hydrogen-atom scrambling. This is considered in the modeling, according to Equations 6.3 - 6.5, by

Table 6.1 – Isotope patterns<sup>a</sup> for the dehydrogenation of methane by the nickel-hydride complexes  $\text{NiH}^+$ ,  $\text{Ni(H)(CO)}^+$ ,<sup>b</sup> and  $\text{Ni(H)(H}_2\text{O)}^+$ .

	- H <sub>2</sub>	- HD	- D <sub>2</sub>	
$\text{NiH}^+ + \text{CD}_4$		92 (93)	8 (7)	$f_{\text{spec}} = 93 \%$
$\text{NiH}^+ + \text{CH}_2\text{D}_2$	60 (60)	39 (39)	1 (1)	$\text{KIE}_{\text{spec}} = 1.70$
$\text{NiD}^+ + \text{CH}_4$	5 (7)	95 (93)		$f_{\text{scr}} = 7 \%$
$\text{NiD}^+ + \text{CH}_2\text{D}_2$	2 (1)	62 (63)	36 (36)	$\text{KIE}_{\text{scr}} = 1.01$
$\text{Ni(H)(CO)}^+ + \text{CD}_4$		67 (67)	33 (33)	$f_{\text{spec}} = 47 \%$
$\text{Ni(H)(CO)}^+ + \text{CH}_2\text{D}_2$	46 (46)	49 (49)	5 (5)	$\text{KIE}_{\text{spec}} = 1.52$
				$f_{\text{scr}} = 53 \%$
				$\text{KIE}_{\text{scr}} = 1.15$
$\text{Ni(H)(H}_2\text{O)}^+ + \text{CD}_4$		72 (73)	28 (27)	$f_{\text{spec}} = 43 \%$
$\text{Ni(H)(H}_2\text{O)}^+ + \text{CH}_2\text{D}_2$	56 (56)	39 (41)	5 (3)	$\text{KIE}_{\text{spec}} = 2.42$
$\text{Ni(D)(H}_2\text{O)}^+ + \text{CH}_4$	39 (42)	61 (58)		$f_{\text{scr}} = 57 \%$
$\text{Ni(D)(H}_2\text{O)}^+ + \text{CH}_2\text{D}_2$	13 (9)	63 (66)	24 (25)	$\text{KIE}_{\text{scr}} = 1.41$

<sup>a</sup> Given in % (modeled numbers are given in parenthesis).

<sup>b</sup> For the formation of  $\text{Ni(H)(CO)}^+$ ,  $^{13}\text{CH}_3\text{OH}$  was used as solvent to avoid isobaric overlap with  $\text{Ni(H)(N}_2\text{)}^+$ .

weight factors  $f_{\text{spec}}$  and  $f_{\text{scr}}$  for the specific hydrogen elimination and for the extent of H/D scrambling, respectively. For the latter, equilibrium isotope effects are known to be usually close to unity and much smaller than KIEs of kinetically controlled reactions, because the incorporation of a heavy isotopes slows down the reaction both in the forward as well as in the reverse direction such that the overall effects on the equilibrium constant  $K_{\text{eq}}$  are relatively small [215]. Thus, to each mode of dehydrogenation a kinetic isotope effect  $\text{KIE}_{\text{spec}}$  and  $\text{KIE}_{\text{scr}}$ , respectively, has been assigned. The statistical probabilities for  $\text{H}_2/\text{HD}/\text{D}_2$  eliminations after complete scrambling of all five H/D atoms are  $p_{\text{scr}}(\text{XY})$  ( $\text{X, Y} = \text{H, D}$ ).

The modeled data obtained with optimized  $f_{spec}$ ,  $f_{scr}$ ,  $KIE_{spec}$ , and  $KIE_{scr}$  are given in Table 6.1.

$$H_2 = f_{spec} \cdot p(H_2) + f_{scr} \cdot p_{scr}(H_2) \quad (6.3)$$

$$HD = \frac{f_{spec} \cdot p(HD)}{KIE_{spec}} + \frac{f_{scr} \cdot p_{scr}(HD)}{KIE_{scr}} \quad (6.4)$$

$$D_2 = \frac{f_{spec} \cdot p(D_2)}{KIE_{spec}^2} + \frac{f_{scr} \cdot p_{scr}(D_2)}{KIE_{scr}^2} \quad (6.5)$$

The significant primary KIEs suggest that C–H bond breaking contributes to the rate-limiting step of the overall process [216]. As expected, the KIE associated to the direct H/CH<sub>3</sub> exchange is larger compared to the  $KIE_{scr}$  determined for the dehydrogenation after scrambling processes. The difference is of the same magnitude as those reported in earlier C–H bond-activation studies on transition-metal dimers  $MM'^+$  of iron, cobalt, and nickel [185], but not as pronounced as the difference between selective and scrambling processes found in other studies [217].

While efficient dehydrogenation of methane is found to occur for the 5*d* hydride complex PtH<sup>+</sup> [218], to the best of our knowledge no reactivity of the related 4*d* PdH<sup>+</sup> towards methane has yet been reported. Thus, the studies have been extended to the PdH<sup>+</sup> system to complete and to compare the group 10 hydride complexes MH<sup>+</sup> in more detail. The results of these investigations are described in the following subsection.

### 6.1.2 Thermal activation of methane by group 10 metal hydrides MH<sup>+</sup>

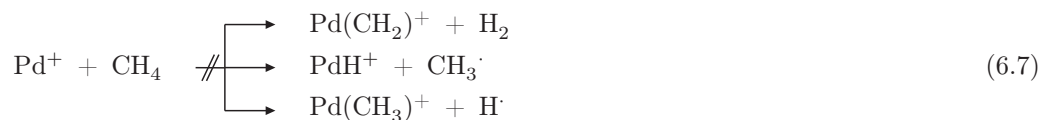
For thermal gas-phase reactions of transition-metal ions with methane, ligand effects are applied to alter the electronic structure of the metal-ion core or to prepare reactive centers, which are then capable to bring about homolytic C–H bond cleavage. While this approach is mainly used for 3*d* transition metals, a second strategy has proven useful; namely, advantage is taken of the huge relativistic stabilization exhibited by 5*d* transition-metal cations in forming metal-carbon bonds *e.g.* for the spontaneous dehydrogenation of CH<sub>4</sub> by “bare” atomic or cluster metal ions (Equation 6.6) [48].



M = Ta, W, Os, Ir, Pt

Much less is known about the potential role of 4*d* transition-metal systems in thermal activation of methane, and elementary considerations suggest that the prospects are much

less promising. For example, atomic  $\text{Pd}^+$  is extremely unreactive in the gas phase owing to the inability of its ground state to undergo oxidative insertion, and its lowest excited quartet state is much too high in energy to engage in thermal bond activation [33]; in fact, none of the processes described in Equation 6.7 occur [219–222].



However,  $\text{Pd}^{\text{II}}$  species exhibit contrasting behavior in their gas-phase reactivity; for example, while  $\text{Pd}^+$  reacts only sluggishly even with the otherwise rather reactive substrate  $\text{CH}_3\text{I}$ , the  $\text{Pd}^{\text{II}}$ -alkyl complex  $\text{Pd}(\text{CH}_3)^+$  undergoes bond activation with collision efficiency at room temperature [221, 223], Equation 6.8, thus pointing to an enhanced reactivity of this oxidation state [221, 224–226].



While  $\text{PdH}^+$  has been characterized computationally at great length [66, 68], its chemical reactivity toward C–H bond activation has not been reported. Upon ESI of a solution of  $\text{PdCl}_2$  in  $\text{CH}_3\text{OH}$ , under relatively harsh ionization conditions (cone voltage ca. 80 V) one can generate  $\text{PdH}^+$  in yields sufficient to permit reactivity studies of mass-selected ions with methane.

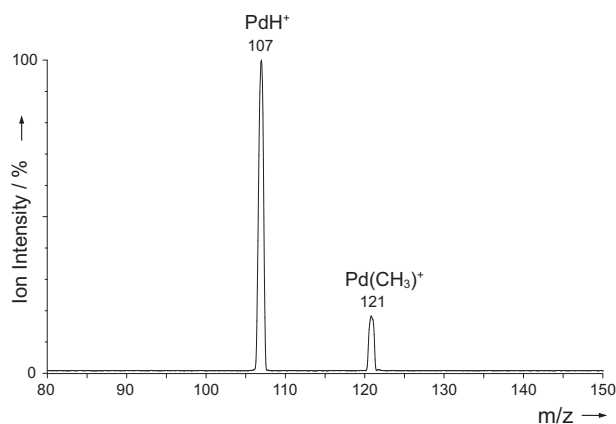
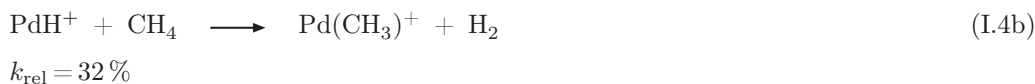


Figure 6.2 – Ion-molecule reaction of thermalized mass-selected  $\text{PdH}^+$  with  $\text{CH}_4$  at  $E_{\text{lab}} = 0 \text{ eV}$ .

In distinct contrast to the completely inert atomic  $\text{Pd}^+$ , the cationic palladium hydride undergoes at room temperature a  $\text{H}/\text{CH}_3$  ligand exchange (Figure 6.2) with a relative rate of 32%.



As to the specificity of the ligand-exchange process (Equation I.4b), isotope-labeling experiments are quite revealing (Table 6.2). An analogous model, as presented for the nickel hydrides (Equations 6.3 - 6.5), has been applied for the analysis of the labeling distributions for these four couples, suggesting that the direct hydrogen/methyl ligand exchange amounts to 70 %, and 30 % of all hydrogen/deuterium atoms undergo scrambling prior to loss of molecular hydrogen (and its isotopic variants). For the direct reaction an averaged kinetic isotope effect of  $\text{KIE} = 1.58$  and for the latter process an averaged  $\text{KIE} = 1.20$  are derived, thus indicating that breaking of the Pd–H(D) and C–H(D) and forming the H–H(D) bonds contribute to the rate of the overall process.

Table 6.2 – Isotope patterns<sup>a</sup> for the dehydrogenation of the PdX<sup>+</sup>/methane couple (X = H, D).

	- H <sub>2</sub>	- HD	- D <sub>2</sub>	
PdH <sup>+</sup> + CD <sub>4</sub>		79 (83)	21 (17)	$f_{\text{spec}} = 30\%$
PdH <sup>+</sup> + CH <sub>2</sub> D <sub>2</sub>	54 (54)	44 (44)	2 (2)	$\text{KIE}_{\text{spec}} = 1.58$
PdD <sup>+</sup> + CH <sub>4</sub>	20 (19)	80 (81)		$f_{\text{scr}} = 70\%$
PdD <sup>+</sup> + CH <sub>2</sub> D <sub>2</sub>	5 (4)	61 (61)	34 (35)	$\text{KIE}_{\text{scr}} = 1.20$

<sup>a</sup> Given in % (modeled numbers are given in parenthesis). For details of the modeling, see section 6.1.

Insight into the mechanistic details of the C–H bond activation of methane by PdH<sup>+</sup> has been obtained by B3LYP calculations. Coordination of the alkane with the cation is associated with a relatively large gain of energy, -84 kJ mol<sup>-1</sup> (Figure 6.3), resulting in  $\eta^2$ -coordination between the palladium atom and a C–H bond of the incoming hydrocarbon. Next, this encounter complex **3b** proceeds via a  $\sigma$ -metathesis-like transition structure (TS **3b/4b**): The formal oxidation state of Pd<sup>II</sup> is retained in the Pd(CH<sub>3</sub>)(H<sub>2</sub>)<sup>+</sup> intermediate **4b** from which, in a barrier-free process, molecular hydrogen is liberated with an overall exothermicity of -21 kJ mol<sup>-1</sup> relative to the reactants. As the transition structure TS **3b/4b** is located energetically below the entrance and exit channels and rotation around the (H<sub>2</sub>)Pd–(CH<sub>3</sub>)<sup>+</sup> bond in **4b** requires at most only a few kJ mol<sup>-1</sup>, the energy profile depicted in Figure 6.3 also explains qualitatively the occurrence of hydrogen/deuterium scrambling processes (Table 6.2).<sup>13</sup> Inspection of the geometric details (see Table A.5 in the

<sup>13</sup> A quantitative discussion of the competition between direct H/CH<sub>3</sub> ligand exchange (70 %) versus prior hydrogen exchange (30 %) in relation to the energy profile in Figure 6.3 is not really meaningful without sufficiently detailed trajectory calculations of the ion-molecule reactions based on a PES calculated at a more accurate level of theory.

Appendix) of the species involved in reaction I.4b reveals a smooth breaking and making of carbon-hydrogen, palladium-hydrogen, and hydrogen-hydrogen bonds, respectively.

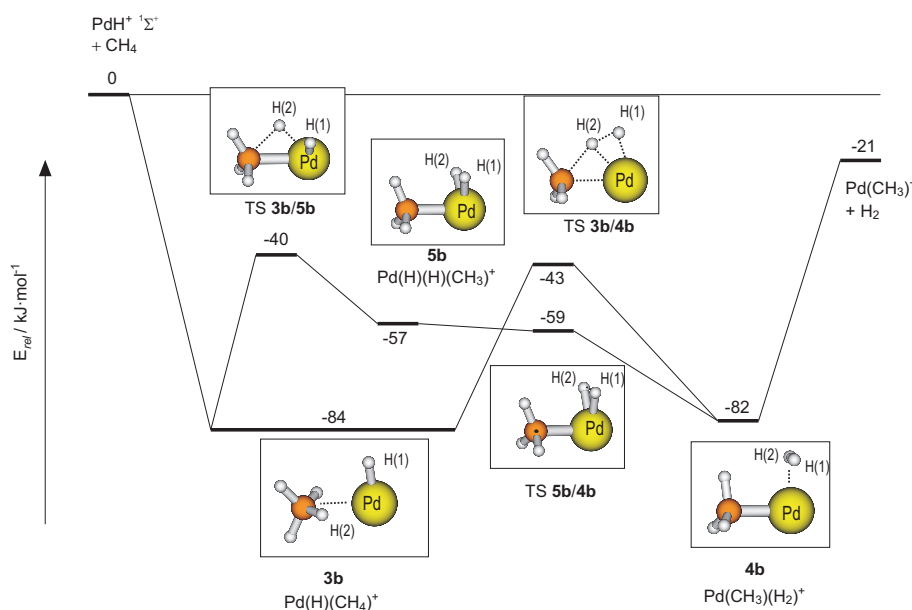


Figure 6.3 – Energy diagram (in  $\text{kJ mol}^{-1}$ ) for the reaction of  $\text{PdH}^+$  and methane. The values are relative to the entrance channel and corrected for zero-point vibrational energies.

Noteworthy are in particular the features of the transition structure **TS 3b/4b** in which the migrating hydrogen atom H(2) interacts with three centers simultaneously, that is, the carbon, palladium, and hydrogen H(1) atoms. As required for a  $\sigma$ -metathesis process, in **TS 3b/4b** the atoms H(1), H(2), Pd, and C are coplanar. Based on intrinsic reaction coordinate calculations [181–183] rotation of the orthogonal Pd-H(1) and C-H(2) vectors in the encounter complex  $\text{Pd(H)(CH}_4\text{)}^+$  (**3b**) en route to the transition structure occurs smoothly with a small rotational barrier ( $<6 \text{ kJ mol}^{-1}$ ) which does not contribute to the overall barrier. The nascent bond formation between H(1) and H(2) in **TS 3b/4b** is indicated by a bond length of  $1.017 \text{ \AA}$ ; in the intermediate  $\text{Pd(CH}_3\text{)(H}_2\text{)}^+$  (**4b**) the H(1)–H(2) bond length ( $0.838 \text{ \AA}$ ) is almost comparable to that in free  $\text{H}_2$ . The characteristic features of the  $\sigma$ -bond-metathesis transition structure are also found for the corresponding  $\text{NiH}^+/\text{CH}_4$  system (Figure 6.1 and Table A.1 in the Appendix). Again, the atoms of the four-membered ring involved in the  $\sigma$ -bond metathesis (Ni, H(1), H(2), and C) are in-plane; the H(1)–H(2) bond is developed to a somewhat smaller, but comparable extent with a bond length of  $0.998 \text{ \AA}$ , and the C–H(2) bond is stretched by a factor of 1.38 (related to free methane) to a little lower degree (1.42 for the palladium system). However, fundamental differences exist with

regard to the details of the PES and thus to the actual reaction mechanisms: Whereas for the NiH<sup>+</sup>/CH<sub>4</sub> system the crossings between the high-spin and low-spin surfaces according to a TSR scenario (Figure 6.1) enable the activation of methane, the PdH<sup>+</sup>/CH<sub>4</sub> couple can be fully explained without invoking a multistate pattern. As the excited states of PdH<sup>+</sup> (<sup>3</sup>Δ and <sup>3</sup>Φ) are >320 kJ mol<sup>-1</sup> higher in energy than the <sup>1</sup>Σ<sup>+</sup> ground state, the whole reaction can proceed on the singlet potential-energy surface in a spin-conserving manner.

As the σ-metathesis process **3b** ⇌ TS **3b/4b** ⇌ **4b** is rather exceptional for a late transition metal like palladium [227–230], alternative routes have been screened. In fact, in addition to the direct equilibrium reaction **3b** ⇌ **4b**, an independent oxidative-addition type path exists (**3b** ⇌ **5b** ⇌ **4b**). At the theoretical level used, the relevant transition structure TS **3b/5b** is energetically comparable to TS **3b/4b**. The assignment of a formal oxidation state IV for palladium in intermediate **5b** is supported by the rather long H(1)–H(2) distance of 1.794 Å, the short Pd–H bonds (each 1.505 Å), and a Pd–C bond length of 2.040 Å. The subsequent reductive elimination proceeds on a flat PES via the practically isoenergetic TS **5b/4b** in a process that is typical and facile for Pd<sup>IV</sup> [231] to give the complex Pd(CH<sub>3</sub>)(H<sub>2</sub>)<sup>+</sup> (**4b**) rather than reverting to **3b**. Thus, path **3b** ⇌ **5b** does not constitute an alternative H/D equilibration variant but simply opens up an additional channel to link **3b** ⇌ **4b**. The oxidative addition/reductive elimination pathway could not be located for the NiH<sup>+</sup>/CH<sub>4</sub> system despite several approaches. As shown in Figure 6.4, the geometry optimization with fixed, increasing H(1)–Ni–H(2) angles starting from 29.9° at the local minimum **4a** results in a steady increase of the relative energy in the form of a shoulder instead of traversing a transition structure or reaching the intermediate dihydride complex Ni(H)<sub>2</sub>(CH<sub>3</sub>)<sup>+</sup> (**5a**).

### 6.1.3 Excursion: σ-bond metathesis *vs* oxidative addition

The reactions of NiH<sup>+</sup> and PdH<sup>+</sup> with methane may serve as good examples to underline the mechanistic manifold operative in formally similar processes of dehydrogenation. Related to these results, general aspects of the mechanisms of bond activation by MX<sup>+</sup> species, with X being a covalently bound ligand, will be discussed in the following. The commonly invoked mechanisms for transition-metal mediated C–H bond activation include oxidative addition (OA)/reductive elimination (RE) and σ-bond metathesis (σ-BM), Scheme 6.1. The latter is typical for *d*<sup>0</sup> metals and requires no intermediates, the former is inherently a multi-step reaction and is associated with a change of formal oxidation states.<sup>14</sup> Examples of OA/RE processes often include complexes of electron-rich, late transition metals mainly of the second

<sup>14</sup> Note that there also exists the ion/dipole mechanism for the C–H bond activation of functionalized hydrocarbons RX by metal cations without σ-BM or a redox step involved [124, 232–234]. In this mechanism, the metal cation first coordinates to X and the charge is transferred to R, followed by proton transfer to the MX unit as the actual C–H bond-activation step.



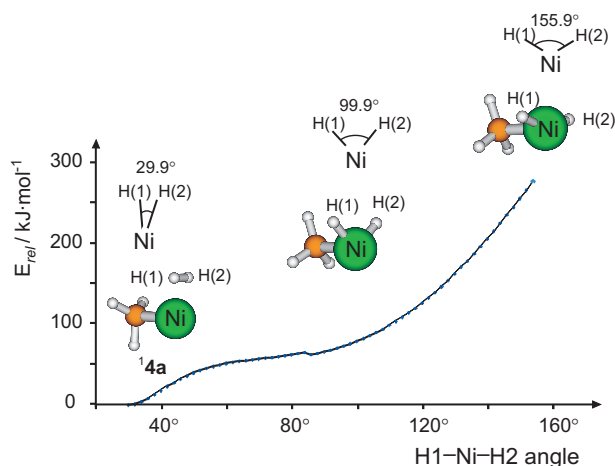
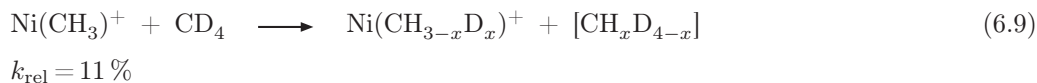


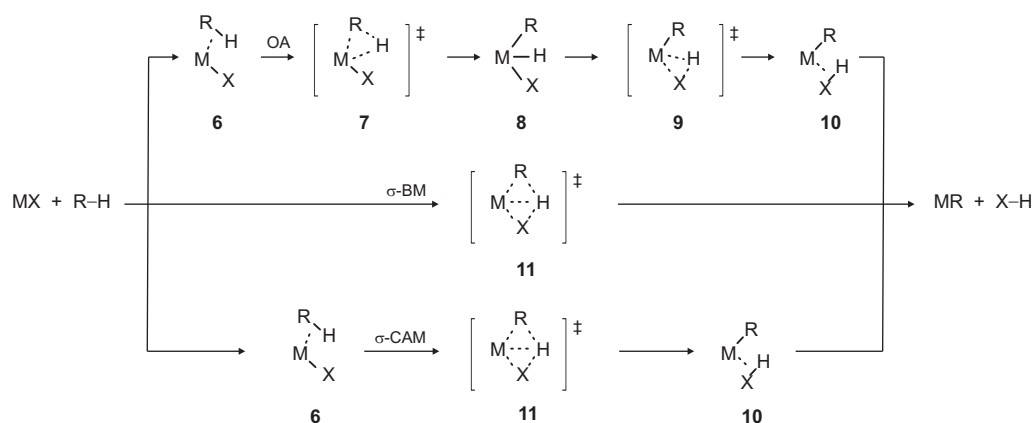
Figure 6.4 – Relative Energy (in  $\text{kJ mol}^{-1}$ ) of the  $\text{Ni(CH}_3\text{)(H(1)-H(2))}^+$  system against the  $\text{H(1)-Ni-H(2)}$  angle. The little cusp at around  $80^\circ$  is due to a rotation of the methyl group.

and third row [52, 235].

As suggested for the  $\text{NiH}^+/\text{CH}_4$  system (section 6.1), quite a few systems were reported in which late transition-metal complexes bring about, for example, isotope exchange without exhibiting the features characteristic of an OA/RE reaction [230]. Therefore, based on experimental data and computational studies, a mechanistic variant was suggested in which  $\sigma$ -complexes undergo a metathesis process, and the term  $\sigma$ -complex-assisted metathesis ( $\sigma$ -CAM) has been introduced to distinguish the route  $\mathbf{6} \rightarrow \mathbf{11} \rightarrow \mathbf{10}$  from a direct four-center  $\sigma$ -BM rearrangement forming straightly via  $\mathbf{11}$  the products (Scheme 6.1). Although attempted distinctions of mechanistic variants may be reminiscent of numerous, occasionally semantic, debates about the role of concepts in chemistry or the nature of chemical bonding [236–242], technical distinctions seem to exist and demarcation into categories can be useful provided one does not forget that the “real” mechanism may well lie in a continuum defined by the extremes of these classifications [227–230, 243].



Not really unexpectedly in view of the high reactivity of  $\text{NiH}^+$ , a mixture of  $\text{Ni(CH}_3\text{)}^+$  and  $\text{CD}_4$  leads to degenerate H/D exchange (Equation 6.9) with a distribution of  $x = 3$  (55%),  $x = 2$  (15%), and  $x = 1$  (30%). In a combined experimental/computational gas-phase study of our group [244, 245] various mechanistic aspects of the degenerate ligand exchange in  $\text{M(CH}_3\text{)}^+/\text{CH}_4$  couples have been revealed for  $\text{M} = \text{Fe, Co, Ni, Ru, Rh, Pd, Os, Ir, and Pt}$ :



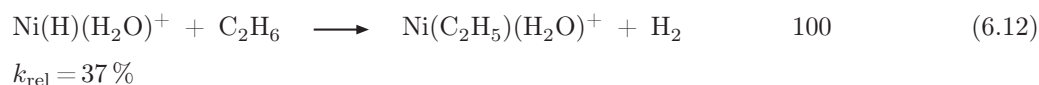
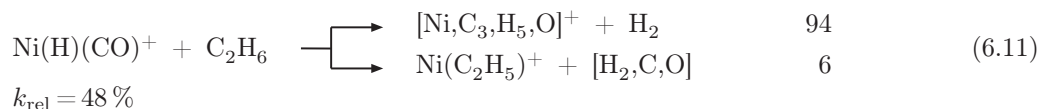
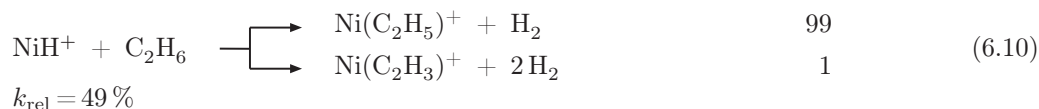
Scheme 6.1

- a) In line with earlier notions [66, 246, 247], for the late  $5d$  systems an OA/RE mechanism is operative. For the  $\text{Pt}(\text{CH}_3)^+/\text{CH}_4$  couple, the reaction is confined to the singlet state; in contrast, for the complexes containing  $\text{M}=\text{Os}$  and  $\text{Ir}$ , the OA/RE variant is entangled with a TSR scenario such that close to the entrance and exit channels, the system switches from the high-spin ground to the excited low-spin states.  $\sigma$ -CAM mechanisms are not operative for any of the  $5d$  complexes investigated.
- b) For the  $4d$  systems with  $\text{M}=\text{Ru}$ ,  $\text{Rh}$ , and  $\text{Pd}$ , another situation has been encountered. In the case of ruthenium and rhodium, the OA/RE mechanism is feasible energetically, and for these two couples the ligand switch is confined to their low-spin electronic states. In contrast, for the  $\text{Pd}(\text{CH}_3)^+/\text{CH}_4$  couple, in the  $^1\text{A}$  ground-state PES both the OA/RE and the  $\sigma$ -CAM mechanisms are energetically comparable, as found for the related  $\text{PdH}^+/\text{CH}_4$  complex, Chapter 6.1.2.
- c) For the  $3d$  congeners with  $\text{M}=\text{Fe}$ ,  $\text{Co}$ , and  $\text{Ni}$ , the  $\sigma$ -CAM mechanism is favored energetically over the OA/RE variant. The  $\text{Fe}$  and  $\text{Co}$  systems do not bring about thermal ligand exchange analogous to Equation 6.9 under ESI conditions due to energetically rather demanding transition structures. The transition structure for the  $\text{Ni}(\text{CH}_3)^+/\text{CD}_4$  couple associated with  $\sigma$ -CAM has been calculated to be  $28\text{ kJ mol}^{-1}$  higher in energy relative to the entrance channel of separated  $\text{Ni}(\text{CH}_3)^+$  and  $\text{CD}_4$  but  $13\text{ kJ mol}^{-1}$  below the transition structure belonging to the OA/RE mechanism [245]. If this computed value is realistic, some thermal energy of the reactants in the ESI experiment is required to surmount the activation barrier. The ligand exchange commences and finishes at the high-spin triplet surface, but the actual bond activation takes place at the excited singlet state (TSR scenario).

These mechanistic aspects are referred to in some of the following reactions of nickel complexes which have been examined in this work. In view of the fact that gas-phase ion-molecule processes proceed through encounter complexes (see section 2.2), the direct  $\sigma$ -metathesis process is not considered here. Rather, the focus is on a comparison of the OA/RE versus the  $\sigma$ -CAM variants.

#### 6.1.4 Reactions with ethane, propane, and *n*-butane

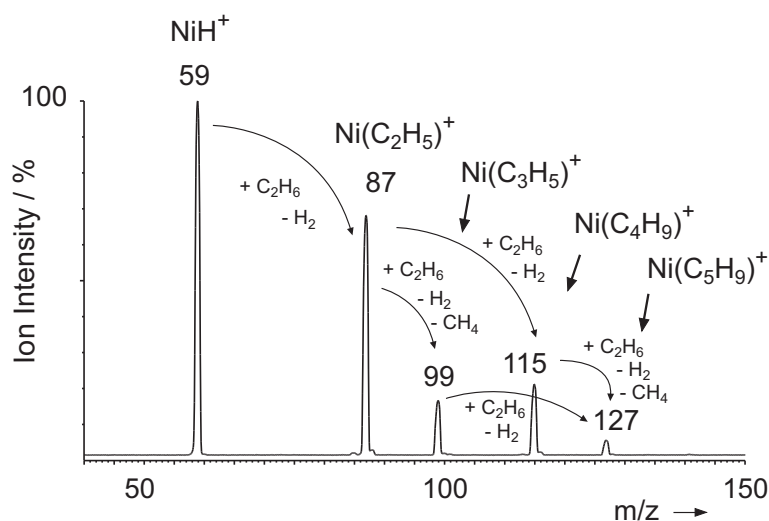
As in the reaction with methane, efficient dehydrogenation of ethane is observed in the reaction with the hydride complexes  $\text{NiH}^+$ ,  $\text{Ni(H)(CO)}^+$ , and  $\text{Ni(H)(H}_2\text{O)}^+$  (Equations 6.10, 6.11, and 6.12).



The isotope patterns of the  $\text{H}_2$ , HD, and  $\text{D}_2$  eliminations in the reaction with  $\text{CH}_3\text{CD}_3$  can be modeled in good agreement with the experimental data (Table 6.3) by separating the reaction in two processes, *i. e.* direct ligand switch and reactions involving scrambling of the H/D atoms (as applied in the reactions with methane). For  $\text{NiH}^+$  and  $\text{Ni(H)(CO)}^+$ , the specificity of dehydrogenation of ethane is comparable to the one observed in the reaction with methane. In contrast, the dehydrogenation of ethane by  $\text{Ni(H)(H}_2\text{O)}^+$  is much more specific ( $f_{\text{spec}} = 43\%$  for methane and  $f_{\text{spec}} = 80\%$  in the reaction with ethane, respectively). This is also true for the KIEs which are similar for the reaction with methane and ethane in the case of  $\text{NiH}^+$  and  $\text{Ni(H)(CO)}^+$ , whereas the KIE for direct ligand switch of  $\text{Ni(H)(H}_2\text{O)}^+$  is relatively large for the bond activation of methane compared to the one obtained for ethane (1.28 *vs* 2.42, respectively). This is indicative of a comparable degree of bond breaking and bond making in the respective transition structures for the former complexes and an unequal extent for the latter since the KIE depends on the relative magnitude of breaking the C–H bond and the progress of the H–H bond formation (see section 2.3).

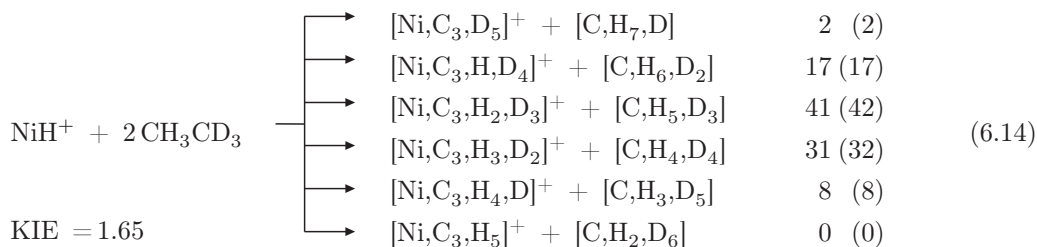
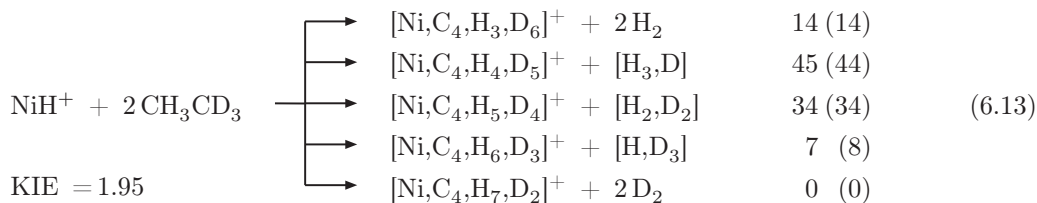
Table 6.3 – Isotope patterns<sup>a</sup> for the dehydrogenation of ethane by the nickel-hydride complexes  $\text{NiH}^+$ ,  $\text{Ni(H)(CO)}^+$ ,<sup>b</sup> and  $\text{Ni(H)(H}_2\text{O)}^+$ .

	- $\text{H}_2$	- $\text{HD}$	- $\text{D}_2$	
$\text{NiH}^+ + \text{C}_2\text{D}_6$		96 (96)	4 (4)	$f_{\text{spec}} = 97\%$
$\text{NiH}^+ + \text{CH}_3\text{CD}_3$	63 (62)	36 (37)	1 (1)	$\text{KIE}_{\text{spec}} = 1.73$
$\text{NiD}^+ + \text{C}_2\text{H}_6$	4 (4)	96 (96)		$f_{\text{scr}} = 3\%$
$\text{NiD}^+ + \text{CH}_3\text{CD}_3$	2 (1)	61 (63)	37 (36)	$\text{KIE}_{\text{scr}} = 0.95$
$\text{Ni(H)(CO)}^+ + \text{C}_2\text{D}_6$		61 (61)	39 (39)	$f_{\text{spec}} = 41\%$
$\text{Ni(H)(CO)}^+ + \text{CH}_3\text{CD}_3$	46 (47)	49 (47)	5 (6)	$\text{KIE}_{\text{spec}} = 1.64$
				$f_{\text{scr}} = 59\%$
				$\text{KIE}_{\text{scr}} = 1.32$
$\text{Ni(H)(H}_2\text{O)}^+ + \text{C}_2\text{D}_6$		85 (86)	15 (14)	$f_{\text{spec}} = 80\%$
$\text{Ni(H)(H}_2\text{O)}^+ + \text{CH}_3\text{CD}_3$	54 (52)	44 (46)	2 (2)	$\text{KIE}_{\text{spec}} = 1.28$
$\text{Ni(D)(H}_2\text{O)}^+ + \text{C}_2\text{H}_6$	17 (17)	83 (83)		$f_{\text{scr}} = 20\%$
$\text{Ni(D)(H}_2\text{O)}^+ + \text{CH}_2\text{D}_2$	7 (4)	52 (57)	41 (39)	$\text{KIE}_{\text{scr}} = 1.14$

<sup>a</sup> Given in % (modeled numbers are given in parenthesis). For details of the modeling, see section 6.1.<sup>b</sup> For the formation of  $\text{Ni(H)(CO)}^+$ ,  $^{13}\text{CH}_3\text{OH}$  was used as solvent to avoid isobaric overlap with  $\text{Ni(H)(N}_2\text{)}^+$ .Figure 6.5 – Reaction of  $\text{NiH}^+$  with ethane involving C–C bond formation

In addition to the observed dehydrogenation of ethane by  $\text{NiH}^+$ ,  $\text{Ni(H)(CO)}^+$ , and

$\text{Ni(H)(H}_2\text{O)}^+$ , the secondary reactions of the primary product ions are of interest as well. Remarkably, product complexes of consecutive reactions containing up to five C atoms are formed in the reaction of  $\text{NiH}^+$  with  $\text{C}_2\text{H}_6$  (Figure 6.5), whereas the higher ligated species  $\text{Ni(H)(CO)}^+$  and  $\text{Ni(H)(H}_2\text{O)}^+$  only react with one molecule of ethane.



In contrast to the primary reaction of  $\text{NiH}^+$  with  $\text{C}_2\text{H}_6$ , in which almost no scrambling processes are involved (Table 6.3), the isotope patterns in the product ions of the secondary reactions are fully in line with an H/D equilibration assuming an averaged KIE of 1.95 and 1.65 for the reactions 6.13 and 6.14, respectively.

Quite likely, the primary product of the reaction of  $\text{NiH}^+$  with ethane corresponds to the nickel-ethyl cation  $\text{Ni}(\text{C}_2\text{H}_5)^+$  (**13**, Figure 6.6) which is suggested to be formed in a TSR reaction sequence similar to  $\text{Ni}(\text{CH}_3)^+$ , generated in the reaction of  $\text{NiH}^+$  with methane (Figure 6.1). At the B3LYP level of theory, the barrier for a  $\beta$ -hydrogen transfer - which is a common decomposition pathway for metal-alkyl complexes to metal-hydride derivatives,  $\text{Ni(H)(C}_2\text{H}_4)^+$  in this case - amounts to  $122 \text{ kJ mol}^{-1}$  on the singlet surface ( $^1\mathbf{13} \rightarrow ^1\mathbf{12}$ , Figure 6.6) which is the corresponding ground state. For the analogous iron system  $[\text{Fe}, \text{C}_2, \text{H}_5]^+$ , the two possible structures  $\text{Fe(H)(C}_2\text{H}_4)^+$  and  $\text{Fe(C}_2\text{H}_5)^+$  possess different ground states, the ethyl complex profits from agostic interaction which is only possible for the low-spin state and thus has a triplet ground state, whereas the ground state of  $\text{Fe(H)(C}_2\text{H}_4)^+$  is a quintet state with the triplet state being  $59 \text{ kJ mol}^{-1}$  higher in energy. The isomerization of  $\text{Fe(H)(C}_2\text{H}_4)^+$  to energetically favored  $\text{Fe(C}_2\text{H}_5)^+$  also profits from hyperconjugation in the associated triplet state; thus, the rearrangement follows a TSR scenario [248]. A somewhat

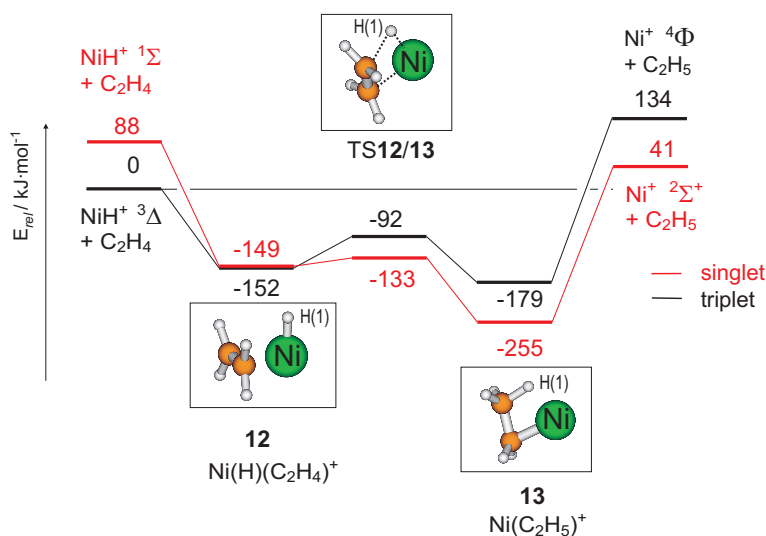


Figure 6.6 – DFT-Based energy diagram of the  $\text{Ni}(\text{H})(\text{C}_2\text{H}_4)^+ \rightleftharpoons \text{Ni}(\text{C}_2\text{H}_5)^+$  isomerization. The values are relative to the energies of the separated building blocks  $\text{NiH}^+$  ( $^3\Delta$ ) and  $\text{C}_2\text{H}_4$ , corrected for contributions of zero-point vibrational energies, and are given in  $\text{kJ mol}^{-1}$ .

different picture emerges for the  $[\text{Ni}, \text{C}_2, \text{H}_5]^+$  system (Figure 6.6): While the nickel-ethyl cation is favored in the low-spin state as it is for the respective iron complex, the high-spin and low-spin states of  $\text{Ni}(\text{H})(\text{C}_2\text{H}_4)^+$  are almost isoenergetic at this level of theory. Thus, a spin flip does not necessarily occur in the isomerization  $\mathbf{12} \rightleftharpoons \mathbf{13}$ . The microscopically reverse reaction of a  $\beta$ -hydrogen elimination is the insertion of alkenes in a metal-hydrogen bond; the corresponding barrier for the  $\mathbf{12} \rightarrow \mathbf{13}$  rearrangement amounts to only  $16 \text{ kJ mol}^{-1}$ . Olefin insertion in a nickel-carbon bond is also expected to be operative in the reaction sequences of  $\text{NiH}^+$  with ethane in which C–C bond formation results in the formation in  $\text{C}_n\text{H}_{2n+1}$  ( $n = 2, 4, 6$ ) and  $\text{C}_n\text{H}_{2n-1}$  ( $n = 3, 5$ ). In line with this, C–C coupling reactions are also observed for the  $\text{NiH}^+/\text{C}_2\text{H}_4$  couple resulting in the formations of complexes containing up to ten C atoms (Figure 6.7). As in the before-mentioned C–C coupling with CO, nickel is widely used in industrial homogeneous catalysis of alkene polymerization [207, 209, 249], *e.g.* in the Shell higher olefin process (SHOP). Here, the active species is assumed to be a nickel(II) olefin-hydride complex [209]; ethene insertion into the Ni–H bond leads to the formation of nickel alkyls with various chain lengths.

In the reactions of  $\text{NiH}^+$  and  $\text{Ni}(\text{H})(\text{CO})^+$  with propane, double dehydrogenation probably results in the formation of stable allyl complexes as the main reaction channel. Although with a lower BR of 34 %, double dehydrogenation is for  $\text{Ni}(\text{H})(\text{H}_2\text{O})^+$  also of importance.

In contrast to the ICR experiments with labeled substrates (see Chapter 4.1), the distinc-

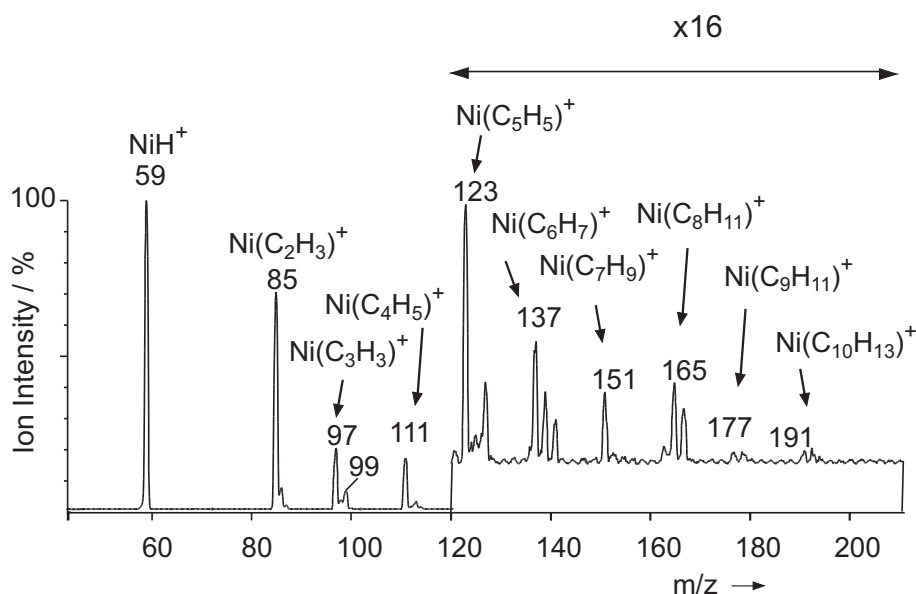


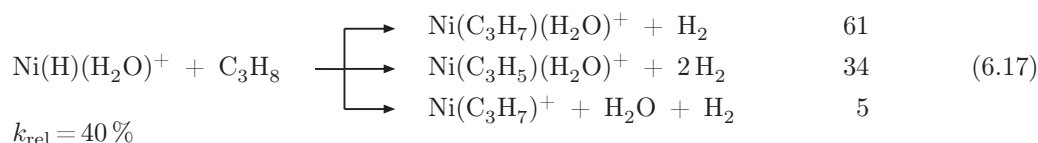
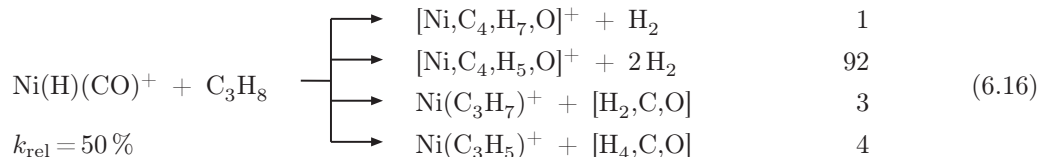
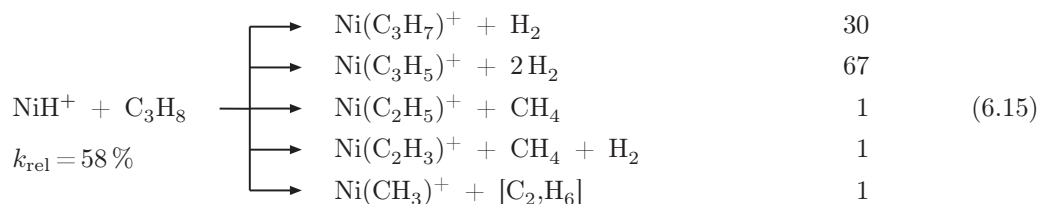
Figure 6.7 – Reaction of  $\text{NiH}^+$  with ethene involving C–C bond formation.

tion between the loss of  $\text{D}_2$  and  $2\text{H}_2$  of single and double dehydrogenation is impossible in the experiments carried out with a quadrupole-mass analyzer. However, using  $\text{CD}_3\text{CH}_2\text{CD}_3$  (**14**) as substrate, the elimination of  $2\text{H}_2$  cannot interfere the elimination of  $\text{D}_2$ ; thus, the reactions of the two hydride complexes  $\text{NiH}^+$ , and  $\text{Ni(H)(H}_2\text{O)}^+$  with **14** have been investigated (Tables 6.4).<sup>15</sup> To model the single dehydrogenation for  $\text{NiH}^+$  and  $\text{Ni(H)(H}_2\text{O)}^+$ , a preference for primary C–D *vs* secondary C–H bond activation of **14** has been assumed. However, the introduction of two more parameters, *i. e.* the ratio of secondary and primary bond activation ( $f_{\text{sec/prim}}$ , Table 6.4), into the calculation leads to an under-determination of the system.<sup>16</sup> To reduce the parameters to be optimized, the separation of the KIE into individual KIEs for the direct ligand switch and scrambling processes has been omitted. With this simplified model, the experimental data are quite well reproduced; obviously, lifetime effects as found for the dehydrogenation of cyclohexane by the transition-metal dimers  $\text{MM}'^+$  do not play a role in single and double dehydrogenation of propane by  $\text{NiH}^+$  and  $\text{Ni(H)(H}_2\text{O)}^+$ .

As mentioned, the ratios for the specific and scrambling processes are different in the reac-

<sup>15</sup> Since the ratio of single dehydrogenation for  $\text{Ni(H)(CO)}^+$  amounts to only 1%, the  $\text{Ni(H)(CO)}^+/\textbf{14}$  couple has not been examined.

<sup>16</sup> Three independent values are derived from the experiment, *i. e.* the ratio  $\text{HD}/\text{D}_2$  in the reaction with  $\text{C}_3\text{D}_8$  together with ratios  $\text{H}_2/\text{HD}$  and  $\text{H}_2/\text{D}_2$  in the reaction with  $\text{CD}_3\text{CH}_2\text{CD}_3$ . Thus, only three independent parameters can be optimized, *i. e.*  $\text{KIE}_{\text{tot}}$ ,  $f_{\text{spec}}$ , and  $f_{\text{sec}}$  whereas  $f_{\text{scr}}$ , and  $f_{\text{prim}}$  are no free parameters but depend on  $f_{\text{spec}}$  and  $f_{\text{sec}}$ , respectively (or vice versa).



tion of  $\text{Ni(H)(H}_2\text{O)}^+$  with methane and ethane, but they are comparable for the substrates ethane and propane. The preference  $f_{\text{sec/prim}}$  for secondary C–H bond activation (Table 6.4) is higher for the “naked”  $\text{NiH}^+$  ( $f_{\text{sec/prim}} = 1.84$ ) relative to  $\text{Ni(H)(H}_2\text{O)}^+$  ( $f_{\text{prim/sec}} = 1.36$ ); however, in comparison to the nickel-halide complexes  $\text{NiX}^+$ , the latter are even more specific in this respect (see Chapter 6.2).

The elimination of  $[\text{H}_4, \text{O}]$  in the reaction of  $\text{Ni(H)(H}_2\text{O)}^+$  with propane (Equation 6.17) corresponds most likely to the elimination of molecular hydrogen and water, whereas the (undetected) neutral loss of  $[\text{C}, \text{H}_2, \text{O}]$  in the reaction of  $\text{Ni(H)(CO)}^+$  with propane (Equation 6.16) can be either assigned to dehydrogenation concomitant with CO loss or to formaldehyde formation; the latter is then eliminated as intact unity. Thermochemical considerations do not give a clear answer because the formation of formaldehyde *vs* CO and  $\text{H}_2$  is thermochemically favored by only  $5.4 \text{ kJ mol}^{-1}$  [250], and the rearrangement that leads to formaldehyde formation might be hampered by more energy-demanding transition structures. However, the above-mentioned ability of nickel to catalyze formylation reactions might suggest the elimination of  $\text{CH}_2\text{O}$ .

So far, only a negligible extent of C–C bond activation has been observed (Equation 6.15); as expected, this reaction mode gains more significance in the reaction with *n*-butane. Concerning the reaction mechanism, a comparison with naked  $\text{Ni}^+$  is quite instructive. By employing  $\text{CD}_3\text{CH}_2\text{CH}_2\text{CD}_3$ , it was shown for  $\text{Ni}^+$  that dehydrogenation of this substrate is a highly specific 1,4-elimination which commences with C(2)–C(3) bond activation followed

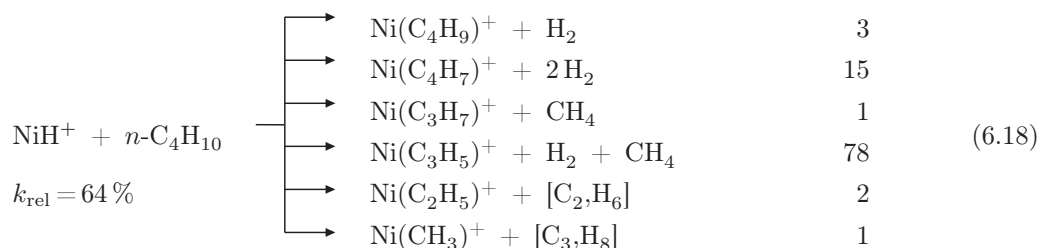


Table 6.4 – Isotope patterns<sup>a</sup> of single dehydrogenation of propane by the nickel-hydride complexes  $\text{NiH}^+$  and  $\text{Ni(H)(H}_2\text{O)}^+$ .

	- $\text{H}_2$	- HD	- $\text{D}_2$	
$\text{NiH}^+ + \text{C}_3\text{D}_8$		89 (89)	11 (11)	$f_{\text{spec}} = 81\%$
$\text{NiH}^+ + \text{CD}_3\text{CH}_2\text{CD}_3$	50 (49)	47 (46)	3 (5)	$f_{\text{scr}} = 19\%$
				$\text{KIE}_{\text{tot}} = 1.45$
				$f_{\text{sec/prim}} = 1.84$
$\text{Ni(H)(H}_2\text{O)}^+ + \text{C}_3\text{D}_8$		87 (87)	13 (13)	$f_{\text{spec}} = 74\%$
$\text{Ni(H)(H}_2\text{O)}^+ + \text{CD}_3\text{CH}_2\text{CD}_3$	41 (41)	53 (54)	6 (5)	$f_{\text{scr}} = 26\%$
				$\text{KIE}_{\text{tot}} = 1.75$
				$f_{\text{sec/prim}} = 1.36$

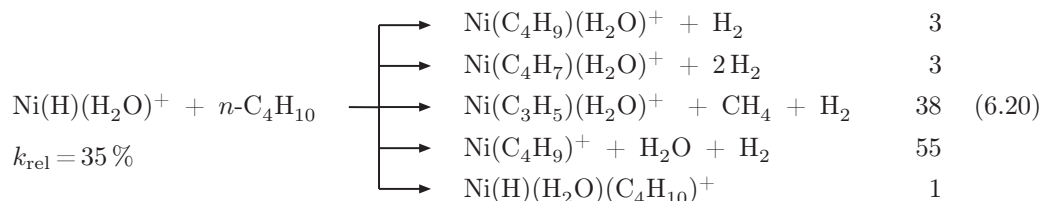
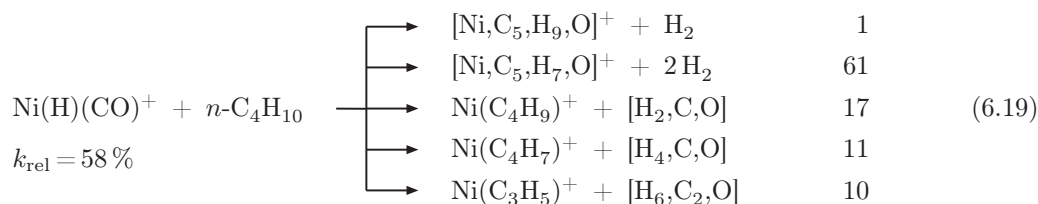
<sup>a</sup> Given in % (modeled numbers are given in parenthesis). See text for details of the modeling.

by two  $\beta$ -deuterium transfers and reductive elimination of  $\text{D}_2$  [251].<sup>17</sup> Considering this, the activation of the slightly weaker  $\text{C}(2)\text{--C}(3)$  bond<sup>18</sup> of butane by  $\text{Ni}^+$  (Equation 5.4, page 51) is favored over  $\text{C}(1)\text{--C}(2)$  insertion by a factor of approximately 1.5. For the nickel hydrides instead, loss of methane is the only reaction that indicates  $\text{C--C}$  bond activation. The finding implies that only the stronger terminal  $\text{C}(1)\text{--C}(2)$  bonds are activated. This and the fact that demethanation by the nickel hydrides occurs almost exclusively in combination with the loss of  $\text{H}_2$  (Equations 6.18 - 6.20) strongly suggest that the reaction starts with  $\text{C--H}$  bond activation - preferably at internal methylen positions - and  $\text{H}_2$  elimination rather than direct insertion into the  $\text{C}(1)\text{--C}(2)$  bond. Subsequent  $\beta$ -methyl migration, by which a propene ligand is formed, followed by allylic  $\text{C--H}$  bond activation, enables finally the formation of methane and stable allyl complexes. Alternatively, the latter can also be formed by an equivalent process commencing with primary  $\text{C--H}$  bond activation.



<sup>17</sup> 1,4-dehydrogenation concomitant with the formation of a metallacycle could be excluded because the presence of two ethene ligands in  $[\text{Ni}, \text{C}_4\text{H}_8]^+$  was proved in an ICR experiment [251].

<sup>18</sup> The bond energies  $D_{298}(\text{CH}_3\text{CH}_2\text{--CH}_3) = 373 \text{ kJ mol}^{-1}$ ,  $D_{298}((\text{CH}_3)_2\text{CH--CH}_3) = 371 \text{ kJ mol}^{-1}$ , and  $D_{298}(\text{CH}_3\text{CH}_2\text{--CH}_2\text{CH}_3) = 368 \text{ kJ mol}^{-1}$  are taken from ref. [252].



The combined elimination of two neutral molecules from the substrate, *i. e.* H<sub>2</sub> and/or CH<sub>4</sub>, corresponds to the main reaction channel in the reaction of NiH<sup>+</sup> and Ni(H)(CO)<sup>+</sup> with propane and *n*-butane (in total, 68 % and 93 % for NiH<sup>+</sup>, 96 % and 82 % for Ni(H)(CO)<sup>+</sup>, respectively) whereas it is less pronounced for Ni(H)(H<sub>2</sub>O)<sup>+</sup> (34 % and 41 %, respectively). In view of the fact that consecutive reactions sequences complicate the modeling and require a couple of parameters and, furthermore, the differentiation of 2 H<sub>2</sub> *vs* D<sub>2</sub> is not possible in the ESI experiments, no experiments with labeled *n*-butanes have been carried out.

## 6.2 Reactivity of nickel-halide complexes NiX<sup>+</sup>

In the following, ligand effects are studied by systematically changing the nature of the anionic ligand X in Ni<sup>II</sup> complexes NiX<sup>+</sup>; in this Chapter, the reactions of four small, saturated hydrocarbons by gaseous nickel cations NiX<sup>+</sup> (X = F, Cl, Br, I) are described.

The organization of this section is such that first the ion-molecule reactions are presented for each NiX<sup>+</sup> complex with the four hydrocarbons employed, followed by a brief discussion of the most abundant or interesting processes. Then, for a selected class of reactant couples, labeling-experiment data are reported to trace the origin of the bonds being activated. Mechanistic details of the reactions experimentally observed for NiF<sup>+</sup> with methane as well as the reaction of NiBr<sup>+</sup> and NiCl<sup>+</sup> with ethane are revealed by B3LYP calculations.

In a first step, let us classify the reactions observed into three different types:

- Bond activation of the organic substrate without obvious occurrence of Ni–X bond cleavage, that is, the losses of H<sub>2</sub>, CH<sub>4</sub>, and C<sub>2</sub>H<sub>6</sub>, which formally lead to the corresponding NiX<sup>+</sup>/olefin complexes.
- Reactions involving Ni–X bond cleavage, namely the expulsions of HX, HX/H<sub>2</sub>, and HX/CH<sub>4</sub>, affording nickel-alkyl or nickel-alkenyl cations, respectively.

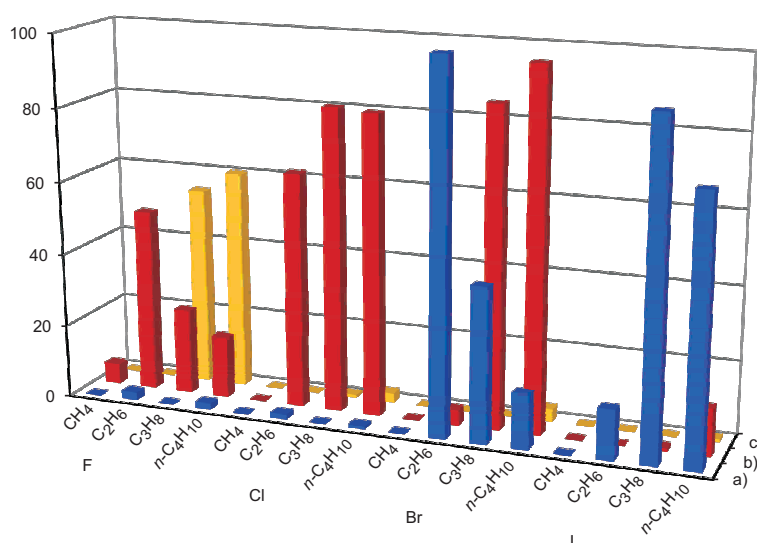


Figure 6.8 – Relative reaction efficiencies for a) activations of the alkane without apparent cleavage of the  $\text{Ni-X}$  bond (■), b) reactions concomitant with  $\text{Ni-X}$  bond cleavage (■), and c) losses of neutral  $\text{RNiX}$  species (■). In the Figure, the data from Table 6.5 are weighted with the relative rates and renormalized to a maximal reaction efficiency of 100 (dehydrogenation of ethane by  $\text{NiBr}^+$ ).

- c) Losses of neutral  $\text{RNiX}$  units ( $\text{R} = \text{H}, \text{CH}_3$ ) concomitant with generation of the corresponding carbenium ions.

Figure 6.8 shows the relative reaction efficiencies of channels a)–c), where the branching ratios given in Table 6.5 are also weighted with respect to the relative rate constants.

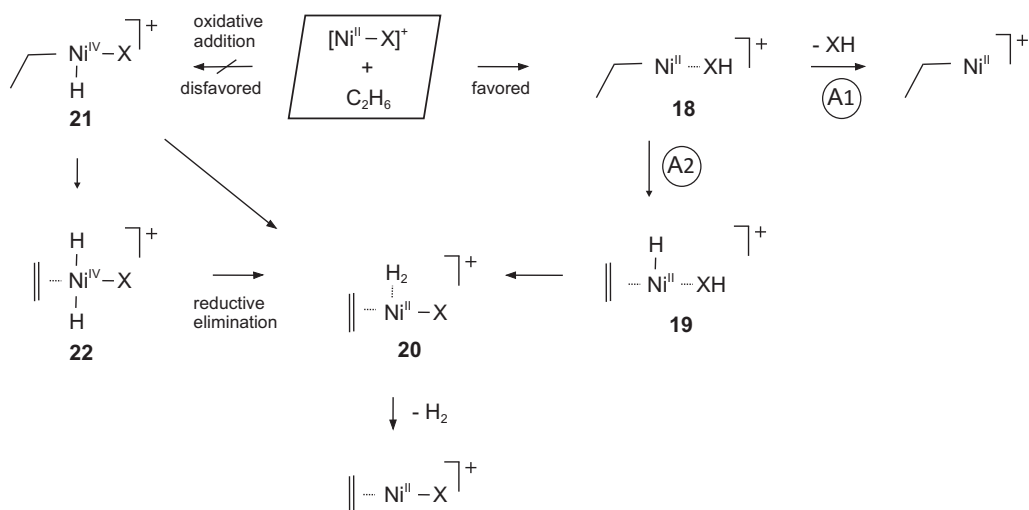
In terms of the classification made in the introduction for  $\text{CrF}_n^+$  systems (see Scheme I.2 on page 5), the eliminations of the closed-shell neutral molecules  $\text{HX}$  ( $\text{X} = \text{F}, \text{Cl}, \text{Br}, \text{I}$ ) belong to reaction category (I), because in these activation steps the nickel ion preserves its formal oxidation state as well as the positive charge in the reactants and products. This is also true for the expulsion of  $\text{H}_2$ ,  $\text{CH}_4$ , and  $\text{C}_2\text{H}_6$  (and combinations thereof); here, however, the cation might well undergo several changes of their oxidation states in the intermediates that are generated in a sequence of oxidative additions and reductive eliminations. Oxidative addition implies an increase of 2 for the formal oxidation state of the nickel center as long as the halide bound to it is not involved in the reaction. However, as illustrated in Chapter 6.1.3, this pathway is known to be avoided for a  $3d$  transition metal like nickel by a mechanism according to a  $\sigma$ -CAM reaction [52, 230, 235, 245]. B3LYP calculation for the dehydrogenation of ethane by  $\text{NiCl}^+$  and  $\text{NiBr}^+$  indeed confirmed this pathway (path (A2) in Scheme 6.2) to be favored for nickel, in which a higher oxidation state is circum-

Table 6.5 – Relative rates<sup>a</sup> and branching ratios<sup>b</sup> of the neutral losses in the reactions of mass-selected NiX<sup>+</sup> cations (X = F, Cl, Br, I) with small alkanes R-H (R = CH<sub>3</sub>, C<sub>2</sub>H<sub>5</sub>, C<sub>3</sub>H<sub>7</sub>, *n*-C<sub>4</sub>H<sub>9</sub>).

R	X	<i>k</i> <sub>rel</sub>	-H <sub>2</sub>	-CH <sub>4</sub>	-C <sub>2</sub> H <sub>6</sub>	-HX	-HX/ H <sub>2</sub>	-HX/ CH <sub>4</sub>	-HNiX	-CH <sub>3</sub> NiX
CH <sub>3</sub>	F	4				100				
	Cl	n.r.								
	Br	n.r.								
	I	n.r.								
C <sub>2</sub> H <sub>5</sub>	F	40	4			95	1			
	Cl	50	2			98				
	Br	80	96			4				
	I	10	100							
C <sub>3</sub> H <sub>7</sub>	F	60				7	23		70	
	Cl	65				68	31		1	
	Br	100	32			50	18			
	I	70	98	1		1	<1			
<i>n</i> -C <sub>4</sub> H <sub>9</sub>	F <sup>c,d</sup>	65			2	2	7	12	63	12
	Cl <sup>c</sup>	65	1			3	9	84	3	
	Br	90	4	8	1	13	34	38	3	
	I <sup>e</sup>	65	77	6	1	8	6	1		

<sup>a</sup> Rates given relative to the fastest reaction observed (NiBr<sup>+</sup> + C<sub>3</sub>H<sub>8</sub>).<sup>b</sup> Normalized to a sum of 100.<sup>c</sup> In addition, loss of HX/C<sub>2</sub>H<sub>4</sub> (or C<sub>2</sub>H<sub>5</sub>X) is observed (<1).<sup>d</sup> In addition, loss of CH<sub>3</sub>F is observed (2).<sup>e</sup> In addition, double dehydrogenation is observed (2 H<sub>2</sub>, 1).

vented by the formation of a complex Ni(C<sub>2</sub>H<sub>5</sub>)(XH)<sup>+</sup> (**18**) (X = Cl: **18a**, X = Br: **18b**) via a  $\sigma$ -metathesis reaction between a C–H bond of ethane and the Ni–X bond (Figures 6.9 and 6.10). After a hydrogen atom is transferred from ethane to the halide to form a closed-shell HX and an open-shell C<sub>2</sub>H<sub>5</sub> ligand, a hydride complex Ni(H)(HX)(C<sub>2</sub>H<sub>4</sub>)<sup>+</sup> (**19**) (X = Cl: **19a**, X = Br: **19b**) is formed by  $\beta$ -hydrogen transfer from the ethyl ligand to the nickel core. A subsequent back transfer of a hydrogen atom from HX to the hydride ligand in a second  $\sigma$ -metathesis-type reaction (which also can be regarded as a proton transfer from the halide to the hydride ligand) allows the generation of molecular hydrogen. Both transition structures of this reaction sequence possess the structural properties postulated for a  $\sigma$ -CAM (Tables A.3 and A.4 in the Appendix), *i. e.* a coplanar, four-center transition



Scheme 6.2

structure in which simultaneously two  $\sigma$ -bonds are going to be broken ( $\text{Ni-X}$  and  $\text{C-H}$  or  $\text{Ni-H}$  and  $\text{X-H}$ , respectively) while two are formed ( $\text{Ni-C}$  and  $\text{X-H}$  or  $\text{H-H}$  and  $\text{Ni-X}$ , respectively). The expulsion of  $\text{H}_2$  from the newly formed  $\text{Ni(X)(H}_2\text{)(C}_2\text{H}_4\text{)}^+$  (**20**) ( $\text{X} = \text{Cl}$ : **20a**,  $\text{X} = \text{Br}$ : **20b**) complex terminates this reaction pathway. In contrast, a  $\text{Ni}^{\text{IV}}$  intermediate  $\text{Ni(X)(C}_2\text{H}_5\text{)(H)}^+$  (**21**), required for a mechanism according to oxidative addition, could not be located on the PES of the  $\text{NiX}^+$ /ethane manifold ( $\text{X} = \text{Cl, Br}$ ); all attempts result either in  $\text{Ni}^{\text{II}}$  complexes  $\text{Ni(X)(C}_2\text{H}_6\text{)}^+$  (**17**) or  $\text{Ni(C}_2\text{H}_5\text{)(HX)}^+$  (**18**), respectively, or - although somewhat less pronounced - display the same hump-like energy gradient against the  $\text{C-Ni-H}$  angle as described for the  $\text{NiH}^+/\text{CH}_4$  system (Chapter 6.1.2).

According to theory, the experimentally observed preference for  $\text{HX}$  loss *vs* dehydrogenation is reversed for the chloride and the bromide complexes  $\text{NiCl}^+$  and  $\text{NiBr}^+$  because the elimination of  $\text{HBr}$  from the intermediate  $\text{Ni(C}_2\text{H}_5\text{)(HBr)}^+$  (**18b**) has been calculated to be endothermic with  $33 \text{ kJ mol}^{-1}$  on the singlet surface and  $45 \text{ kJ mol}^{-1}$  on the triplet surface with respect to the entrance channel, *i. e.* separated  $\text{NiBr}^+$  ( $^3\Delta$ ) and ethane. An excess of thermal energy of the reactants on the high tail of the kinetic energy distribution [253] provides a convincing explanation for the experimentally observed ratio of 4 % for  $\text{HBr}$  loss, given that the computed number is realistic. However, for 96 % of the intermediates the reaction can proceed to eliminate molecular hydrogen as described above and shown in Figure 6.10. Instead, the expulsion of  $\text{HCl}$  from the respective  $\text{Ni(C}_2\text{H}_5\text{)(HCl)}^+$  complex (**18a**), is estimated to be exothermic with  $\Delta_r H = -2 \text{ kJ mol}^{-1}$  on the ground state triplet surface of  $\text{NiCl}^+$  ( $^3\Pi$ ) and ethane.

As far as general trends of the effects of the halogen ligands are concerned, activation

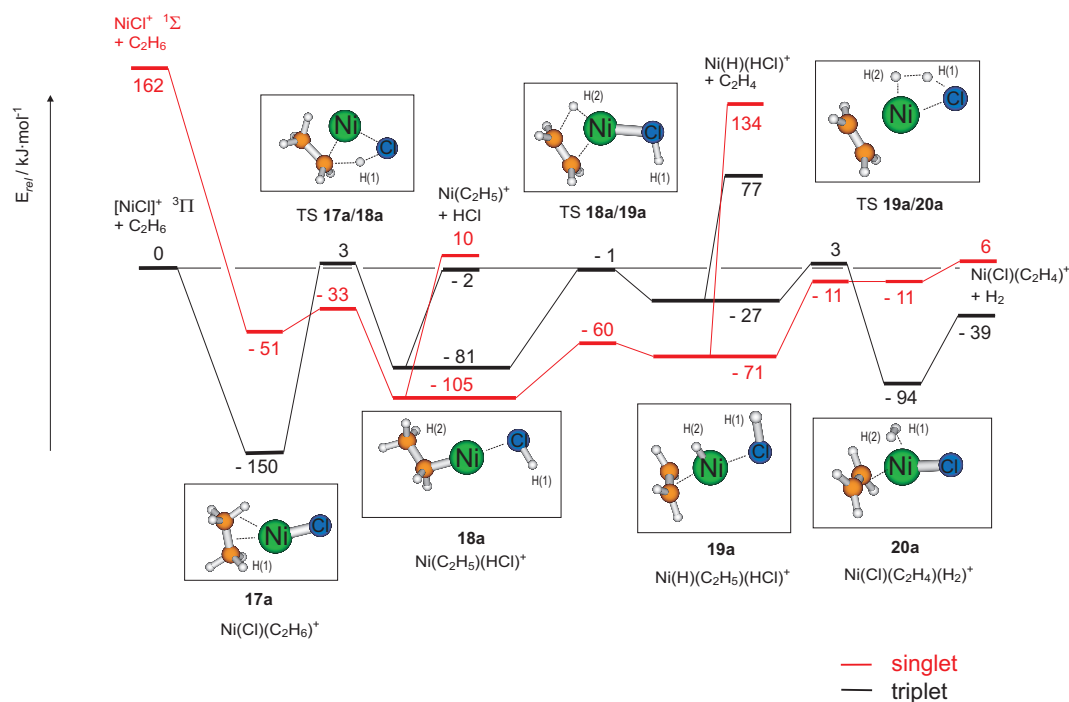


Figure 6.9 – Energy diagram (in  $\text{kJ mol}^{-1}$ ) for the reaction of  $\text{NiCl}^+$  and ethane. The values are relative to the entrance channel and corrected for zero-point vibrational energies.

of the alkane with maintaining the  $\text{Ni-X}$  bond intact is most effective for  $\text{X} = \text{Br}$  and  $\text{I}$ , whereas  $\text{Ni-X}$  bond cleavage is abundant for all halogen substituents<sup>19</sup> except  $\text{X} = \text{I}$ , and the formation of neutral  $\text{RNiX}$  species is of larger importance only for  $\text{X} = \text{F}$  (see Figure 6.8). With regard to the size effect of the alkanes, consideration of the overall rates (Table 6.5) is quite instructive. In general, the observed trends are gradual in that most reactions occur in the same order of magnitude with the exception of  $\text{NiF}^+$ , which is the only nickel-halide cation capable of activating methane, and for the reaction of  $\text{NiI}^+$  with ethane which is relatively inefficient.

A closer inspection of the reactions described in Table 6.5 reveals that some features are unique for a particular  $\text{NiX}^+/\text{RH}$  couple and others which several systems have in common. As mentioned,  $\text{NiF}^+$  occupies a special position in that it brings about thermal activation of methane according to Equation 6.21.



<sup>19</sup> For  $\text{NiBr}^+$ , the classification is strongly influenced by the nature of the substrate (Figure 6.8).

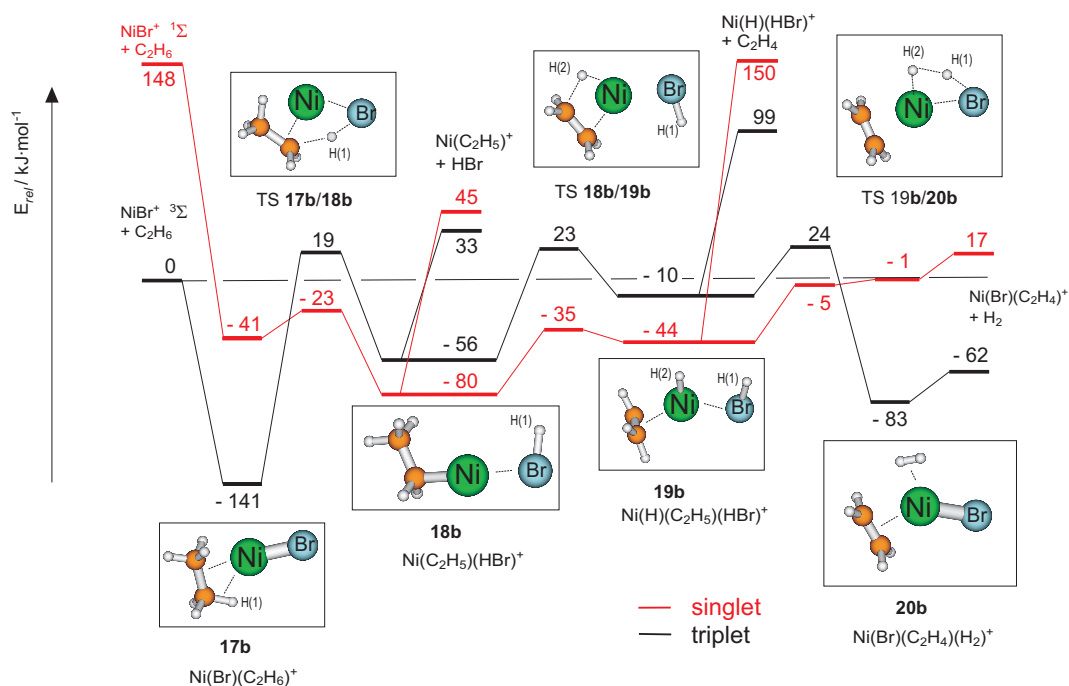


Figure 6.10 – Energy diagram (in  $\text{kJ mol}^{-1}$ ) for the reaction of  $\text{NiBr}^+$  and ethane. The values are relative to the entrance channel and corrected for zero-point vibrational energies.

Based on available experimental data [73, 250, 254] the reaction is exothermic<sup>20</sup> with  $\Delta_r H = -35 \pm 29 \text{ kJ mol}^{-1}$ . B3LYP calculations confirm this estimate by providing an exothermicity of  $-63 \text{ kJ mol}^{-1}$  for process 6.21. The driving force of this reaction as well as the abundant losses of either HF alone or in combination with other thermochemically favorable neutral products is provided by the exceptionally high stability of HF [250]. This way of reasoning has also been used previously to account for the reactions of, for example,  $\text{FeF}^+$  with acetone [78] or water [255] and of  $\text{CrF}_n^+$  with hydrocarbons [79], water [256] or phosphanes [257], respectively, all of which spontaneously liberate HF. Further, the  $\sigma$ -metathesis-like transition structure TS 15a/16a for this reaction has been located at  $-19 \text{ kJ mol}^{-1}$  relative to separated  $\text{NiF}^+/\text{CH}_4$  (Figure 6.11). Interestingly, the mechanistic details of the ligand switch for the  $\text{NiF}^+/\text{CH}_4$  system are again different from the  $\text{NiH}^+/\text{CH}_4$  reactants (Figure 6.1) as well as from the  $\text{PdH}^+/\text{CH}_4$  couple (Figure 6.3). As for  $\text{PdH}^+$ , the ligand switch proceeds according to single-state reactivity (SSR) in contrast to TSR found for  $\text{NiH}^+$ ; however, in the case of  $\text{NiF}^+$  it is not the low-spin but the high-spin

<sup>20</sup> Value derived from:  $\Delta_0 H(\text{Ni}^+ - \text{CH}_3) = 170 \pm 7 \text{ kJ mol}^{-1}$  [73],  $\Delta_0 H(\text{Ni} - \text{F}) = 437 \pm 6 \text{ kJ mol}^{-1}$ ,  $IE(\text{NiF}) = 9.4 \pm 0.3 \text{ eV}$  [254],  $IE(\text{Ni}) = 7.6398 \text{ eV}$ ,  $\Delta_f H(\text{CH}_4) = -74.9 \text{ kJ mol}^{-1}$ ,  $\Delta_f H(\text{CH}_3) = 145.7 \text{ kJ mol}^{-1}$ ,  $\Delta_f H(\text{HF}) = -273.3 \text{ kJ mol}^{-1}$ ,  $\Delta_f H(\text{Ni}) = 430 \text{ kJ mol}^{-1}$  [250].

triplet state on which both intermediates and the transition structure are energetically below the entrance channel. As mentioned, the transition structure associated with a  $\sigma$ -bond metathesis is favorable in the low spin state because of the ability to accept electrons delivered by the incoming  $\sigma\text{-C-H}$  bond of methane which experience more repulsion in the triplet state. This effect overcompensates the energy gap between the triplet ground state and the singlet excited state of  $\text{NiH}^+$ . Qualitatively speaking, the electron-withdrawing fluoride ligand obviously reduces the electron density at the nickel center in  $\text{NiF}^+$  and thus decreases the repulsion between the  $3d$  electrons and the  $\text{C-H}$  bond. Accordingly, the ligand switch  $\text{NiF}^+/\text{CH}_4 \rightarrow \mathbf{15a} \rightarrow \text{TS } \mathbf{15a}/\mathbf{16a} \rightarrow \mathbf{16a} \rightarrow \text{Ni}(\text{CH}_3)^+/\text{HF}$  can proceed throughout on the triplet surface in contrast to the reaction of  $\text{NiH}^+$  with  $\text{CH}_4$ .

Whereas the mechanism of a OA/RE reaction could not be located for  $\text{NiH}^+$ , the respective intermediates and transition structure in the case of  $\text{NiF}^+$  on the singlet surface could be determined. However, the inserted species  $\text{Ni}(\text{F})(\text{H})(\text{CH}_3)^+$  is  $70 \text{ kJ mol}^{-1}$  higher in energy than the entrance channel and almost isoenergetic to its preceding TS  $\mathbf{15a}/\mathbf{23a}$ . Reductive elimination is energetically the most demanding step: The associated TS is  $112 \text{ kJ mol}^{-1}$  higher in energy than the one calculated for the  $\sigma\text{-CAM}$  mechanism on the triplet surface; thus, the activation of methane by  $\text{NiF}^+$  proceeds very likely via the latter process (Figure 6.11).

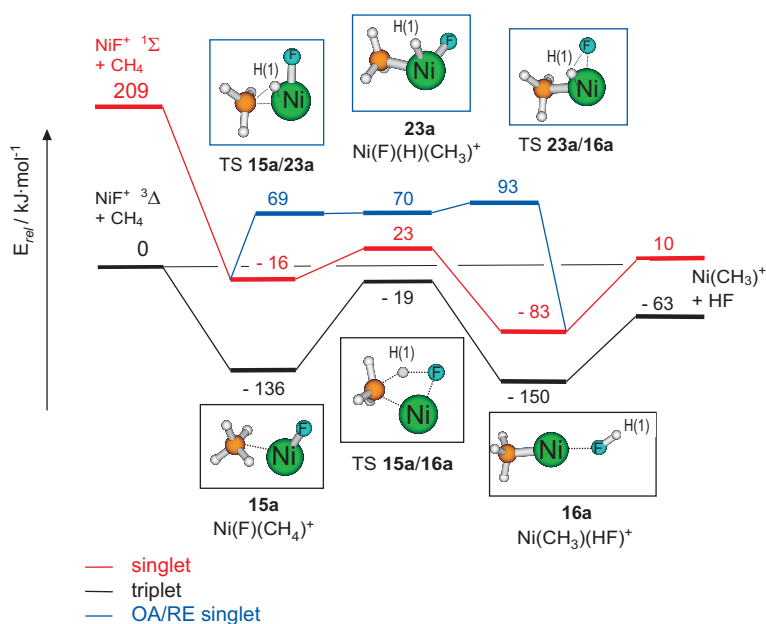


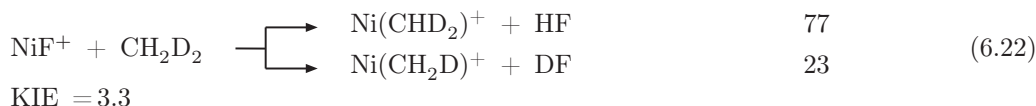
Figure 6.11 – Energy diagram (in  $\text{kJ mol}^{-1}$ ) for the reaction of  $\text{NiF}^+$  and methane. The values are relative to the entrance channel and corrected for zero-point vibrational energies.



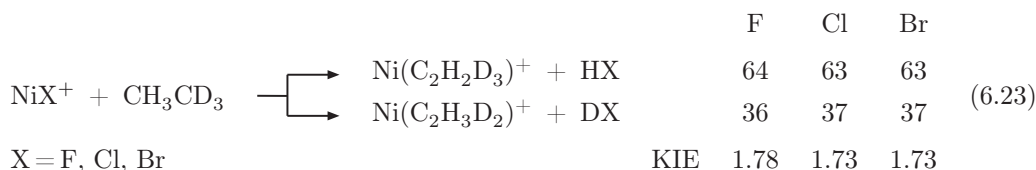
Inner-sphere electron-transfer reactions<sup>21</sup> (category  $\textcircled{II}$  of Scheme I.2, page 5), that is, the delivery of hydride or methanide ions from the hydrocarbon to  $\text{NiX}^+$ , are very pronounced for the  $\text{NiF}^+/\text{RH}$  couples ( $\text{R} = \text{C}_3\text{H}_7$ ,  $n\text{-C}_4\text{H}_9$ ), much less abundant for  $\text{NiCl}^+$  and  $\text{NiBr}^+$ , and absent in the reactions of  $\text{NiI}^+$  with any of the alkanes studied. Based on thermochemical considerations, for the neutral product the inserted  $\text{R-Ni-X}$  structure rather than the much less stable  $\text{Ni(RX)}$  isomer is assigned ( $\text{R} = \text{H}, \text{CH}_3$ ;  $\text{X} = \text{F}, \text{Cl}, \text{Br}$ ). Clearly, the stabilities of the resulting carbenium ions also play a decisive role, and this channel is accordingly only observed with propane and  $n$ -butane which can yield secondary carbenium ions. Outer-sphere electron transfer (category  $\textcircled{III}$  of Scheme I.2, page 5), has not been observed for any of the  $\text{NiX}^+/\text{RH}$  couples studied, thus implying  $IE(\text{RH}) > IE(\text{NiX})$ .

For a further elucidation of the actual C–H and C–C bonds of  $\text{RH}$  being activated by  $\text{NiX}^+$ , ion-molecule reactions of the latter have been performed with  $\text{CH}_2\text{D}_2$  (**24**),  $\text{CH}_3\text{CD}_3$  (**2**),  $\text{CD}_3\text{CH}_2\text{CD}_3$  (**14**),  $\text{CH}_3\text{CD}_2\text{CH}_3$  (**25**),  $\text{CH}_3\text{CH}_2\text{CH}_2\text{CD}_3$  (**26**) and  $\text{CD}_3\text{CH}_2\text{CH}_2\text{CD}_3$  (**27**). In the following, some selected results are presented aimed at revealing the more general trends. The discussion will center around four subclasses of processes:

**Loss of HX** Except for  $\text{X} = \text{I}$ , this elimination is observed for all  $\text{NiX}^+$  complexes. In the unique  $\text{F}/\text{CH}_3$  ligand switch in the reaction of  $\text{NiF}^+$  with methane, Equation 6.21, the investigation of  $\text{CH}_2\text{D}_2$  reveals a rather large intramolecular kinetic isotope effect of 3.3; this demonstrates that breaking the C–H(D) and forming the F–H(D) bonds constitute the rate-limiting step.



For ethane, the eliminations of HX and DX in the reaction with  $\text{CH}_3\text{CD}_3$  (**2**) imply KIEs of 1.73–1.78 for all three couples  $\text{NiX}^+$  ( $\text{X} = \text{F}, \text{Cl}, \text{Br}$ ), irrespective of their significantly different thermochemistry and branching ratios, that is, HX versus  $\text{H}_2$  eliminations.



<sup>21</sup> The term “inner-sphere electron transfer” is used here without implying any mechanistic distinctions, for example, transfer of genuine  $\text{H}^-$  versus consecutive transfer of  $\text{H}/\text{e}^-$ .

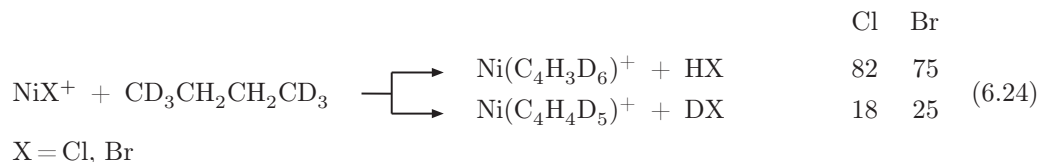
For the NiX<sup>+</sup>/C<sub>3</sub>H<sub>8</sub> systems, the loss of HX exhibits a clear preference for activation of the secondary rather than the primary C–H bond of the substrate. The modeling of HX elimination in the reactions of NiX<sup>+</sup> (X = F, Cl, Br) with the complementary substrates CD<sub>3</sub>CH<sub>2</sub>CD<sub>3</sub> (**14**) and CH<sub>3</sub>CD<sub>2</sub>CH<sub>3</sub> (**25**) yield the following selectivities<sup>22</sup> for (C–H)<sub>sec</sub>- versus (C–H)<sub>prim</sub>-bond activation: X = F (9.0), Cl (7.3), and Br (5.8) (Table 6.6).

Table 6.6 – Ratios<sup>a</sup> of HX *vs* DX elimination in the reaction of NiX<sup>+</sup> (X = F, Cl, and Br) with isotopomers of propane.

	- HX	- DX	KIE	$f_{sec/prim}$
NiF <sup>+</sup> + CD <sub>3</sub> CH <sub>2</sub> CD <sub>3</sub>	77 (77)	23 (23)	1.14	9.0
NiF <sup>+</sup> + CH <sub>3</sub> CD <sub>2</sub> CH <sub>3</sub>	28 (28)	72 (72)		
NiCl <sup>+</sup> + CD <sub>3</sub> CH <sub>2</sub> CD <sub>3</sub>	80 (80)	20 (20)	1.59	7.3
NiCl <sup>+</sup> + CH <sub>3</sub> CD <sub>2</sub> CH <sub>3</sub>	39 (39)	61 (61)		
NiBr <sup>+</sup> + CD <sub>3</sub> CH <sub>2</sub> CD <sub>3</sub>	73 (73)	27 (27)	1.40	5.8
NiBr <sup>+</sup> + CH <sub>3</sub> CD <sub>2</sub> CH <sub>3</sub>	42 (42)	58 (58)		

<sup>a</sup> Given in % (modeled numbers are given in parenthesis). See text for details of the modeling.

A less pronounced selectivity prevails in the formation of HBr from the NiBr<sup>+</sup>/*n*-C<sub>4</sub>H<sub>10</sub> couple, as determined from the HBr/DBr ratio in the reaction with CD<sub>3</sub>CH<sub>2</sub>CH<sub>2</sub>CD<sub>3</sub> (**27**), Equation 6.24.<sup>23</sup> After statistical correction and consideration of the kinetic isotope effects operative in the reactions with the isotopomers **14** and **25**,<sup>24</sup> the activation of a secondary versus a primary carbon-hydrogen bond of *n*-butane is favored by a factor of 5.0, and for the related system NiCl<sup>+</sup>/**27** the corresponding ratio amounts to 2.8.



While for homolytic bond cleavages of primary versus secondary C–H bonds varying preferences have been noted previously, for example, in iron- and copper-mediated gas-phase

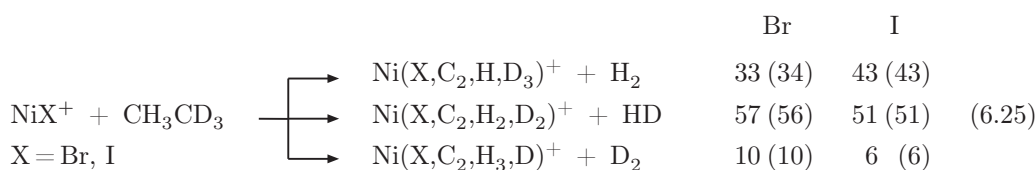
<sup>22</sup> In reference [258], due to a lower amount of experimental data, the KIE values obtained for the HX elimination of ethane have been taken into account to determine the respective selectivities. In this work, the data set of the NiX<sup>+</sup>/CD<sub>3</sub>CH<sub>2</sub>CD<sub>3</sub> and NiX<sup>+</sup>/CH<sub>3</sub>CD<sub>2</sub>CH<sub>3</sub> couples allows the determination of a KIE for HX elimination in the reaction with propane. Thus, the values reported here differ from the numbers provided in reference [258].

<sup>23</sup> A generally low signal intensity of NiF<sup>+</sup> and, furthermore, a BR of only 2 % for the loss of HF from *n*-butane result in very large uncertainties for the ratio of HF/DF loss; thus, these data are omitted.

<sup>24</sup> The selectivities reported here differ from the one reported in reference [258]. See footnote 22.

oxygenation of propane [60, 217], the trend mentioned above for  $\text{NiX}^+$ /propane is opposite to what is usually observed for radical-based processes but is in line to what would be expected taking into consideration the reactivity-selectivity principle [259].

**Dehydrogenation** This bond-activation mode dominates the ion-molecule reactions of the couples  $\text{NiBr}^+/\text{C}_2\text{H}_6$  and  $\text{NiI}^+/\text{RH}$  ( $\text{R} = \text{C}_2\text{H}_5$ ,  $\text{C}_3\text{H}_7$ ,  $n\text{-C}_4\text{H}_9$ ), Table 6.5. The investigation of the labeled substrates **2**, **25**, **26**, and **27** reveals several interesting mechanistic details. For example, in the reactions of  $\text{NiX}^+$  ( $\text{X} = \text{Br}$ ,  $\text{I}$ ) with  $\text{CH}_3\text{CD}_3$ , dehydrogenation is preceded by extensive H/D-exchanges with  $\text{KIE} = 1.78$  (for  $\text{NiBr}^+$ ) and  $\text{KIE} = 2.59$  (for  $\text{NiI}^+$ ) (Equation 6.25, modeled numbers assuming a complete scrambling of all H/D atoms are given in parenthesis).<sup>25</sup>

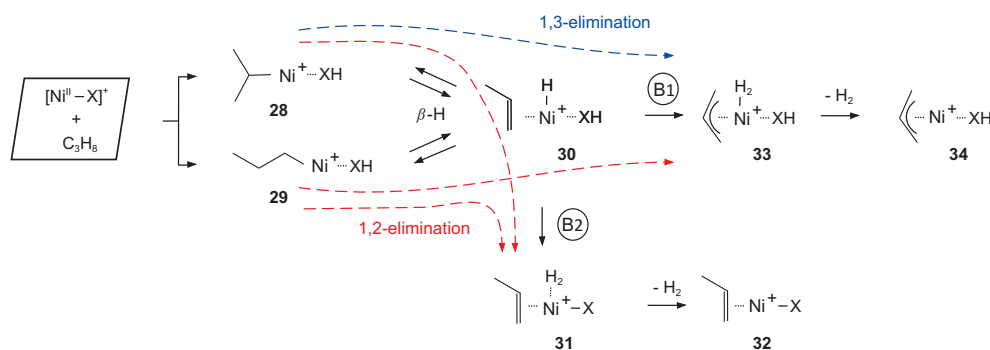


Whereas H/D scrambling is also observed in the dehydrogenation of the homologous  $\text{NiX}^+/\text{C}_3\text{H}_8$  couples, there exist some subtle differences. Here, a complete scrambling cannot account for the isotope patterns in the reaction of  $\text{NiBr}^+$  and  $\text{NiI}^+$  with  $\text{CDCH}_2\text{CD}_3$  (**14**) and  $\text{CH}_3\text{CD}_2\text{CH}_3$  (**25**) (Table 6.7). Considering the high abundances of the HD loss channel in the experiments, the amount of specific 1,2-eliminations to generate  $\text{NiX}^+$ /propene must be rather substantial for both nickel-halide cations. A quantitative analysis is given by a model in which the reaction is classified in three different channels: The ratios  $f_{1,2}$  and  $f_{1,3}$  belong to specific 1,2- and 1,3-eliminations, respectively, and  $f_{scr}$  stands for the ratio of scrambling processes. Assuming a complete scrambling of all six H/D atoms of the substrate (model 1, Table 6.7, first entrees in parenthesis), yields quite some deviations; a better agreement is obtained if the scrambling process is confined to only five out of the six H/D atoms (model 2, Table 6.7, second entrees in parenthesis) provided by a mechanism which starts with a hydrogen transfer from the internal methylene group to the bromide or iodide ligand, respectively, followed by a fast equilibration between the propyl and propene-hydride complexes (**28**  $\rightleftharpoons$  **30**, Scheme 6.3) before molecular hydrogen is formed and finally expelled from the complex.

<sup>25</sup> Confining the scrambling process to only five H/D atoms via the equilibration of  $\text{Ni}(\text{C}_2\text{H}_5)(\text{HX})^+ \rightleftharpoons \text{Ni}(\text{H})(\text{C}_2\text{H}_4)(\text{HX})^+$  (**18**  $\rightleftharpoons$  **19**, Scheme 6.2) gives identical results if only a common KIE for the overall process is considered. Introducing individual KIEs for the initial C–H bond activation and the subsequent scrambling processes is not warranted in this case. Clearly, a similarly good fitting can be achieved; however, several couples of KIEs can reproduce the limited set of the experimental data with similar good agreement.

Table 6.7 – Isotope patterns<sup>a,b</sup> for the dehydrogenation of isotopomers of propane by NiBr<sup>+</sup> and NiI<sup>+</sup>.

	exp. (model 1/model 2)		
	- H <sub>2</sub>	- HD	- D <sub>2</sub>
NiBr <sup>+</sup> + CH <sub>3</sub> CD <sub>2</sub> CH <sub>3</sub>	36 (42/36)	58 (57/60)	6 (1/ 4)
NiBr <sup>+</sup> + CD <sub>3</sub> CH <sub>2</sub> CD <sub>3</sub>	13 (4/11)	69 (72/71)	18 (24/18)
		$f_{1,2}^a = (42/42)$	$\text{KIE}_{\text{spec}} = (1.64/1.88)$
		$f_{1,3}^a = (0/26)$	$\text{KIE}_{\text{scr}} = (1.51/1.32)$
		$f_{\text{scr}}^a = (58/32)$	
NiI <sup>+</sup> + CH <sub>3</sub> CD <sub>2</sub> CH <sub>3</sub>	42 (44/44)	54 (55/54)	4 (1/ 2)
NiI <sup>+</sup> + CD <sub>3</sub> CH <sub>2</sub> CD <sub>3</sub>	12 (4/ 8)	68 (72/71)	20 (24/21)
		$f_{1,2}^a = (43/38)$	$\text{KIE}_{\text{spec}} = (1.95/1.65)$
		$f_{1,3}^a = (0/32)$	$\text{KIE}_{\text{scr}} = (1.58/1.57)$
		$f_{\text{scr}}^a = (57/30)$	

<sup>a</sup> Given in %.<sup>b</sup> Modeled numbers are given in parenthesis. See text for details of the modeling.

Scheme 6.3

Furthermore, the isotopic pattern provides an even more subtle determination of the reaction mechanism although being only qualitative in nature. Considering a 1,2-elimination, this dehydrogenation mode is obtained via three different pathways:

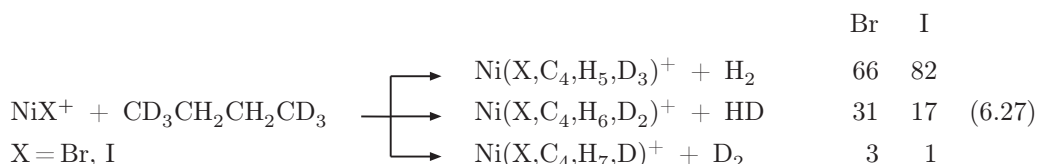
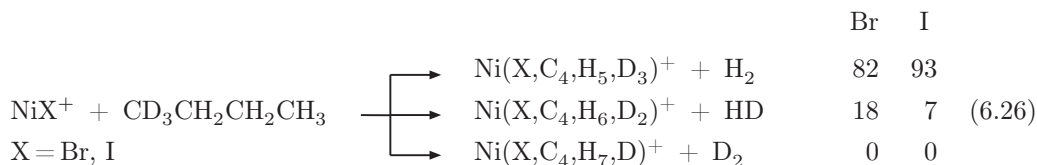
- Starting with a C-H bond activation at the terminal methyl groups of propane and following path (B1) in Scheme 6.3 (29 → 30 → 33), or
- Starting again with the activation of a primary C-H bond and following path (B2) in

Scheme 6.3 ( $\mathbf{29} \rightarrow \mathbf{30} \rightarrow \mathbf{31}$ ),<sup>26</sup> or

c) Initial bond activation of a secondary C–H bond preceding path  $\textcircled{\text{B2}}$  ( $\mathbf{28} \rightarrow \mathbf{30} \rightarrow \mathbf{31}$ ).

A 1,3-elimination is only occurring in the sequence  $\mathbf{28} \rightarrow \mathbf{30} \rightarrow \mathbf{33}$ , *i. e.* a reaction channel beginning with the activation of an internal C–H bond which is followed by  $\beta$ -hydrogen transfer and allylic C–H bond activation. Taking the relative large amount of 1,2-elimination into account, path  $\textcircled{\text{B2}}$  in Scheme 6.3 is obviously also of importance since its exclusion implies a favored bond activation of primary C–H bonds. This is rather unlikely in consideration of the observed large preference for secondary bond activation noted in the case of HX elimination for the  $\text{NiX}^+/\text{C}_3\text{H}_8$  couples. Thus, path  $\textcircled{\text{B1}}$  as well as  $\textcircled{\text{B2}}$  are assumed to be operative in the dehydrogenation of propane by  $\text{NiBr}^+$  and  $\text{NiI}^+$ .

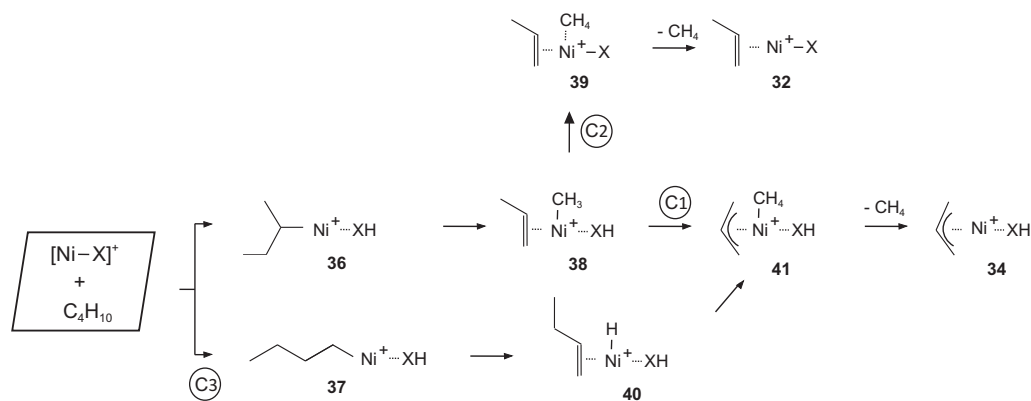
Quite unexpectedly, H/D scrambling appears not to play a major role in the dehydrogenation of the  $\text{NiI}^+/n\text{-C}_4\text{H}_{10}$  couple. Rather, based on the investigations of  $\text{CH}_3\text{CH}_2\text{CH}_2\text{CD}_3$  ( $\mathbf{26}$ ) and  $\text{CD}_3\text{CH}_2\text{CH}_2\text{CD}_3$  ( $\mathbf{27}$ ), the labeling data (Equations 6.26 and 6.27) can be explained in terms of generating a mixture of 1- and 2-butene, complexed to  $\text{NiI}^+$ , in formal 1,2-elimination reactions with a high preference for generating an internal carbon-carbon double bond. For  $\text{NiBr}^+$ , this specificity is less pronounced, Equation 6.26 and 6.27.



**C–C Bond activation** Here, the reactions are confined to category  $\textcircled{\text{I}}$  (Scheme I.2, page 5), that is the metal ion's formal oxidation state is conserved in the course of bond activation. Further below, a C–C bond-cleavage mode involving an inner-sphere electron-transfer process (path  $\textcircled{\text{II}}$ , Scheme I.2) will be presented. As expected, C–C bond activation is only significant for *n*-butane since a minimal chain length of the hydrocarbon is required. The reactions of  $\text{NiI}^+$ ,  $\text{NiBr}^+$ , and  $\text{NiCl}^+$  deserve mentioning: In the reaction of *n*- $\text{C}_4\text{H}_{10}$

<sup>26</sup> This pathway corresponds to path  $\textcircled{\text{A2}}$  which has been proposed for the dehydrogenation of ethane, Scheme 6.2.

with  $\text{NiI}^+$ , methane is liberated, and a modeling of the data obtained for the isotopomers  $\text{CH}_3\text{CH}_2\text{CH}_2\text{CD}_3$  (**26**) and  $\text{CD}_3\text{CH}_2\text{CH}_2\text{CD}_3$  (**27**), given in parenthesis in Equations 6.28 and 6.29, suggests that in the formation of methane a hydrogen transfer from the HI ligand to a methyl ligand is also of importance, in analogy to the hydrogen back transfer proposed for ethane dehydrogenation (Scheme 6.2, **19**  $\rightarrow$  **20**, page 75). This conjecture is based on the large amount of  $\text{CHD}_3$  elimination found in the reaction of  $\text{NiI}^+$  with **27** (Equation 6.29) which neither conforms with scrambling processes nor with the pathway **36**  $\rightarrow$  **38**  $\rightarrow$  **41**  $\rightarrow$  **34** (path  $\textcircled{\text{C1}}$  in Scheme 6.4,  $\text{X} = \text{I}$ ); the latter would result specifically in  $\text{CD}_4$  loss in the reaction with  $\text{CD}_3\text{CH}_2\text{CH}_2\text{CD}_3$  (**27**); instead, perdeuterated methane is with 6 % only eliminated to a minor fraction. However, the alternative routes  $\textcircled{\text{C2}}$  and  $\textcircled{\text{C3}}$  both yield a specific elimination of  $\text{CHD}_3$  from the  $\text{NiI}^+/\text{27}$  couple and cannot be distinguished by the isotopic patterns of the product ions. Again, taking into account the preference for secondary C–H bond activation, the latter pathway **37**  $\rightarrow$  **40**  $\rightarrow$  **41**,  $\textcircled{\text{C3}}$ , starting with the bond activation of a primary C–H bond, is not clearly ruled out but is not expected to account for the main share of the overall reaction. Thus, path  $\textcircled{\text{C2}}$  obviously contributes to a considerable amount to demethanation of *n*-butane by  $\text{NiI}^+$ . Considering a combination of the indistinguishable pathways  $\textcircled{\text{C2}}$  or  $\textcircled{\text{C3}}$  in competition to demethanation via  $\beta$ -hydrogen transfer from the propene ligand, path  $\textcircled{\text{C1}}$ , and, in addition, a complete scrambling of nine H/D atoms of the *i*-butyl ligand subsequent to secondary bond activation<sup>27</sup> as third alternative route can reflect the experimental data in Equations 6.28 and 6.29 relatively good.

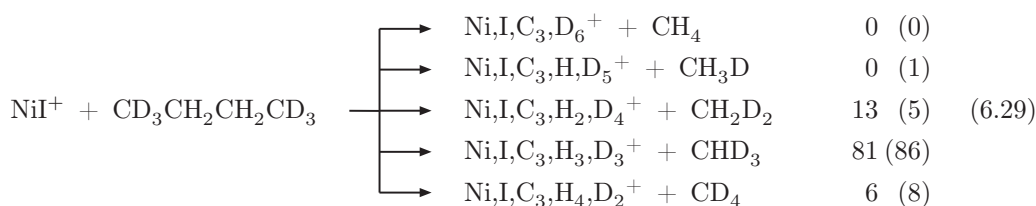
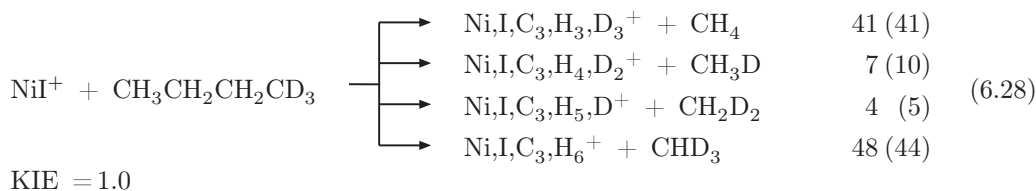


Scheme 6.4

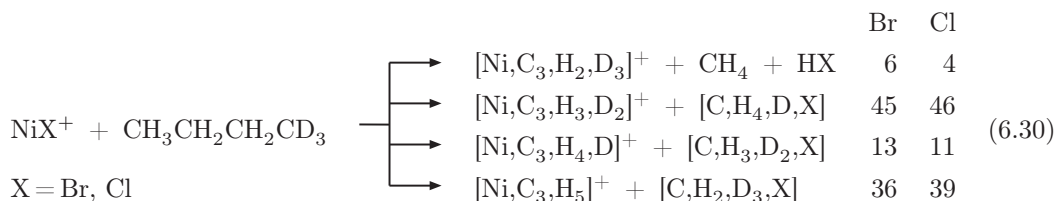
According to this model, the majority (ca. 80 %) of methane is generated via paths  $\textcircled{\text{C2}}$  or

<sup>27</sup> Alternative constraints with respect to the scrambling processes, *e. g.* a complete scrambling of all ten H/D atom or an equilibration of the H/D positions after the activation of primary C–H bonds, are almost noneffective on the modeled data; the resulting H/D distributions are similar and scrambling processes amounts in any case only to a minor part of ca. 15 % to the overall reaction. Thus, it is not possible by the set of the experimental data to distinguish definitively between these alternatives.

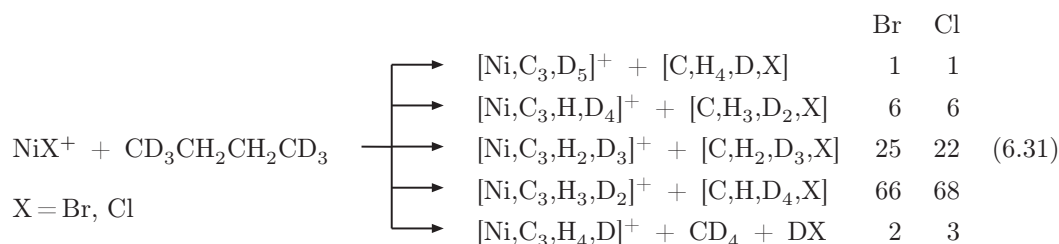
Ⓒ3); less important (6 %) is the mechanism according to path Ⓒ1, and finally, H/D scrambling contributes with 15 % also to a limited extent. In view of the deviations between the model and the experimental data, however, alternative and more complex reaction mechanism, *e. g.* involving C–C or primary C–H bond activation as well as oxidative addition as the first step, cannot be ruled out.



In contrast to  $\text{NiI}^+$ , the analogous nickel(II) cations  $\text{NiCl}^+$  and  $\text{NiBr}^+$  give rise to combined eliminations of  $\text{HX}$  ( $\text{X} = \text{Cl}, \text{Br}$ ) and  $\text{CH}_4$  in their reactions with  $n\text{-C}_4\text{H}_{10}$ . Labeling experiments are, once more, helpful in delineating the origin of the eliminated closed-shell neutral molecules, although a perfectly quantitative analysis is impossible due to the fact that already the loss of  $\text{HX}$  ( $\text{X} = \text{Cl}, \text{Br}$ ) involves both primary and (preferentially) secondary C–H bonds of *n*-butane (see above).

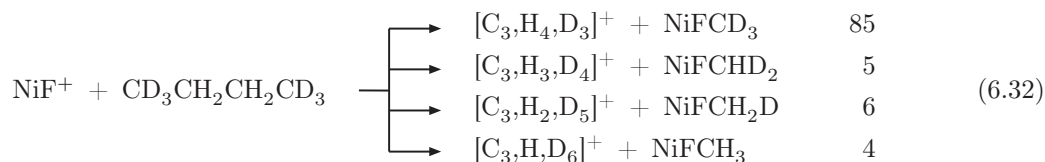


For both,  $\text{NiCl}^+$  and  $\text{NiBr}^+$  in their reactions with the two labeled *n*-butanes **26** and **27**, the isotope distributions are quite similar (Reactions 6.30 and 6.31). An analysis of the data given in these reactions combined with the above discussed regioselectivities for the losses of  $\text{HCl}$  and  $\text{HBr}$  from **26** and **27**, suggests the following scenario. The major component corresponds to the formation of  $\text{HCl/HBr}$  involving the secondary C–H bond of the substrate, followed by a  $\beta$ -methyl-migration in the course of which the C(1)–C(2) bond is activated. This pathway corresponds to path Ⓒ1 in Scheme 6.4 (**36**  $\rightarrow$  **38**  $\rightarrow$  **41**). A less



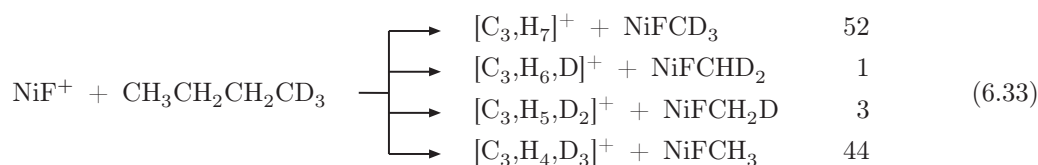
important path commences with activation of a methyl C–H bond, which is completed by a  $\beta$ -hydrogen transfer and allylic C–C bond activation involving the other terminus of the hydrocarbon (**37**  $\rightarrow$  **40**  $\rightarrow$  **41**, path  $\textcircled{\text{C3}}$ , Scheme 6.4). These two “clean” channels account for most of the combined HX/CH<sub>4</sub> losses, but some product ions, for example, [Ni, C<sub>3</sub>, H<sub>2</sub>, D<sub>3</sub>]<sup>+</sup> from NiCl<sup>+</sup>/**27** (Reaction 6.31), indicate that partial H/D scrambling precedes the actual dissociation step(s).

**Hydride and methanide transfers from RH to NiX<sup>+</sup>** All reactions so far discussed belong to category  $\textcircled{\text{I}}$  (Scheme I.2, page 5), because the metal remains charged in the reactant and product ions. A different situation is encountered when inner-sphere electron transfer becomes possible (path  $\textcircled{\text{II}}$ , Scheme I.2) in the course of which the neutral hydrocarbon is converted to a carbenium ion; concurrently, the cationic metal complex is transferred to a neutral molecule RNiX. Predictably, the driving forces for these processes are the stability of the resulting carbenium ions and the R<sup>−</sup> affinities of NiX<sup>+</sup>. While for the former there is plenty of reliable data substantiating the well-established stability order tert. > sec. > prim. carbocation [159], much less is known about the thermochemistry of the resulting RNiX system, except for rather crude and - at best - qualitative guidelines. For example, one can argue that NiF<sup>+</sup> is more susceptible toward reaction with a nucleophile than, for example, NiI<sup>+</sup> simply due to the effects caused by the different electronegativities of the two ligands, etc. In short, inner-sphere electron transfer are not expected to play an important role for substrates as small as CH<sub>4</sub> or C<sub>2</sub>H<sub>6</sub> or for the couples containing NiI<sup>+</sup>/RH. These expectations are born out by the experiments, and in the following the focus is on NiX<sup>+</sup>/RH with X = F, Cl; R = C<sub>3</sub>H<sub>7</sub>, *n*-C<sub>4</sub>H<sub>9</sub>. To begin with the methanide transfer, this pathway is



exclusively observed for the NiF<sup>+</sup>/*n*-C<sub>4</sub>H<sub>10</sub> system (Table 6.5). In the reaction of NiF<sup>+</sup> with





the isotopologue  $\text{CH}_3\text{CH}_2\text{CH}_2\text{CD}_3$  (**26**), the two dominant processes amount to transfer of  $\text{CD}_3$  (52 %) and  $\text{CH}_3$  (44 %) with minor contributions of “scrambled” methanides (in total 4 %). This selectivity trend is further substantiated by an overwhelmingly large transfer of  $\text{CD}_3$  (85 %) in the  $\text{NiF}^+/\text{27}$  couple. Thus, in the course of the heterolytic C(1)–C(2) bond cleavage an intact (or nearly intact) terminal methyl group is transferred to the  $\text{NiF}^+$  core. Quite likely, this reaction is coupled with facile isomerization of the nascent primary  $\text{C}_3\text{H}_7^+$  cation to the substantially more stable secondary cation. The conceptually related hydride transfer has been observed for both  $\text{NiF}^+$  and  $\text{NiCl}^+$  when reacted with either  $\text{C}_3\text{H}_8$  or  $n\text{-C}_4\text{H}_{10}$ , though with only small relative abundances for the  $\text{NiCl}^+/\text{RH}$  systems. As to the origin of the transferred hydride species, based on the reactions with  $\text{CH}_3\text{CD}_2\text{CH}_3$  and  $\text{CD}_3\text{CH}_2\text{CH}_2\text{CD}_3$  and after statistical corrections for the different number of hydrogen versus deuterium atoms in the given substrates, and taking into account the respective KIE values, one arrives at the following conclusions with regard to the regioselectivity of secondary versus primary heterolytic carbon-hydrogen bond cleavage:<sup>28</sup> For  $\text{NiF}^+/\text{C}_3\text{H}_8$ , the selectivity amounts to 240,<sup>29</sup> and for  $n$ -butane it is as high as 23. In the  $\text{NiCl}^+$  system, the regioselectivities are somewhat smaller, but still rather impressive with numbers of 58 for propane and 14 for  $n$ -butane, favoring the cleavage of secondary carbon-hydrogen bonds.

### 6.3 Reactivity of $\text{Ni}(\text{OH})^+$ and $[\text{Ni}, \text{C}, \text{H}_3, \text{O}]^+$

As already mentioned in the introduction, the nickel complexes  $\text{NiX}^+$  ( $\text{X} = \text{OH}, \text{OCH}_3$ ) are not able to activate C–H bonds of methane (Equation I.5). Since the ligand exchanges are exothermic [73, 74],<sup>30</sup> their non-occurrence points to the existence of kinetic barriers (see also [75]). To elucidate the difference between these non-reactive complexes and the reactive cations  $\text{NiH}^+$  and  $\text{NiF}^+$ , the PES of the  $\text{Ni}(\text{OH})^+/\text{CH}_4$  system has also been investigated. Theory reveals a similar reaction pattern as found for the reaction of  $\text{NiF}^+$ : All intermediates and transition structure on the singlet surface according to  $\sigma$ -CAM (**15b**  $\rightarrow$  **16b**) and also via an OA/RE sequence (**15b**  $\rightarrow$  **23b**  $\rightarrow$  **16b**) are too high energy to be accessible

<sup>28</sup> The selectivities reported here differ from the one reported in reference [258]. See footnote 22 on page 80.

<sup>29</sup> The statistical elimination of  $\text{HNiF}$  versus  $\text{DNI}^+\text{F}$  from  $\text{CH}_3\text{CD}_2\text{CH}_3$ , corrected by a KIE of 1.14, amounts to 3.42, whereas in the experiment one obtains a ratio of only 0.014.

<sup>30</sup> Value derived from:  $\Delta_0 H(\text{Ni}^+ - \text{CH}_3) = 170 \pm 7 \text{ kJ mol}^{-1}$  [73],  $\Delta_0 H(\text{Ni}^+ - \text{OH}) = 176 \text{ kJ mol}^{-1}$ ,  $\Delta_f H(\text{CH}_4) = -74.9 \text{ kJ mol}^{-1}$ ,  $\Delta_f H(\text{CH}_3) = 145.7 \text{ kJ mol}^{-1}$ ,  $\Delta_f H(\text{H}_2\text{O}) = -241.8 \text{ kJ mol}^{-1}$  [250].

from the entrance channel (Figure 6.12). On the triplet surface, no relevant structures of a OA/RE process could be located. The triplet TS associated to a  $\sigma$ -CAM is with  $-0.9 \text{ kJ mol}^{-1}$  very close to the entrance channel; however, considering the uncertainties of the theoretical level applied, the experimental and theoretical results are not necessarily inconsistent. Although smaller compared to the fluoride ligand, the inductive effect of oxygen is also indicated in the lower relative energy of the  $\sigma$ -CAM transition structure  $^3\text{TS } 15\text{b}/16\text{b}$  on the triplet surface compared to  $^3\text{TS } 3\text{a}/4\text{a}$  of the respective  $\text{NiH}^+/\text{CH}_4$  system. This reasoning is also indicated in the increased Mulliken charges of the nickel atom in the respective triplet intermediates  $\text{Ni}(\text{X})(\text{CH}_4)^+$  (0.69, 0.75, and 0.91) and the transition structures  $^3\text{TS } \text{Ni}(\text{X})(\text{CH}_4)^+/\text{Ni}(\text{CH}_3)(\text{HX})^+$  (0.67, 0.79, and 0.86) on the triplet surface with  $\text{X} = \text{H}$ ,  $\text{OH}$ , and  $\text{F}$ , respectively. This trend reflects the relative stabilities of  $^3\text{TS } 3\text{a}/4\text{a}$ ,  $^3\text{TS } 15\text{a}/16\text{a}$  and  $^3\text{TS } 15\text{b}/16\text{b}$  (Figures 6.1, 6.11, and 6.12). Furthermore, an increase of the agostic interactions between the C–H bond of methane and the nickel center is indicated in the trend of decreasing Ni–C and Ni–H bond lengths in the adducts  $\text{Ni}(\text{X})(\text{CH}_4)^+$  (Ni–C: 2.307 Å, 2.185 Å, and 2.186 Å; Ni–H: 1.987 Å, 1.929 Å, and 1.917 Å for  $\text{X} = \text{H}$ ,  $\text{OH}$ , and  $\text{F}$ , respectively); in line with this, a slight elongation of the strong C–H bond is observed (1.115 Å, 1.118 Å, and 1.121 Å for  $\text{X} = \text{H}$ ,  $\text{OH}$ , and  $\text{F}$ ).

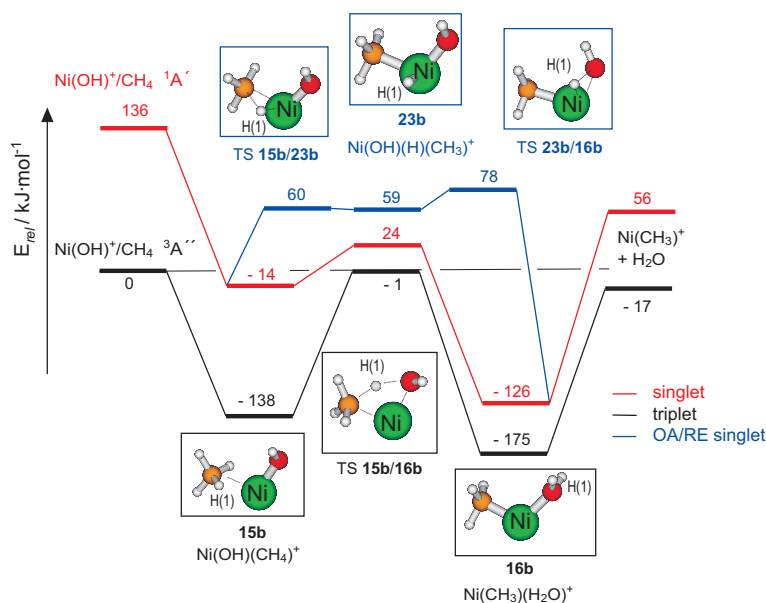
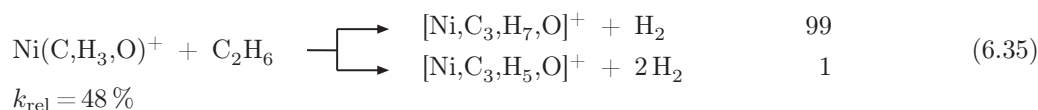
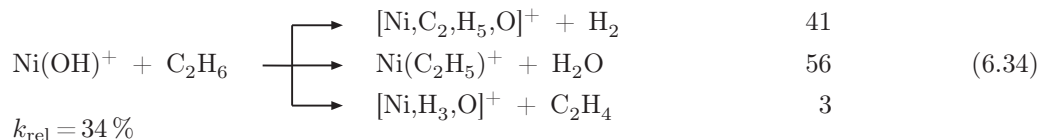


Figure 6.12 – Energy diagram (in  $\text{kJ mol}^{-1}$ ) for the reaction of  $\text{Ni}(\text{OH})^+$  and methane. The values are relative to the entrance channel on the triplet surface and corrected for zero-point vibrational energies.

## 6.3.1 Reactions with ethane

Although  $\text{Ni}(\text{OH})^+$  and  $[\text{Ni}, \text{O}, \text{C}, \text{H}_3]^+$  do not react with methane under ESI conditions (Equation I.5), they are more reactive compared to naked  $\text{Ni}^+$  since they are capable of bond activation starting from ethane, Equation 6.34 and 6.35; as stated above, propane is the smallest alkane that is activated by  $\text{Ni}^+$ .



Dehydrogenation according to consecutive  $\sigma$ -bond-metathesis reactions as suggested for the nickel bromide systems (**18**  $\rightarrow$  **19**  $\rightarrow$  **20**, Scheme 6.2) are not of importance for  $\text{Ni}(\text{OH})^+$ . This finding is evident from the exclusive elimination of  $\text{D}_2$  observed for the  $\text{Ni}(\text{OH})^+/\text{C}_2\text{D}_6$  couple (Table 6.8); the elimination of HD via a H transfer from HDO to the deuteride ligand in  $\text{Ni}(\text{D})(\text{C}_2\text{D}_4)(\text{HDO})^+$  should also be observed. To determine whether the alternative pathway of a OA RE mechanism which was found to be unfavorable for the other  $\text{NiX}^+/\text{C}_2\text{H}_6$  systems might possibly take place in the reaction of  $\text{Ni}(\text{OH})^+$  with  $\text{C}_2\text{H}_6$ , the  $\text{Ni}(\text{OH})^+/\text{C}_2\text{H}_6$  PES has been scanned related to this pathway. The associated intermediates and transition structure on the excited low-spin, singlet surface could be located; however, according to B3LYP calculations, this pathway is not feasible for the  $\text{Ni}(\text{OH})^+$  system, Figure 6.13: Although the insertion of the nickel atom into a C–H bond of ethane to form the high-valent  $\text{Ni}(\text{C}_2\text{H}_5)(\text{H})(\text{OH})^+$  (**21c**) is not clearly ruled out (with the associated  $^1\text{TS } \mathbf{17c}/\mathbf{21c}$  being  $10 \text{ kJ mol}^{-1}$  above the entrance channel), the subsequent transition structure  $\text{TS } \mathbf{21c}/\mathbf{20c}$  to form  $\text{H}_2$  is  $49 \text{ kJ mol}^{-1}$  higher in energy relative to the entrance channel of ground state  $\text{Ni}(\text{OH})^+$  and ethane, and should thus not occur under thermal conditions.<sup>31</sup> Instead, theory does not rule out the dehydrogenation mode proposed for  $\text{NiBr}^+$  and  $\text{NiI}^+$ . The  $\sigma$ -bond metathesis in the course of which molecular hydrogen is formed (**19c**  $\rightarrow$  **20c**, Figure 6.13), is accessible on the triplet surface with  $^3\text{TS } \mathbf{19c}/\mathbf{20c}$  being  $12 \text{ kJ mol}^{-1}$  below the entrance channel. However, since this pathway is not supported for  $\text{Ni}(\text{OH})^+$  by the experiments, another mode of dehydrogenation must exist which can ex-

<sup>31</sup> A TS which connects **21c** with a dihydride complex  $\text{Ni}(\text{H})_2(\text{C}_2\text{H}_4)(\text{OH})^+$  (**22c**), formed by a  $\beta$ -hydrogen transfer from **21c**, could not be located.

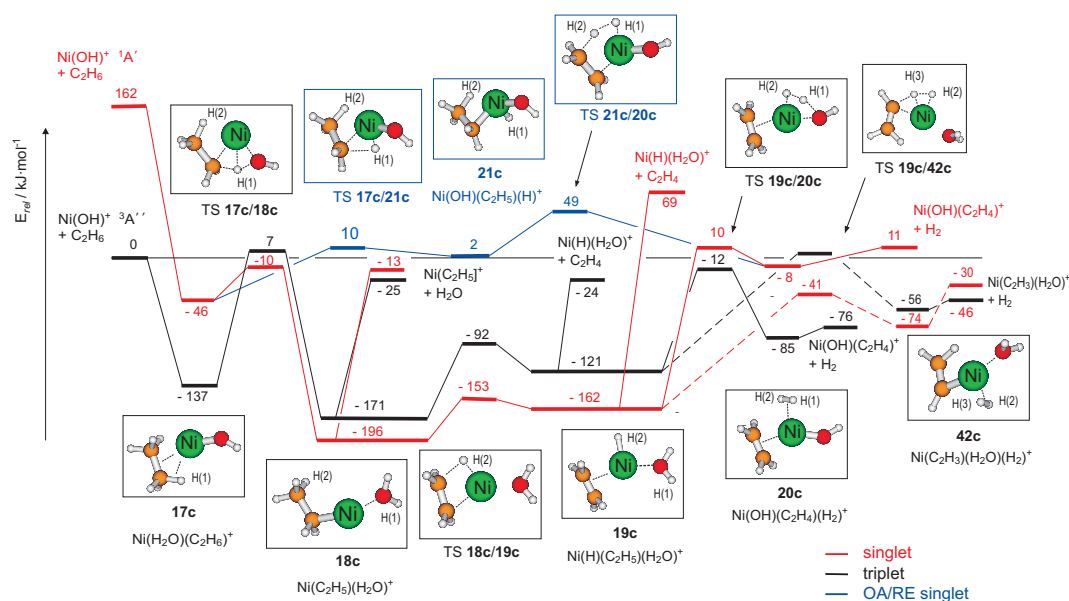


Figure 6.13 – Energy diagram (in  $\text{kJ mol}^{-1}$ ) for the reaction of  $\text{Ni}(\text{OH})^+$  and ethane. The values are relative to the entrance channel on the triplet surface and corrected for zero-point vibrational energies.

plain the exclusive loss of  $\text{D}_2$  in the reaction of  $\text{Ni}(\text{OH})^+$  with  $\text{C}_2\text{D}_6$ . Indeed, an alternative route has been located as the lowest-energy path shown in Figure 6.13: After the formation of the hydride complex  $\text{Ni}(\text{H})(\text{C}_2\text{H}_4)(\text{H}_2\text{O})^+$  (**19c**), additional C–H bond activation is still feasible under thermal conditions thus forming an ethenyl complex  $\text{Ni}(\text{C}_2\text{H}_3)(\text{H}_2)(\text{H}_2\text{O})^+$  (**19c** → **42c**), the connecting transition structure is found to be  $41 \text{ kJ mol}^{-1}$  below the entrance channel (Figure 6.13). This mode of dehydrogenation is specific for  $\text{Ni}(\text{OH})^+$  when compared to  $\text{NiCl}^+$  and  $\text{NiBr}^+$ ; for the latter, the transition structure of the rearrangement  $\text{Ni}(\text{H})(\text{C}_2\text{H}_4)(\text{HX})^+ \rightarrow \text{Ni}(\text{C}_2\text{H}_3)(\text{H}_2)(\text{HX})^+$  (TS **19a/42a** and TS **19b/42b**; a: Cl, b: Br) are located at  $49 \text{ kJ mol}^{-1}$  ( $109 \text{ kJ mol}^{-1}$ ) and  $75 \text{ kJ mol}^{-1}$  ( $133 \text{ kJ mol}^{-1}$ ), respectively, above the entrance channel (in the corresponding singlet states, the numbers for the triplet states are given in parenthesis). Thus, this reaction channel is too high in energy to account for dehydrogenation of ethane by  $\text{NiCl}^+$  and  $\text{NiBr}^+$  and has not been further considered in the calculations of the chloride and bromide systems. Furthermore, the elimination of ethene which is also exclusively observed in the reaction of  $\text{Ni}(\text{OH})^+$  with ethane is in nice agreement with the energies obtained by B3LYP calculation. While this reaction channel is endothermic with  $77 \text{ kJ mol}^{-1}$  and  $99 \text{ kJ mol}^{-1}$  for the  $\text{NiCl}^+/\text{C}_2\text{H}_6$  and  $\text{NiBr}^+/\text{C}_2\text{H}_6$  couples, the uptake of two hydrogen atoms from ethane by  $\text{Ni}(\text{OH})^+$  is with  $-30 \text{ kJ mol}^{-1}$  exothermic related to the reactants. Hydrogen uptake has been referred to oxidative dehy-

drogenation (ODH) which was found preferentially for high-valent vanadium oxide clusters, whereas low-valent clusters tend to eliminate hydrogen in the reaction with isomeric butenes [260].

Table 6.8 – Isotope patterns<sup>a,b</sup> for the dehydrogenation of ethane by the nickel complexes  $\text{Ni}(\text{OH})^+$  and  $[\text{Ni},\text{C},\text{H}_3,\text{O}]^+$ .

	- H <sub>2</sub>	- HD	- D <sub>2</sub>
$\text{Ni}(\text{OH})^+ + \text{C}_2\text{D}_6$			100
$\text{Ni}(\text{OH})^+ + \text{CH}_3\text{CD}_3$	21 (21)	60 (60)	19 (19)
	$f_{scr}^a = 100$	$\text{KIE}_{scr} = 1.05$	
	experiment (model 1/model 2)		
$\text{Ni}(\text{C},\text{H}_3,\text{O})^+ + \text{C}_2\text{D}_6$	15 (15/14)	58 (56/56)	27 (29/30)
$\text{Ni}(\text{C},\text{H}_3,\text{O})^+ + \text{CH}_3\text{CD}_3$	52 (56/55)	43 (40/41)	5 (4/ 4)
$\text{Ni}(\text{C},\text{D}_3,\text{O})^+ + \text{CH}_6$	58 (59/60)	37 (38/37)	5 (3/ 3)
$\text{Ni}(\text{C},\text{D}_3,\text{O})^+ + \text{CH}_3\text{CD}_3$	19 (17/17)	56 (56/56)	25 (27/27)
	$f_{spec}^a = (9/30)$	$f_{scr}^a = (91/70)$	
	$\text{KIE}_{spec} = (2.4/2.0)$	$\text{KIE}_{scr} = (1.7/1.6)$	

<sup>a</sup> Given in %.

<sup>b</sup> Modeled numbers are given in parenthesis. For the modeling of the  $[\text{Ni},\text{C},\text{H}_3,\text{O}]^+$ /ethane system, see page 98f for details.

A mechanistically unprecedented situation characterizes the gas-phase ion chemistry of  $[\text{Ni},\text{C},\text{H}_3,\text{O}]^+$  when reacted under thermal, single-collision conditions with ethane (see below); before going into the detail of the reaction, it is indicated to illustrate some aspects of the structure and formation of the  $[\text{Ni},\text{C},\text{H}_3,\text{O}]^+$  cation.

**Structure and formation of gaseous  $[\text{Ni},\text{C},\text{H}_3,\text{O}]^+$**  To characterize the intermediates and product ions involved in the  $[\text{Ni},\text{C},\text{H}_3,\text{O}]^+/\text{RH}$  couples ( $\text{R} = \text{C}_2\text{H}_5$ ,  $\text{C}_3\text{H}_7$ ,  $n\text{-C}_4\text{H}_9$ ), part of this complex issue has been addressed by an exploratory investigation of the  $[\text{Ni},\text{C},\text{H}_3,\text{O}]^+$ -manifold<sup>32</sup> by means of labeling studies, ligand-exchange reactions and DFT calculations.

To begin with the results of the calculations, the global minimum **43** corresponds to a complex of triplet  $\text{NiH}^+$  ( $^3\Delta$ ) with  $\text{CH}_2\text{O}$  (Figure 6.14(a)). At the theoretical level used, the binding energy of  $\text{CH}_2\text{O}$  amounts to  $181 \text{ kJ mol}^{-1}$ , and isomerization **43**  $\rightarrow$  **44a** via  $\beta$ -H migration requires  $117 \text{ kJ mol}^{-1}$  to yield the  $\text{Ni}(\text{OCH}_3)^+$  isomer **44a**, which is less stable than **43** by  $22 \text{ kJ mol}^{-1}$ . Two other minima have been located on the triplet surface. One corresponds to the  $\text{Ni}^{\text{II}}$  isomer  $\text{Ni}(\text{CH}_2\text{OH})^+$  (**45**) with a Ni–C bond, and the second to the

<sup>32</sup> For a detailed discussion of the structurally related system  $\text{Fe}(\text{OCH}_3)^+ \rightleftharpoons \text{Fe}(\text{H})(\text{CH}_2\text{O})^+$ , see [112].

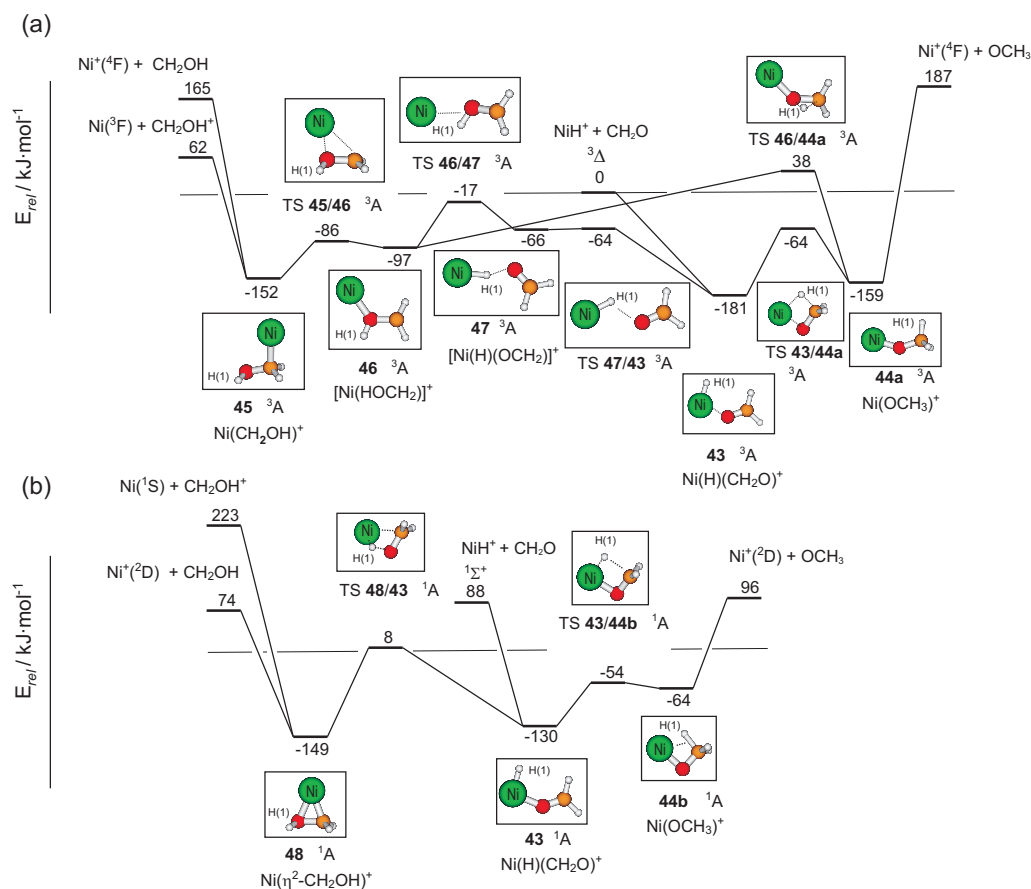


Figure 6.14 – DFT-Based energy diagram for various  $[\text{Ni}, \text{C}, \text{H}_3, \text{O}]^+$  isomers, their connecting transition structures, and the asymptotes for ligand losses. The values are relative to the energies of the separated building blocks  $\text{NiH}^+$  ( $^3\Delta$ ) and  $\text{CH}_2\text{O}$ , corrected for contributions of zero-point vibrational energies, and are given in  $\text{kJ} \cdot \text{mol}^{-1}$ . (a) Triplet related species; (b) singlet electromers.

less stable  $\text{Ni}^{\text{I}}$  complex **46**, in which  $\text{Ni}^+$  interacts with the O-atom of the  $\text{CH}_2\text{OH}$  radical. This structural assignment is supported by the computed spin and charge densities. The spin is nearly equally distributed between the C- and the Ni-atoms of **46**, whereas most of the charge (82 %) is located on the Ni-atom. Isomer **46** is connected with **45** by a transition structure for a haptotropic Ni shift, and, for the isomerization  $\mathbf{46} \rightleftharpoons \mathbf{43}$ , an unusual reaction path has been located. This involves a series of ion-dipole complexes [261–263], *i. e.*, **46** converts to a transition structure in which the Ni-atom interacts weakly with the  $\text{CH}_2\text{OH}$  fragment; the charge is nearly equally distributed between the two building blocks. Next, a H-atom is pulled away to generate a  $\text{NiH}^+/\text{OCH}_2$  complex which, upon rotation, collapses to

**43.** Note, that the whole transformation  $\mathbf{46} \rightarrow \mathbf{43}$  occurs below the asymptote for generating separated  $\text{NiH}^+$  and  $\text{CH}_2\text{O}$ . A transition structure for the direct conversion  $\mathbf{46} \rightarrow \mathbf{44a}$  has also been located. However, in line with experimental findings (see below), this high-energy path ( $38 \text{ kJ mol}^{-1}$  above separated  $\text{NiH}^+$  and  $\text{CH}_2\text{O}$ ) is not relevant in the present context.

As to the relevance of the computational findings, circumstantial experimental evidence are provided for some of the predictions. For example, CID studies of mass-selected  $[\text{Ni},\text{C},\text{H}_3,\text{O}]^+$ ,  $m/z$  89, give rise to losses of  $\text{H}_2$  ( $\rightarrow m/z$  87),  $\text{CH}_2\text{O}$  ( $\rightarrow m/z$  59),  $(\text{C},\text{H}_3,\text{O})$  ( $\rightarrow m/z$  58), and neutral Ni ( $\rightarrow m/z$  31).<sup>33</sup> Based on thermochemical considerations, these channels are indicative of  $\text{Ni}^+$  complexes having the connectivities of  $\text{Ni}(\text{H})(\text{CH}_2\text{O})^+$  (**43**) and any of the three  $\text{Ni}(\text{CH}_2\text{OH})^+$  isomers **45**, **46**, or **48**; the CID of the latter is expected to yield significant amount of the hydroxymethyl cation,  $\text{CH}_2\text{OH}^+$ , concomitant with loss of neutral Ni, because the ionization energy of  $\cdot\text{CH}_2\text{OH}$  (7.56 eV) is lower than that of atomic Ni (7.64 eV) [250]. Further, the formation of  $\text{CH}_2\text{OH}^+$  via proton transfer to formaldehyde in  $\text{Ni}(\text{H})(\text{CH}_2\text{O})^+$  is ruled out by the higher proton affinity of Ni ( $737 \text{ kJ mol}^{-1}$  [250]) compared to the proton affinity of  $\text{CH}_2\text{O}$  ( $713 \text{ kJ mol}^{-1}$  [250]). The CID product pattern of  $[\text{Ni},\text{C},\text{H}_3,\text{O}]^+$  is in distinct contrast to the related iron species  $[\text{Fe},\text{C},\text{H}_3,\text{O}]^+$  for which the formation of  $\text{CH}_2\text{OH}^+$  is barely observed ( $<1\%$  in Xe-CID mass spectrum applying a guided ion beam (GIB) apparatus [112]);  $\text{Fe}(\text{D})(\text{Xe})^+$ ,  $\text{FeD}^+$ ,  $\text{FeO}^+$ , and  $\text{Fe}^+$  are the main product ions formed from  $[\text{Fe},\text{C},\text{D}_3,\text{O}]^+$  in low energy collisions with Xe. Although a comparison between the respective CID experiments is delicate since the routes of formation of the corresponding  $[\text{M},\text{C},\text{H}_3,\text{O}]^+$  cations are completely different,<sup>34</sup> the ESI source spectra from labeled methanolic solutions of  $\text{NiI}_2$  and  $\text{FeI}_2$ , respectively, recorded under the same conditions, also indicate different structures for the  $[\text{Ni},\text{C},\text{H}_3,\text{O}]^+$  and  $[\text{Fe},\text{C},\text{H}_3,\text{O}]^+$  manifold (see below and Figure A.4 in the Appendix).

Although the VG Bio-Q does not allow directly to extract quantitative threshold information from CID experiments owing to several limitations of the commercial instrument [265],<sup>35</sup> the energy dependence of the product distributions in the CID spectra can be modeled to a first approximation by a sigmoid function [267] as described in section 2.1, which allows an extraction of some semi-quantitative information about the energetics of the ions examined [268]. To model the BR of CID spectra of  $[\text{Ni},\text{C},\text{H}_3,\text{O}]^+$  at different collision energies  $E_{\text{lab}}$ , the formation of  $\text{NiH}^+$  ( $m/z$  59) has been treated as a product ion generated via

<sup>33</sup> In addition, water elimination concomitant with the formation of the product ion  $\text{Ni}(\text{CH}_2)^+$  - which corresponds most likely to a carbene complex - is observed to a small amount at relative high collision energies ( $E_{\text{lab}}$  ca.  $\geq 8 \text{ eV}$ ).

<sup>34</sup> In the GIB CID experiment,  $[\text{Fe},\text{C},\text{H}_3,\text{O}]^+$  was produced in the reaction of  $\text{Fe}^+$  with nitromethane [63, 264].

<sup>35</sup> For weakly bound ions for example [266], even at  $E_{\text{lab}} = 0 \text{ eV}$  a non-negligible amount of ion decay is observed, which is in part attributed to the presence of collision gas not only in the hexapole, but also in the focusing regions between the mass analyzers. Note that these dissociations do not correspond to metastable ions because they do not occur in the absence of collision gas.

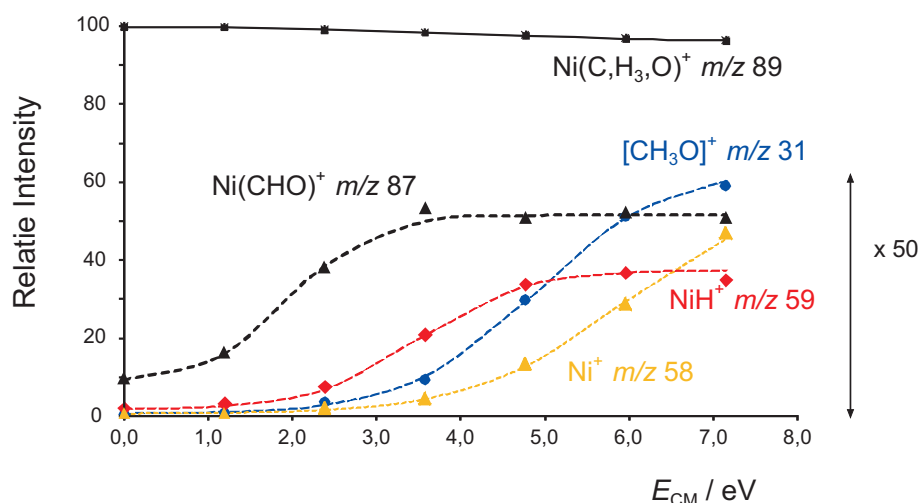


Figure 6.15 – Relative intensities of the precursor cation  $[\text{Ni,C,H}_3\text{O}]^+$  and the fragments  $[\text{Ni,C,H,O}]^+$ ,  $\text{NiH}^+$ ,  $\text{Ni}^+$ , and  $[\text{C,H}_3\text{O}]^+$ , considered all as primary fragments, as a function of collision energy ( $E_{\text{CM}}$  given in eV in the center-of-mass frame). The symbols represent the experimental data, whereas the lines show the fitting with sigmoid functions; see text for details. The fragment channels are expanded by a factor of 50.

loss of formaldehyde from the parent  $[\text{Ni,C,H}_3\text{O}]^+$  ( $m/z$  89), rather than being formed via the successive losses of  $\text{H}_2$  and  $\text{CO}$ . Further, non-negligible ion decay at  $E_{\text{lab}} = 0$  eV as well as some fraction of non-fragmenting parent ions at higher collision energies were acknowledged by means of appropriate scaling and normalization procedures. Phenomenological threshold energies are then derived from linear extrapolations of the rise of the sigmoid curves at  $E_{1/2}$  to the baseline (see Equations 2.1 and 2.2, page 25). This empirical, yet physically reasonable approach is able to reproduce the measured ion yields quite well (Figure 6.15). It is obvious, however, that the term  $E_{1/2}$  used in the exponent of Equations 2.1 and 2.2 does not correspond to the intrinsic appearance energies of the fragmentation of interest. Nevertheless, it has been demonstrated in earlier work that this approach provides a quantitative frame for the energy demands of the various fragmentations [234, 269, 270].

A detailed consideration of the energy-dependent CID patterns in Figure 6.15 reveals the following. Loss of molecular hydrogen is already observed at a collision energy nominally set to  $E_{\text{CM}} = 0$  eV, indicating that the activation energy of this process is rather low. In contrast, the losses of the either neutral Ni or intact  $\text{CH}_2\text{OH}/\text{OCH}_3$  have significantly higher energy demands, but are more significant with increasing collision energy. In consideration of common understanding of unimolecular dissociations of gaseous ions [145, 271], the finding that  $\text{H}_2$  and  $\text{CH}_2\text{O}$  losses dominate over the elimination of Ni and  $\text{CH}_2\text{OH}$  or  $\text{OCH}_3$  at lower



collision energies, whereas the opposite behavior prevails at higher energies, implies that Ni and  $\text{CH}_2\text{OH}/\text{OCH}_3$  losses by a direct cleavage of the Ni–C or Ni–O bond are entropically favored compared to the obviously more complex, but less energy-demanding rearrangements accompanying the eliminations of  $\text{H}_2$  as well as of  $\text{CH}_2\text{O}$ . The formation of the latter, however, cannot clearly be specified of being either a rearrangement or a direct bond cleavage process. The hydride complex can be formed directly from  $\text{Ni}(\text{H})(\text{CH}_2\text{O})^+$ ; however, the intensity of  $\text{NiH}^+$  levels off at higher energies parallel to the intensity of  $\text{Ni}(\text{CHO})^+$  which indicates that a consecutive loss of  $\text{H}_2$  and CO to form  $\text{NiH}^+$  might also be involved.

Phenomenological analysis of the energy behavior leads to appearance energies  $AE$  of 3.2 eV, 4.1 eV, 2.1 eV, and 0.9 eV for  $\text{CH}_2\text{OH}^+$ ,  $\text{Ni}^+$ ,  $\text{NiH}^+$ , and  $[\text{Ni,C,H},\text{O}]^+$ , respectively. The  $AE$ s might be affected by the lack of ion thermalization in our experiments as well as the kinetic energy spread of the incident beam and are thus only to be considered as a semi-quantitative guidance [253]. However, the computed energies for Ni and  $\text{CH}_2\text{OH}$  eliminations are 2.2 eV and 3.3 eV and are lower than the experimentally estimates of 3.2 eV and 4.1 eV, respectively. These difference can be explained by a kinetic shift [272, 273].<sup>36</sup> Though kinetic shifts can be very large [273], they are normally almost negligible; uncertainties in the experimental and computed values might as well be the reason for these discrepancies. Problematic in this case is also the fact that competing reaction channels are involved in the CID which might cause a competitive shift [273, 275]. The competition of fragmentation processes may result in an increase in the measured appearance energy. Nevertheless, the order of Ni *vs*  $\text{CH}_2\text{OH}$  loss agrees for both the calculated and the experimental estimates.

To continue with the experimental findings, a parent-ion scan of  $[\text{Ni,C,H}_3,\text{O}]^+$ ,  $m/z$  89, identifies four precursors. Whereas three of them, *i. e.*, losses of  $\Delta m = -28$  (CO or  $\text{N}_2$ ),  $\Delta m = -30$  ( $\text{CH}_2\text{O}$ ), and  $\Delta m = -32$  ( $\text{CH}_3\text{OH}$ ), are not indicative of the structure(s) of the resulting  $m/z$  89 ion, elimination of HBr,  $\Delta m = -80$  and  $-82$ , points to  $\text{Ni}(\text{Br})(\text{CH}_3\text{OH})^+$  as a crucial, structure-indicative precursor candidate. For example, ESI experiments in which  $\text{CD}_3\text{OH}/\text{H}_2\text{O}$  or  $\text{CH}_3\text{OD}/\text{D}_2\text{O}$  were employed as solvents, establish a specific activation of the methyl C–H(D) bond of methanol, followed by reductive elimination of HBr (DBr), *i. e.*, the former solvent gives rise to  $[\text{Ni,C,H,D}_2,\text{O}]^+$  and the latter to  $[\text{Ni,C,H}_2,\text{D},\text{O}]^+$ . This process obviously also takes place in the source region and contrast as mentioned the fragmentation pattern observed for the corresponding iron system (Figure A.4 in the Appendix): The electrospray of a solution of  $\text{FeI}_2$  in  $\text{CD}_3\text{OH}/\text{H}_2\text{O}$  causes a mass gain of  $\Delta m = +3$  in comparison to the unlabeled system  $\text{FeI}_2/\text{CH}_3\text{OH}/\text{H}_2\text{O}$  whereas for  $\text{FeI}_2/\text{CH}_3\text{OD}/\text{D}_2\text{O}$  no mass shift is observed, meaning that in both cases the O–H bond and not a C–H bond

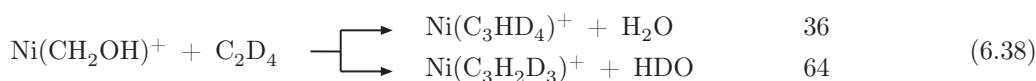
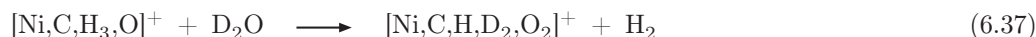
<sup>36</sup> The observation of an fragment ion in a mass spectrometer depends on the lifetime and the distribution of the internal energy, *i. e.* kinetic aspects are important. According to QET, the rate constant of an ion dissociation is a function of excess energy in the transition structure of the respective reaction; thus, a certain amount of excess energy is required for mass spectrometric fragmentation to be observed. This phenomenon is called a kinetic shift (for a review, see [274]).

is activated in the formation of the methoxy complex Fe(OCH<sub>3</sub>)<sup>+</sup>. For nickel, however, in agreement with the CID experiments described above, mass gains of  $\Delta m = +2$  and  $\Delta m = +1$  are obtained from NiI<sub>2</sub>/CD<sub>3</sub>OH/H<sub>2</sub>O and NiI<sub>2</sub>/CH<sub>3</sub>OD/D<sub>2</sub>O in comparison to a unlabeled solution of NiI<sub>2</sub> in CH<sub>3</sub>OH and H<sub>2</sub>O, respectively, as required for a supposed C–H bond activation of the methyl group. Cobalt exhibits an intermediate behavior between that of iron and nickel showing both processes, *i. e.* O–H as well as C–H bond activation in the formation of Co(CH<sub>2</sub>OH)<sup>+</sup> and Co(OCH<sub>3</sub>)<sup>+</sup>.

For nickel, these findings strongly suggest that initially any of the isomers **45**, **46**, or **48** - perhaps with a preference for **45** - are formed. A fraction of this ion mixture subsequently undergoes isomerization to the **43/44a** manifold. The latter is supported by a CID experiment of the ion Ni(CD<sub>2</sub>OH)<sup>+</sup>, generated via DBr elimination from Ni(Br)(CD<sub>3</sub>OH)<sup>+</sup>. Upon CID at a collision energy  $E_{\text{lab}} = 10$  eV, in addition to the structure-unspecific losses of (C,H,D<sub>2</sub>,O) and neutral Ni, the products NiH<sup>+</sup> (loss of CD<sub>2</sub>O), NiD<sup>+</sup> (elimination of CHDO), formed in a ratio 3:1, and NiCDO<sup>+</sup> (dehydrogenation) indicate an isomerization Ni(CD<sub>2</sub>OH)<sup>+</sup> (**45**) → Ni(H)(CD<sub>2</sub>O)<sup>+</sup> (**43**) rather than a direct conversion Ni(CD<sub>2</sub>OH)<sup>+</sup> (**45**) → Ni(OCHD<sub>2</sub>)<sup>+</sup> (**44a**). Further, the complex Ni(H)(CD<sub>2</sub>O)<sup>+</sup> (**43**) has the options to lose directly CD<sub>2</sub>O - in line with Figure 6.14 -, rearrange, and finally eliminate HD, or, prior to formaldehyde evaporation or dehydrogenation, undergo partial, degenerate isomerization according to Ni(H)(CD<sub>2</sub>O)<sup>+</sup> ⇌ Ni(OCHD<sub>2</sub>)<sup>+</sup> ⇌ Ni(D)(CHDO)<sup>+</sup>.

With regard to the interconversions of [Ni,C,H<sub>3</sub>,O]<sup>+</sup>, in addition to the ground-state triplet surface, the singlet surface of this system has been also briefly analyzed (Figure 6.14 (b)) in order to probe whether or not the rearrangements are subject to a TSR scenario [43, 69–72, 204]. As mentioned, the latter has been identified to play a crucial role in the reversible β-H transfer between Fe(C<sub>2</sub>H<sub>5</sub>)<sup>+</sup> and Fe(H)(C<sub>2</sub>H<sub>4</sub>)<sup>+</sup> in that a spin flip from the quintet ground state to the excited triplet surface opens up a pathway which is 33.5 kJ mol<sup>−1</sup> lower in energy than the corresponding quintet transition structure [248]. However, as illustrated in Figure 6.14, inclusion of the excited singlet surface does not offer an energetic advantage for the Ni(H)(CH<sub>2</sub>O)<sup>+</sup> → Ni(OCH<sub>3</sub>)<sup>+</sup> isomerization. In contrast, at the theoretical level used, all relevant stationary points are higher in energy for the singlet states as compared to their triplet electromers. A one-state scenario has also been reported for the related Fe(H)(CH<sub>2</sub>O)<sup>+</sup> → Fe(OCH<sub>3</sub>)<sup>+</sup> rearrangement [112]. As to the role of singlet states for the isomers **45**, **46**, and **47**, no minima have been located for the <sup>1</sup>A-Ni<sup>+</sup> complexes structurally analogous to **45** and **46**. The η<sup>2</sup>-bridged structure **48**, however, resides in its <sup>1</sup>A state in a rather deep potential well, and it takes 157 kJ mol<sup>−1</sup> to bring about isomerization of **48** to **43** (<sup>1</sup>A). Further, two different structures for the classical methoxy complex Ni(OCH<sub>3</sub>)<sup>+</sup> have been located in the singlet state: The isomer <sup>1</sup>**44a** (not shown in Figure 6.14) with similar geometric features as found for triplet <sup>3</sup>**44a** is 45 kJ mol<sup>−1</sup> higher in energy compared to the more stable structure <sup>1</sup>**44b** with a much lower Ni–O–C angle (89.0° compared to 142.5° for

$^1\mathbf{44a}$ ) which profits from agostic interaction between a C–H bond and the nickel core and could thus be located only in the singlet state. Due to unexpected difficulties,<sup>37</sup> a connecting transition structure TS  $^1\mathbf{44a}/^1\mathbf{44b}$  of these isomers has not yet been located. Verslius et al. reported a substantial barrier between the agostic cobalt methoxy and the classical cobalt methoxy for the related neutral  $\text{Co}(\text{CO})_3(\text{OCH}_3)$  system in the order of  $80 \text{ kJ mol}^{-1}$  [151].

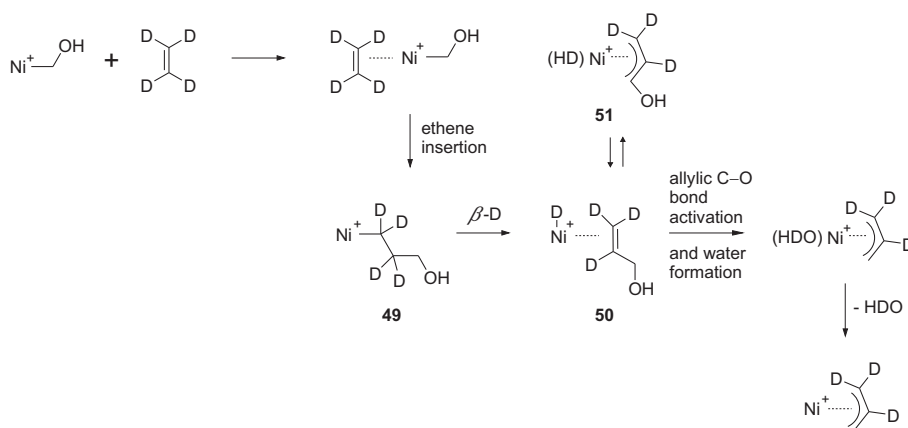


Finally, ligand exchange reactions were probed with acetone,  $\text{D}_2\text{O}$ , and  $\text{C}_2\text{D}_4$  (Equations 6.36, 6.37, and 6.38) to get further information about the structure of  $[\text{Ni},\text{C},\text{H}_3,\text{O}]^+$  generated in the ESI source. In the reaction with acetone, a ligand exchange is observed in which formaldehyde is eliminated and the respective hydride complexes  $\text{Ni}(\text{H})(\text{C}_3\text{H}_6\text{O})^+$  is formed according to Equation 6.36. This points to the presence of  $\text{Ni}(\text{H})(\text{CH}_2\text{O})^+$ . In line with this, the loss of HD is observed for the  $[\text{Ni},\text{C},\text{D}_3,\text{O}]^+/\text{C}_3\text{H}_6\text{O}$  couple in addition to the ligand exchange.<sup>38</sup> However, rearrangements which are facilitated upon ligation might also take place preceding the observed reactions. For example, in the reaction of  $[\text{Ni},\text{C},\text{H}_3,\text{O}]^+$  with  $\text{D}_2\text{O}$ ,  $\text{H}_2$  is eliminated without any scrambling processes between the ligand and the substrate (Equation 6.37), *i. e.* dehydrogenation is triggered by the energy gained upon adduct formation with  $\text{D}_2\text{O}$ . To conclude, a hydride complex is clearly involved in the reactions with both  $\text{D}_2\text{O}$  and acetone, but it is not clear, if either  $\text{Ni}(\text{CH}_2\text{OH})^+ \rightleftharpoons \text{Ni}(\text{H})(\text{CH}_2\text{O})^+$  or  $\text{Ni}(\text{OCH}_3)^+ \rightleftharpoons \text{Ni}(\text{H})(\text{CH}_2\text{O})^+$  interconversions are operative.

While the reactions with acetone and  $\text{D}_2\text{O}$  do not provide a clear answer about which structure is present in the ESI mass spectrometer, the reaction with  $\text{C}_2\text{D}_4$  is more instructive (Equation 6.38). The main reaction channel corresponds to the loss of water; this process originates most likely from the  $\text{Ni}(\text{CH}_2\text{OH})^+$  isomer via insertion of  $\text{C}_2\text{D}_4$  into the Ni–C bond as depicted in Scheme 6.5. As suggested for the reaction of  $\text{NiH}^+$  with ethane and ethene, olefin insertion into a Ni–H bond is energetically not very demanding. Subsequent  $\beta$ -D elimination and allylic C–O bond insertion finally allows the formation of

<sup>37</sup> An artefact in the calculations results in an energy jump of about  $140 \text{ kJ mol}^{-1}$  if the fixed Ni–O–C angle is enlarged by less than  $1^\circ$  at a certain degree. At the same point, the C–H bond shortens from  $1.184 \text{ \AA}$  to  $1.112 \text{ \AA}$ .

<sup>38</sup> The ratio of  $\text{H}_2/\text{HD}/\text{D}_2$  elimination has been determined to 20:76:4. Since double dehydrogenation is also observed, the loss of  $\text{D}_2$  might overlap with the elimination of  $2\text{H}_2$ .



Scheme 6.5

an intact water ligand. The observed scrambling processes can be explained by the equilibration  $\text{Ni}(\text{D})(\text{CD}_2\text{CDCH}_2\text{OH})^+ \rightleftharpoons \text{Ni}(\text{CD}_2\text{CDCHOH})(\text{HD})^+ \rightleftharpoons \text{Ni}(\text{H})(\text{CD}_2\text{CDCHDOH})^+ (\mathbf{50} \rightleftharpoons \mathbf{51})$ , Scheme 6.5).

**Gas-phase ion chemistry of the  $[\text{Ni}, \text{C}, \text{H}_3, \text{O}]^+/\text{C}_2\text{H}_6$  Couple** According to the experimental and theoretical findings regarding the structure of  $[\text{Ni}, \text{C}, \text{H}_3, \text{O}]^+$  and its formation in the ESI source, the reactions with ethane, propane, and butane can probably not be ascribed to only one single structural isomer. In the following section, the system of interest is the  $[\text{Ni}, \text{C}, \text{H}_3, \text{O}]^+/\text{C}_2\text{H}_6$  couple for which a mechanistically unusual case will be described in which various modes of H-transfer processes occur, *i. e.* scrambling and specific C-H bond activation, in the dehydrogenation of ethane, and in a degenerate H-exchange process. It will be shown that the assumptions made before with respect to dehydrogenation [276] are not confirmed by B3LYP calculations but that both theory and experiment are fully in line with an alternative model presented in this Thesis.

The thermal ion-molecule reaction of mass-selected  $[\text{Ni}, \text{C}, \text{H}_3, \text{O}]^+$  with  $\text{C}_2\text{H}_6$  is dominated by single dehydrogenation, double dehydrogenation amounts to only 1 %, and is not considered any further here (Equation 6.35).

Based on detailed kinetic modeling, a complete scrambling of all nine H/D atoms cannot account for the experimental results (Table 6.8), but the following conclusions have been drawn previously from the isotopic-labeling experiments: Phenomenologically, the dehydrogenation channel leading to  $[\text{Ni}, \text{C}_3, \text{H}_7, \text{O}]^+$  is to 90 % preceded by a complete loss of positional identity of all nine H-atoms of the encounter complex (“scrambling”), whereas ca. 10 % of the reaction exhibit a selective C-H bond activation of the alkane in which one H (D) atom of ethane and eight statistically equivalent H-atoms combine to molecular hydrogen.

The kinetic isotope effect (KIE) for the unspecific processes amounts to  $\text{KIE} = 1.6$ -1.7 per D-atom, and for the specific bond activation a value of  $\text{KIE} = 2.3$ -2.9 has been obtained; for the latter, due to its relatively small contribution (ca. 10 %), the modeling is rather insensitive to variations of the KIE.<sup>39</sup> These results are consistent with previous KIE data for iron-alkoxide cation systems [277, 278].

To account for the fact that in 10 % of the reaction one hydrogen from ethane occupies a position which is distinguished from the other, a hydrogen transfer from ethane to the methoxy ligand in  $\text{Ni}(\text{OCH}_3)^+$  is conceivable thus forming the methanol complex  $\text{Ni}(\text{C}_2\text{H}_5)(\text{CH}_3\text{OH})^+$ . In order to verify or to disprove this assumption, B3LYP calculations of the  $[\text{Ni}, \text{C}_3, \text{H}_9, \text{O}]^+$  PES have been performed and the results are described in the following. First, let us discuss the reaction pathway being in agreement with complete scrambling of all nine H/D positions of the system, Figure 6.16, which accounts for the main part of the reaction with a ratio of 90 %.

As found for “naked”  $\text{Ni}(\text{OCH}_3)^+$ , the adduct complex  $\text{Ni}(\text{OCH}_3)(\text{C}_2\text{H}_6)^+$  (**17d**) has a triplet ground state. Interestingly, the isomerization to the hydride complex  $\text{Ni}(\text{H})(\text{CH}_2\text{O})(\text{C}_2\text{H}_6)^+$  (**17d**  $\rightarrow$  **17e**) takes place according to a TSR scenario: The singlet states of both the associated TS **17d/17e** and the hydride complex **17e** are lower in energy compared to the triplet states. In contrast, no spin flip has to be considered for the lowest energy pathway of the rearrangement of “naked”  $\text{Ni}(\text{OCH}_3)^+$  to  $\text{Ni}(\text{H})(\text{CH}_2\text{O})^+$ , all relevant structures are more stable on the triplet surface (Figure 6.14, page 92). Thus, the order of multiplicity of the ligated hydride species  $\text{Ni}(\text{H})(\text{CH}_2\text{O})(\text{C}_2\text{H}_6)^+$  (**17e**) and “naked”  $\text{Ni}(\text{H})(\text{CH}_2\text{O})^+$  is reversed, the latter possessing a triplet ground state whereas the former is more stable in the singlet state. The energy demand for  $\beta$ -H migration in various  $\text{M}(\text{OCH}_3)\text{L}^+$  systems has been reported to highly depend on the presence and nature of additional ligands L [112, 151, 235, 277, 278]; taking spin crossing into account, the isomerization of the ligated species (**<sup>3</sup>17d**  $\rightarrow$  **<sup>1</sup>17e**) is with  $82 \text{ kJ mol}^{-1}$  somewhat less energy demanding compared to the energy barrier of  $95 \text{ kJ mol}^{-1}$  for the isomerization of “naked”  $\text{Ni}(\text{OCH}_3)^+ \rightarrow \text{Ni}(\text{H})(\text{CH}_2\text{O})^+$  on the triplet surface. Subsequent C–H bond activation of ethane under the formation of molecular hydrogen via a  $\sigma$ -CAM mechanism can easily proceed on the singlet surface (**17e**  $\rightarrow$  **18e**). The finding that the entrance channel as well as the singlet exit channel are higher in energy than all related intermediates of the sequence **<sup>1</sup>17d**  $\rightleftharpoons$  **<sup>1</sup>17e**  $\rightleftharpoons$  **<sup>1</sup>18e** can explain the equilibration of the six hydrogen atoms of ethane and the three of the methoxy group; the  $[\text{Ni}, \text{C}_3, \text{H}_9, \text{O}]^+$  isomers are trapped into a energy well and enabled to react back and forth resulting in equilibration of all the hydrogen positions. The same picture evolves assuming the hydride complex  $\text{Ni}(\text{H})(\text{OCH}_2)^+$  to be the reactive reactant ion; this scenario lowers the entrance channel by  $22 \text{ kJ mol}^{-1}$ . All intermediates

<sup>39</sup> Furthermore, degenerate H-atom exchange as a competitive reaction channel (see below) contributes to 10 % error of the relative branching ratios.

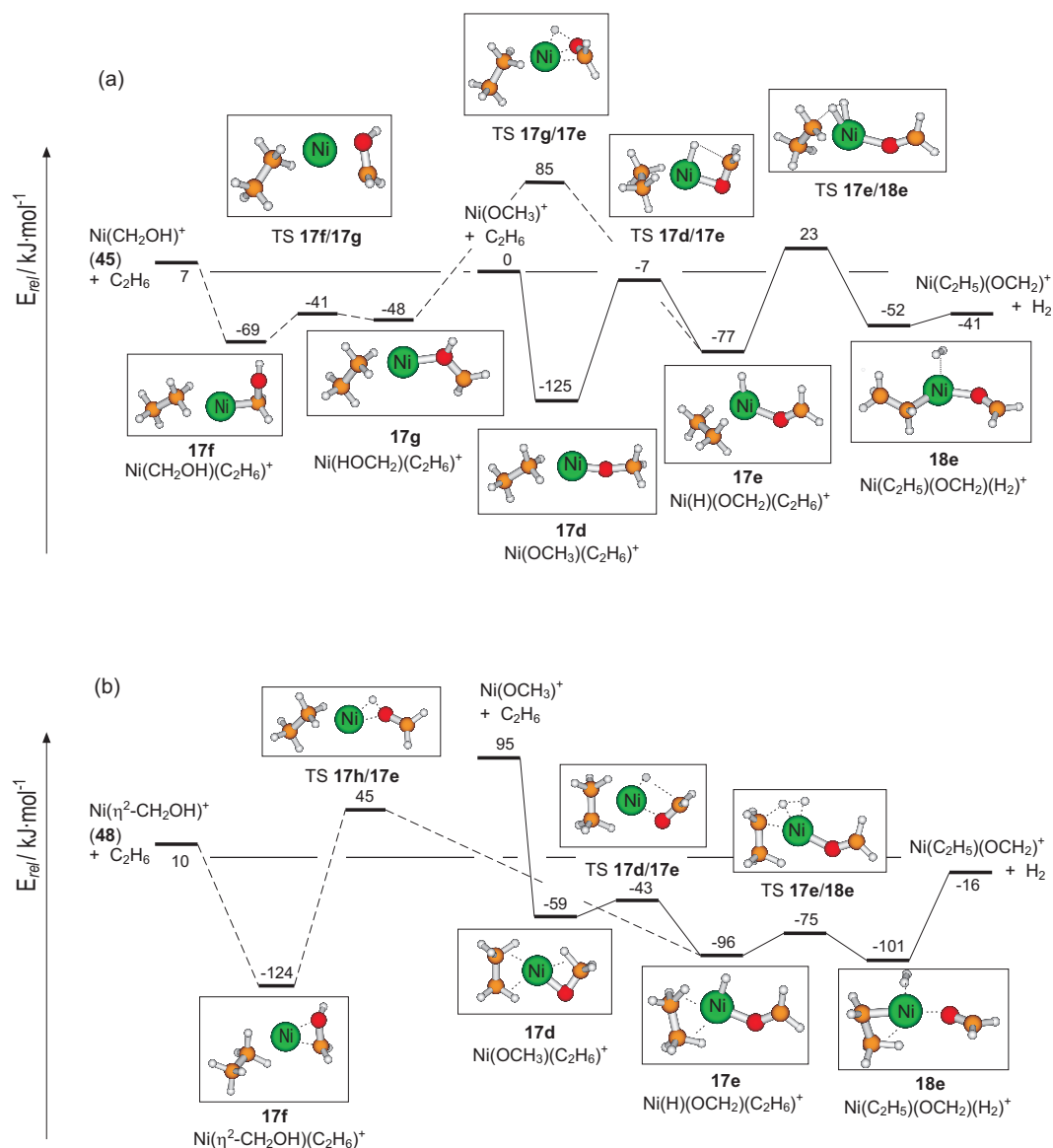


Figure 6.16 – Energy diagram (in  $\text{kJ mol}^{-1}$ ) for the reaction of  $[\text{Ni}(\text{OCH}_3)]^+$  and  $[\text{Ni}(\text{CH}_2\text{OH})]^+$  with ethane. In contrast to the isomerization  $17\text{f} \rightleftharpoons 17\text{e}$  (dashed line), the rearrangement  $17\text{d} \rightleftharpoons 17\text{e} \rightleftharpoons 18\text{e}$  prior to  $\text{H}_2$  elimination is accessible on the singlet surface under thermal conditions and allows a complete scrambling of all nine hydrogen atoms. The values are relative to the triplet state of the entrance channel and corrected for zero-point vibrational energies. (a) Triplet species, (b) singlet electromers.

and transition structures of this equilibration process are still lower in energy.

The interconversion between the  $\text{Ni}(\text{CH}_2\text{OH})(\text{C}_2\text{H}_6)^+$  (17f) and the

$\text{Ni}(\text{OCH}_3)(\text{C}_2\text{H}_6)^+/\text{Ni}(\text{H})(\text{CH}_2\text{O})(\text{C}_2\text{H}_6)^+$  (**17d/17e**) manifold on the triplet surface proceeds similar to the naked  $\text{Ni}(\text{CH}_2\text{OH})^+/\text{Ni}(\text{OCH}_3)^+/\text{Ni}(\text{H})(\text{CH}_2\text{O})^+$  triplet systems. The rearrangement  $\text{Ni}(\text{HOCH}_2)^+ \rightarrow \text{Ni}(\text{H})(\text{CH}_2\text{O})^+$  of the “naked” species (**46**  $\rightarrow$  **43**) is a two-step process in which a hydride complex with a hydrogen bound formaldehyde is an intermediate (**47**). For the ligated species, a transition structure  $^3\text{TS } \mathbf{17g/17e}$  has been located which directly connects  $\text{Ni}(\text{H})(\text{CH}_2\text{O})(\text{C}_2\text{H}_6)^+$  and  $\text{Ni}(\text{HOCH}_2)(\text{C}_2\text{H}_6)^+$ . Nevertheless,  $^3\text{TS } \mathbf{17g/17e}$  is  $85 \text{ kJ mol}^{-1}$  higher in energy relative to the entrance channel of separated  $\text{Ni}(\text{CH}_2\text{OH})^+/\text{C}_2\text{H}_6$  (Figure 6.18). On the singlet surface, the barrier for the interconversion **17f**  $\rightarrow$  **17e** amounts to  $45 \text{ kJ mol}^{-1}$ . Thus, a rearrangement between **17f** and the **17d/17e** manifold is most likely not involved in the reaction of  $[\text{Ni}, \text{C}, \text{H}_3, \text{O}]^+$  with ethane.

While the isomerization **17d**  $\rightleftharpoons$  **17e**  $\rightleftharpoons$  **18e** is possibly the origin of the extensive equilibration of all H/D atoms of the substrate and the methoxy ligand, for the “specific” process, no such clear explanation is provided by the calculations. The hydrogen transfer from ethane to the methoxy ligand in  $\text{Ni}(\text{OCH}_3)(\text{C}_2\text{H}_6)^+$  (**17d**  $\rightarrow$  **18d**, Figure 6.17) is with  $40 \text{ kJ mol}^{-1}$  and  $23 \text{ kJ mol}^{-1}$  energetically too demanding for triplet ground state as well for the excited singlet state of  $\text{Ni}(\text{OCH}_3)^+$  relative to the entrance channel, respectively.

The processes for activation and formation of C–H bonds of the methyl group are shown in Figure 6.18. If  $\text{Ni}(\text{CH}_2\text{OH})^+$  were the reactive species, the transfer of a hydrogen from ethane to  $\text{Ni}(\text{CH}_2\text{OH})^+$  is possible under ESI conditions; the corresponding transition structure  $^1\text{TS } \mathbf{17f/18d}$  lies energetically below the entrance channel of separated  $\text{Ni}(\text{CH}_2\text{OH})^+/\text{C}_2\text{H}_6$ . The isotope pattern, one would expect from the reaction pathway shown in Figure 6.18, corresponds to a complete scrambling of all hydrogen atoms of ethane and two hydrogens of the  $[\text{C}, \text{H}_3, \text{O}]$  ligand. Indeed, a model in which a combination of a complete scrambling ( $f_{\text{scr}}$ ) and the reaction path  $\text{Ni}(\text{CH}_2\text{OH})^+/\text{C}_2\text{H}_6 \rightarrow \mathbf{17f} \rightleftharpoons \mathbf{18d} \rightleftharpoons \mathbf{19d} \rightleftharpoons \mathbf{20e} \rightarrow \text{Ni}(\text{CH}_2\text{OH})(\text{C}_2\text{H}_4)^+/\text{H}_2$  ( $f_{\text{spec}}$ ) in Figure 6.18 is assumed (model 2), can reproduce the experimental data as good as the former model 1 [276] (Table 6.8, model 1: first entries, model 2: second numbers in parenthesis). The finding that model 2 complies with the experimental as well as with the results of the calculations strongly suggests that both structural isomers, *i. e.* the hydroxymethyl and the methoxy/hydride-formaldehyde manifolds are formed in the gas phase upon ESI.

In the course of studying dehydrogenation of  $\text{C}_2\text{H}_6$ , an exchange of the H-atoms of the  $[\text{Ni}, \text{C}, \text{H}_3, \text{O}]^+$  complex with those of ethane has been observed also. While this degenerate isomerization remains unnoticed in the unlabeled couple, a few details of the “hidden” H-atom transfer (for the concept of “hidden” H-rearrangements, see [279]) can be derived from

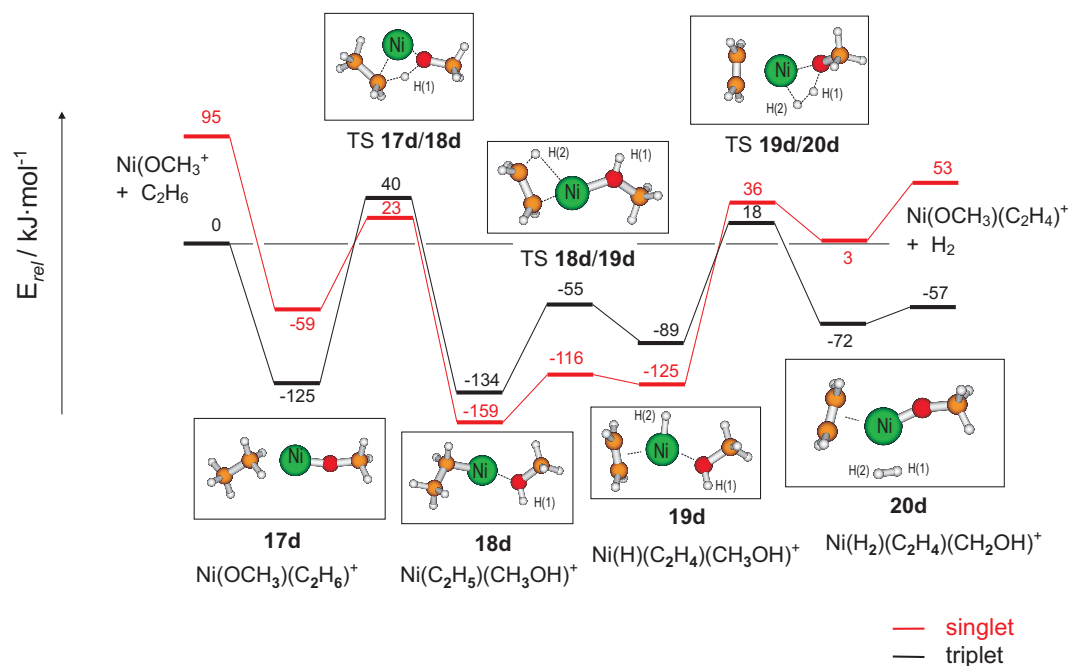


Figure 6.17 – Energy diagram (in  $\text{kJ mol}^{-1}$ ) for the reaction of  $[\text{Ni}(\text{OCH}_3)]^+$  and ethane according to  $\sigma$ -bond-metathesis reactions involving the O-H bond. The values are relative to the entrance channel on the triplet surface and corrected for zero-point vibrational energies.

studying isotopically labeled variants (Equations 6.39 - 6.42):<sup>40</sup>

- Thermochemical considerations, performed at the B3LYP level, as well as the labeling data obtained for dehydrogenation of ethane (Table 6.8), rule out the formation of separate  $\text{C}_2\text{H}_4/\text{H}_2$  products; rather, intact  $\text{C}_2\text{H}_6$  has to be regenerated in the degenerate hydrogen exchange.
- The experimental findings can be modeled in terms of various scenarios. For example, a good fit can be obtained by assuming the following: Each methyl group of the incoming ethane molecule delivers one H-atom, which together with the three of the Ni-bound  $(\text{C},\text{H}_3,\text{O})$  ligand form a pool of five indistinguishable H-atoms, from which two are transferred back to the hydrocarbon fragment. However, due to the ca. 10% of scrambling, indicated by the formations of  $\text{Ni}(\text{C},\text{H},\text{D}_2)^+$  in Equation 6.41 and  $\text{Ni}(\text{C},\text{H}_2,\text{D})^+$  in Equation 6.42, and the fact that the extent of degenerate exchange is

<sup>40</sup> Note that, in addition to the exchange products shown in Equation 6.39 - 6.42, for some couples also isotope variants are formed which are identical with the starting  $\text{Ni}(\text{C},\text{H}_{3-x},\text{D}_x,\text{O})^+$  complexes. Of course, their amount cannot be extracted from the data.



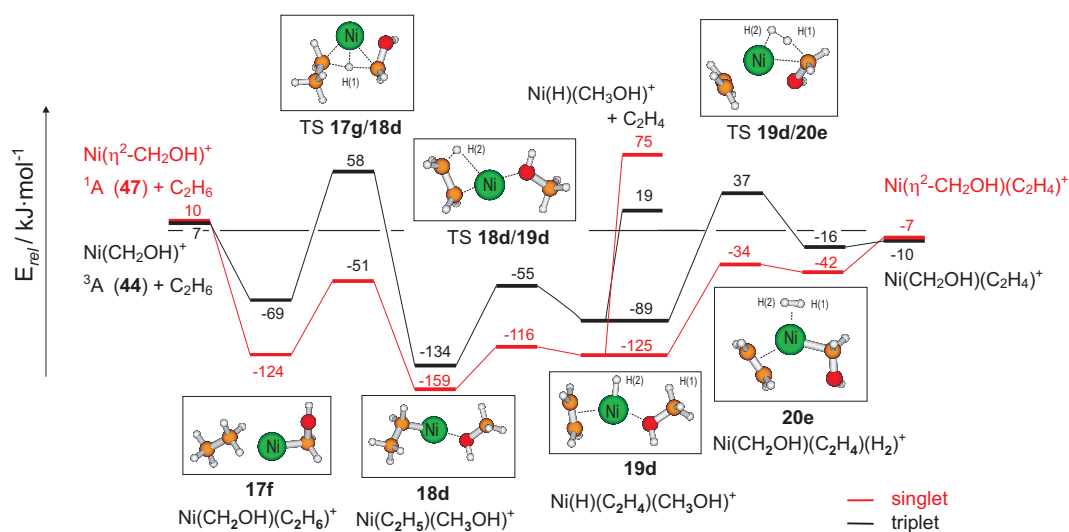
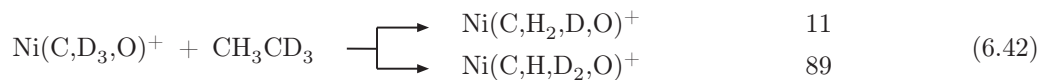
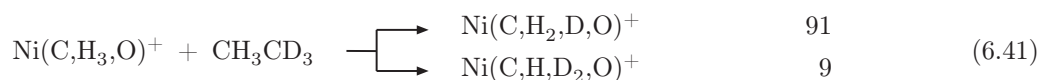
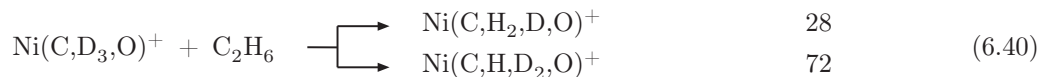
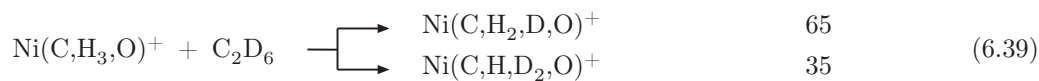


Figure 6.18 – Energy diagram (in  $\text{kJ mol}^{-1}$ ) for the reaction of  $[\text{Ni}(\text{CH}_2\text{OH})]^+$  and ethane according to  $\sigma$ -bond-metathesis reactions involving a C–H bond. The values are relative to the entrance channel on the triplet surface and corrected for zero-point vibrational energies.

pressure-dependent, a more detailed analysis of the complex data is not warranted.<sup>41</sup>



<sup>41</sup> For a highly specific, interligand *triple* hydrogen migration in  $\text{Fe}^+$ -alkyne complexes, see [280].

6.3.2 Reactions with propane and *n*-butane

A large complexity of reaction pathways is observed for the reaction of Ni(OH)<sup>+</sup> and [Ni,C,H<sub>3</sub>,O]<sup>+</sup> with propane and *n*-butane, Table 6.9. Interestingly, significant C–C bond activation is observed for the Ni(OH)<sup>+</sup>/propane system, in contrast to the other nickel complexes for which C–C bond activation mainly takes place only from *n*-butane. This finding is less pronounced in the reaction of [Ni,C,H<sub>3</sub>,O]<sup>+</sup> with C<sub>3</sub>H<sub>8</sub>. For the latter complex, the relative high extent of internal C(2)–C(3) bond activation of *n*-butane in contrast to the reaction with halides NiX<sup>+</sup> (X = F, Cl, Br, I) is remarkable. The reactions can be classi-

Table 6.9 – Relative rates<sup>a</sup> and branching ratios<sup>a</sup> of the neutral losses in the reactions of mass-selected NiX<sup>+</sup> cations (X = OH, OCH<sub>3</sub>) with propane and *n*-butane.

	C <sub>3</sub> H <sub>8</sub>		<i>n</i> -C <sub>4</sub> H <sub>10</sub>	
	L =		L =	
	OH	OCH <sub>3</sub>	OH	OCH <sub>3</sub>
-H <sub>2</sub>	2	77	1	9
-2 H <sub>2</sub>		3		3
-CH <sub>3</sub>	12	1	6	
-CH <sub>4</sub>	4	1	2	28
-CH <sub>4</sub> /H <sub>2</sub>				2
-C <sub>2</sub> H <sub>4</sub>	16	5	4	16
-C <sub>2</sub> H <sub>6</sub>	1	1		1
-C <sub>3</sub> H <sub>6</sub>			5	4
-HX	12	8	3	21
-HX/H <sub>2</sub>	53	3	22	6
-CH <sub>3</sub> L				2
-HX/CH <sub>4</sub>			57	8
adduct formation		1		
<i>k</i> <sub>rel</sub>	50	42	51	40

<sup>a</sup> Rates given relative to the fastest reaction observed (NiBr<sup>+</sup> + C<sub>3</sub>H<sub>8</sub>).

<sup>b</sup> Normalized to a sum of 100.

fied according to the categories a) and b) on page 72 proposed for the reactions of nickel halides NiX<sup>+</sup> (X = F, Cl, Br, and I), *i. e.* bond activation of the organic substrate without obvious occurrence of Ni–X bond cleavage leading to the losses of H<sub>2</sub>, CH<sub>4</sub>, C<sub>2</sub>H<sub>4</sub>, C<sub>2</sub>H<sub>6</sub>, and/or C<sub>3</sub>H<sub>6</sub>, *vs* reactions involving Ni–X bond cleavage, namely the expulsions of ROH, ROH/H<sub>2</sub>, and ROH/CH<sub>4</sub> (R = H, CH<sub>3</sub>). Almost the same reaction channels are observed

for  $\text{Ni}(\text{OH})^+$  and  $[\text{Ni},\text{C},\text{H}_3,\text{O}]^+$ ; however, large differences are found with respect to the BRs. In the case of  $[\text{Ni},\text{C},\text{H}_3,\text{O}]^+$ , reactions of type a) amount to the largest part of all reaction channels (8:1 and 1.7:1 in favor of type a) compared to type b) in the reactions with propane and *n*-butane, respectively). In contrast, for  $\text{Ni}(\text{OH})^+$  type b) reactions involving a Ni–O bond cleavage and the elimination of water are more important (here, the ratio a):b) adds up to 1:2.8 for propane and 1:6.8 for *n*-butane). The elimination of a methyl radical observed prominently for  $\text{Ni}(\text{OH})^+$  is quite surprising. This reaction channel resembles the radical-like behavior of  $\text{FeO}^+$  [281] and  $\text{MnO}^+$  [58] in the reactions with propane; the formation of the  $\text{M}(\text{OH})(\text{C}_2\text{H}_4)^+$  product ions are suggested to occur through an initial hydrogen-abstraction process followed by metal-induced C–C bond cleavage [45, 58]. For  $\text{Ni}(\text{OH})^+$ , the expulsion of  $\cdot\text{CH}_3$  has been calculated to be exothermic with  $-92\text{ kJ mol}^{-1}$  when  $\text{Ni}(\text{H}_2\text{O})(\text{C}_2\text{H}_4)^+$  is formed, whereas an endothermicity of  $108\text{ kJ mol}^{-1}$  is obtained if  $\text{Ni}(\text{OH})(\text{C}_2\text{H}_5)^+$  constitutes the product ion. Again, this finding demonstrates that this reaction most likely starts with the formation of water by H-transfer from ethane to the hydroxy ligand; a subsequent  $\beta\text{-CH}_3$  migration yields the complex  $\text{Ni}(\text{CH}_3)(\text{C}_2\text{H}_4)(\text{H}_2\text{O})^+$  which contains a sufficient amount of internal energy to break the Ni–C bond and to expel a methyl radical.

Table 6.10 – Isotope patterns<sup>a</sup> of dehydrogenation of propane by  $[\text{Ni},\text{C},\text{H}_3,\text{O}]^+$ .

	- H <sub>2</sub>	- HD	- D <sub>2</sub>	
$\text{Ni}(\text{C},\text{H}_3,\text{O})^+ + \text{C}_3\text{D}_8$	0 (1)	8 (6)	92 (93)	$f_{1,2} = 31\%$
$\text{Ni}(\text{C},\text{H}_3,\text{O})^+ + \text{CH}_3\text{CD}_2\text{CH}_3$	68 (70)	28 (30)	4 (0)	$f_{1,3} = 60\%$
$\text{Ni}(\text{C},\text{H}_3,\text{O})^+ + \text{CD}_3\text{CH}_2\text{CD}_3$	3 (2)	41 (41)	56 (57)	$f_{scr} = 9\%$
				$\text{KIE}_{spec} = 1.25$
				$\text{KIE}_{scr} = 1.00$

<sup>a</sup> Given in % (modeled numbers are given in parenthesis). See text for details of the modeling.

Unfortunately, labeling experiments are not instructive to elucidate the reaction mechanisms, either because the combined elimination of closed-shell ROH, H<sub>2</sub>, or CH<sub>4</sub> is observed, or due to isobaric overlap. For example, the distinction between the loss of H<sub>2</sub>O, CD<sub>3</sub>, and CH<sub>2</sub>D<sub>2</sub> is impossible with the given mass resolution of the ESI mass spectrometer. However, neglecting double dehydrogenation, the ratio of H<sub>2</sub>/HD/D<sub>2</sub> elimination has been determined for the reaction of  $[\text{Ni},\text{C},\text{H}_3,\text{O}]^+$  with CH<sub>3</sub>CD<sub>2</sub>CH<sub>3</sub> (**25**), CD<sub>3</sub>CH<sub>2</sub>CD<sub>3</sub> (**14**), and C<sub>3</sub>D<sub>6</sub>. Interestingly, an equilibration of all H/D position of the system as found in the reaction with ethane is only observed to a relative small degree ( $f_{scr} = 9\%$ , Table 6.10) which is obvious from the lack of H<sub>2</sub> loss and the small amount of HD elimination in the reaction of  $[\text{Ni},(\text{C},\text{H}_3,\text{O})]^+$  with C<sub>3</sub>D<sub>8</sub>. Moreover, the isotopic pattern suggest a rarely observed 1,3-

hydrogenation [282–284] for 60 % of the reactions; the usually found 1,2-mode of dehydrogenation amounts to 31% according to the modeled data. However, a specific bond activation at the terminal methyl group leading to the formation of a metalla-cycle is probably not the reason for this observation, but, as discussed for the reactions of NiX<sup>+</sup> with propane (X = Br, I), the 1,3-elimination is fully in line with the reaction sequence Ni(C,H<sub>3</sub>,O)(C<sub>3</sub>H<sub>8</sub>)<sup>+</sup> → Ni(<sup>i</sup>C<sub>3</sub>H<sub>7</sub>)(CH<sub>3</sub>OH)<sup>+</sup> → Ni(H)(C<sub>3</sub>H<sub>6</sub>)(CH<sub>3</sub>OH)<sup>+</sup> → Ni(C<sub>3</sub>H<sub>5</sub>)(H<sub>2</sub>)(CH<sub>3</sub>OH)<sup>+</sup> corresponding to **28** → **30** → **33** → **34**/H<sub>2</sub> in Scheme 6.3, page 82, path (B1), *i. e.* elimination takes place starting specifically with the activation of internal C–H bonds, whereas in the case of 1,2-dehydrogenation the activation of a C–H bond at the terminal methyl group is the first step (according to **29** → **30** → **33** → **34**/H<sub>2</sub> in Scheme 6.3, path (B1)). Thus, the numbers for  $f_{1,2}$  and  $f_{1,3}$  commensurate the specificity of primary and secondary C–H bonds of propane, respectively. In contrast to NiI<sup>+</sup>, path (B2) is suggested to play only a minor role if it matters at all. This pathway implies that hydrogen atoms are transferred from the ligand to form molecular hydrogen which is not supported by the isotope patterns given in Table 6.10 due to the relatively low amount of HD elimination in the reaction of [Ni,C,H<sub>3</sub>,O]<sup>+</sup> with C<sub>3</sub>D<sub>8</sub>.

Table 6.11 – Isotope patterns<sup>a</sup> for the elimination of methane in the reactions of [Ni,C,H<sub>3</sub>,O]<sup>+</sup> with isotopomers of *n*-butane.

	- CH <sub>4</sub>	- CH <sub>3</sub> D	- CH <sub>2</sub> D <sub>2</sub>	- CHD <sub>3</sub>	- CD <sub>4</sub>
Ni(C,D <sub>3</sub> ,O) <sup>+</sup>	100				
+ <i>n</i> -C <sub>4</sub> H <sub>10</sub>					
Ni(C,H <sub>3</sub> ,O) <sup>+</sup>	14 (21)	38 (37)	23 (15)	25 (27)	0 (0)
+ CH <sub>3</sub> CH <sub>2</sub> CH <sub>2</sub> CD <sub>3</sub>					
Ni(C,H <sub>3</sub> ,O) <sup>+</sup>	0 (0)	6 (6)	22 (21)	42 (44)	30 (29)
+ CD <sub>3</sub> CH <sub>2</sub> CH <sub>2</sub> CD <sub>3</sub>					
$f_{prim} = 25\%$ $f_{sec} = 25\%$ $f_{scr} = 50\%$					

<sup>a</sup> Given in % (modeled numbers are given in parenthesis). See text for details of the modeling.

In distinct contrast to the dehydrogenation of ethane, no scrambling processes are involved in neither dehydrogenation, demethanation, nor ethene loss in the reaction of [Ni,C,H<sub>3</sub>,O]<sup>+</sup> and *n*-butane as revealed by the exclusive eliminations of H<sub>2</sub>, CH<sub>4</sub>, and C<sub>2</sub>H<sub>4</sub> for the Ni(C,D<sub>3</sub>,O)<sup>+</sup>/*n*-C<sub>4</sub>H<sub>10</sub> couple. To reproduce the experimental data for the loss of methane in the reaction of [Ni,C,H<sub>3</sub>,O]<sup>+</sup> with CH<sub>3</sub>CH<sub>2</sub>CH<sub>2</sub>CD<sub>3</sub> (**26**) and CD<sub>3</sub>CH<sub>2</sub>CH<sub>2</sub>CD<sub>3</sub> (**27**),<sup>42</sup> Table 6.11, several combinations of reaction mechanism, *i. e.* reactions involving scrambling

<sup>42</sup> The combined elimination of CH<sub>4</sub> and H<sub>2</sub>, observed with a ratio of 2%, has been neglected.

processes<sup>43</sup> ( $f_{scr}$ ) of the substrate concomitant with pathways starting with primary C–H ( $f_{prim}$ ) or secondary C–H ( $f_{sec}$ ) bond activation, have been checked. Quite large differences between the respective models and the experiment emerge; however, a tolerable fit is achieved disregarding KIEs and assuming a ratio of 50:25:25 for  $f_{scr} : f_{prim} : f_{sec}$ , the modeled numbers are given in parenthesis in Table 6.11.

---

<sup>43</sup> Only H/D exchange processes of *n*-butane have been taken into account.



## 7 Reactivity of the Ni<sup>III</sup> complex Ni(H)(OH)<sup>+</sup>

### 7.1 Structure and formation of Ni(H)(OH)<sup>+</sup>

Interestingly, two different structural isomers with the composition [Ni,H<sub>2</sub>,O]<sup>+</sup> generated in the ESI source have been identified in the gas phase. Previous B3LYP calculations predicted the existence of Ni(H<sub>2</sub>O)<sup>+</sup>, Ni(O)(H<sub>2</sub>)<sup>+</sup>, and Ni(H)(OH)<sup>+</sup>, two of which are of interest in the present context [285]. The global minimum of the system corresponds to a C<sub>2v</sub>-symmetric <sup>2</sup>A<sub>1</sub> state of the Ni(H<sub>2</sub>O)<sup>+</sup> (**53**) complex; the structurally analogous <sup>4</sup>A<sub>2</sub> state (C<sub>2v</sub>) is 172 kJ mol<sup>-1</sup> higher in energy, and the formal Ni<sup>III</sup>-insertion complex Ni(H)(OH)<sup>+</sup> (**52**, <sup>4</sup>A'') is even less stable by additional 85 kcal mol<sup>-1</sup>. Whereas the quartet state of Ni(H)(OH)<sup>+</sup> is separated by a barrier of 65 kJ mol<sup>-1</sup> from the quartet-state of the Ni(H<sub>2</sub>O)<sup>+</sup> complex, on the doublet surface, the <sup>2</sup>A'' insertion species Ni(H)(OH)<sup>+</sup> undergoes spontaneous isomerization to <sup>2</sup>A<sub>1</sub> Ni(H<sub>2</sub>O)<sup>+</sup> as a result of the negligibly small barrier of less than 2 kJ mol<sup>-1</sup> [285]. Experimental confirmation of these predictions has not yet been reported. However, the CID spectra shown in Figure 7.1 reveals that two structurally different, non-interconvertible isomers with the composition [Ni,H<sub>2</sub>,O] must indeed exist in the gas phase.

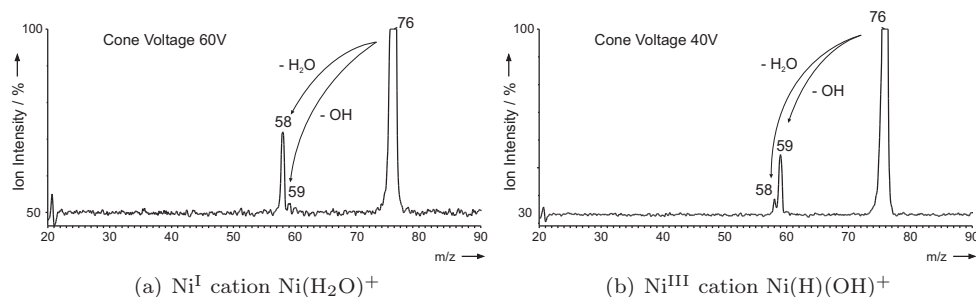
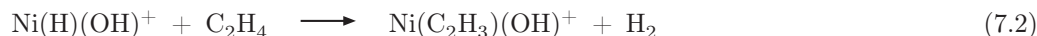
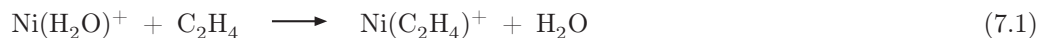


Figure 7.1 – CID spectrum of two structural isomers of [Ni,H<sub>2</sub>,O]<sup>+</sup> at  $E_{\text{lab}} = 10$  eV.

Whereas the CID spectrum in Figure 7.1(a) is compatible with the presence of a Ni(H<sub>2</sub>O)<sup>+</sup> complex (**53**), the spectrum in Figure 7.1(b) is in keeping with the insertion product Ni(H)(OH)<sup>+</sup> (**52**). Furthermore, a CID examination of the complex <sup>58</sup>Ni(D)(OH)<sup>+</sup>, generated from NiI<sub>2</sub>/CD<sub>3</sub>OH/H<sub>2</sub>O, reveal the specific eliminations of D<sup>•</sup> ( $m/z$  77 →  $m/z$  75) and OH<sup>•</sup> ( $m/z$  77 →  $m/z$  60). A signal corresponding to the cleavage of the Ni–H bond of **52** is, most likely, also present in Figure 7.1 b; however, owing to the asymmetric broadening

of the parent ion and the limited mass resolution of the instrument, the signal at  $m/z$  75 cannot be resolved from the precursor ion at  $m/z$  76.



Although the actual spin states of the two isomers cannot be determined, in conjunction with theoretical work of Ugalde and co-workers [285], it is obvious that, depending on the cone voltage and the composition of the solution, ESI of a solution of  $\text{NiX}_2/\text{CH}_3\text{OH}/\text{H}_2\text{O}$  ( $\text{X} = \text{F}, \text{Cl}, \text{Br}, \text{I}$ ) produces two structurally distinct  $[\text{Ni}, \text{H}_2, \text{O}]^+$  species. The exact origin and genesis of these two isomers remains to be elucidated; some details, however, are hinted by the experiments: For example, an ESI of  $\text{NiI}_2/\text{CH}_3\text{OD}/\text{D}_2\text{O}$  gives rise to  $\text{Ni}(\text{H})(\text{OD})^+$  and  $\text{Ni}(\text{D}_2\text{O})^+$ . Further, a parent-ion scan demonstrates that  $\text{Ni}(\text{H}_2\text{O})^+$  (**53**) is produced from  $\text{Ni}(\text{H}_2\text{O})(\text{CH}_3\text{OH})^+$  ( $m/z$  108). In contrast, isomeric  $\text{Ni}(\text{H})(\text{OH})^+$  (**52**) originates from  $\text{Ni}(\text{CH}_2\text{OH})(\text{OH})^+$  ( $m/z$  106) in a rather complex sequence of events in which the intermediate  $[\text{Ni}, \text{C}, \text{H}_2, \text{O}_2]^+$  ( $m/z$  104) plays a key role. On the basis of exploratory labeling experiments, this species is assigned to the formal  $\text{Ni}^{\text{III}}$  compound  $\text{Ni}(\text{CHO})(\text{OH})^+$ . As expected, a CID experiment of this complex leads to losses of  $\text{OH}^\cdot$ ,  $\text{CO}$ , and  $\text{CHO}$  (in the ratio 5:16:1). Further experiments suggest that the  $\text{Ni}^{\text{III}}$  ions are generated already in solution rather than in the gas phase. Thus, at lowest cone voltage (10 V), a complex formally corresponding to  $\text{Ni}(\text{CH}_2\text{OH})(\text{OH})(\text{CH}_3\text{OH})_3^+$  is detected, from which, upon increasing the cone voltage, methanol ligands are evaporated sequentially ( $m/z$  202  $\rightarrow$   $m/z$  170  $\rightarrow$   $m/z$  138  $\rightarrow$   $m/z$  106) until the “bare”  $\text{Ni}^{\text{III}}$  complex  $\text{Ni}(\text{CH}_2\text{OH})(\text{OH})^+$  is formed. Classical ligand-field theory predicts the quartet state of  $\text{Ni}^{\text{III}}$  to dominate in solution which should be valid if more ligands are around the nickel center at the time when it gets formed by redox processes in the solution or by oxidation at the high voltage capillary from  $\text{Ni}^{\text{II}}$ . As mentioned, theory predicts gaseous  $\text{Ni}(\text{H})(\text{OH})^+$  (**52**) to exist in the quartet state, since it easily isomerizes to  $\text{Ni}(\text{H}_2\text{O})^+$  (**53**) on the doublet surface. However, it yet remains unclear why it remains in the quartet state. A potential energy scan on the B3LYP level of theory was performed by Zhang in collaboration with Baik to estimate the possibility of spin state conversion, the crossing of the smooth doublet and quartet curves being ca.  $6 \text{ kJ mol}^{-1}$  higher in energy than  $^4\text{52}$ . Due to spin contamination found in the calculation of the doublet surface, this estimate might suffer from considerable uncertainties. However, since the potential-energy surfaces around the two minima  $^2\text{52}$  and  $^4\text{52}$  are quite flat, the crossing-point energy is according to B3LYP calculations probably not very high. An alternative reason why this ion can exist and be detected in the gas phase is the hinderance of a spin flip from the quartet to the doublet state due to a inefficient spin-orbit coupling (SOC). Currently, further high level calculations are



carried out by Zhang in collaboration with Baik and co-workers to elucidate the structural and energetic properties of the crossing point. While theory does not yet provide an unambiguous explanation for the existence of  $\text{Ni}(\text{H})(\text{OH})^+$  in the gas phase so far, reactivity and labeling studies with several substrates clearly indicate the actual co-formation of gaseous  $\text{Ni}(\text{H})(\text{OH})^+$  (see below). In the computational studies of the ion-molecule reactions with methane and molecular oxygen observed in the experiments (sections 7.2 and 7.3), quartet  $\text{Ni}(\text{H})(\text{OH})^+$  (**52**) is assumed to be the reactant species.

The actual composition of the two isomers **52** and **53** is affected by both the cone voltage and (to a smaller extent) by the  $\text{CH}_3\text{OH}/\text{H}_2\text{O}$  mixture composition. The rather independent pathways for the production of these isomers may explain the counterintuitive preferential formation of the high-energy isomer **52** at low cone voltages. The ratio of the structural isomers against the applied cone voltage (Figure 7.2) can be estimated by measuring the reactions with ethene at increasing cone voltages and a constant pressure since both isomers display distinct reactivity towards  $\text{C}_2\text{H}_4$ : In contrast to  $\text{Ni}(\text{H}_2\text{O})^+$ , for which a simple ligand exchange reaction is observed (Equation 7.1),  $\text{Ni}(\text{H})(\text{OH})^+$  dehydrogenates ethene according to reaction 7.2.

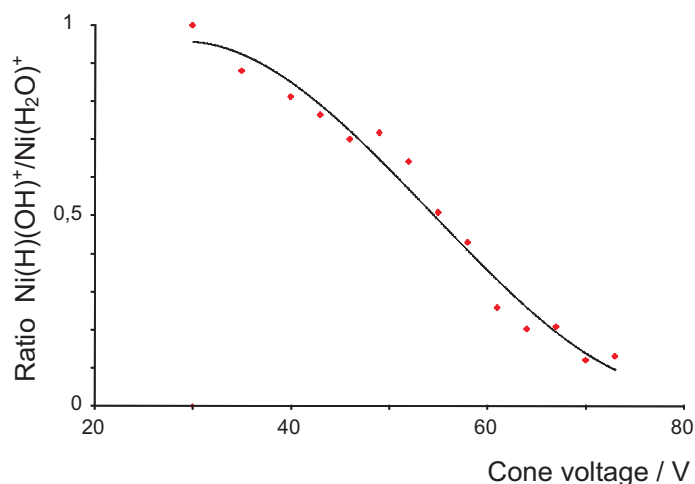


Figure 7.2 – Ratio of the structural isomers  $[\text{Ni}(\text{H})(\text{OH})]^+$  and  $[\text{Ni}(\text{H}_2\text{O})]^+$  as determined by the different reactions with ethene, Equations 7.1 and 7.2. See text for details.

The  $m/z$  76 signal appears at a cone voltage of 30 V; here, only the high-valent nickel complex  $\text{Ni}(\text{H})(\text{OH})^+$  is formed since no  $\text{H}_2\text{O}/\text{C}_2\text{H}_4$  ligand exchange according to Equation 7.1 is observed. Increasing the cone voltage step by step up to 70 V leads to a decrease of the  $\text{Ni}(\text{H})(\text{OH})^+/\text{NiH}_2\text{O}^+$  ratio down to approximately 0.1, Figure 7.2; the signal  $m/z$  76 disappears completely at cone voltages above ca. 80 V.

## 7.2 Activation of methane

The structural assignments of  $\text{Ni}(\text{H})(\text{OH})^+$  (**52**) and  $\text{Ni}(\text{H}_2\text{O})^+$  (**53**) described in the last Chapter are further supported by ion/molecule reactions of the  $[\text{Ni}, \text{H}_2, \text{O}]^+$  isomers with  $\text{D}_2\text{O}$  and  $\text{D}_2$ . In the reaction of  $\text{D}_2\text{O}$  with  $\text{Ni}(\text{H}_2\text{O})^+$ , generated at a cone voltage of 60 V, complete ligand exchange is preferentially (78 %) observed, whereas the isomer  $\text{Ni}(\text{H})(\text{OH})^+$ , generated at 40 V, gives rise exclusively to  $\text{Ni}(\text{D})(\text{OH})^+$  and  $\text{Ni}(\text{H})(\text{OD})^+$  upon reaction with  $\text{D}_2$  and  $\text{D}_2\text{O}$ , respectively.

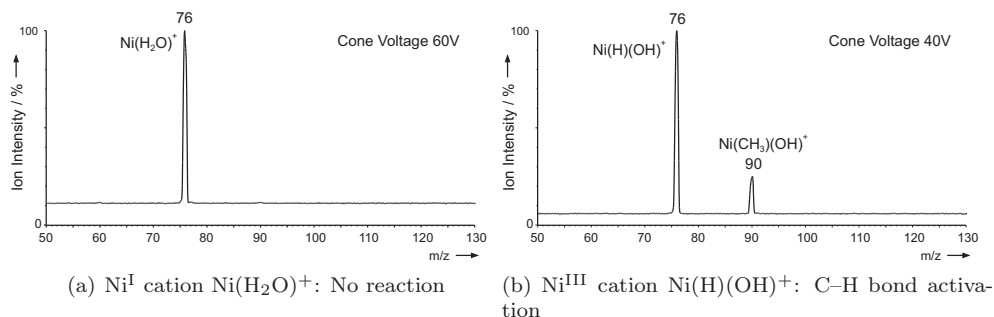
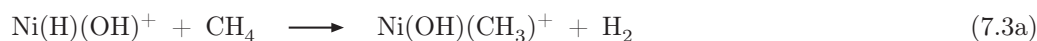


Figure 7.3 – Mass selected  $[\text{Ni}, \text{H}_2, \text{O}]^+$  isomers allowed to react with  $\text{CH}_4$  at  $E_{\text{lab}} = 0 \text{ eV}$ .

An unprecedented reactivity of the  $[\text{Ni}, \text{H}_2, \text{O}]^+$  system toward methane has also been encountered. In line with expectations and described in Chapter 5, activation of the C–H bond is not observed in the reaction of the  $\text{Ni}^{\text{I}}$ -aqua complex with methane (Figure 7.3(a)). In contrast, the  $\text{Ni}^{\text{III}}$  isomer **52** undergoes thermal H/ $\text{CH}_3$  ligand exchange (Figure 7.3(b)) with a relative rate constant greater than or equal to 12 % (relative to the  $\text{NiBr}^+/\text{C}_3\text{H}_8$  system).



$$k_{\text{rel}} = 12 \%$$

The naturally occurring nickel is composed of five stable isomers; the masses and the corresponding abundances are given in Figure 7.4. To confirm the reactive ion to be a nickel complex, the respective complexes containing the second most frequent isotope ( $^{60}\text{Ni}$ ) have been isolated and exposed to neutral methane as well. For the same purpose, a neutral-gain experiment ( $\Delta m = +14$ ) which corresponds to adduct formation and subsequent dehydrogenation of methane has been carried out. As required, the isotope pattern of nickel is displayed in the spectrum, Figure 7.4, and corresponds to the modeled composition of

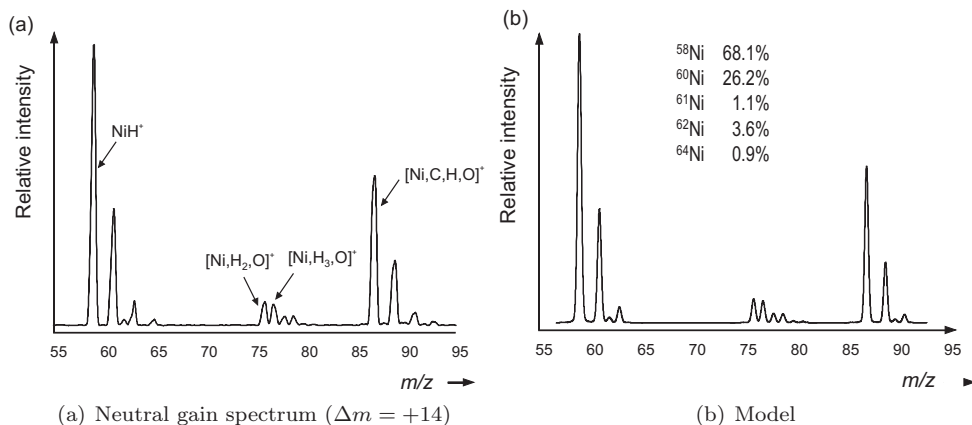
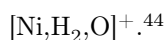


Figure 7.4 – Neutral gain spectrum ( $\Delta m = +14$ ) from a solution of  $\text{NiI}_2$  in methanol/water at a cone voltage of 40 V. All ions from the source are exposed to methane; the cations being capable of methane dehydrogenation are recorded. See text and chapter 1.2.3 for details.

The hydroxy group does not participate in this reaction and remains intact, as the reaction of  $\text{Ni}(\text{H})(\text{OD})^+$  with  $\text{CH}_4$  liberates exclusively  $\text{H}_2$  (Table 7.1). In contrast, the reaction with other isotopologues show that partial exchange of the hydrido ligand with the incoming hydrocarbon occurs prior to or during the formation of the nickel-carbon bond. For example, HD and  $\text{D}_2$  are produced from  $\text{Ni}(\text{H})(\text{OH})^+/\text{CD}_4$ , HD and  $\text{H}_2$  from  $\text{Ni}(\text{D})(\text{OH})^+/\text{CH}_4$ , and  $\text{H}_2$ , HD, and  $\text{D}_2$  from  $\text{Ni}(\text{H})(\text{OH})^+/\text{CH}_2\text{D}_2$  (Table 7.1).

Table 7.1 – Isotope patterns<sup>a</sup> for the dehydrogenation of methane by the  $\text{Ni}^{\text{III}}$  complex  $\text{Ni}(\text{H})(\text{OH})^+$ .

	- $\text{H}_2$	- HD	- $\text{D}_2$	
$\text{Ni}(\text{H})(\text{OD})^+ + \text{CH}_4$			100	$f_{\text{spec}} = 60\%$
$\text{Ni}(\text{H})(\text{OH})^+ + \text{CD}_4$		69 (72)	31 (28)	$f_{\text{scr}} = 40\%$
$\text{Ni}(\text{D})(\text{OH})^+ + \text{CH}_4$	35 (37)	65 (63)		$\text{KIE}_{\text{spec}} = 1.99$
$\text{Ni}(\text{H})(\text{OH})^+ + \text{CH}_2\text{D}_2$	52 (51)	43 (45)	5 (4)	$\text{KIE}_{\text{scr}} = 1.09$

<sup>a</sup> Given in % (modeled numbers are given in parenthesis). For details of the modeling, see section 6.1 on page 55.

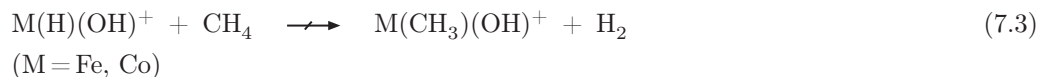
A modeling study [185, 217] of the labeling distributions in the products of these three

<sup>44</sup> In addition to  $\text{Ni}(\text{H})(\text{OH})^+$ , the spectra in Figure 7.4 show also the signals of the reactive nickel-hydrides isotopomers  $\text{NiH}^+$ ,  $\text{Ni}(\text{H})(\text{CO})^+$ , and  $\text{Ni}(\text{H})(\text{H}_2\text{O})^+$ .

reactant couples reveals that direct hydrogen/methyl ligand exchange amounts to 40 %, while 60 % of the H and D atoms undergo scrambling prior to loss of molecular hydrogen. For the former, the kinetic isotope effect is 1.99, and for the latter KIE = 1.09, thus suggesting that cleavage of the nickel-hydrogen and carbon-hydrogen bonds are involved in the rate-limiting step.

DFT calculations supports that the H/CH<sub>3</sub> ligand switch in the reaction of Ni(H)(OH)<sup>+</sup> is energetically feasible in the gas phase according to a  $\sigma$ -bond-metathesis reaction as depicted on the right-hand side of Figure 7.5; the associated transition structure is with 13 kJ mol<sup>-1</sup> below the entrance channel. However, questions remain with respect to the experimentally observed scrambling processes: Once the system passes over TS **54/55**, the reverse reaction is very unlikely in consideration of the fact that the exit channel Ni(CH<sub>3</sub>)(OH)<sup>+</sup>/H<sub>2</sub> is much lower in energy than TS **54/55** such that H<sub>2</sub> is immediately lost once **55** is formed. A transition structure of a degenerate H(1)/H(2) interchange Ni(OH)(H)(H-CH<sub>3</sub>)<sup>+</sup>  $\rightleftharpoons$  Ni(OH)(H)(H-CH<sub>3</sub>)<sup>+</sup> has been located that could explain the scrambling process; however, the transition structure of this equilibration is with 187 kJ mol<sup>-1</sup> much too high in energy and not accessible from the entrance channel under thermal conditions. However, an alternative pathway may exist which can explain the experimental results of the labeling study (Figure 7.5, left-hand side). For the isomerization Ni(H)(OH)(CH<sub>4</sub>)<sup>+</sup>  $\rightarrow$  Ni(H<sub>2</sub>O)(CH<sub>4</sub>)<sup>+</sup> a barrier of 62 kJ mol<sup>-1</sup> has been calculated which is comparable to that reported in the work of Ugalde and co-workers for the unligated system (65 kJ mol<sup>-1</sup>). Since the adduct formation Ni(H)(OH)<sup>+</sup> + CH<sub>4</sub>  $\rightarrow$  Ni(H)(OH)(CH<sub>4</sub>)<sup>+</sup> gains 77 kJ mol<sup>-1</sup> in energy, it allows the rearrangement **54/56** from the Ni<sup>III</sup> complex to the more stable Ni<sup>I</sup> compound by forming an intact water ligand. The energetically most demanding step (6 kJ mol<sup>-1</sup> above separated Ni(H)(OH)<sup>+</sup>/CH<sub>4</sub>) of the subsequent dehydrogenation of  $\sigma$ -bound methane (**56**  $\rightarrow$  **57**  $\rightarrow$  **58**) is the oxidative addition of methane to the nickel center; all other intermediates and transition structures involved in the reaction sequence are below the entrance channel. However, with regard to the uncertainties of the level of theory used and of kinetically excited ions possibly present in the reaction hexapole, it cannot be ruled out that the elimination of D<sub>2</sub> in the reaction of Ni(H)(OH)<sup>+</sup> with CD<sub>4</sub> is originated by the formation of a corresponding carbene complex **58** which subsequently liberates molecular hydrogen.

The thermal activation of methane by both Ni(H)(OH)<sup>+</sup> (Equation 7.3a) and the diatomic cations MH<sup>+</sup> (Equation I.4; M = Fe, Co, Ni) prompted us to extend our studies to the complexes Fe(H)(OH)<sup>+</sup> and Co(H)(OH)<sup>+</sup>. Both these ions can be generated - and distinguished



from their structural isomers M(H<sub>2</sub>O)<sup>+</sup> - under ESI conditions; however, thermal reaction

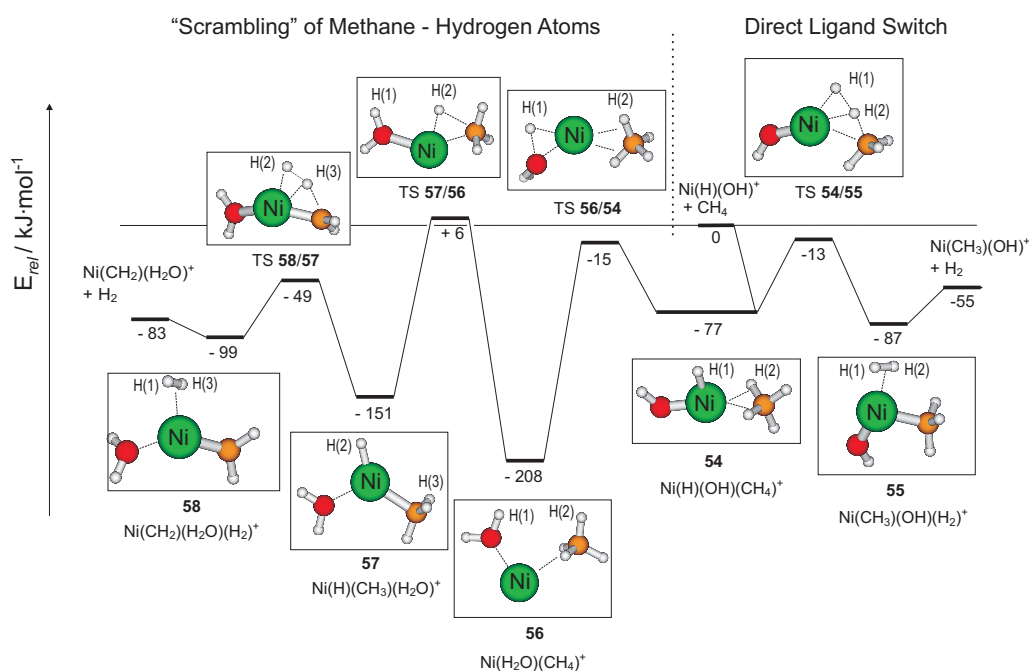


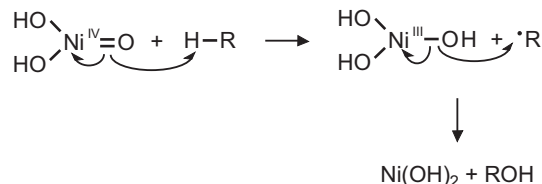
Figure 7.5 – Energy diagram (in  $\text{kJ} \cdot \text{mol}^{-1}$ ) for the reaction of  $\text{Ni(H)(OH)}^+$  and methane. The values are relative to the entrance channel and corrected for zero-point vibrational energies.

with methane according to Equation 7.3 ( $\text{M} = \text{Fe, Co}$ ) does not take place at any measurable rate. B3LYP/TZVP calculations predict [286–288] the ligand exchange in Equation 7.3 ( $\text{M} = \text{Fe, Co}$ ) to be exothermic, and, thus, a kinetic barrier could be the reason that this process is not observed for the iron and cobalt systems.

### 7.3 Activation of molecular oxygen

As outlined in the introduction, activation of dioxygen for the selective oxidation of hydrocarbons is of special interest. In a simple gas-phase model, the coupled activation of molecular oxygen and C–H and C–C bond has been investigated in the reaction of the first-row transition-metal complexes  $\text{M(C}_2\text{H}_4\text{)}^+$  with  $\text{O}_2$  in which the iron complex is found to react very efficiently [289]. Iron-centered enzymes are essential in numerous redox processes involving C–H and C–C bond activations [290–292]. In homogeneous catalysis, palladium-catalyzed aerobic oxidations continue to emerge as versatile methods for selective oxidations of organic molecules involving either of the two mechanistic possibilities described in the introduction (Scheme I.3 on page 7), *i. e.* direct insertion of  $\text{O}_2$  into a Pd–H bond or reductive

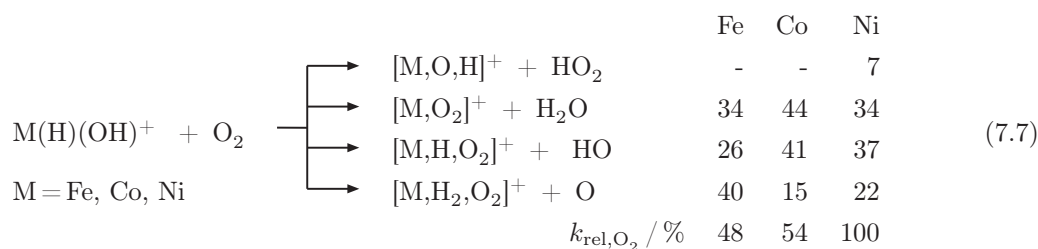
elimination of HX followed by O<sub>2</sub> and HX uptakes. With respect to nickel-based catalysts for oxidation, a catalytic system is known [293, 294] which is prepared by treating a nickel salt with NaOCl and which is used both as a catalyst for oxidation of organic compounds in water as well as an active phase in various oxide catalysts. The composition of this high valent catalyst has been assigned to Ni(O)(OH)<sub>2</sub> and the oxidation mechanism suggested in reference [294] is depicted in Scheme 7.1.



Scheme 7.1

In the following, the thermal ion-molecule reactions of  $\text{O}_2$  with three basic systems, *i. e.* the transition-metal(III) hydride complexes  $\text{M}(\text{H})(\text{OH})^+$ , diatomic metal hydrides  $\text{MH}^+$ , and their mono-hydrated analogues  $\text{M}(\text{H})(\text{H}_2\text{O})^+$  ( $\text{M} = \text{Fe}, \text{Co}, \text{Ni}$ ), are described. Details about the insertion of molecular oxygen in the hydride bonds, the oxygen-bond activation, and the unimolecular dissociation of the metal-hydroperoxide intermediates are discussed. The relative rates provided in the following sections (given in % throughout) are related to  $k_{\text{rel}, \text{O}_2} = 100\%$  for the reaction of  $\text{Ni}(\text{H})(\text{OH})^+$  with  $\text{O}_2$ , the fastest reaction observed in this study for the activation of molecular oxygen.<sup>45</sup>

**The M(H)(OH)<sup>+</sup>/O<sub>2</sub> couples** The reactions of Ni(H)(OH)<sup>+</sup> with molecular oxygen are given in Equation 7.7 (M = Ni).

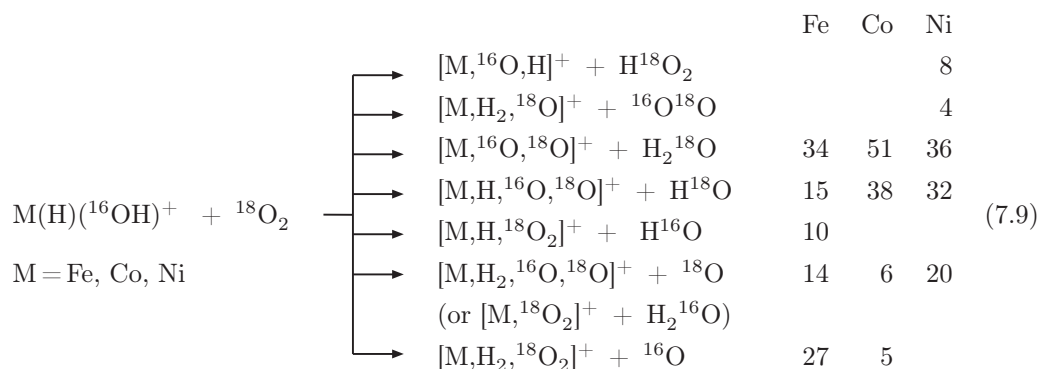
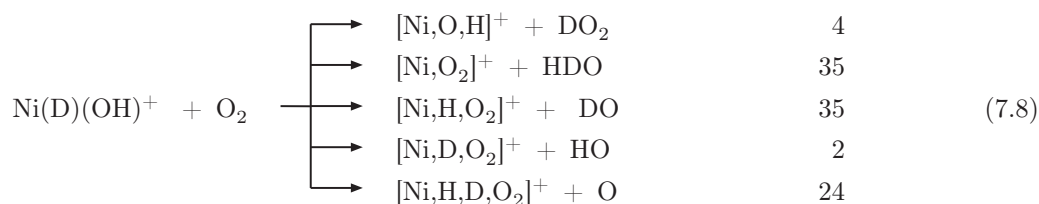


While the actual structures of the ionic products generated remain by and large unknown in these types of mass-spectrometric experiments, details of the course of the reactions can be extracted from appropriate labeling experiments (Equations 7.8 and 7.9). Furthermore, the

<sup>45</sup> The relative rate of the reaction of Ni(H)(OH)<sup>+</sup> with O<sub>2</sub> compared to the NiBr<sup>+</sup>/C<sub>3</sub>H<sub>8</sub> couple amounts to 5.8 %.

PES of the  $[\text{Ni}, \text{H}_2, \text{O}_3]^+$  manifold has been studied by Zhang in our group using the B3LYP level of theory, and the results are included in the following. The energies of the intermediates and transition structures associated with the reaction pathways of Equation 7.7 ( $M = \text{Ni}$ ) are in line with the experimental results. Altogether, a quite complex reaction scheme forms the basis of these reactions. In the following, each process is discussed and the predictions obtained by theory are compared with the experimental findings. The indicated energies in the Schemes are given in  $\text{kJ mol}^{-1}$ , related to separated  $\text{O}_2$  and quartet  $\text{Ni}(\text{H})(\text{OH})^+$  (**52**), and belong to the quartet state; the values for the doublet states are given in parenthesis.

The combination of quartet **52** with triplet oxygen gives doublet, quartet, and sextet adducts  $\text{Ni}(\text{H})(\text{OH})(\text{O}_2)^+$  (**59** and **61**).<sup>46</sup> The latter spin state has been found to be much higher in energy compared to the doublet and quartet states and has not further been taken into account in the calculations.

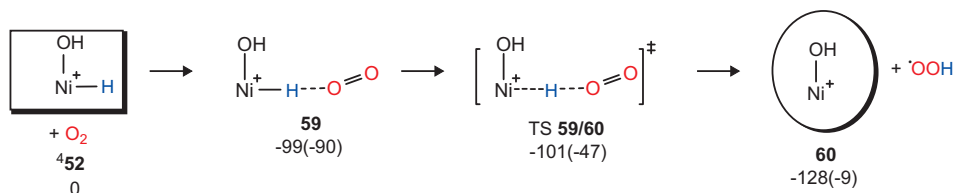


Two different binding modes have been assigned by theory:  $\text{O}_2$  can coordinate to the hydride ligand (**59**, Scheme 7.2)<sup>47</sup> or bind to the nickel center (**61**, Scheme 7.3). In the experiments, the labeling data reveals a selectivity in the formation of  $\text{HO}_2$  in that the OH

<sup>46</sup> The possible spin coupling of two separated fragments is the result of a vector model [295] using a multireference approach, see also the formation of  $\text{Cr}(\text{O}_2)^+$  from  $\text{Cr}^+$  and  $\text{O}_2$  [112].

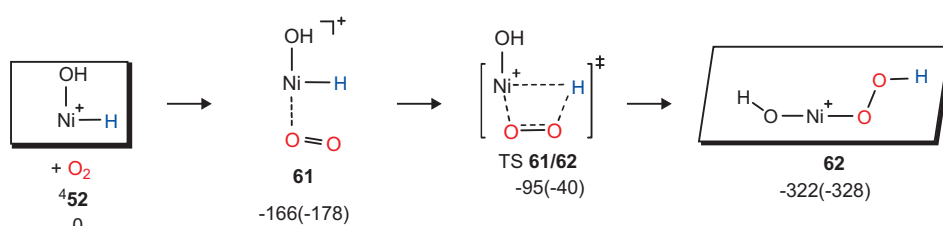
<sup>47</sup> In Schemes 7.2 - 7.6, the reactant ion  $\text{Ni}(\text{H})(\text{OH})^+$  (**52**) has been marked by rectangles, the intermediate  $\text{Ni}(\text{OH})(\text{OOH})^+$  (**62**) which proved to be crucial in most of the reaction channels is indicated by inclined rectangles, and the product ions observed in the experiment are labeled by circles. As mentioned before, the energy values are given in  $\text{kJ mol}^{-1}$  and belong to the quartet state, the values for the doublet states are given in parenthesis.

group of  $\text{Ni}(\text{H})(\text{OH})^+$  is not involved at all (Equation 7.8). Most likely, hydrogen abstraction is responsible for this reaction channel which is favored on the quartet state but also viable on the doublet surface (Scheme 7.2).



Scheme 7.2

While  $\text{HO}_2$  could be formed by direct hydrogen abstraction, the other product channels require the initial activation of the Ni–H bond giving rise to a hydroperoxide intermediate (Scheme 7.3). Its formation has been calculated to be very exothermic ( $-322 \text{ kJ mol}^{-1}$  and  $-328 \text{ kJ mol}^{-1}$  on the quartet and doublet surfaces, respectively) and the transition structure TS **61/62** for the insertion of  $\text{O}_2$  into the Ni–H bond to form  $\text{Ni}(\text{OH})(\text{OOH})^+$  (**62**) is energetically well below the entrance channel for both spin states considered ( $-95 \text{ kJ mol}^{-1}$  and  $-40 \text{ kJ mol}^{-1}$  on the quartet and doublet surfaces, respectively).

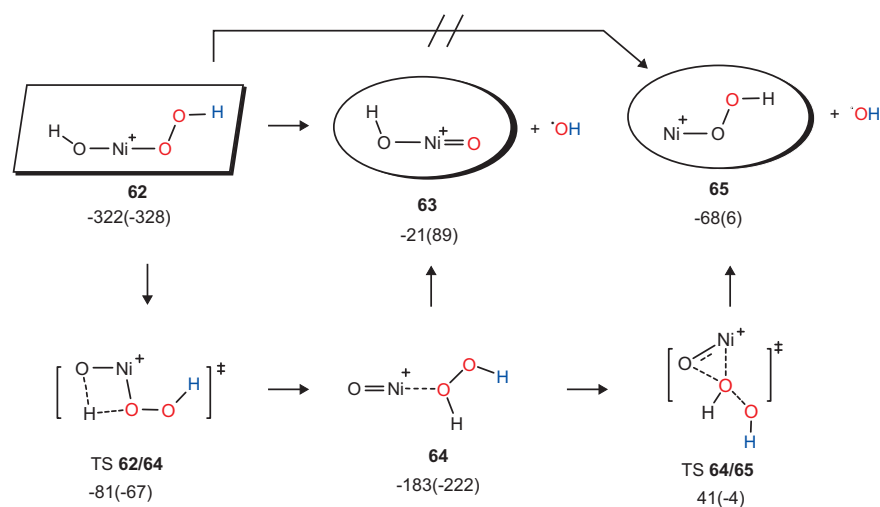


Scheme 7.3

The liberation of the  $\cdot\text{OH}$  radical is similarly specific as hydrogen abstraction: It contains the hydride atom and its oxygen originates from  $\text{O}_2$ ; obviously, the OH ligand of the nickel complex remains intact. The direct  $\cdot\text{OH}$  loss from  $\text{Ni}(\text{OH})(\text{OOH})^+$  is accordingly no option, although the formation of triplet **65** and a hydroxy radical has been calculated to be exothermic with  $-68 \text{ kJ mol}^{-1}$ . A O–O bond cleavage of the hydroperoxide ligand to yield  $\text{Ni}(\text{O})(\text{OH})^+$  (**63**) and a hydroxide radical is in line with the experimental results; this fragmentation has been determined to be exothermic with  $-21 \text{ kJ mol}^{-1}$  on the quartet surface forming triplet **63** (Scheme 7.4). Alternative routes to  $\text{Ni}(\text{OOH})^+$  as well as to  $\text{Ni}(\text{O})(\text{OH})^+$  are given by the energetically accessible formation of the intermediate  $\text{Ni}(\text{O})(\text{HOOH})^+$  (**64**) by H-transfer from the hydroxy ligand to OOH in  $\text{Ni}(\text{OH})(\text{OOH})^+$  (**62**  $\rightarrow$  TS **62/64**  $\rightarrow$  **64**, Scheme 7.4). The formation of **64** is very exothermic; the energies relative to the entrance



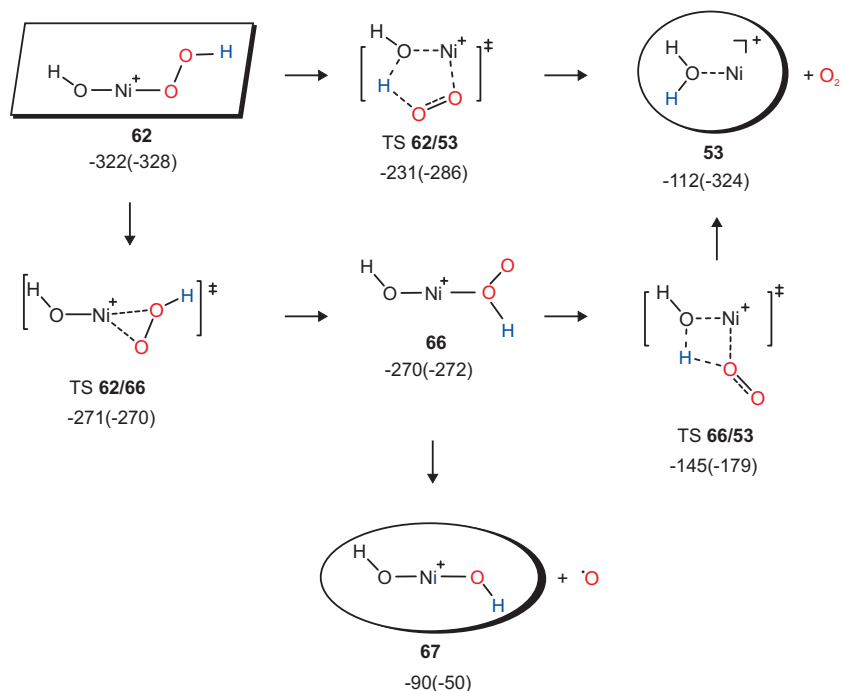
channel are  $-183 \text{ kJ mol}^{-1}$  in the quartet and  $-222 \text{ kJ mol}^{-1}$  in the doublet state, respectively. From here, two subsequent routes are in line with the experiments: First, the direct expulsion of a hydroxy radical ( $\mathbf{64} \rightarrow \mathbf{63}/\cdot\text{OH}$ ) to form the complex  $\text{Ni}(\text{O})(\text{OH})^+$  whose formation has already been mentioned to be accessible on the quartet surface. The second possible pathway constitutes the sequence  $\mathbf{64} \rightarrow \text{TS } \mathbf{64}/\mathbf{65} \rightarrow \mathbf{65}/\cdot\text{OH}$  via the attack of the oxo group to the hydrogen-peroxide ligand concomitant with  $\cdot\text{OH}$  loss (Scheme 7.4); this reaction channel is hindered by a kinetic barrier of  $41 \text{ kJ mol}^{-1}$  on the quartet surface but feasible in the doublet state with  ${}^2\text{TS } \mathbf{64}/\mathbf{65}$  being  $-4 \text{ kJ mol}^{-1}$  lower in energy relative to the reactants. The elimination of  $\cdot\text{OH}$  has been observed in previous gas-phase experiments from  $\text{M}^+/\text{H}_2\text{O}_2$  couples [296, 297] and  $\cdot\text{OH}$  formation initiates oxidation and degradation reactions in the well-know Fenton chemistry [298–300].



Scheme 7.4

Furthermore, the labeling data indicate that the oxygen atom eliminated in the ion-molecule reaction stems specifically from molecular oxygen. Thus, O–O bond activation also occurs in the course of this reaction. A favorable pathway is achieved by the isomerization of **62** to **66** from which the distal O atom is expelled to form dihydroxide  $\text{Ni}(\text{OH})(\text{OH})^+$  (**67**, Scheme 7.5). In addition, two routes are shown in Scheme 7.5 in which reactive  $\text{Ni}(\text{H})(\text{OH})^+$  (**52**) isomerizes to the unreactive  $\text{Ni}^{\text{I}}$  complex  $\text{Ni}(\text{H}_2\text{O})^+$  (paths  $\mathbf{62} \rightarrow \mathbf{53}$  and  $\mathbf{62} \rightarrow \mathbf{66} \rightarrow \mathbf{53}$ ); this hidden isomerization can lead to an undervalued relative rate constant.

Finally, a comparison of the branching ratios for  $\text{H}_2\text{O}$  loss in Equations 7.7–7.9 ( $\text{M} = \text{Ni}$ ) indicates that the production of water follows a path in which obviously the oxygen atom is exclusively provided by molecular oxygen. This finding rules out a simple ligand exchange reaction; instead, both hydrogen of **52** have to be transferred to one oxygen atom of  $\text{O}_2$ .



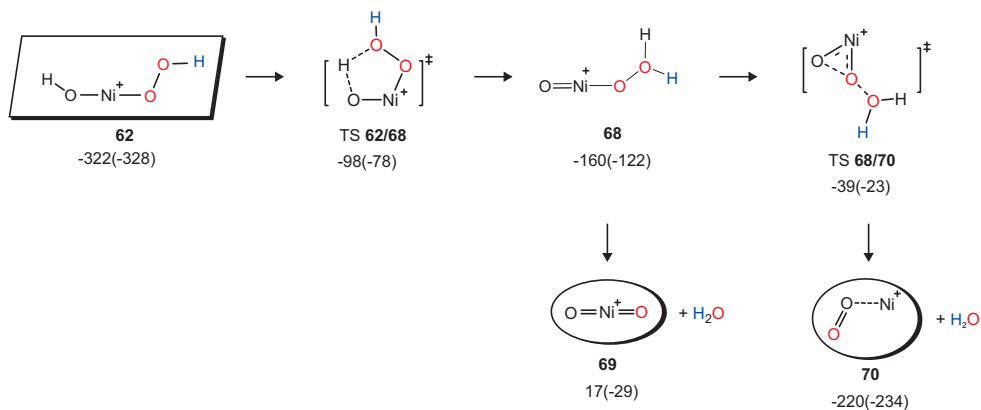
Scheme 7.5

A conceivable pathway which is accessible on the doublet as well as on the quartet surface involves the formation of an oxo/water-oxide complex  $\text{Ni}(\text{O})(\text{OOH}_2)^+$  (**68**, Scheme 7.6)<sup>48</sup> generated by hydrogen migration from the hydroxy group to the terminal oxygen atom of the hydroperoxide ligand of **62** via TS **62/68**. Intermediate **68** can either lose water by direct dissociation forming nickel dioxide  $\text{Ni}(\text{O})_2^+$ ; this fragmentation is with  $-29 \text{ kJ mol}^{-1}$  exothermic on the doublet surface. An alternative pathway exists in which, again, the oxo ligand attacks the nickel bound oxygen of the  $\text{OOH}_2$  ligand in  $\text{Ni}(\text{O})(\text{OOH}_2)^+$  resulting in the formation of  $\text{O}_2$  concomitant with the expulsion of  $\text{H}_2\text{O}$ . This process is possible on both spin surfaces; furthermore, the product ion  $\text{Ni}(\text{O}_2)^+$  (**70**) which can be described as a metal superoxide is  $237 \text{ kJ mol}^{-1}$  ( $205 \text{ kJ mol}^{-1}$ ) more stable compared to the dioxide  $\text{Ni}(\text{O})_2^+$  (**69**).

As depicted in Schemes 7.3-7.6, the experimental and theoretical results clearly indicate that the peroxide derivative **62** acts as central intermediates en route to the dissociations according to Equations 7.7 ( $\text{M} = \text{Ni}$ ). Given the nature of the experiment, *i. e.* single-collision

<sup>48</sup> For experimental and theoretical studies on metal-free water oxide, see [301, 302].

conditions, any chain reactions or reductive elimination of  $\text{H}_2\text{O}$  from the Ni center preceding the O–O bond activation, according to path (II) in Scheme I.3, can be excluded as conceivable mechanistic variants.

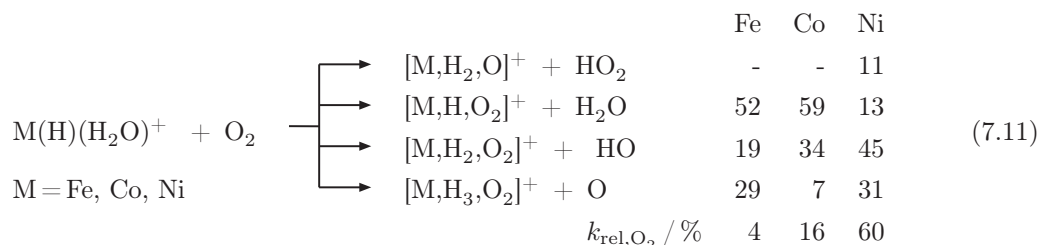
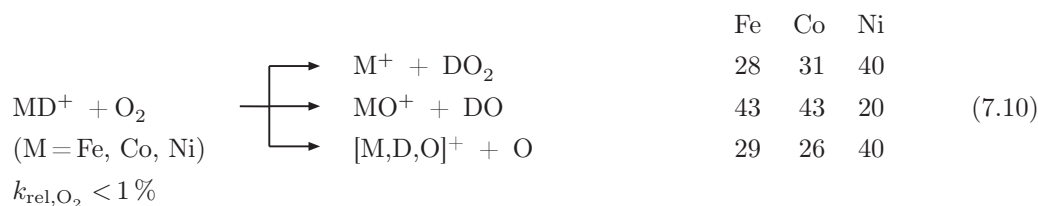


Scheme 7.6

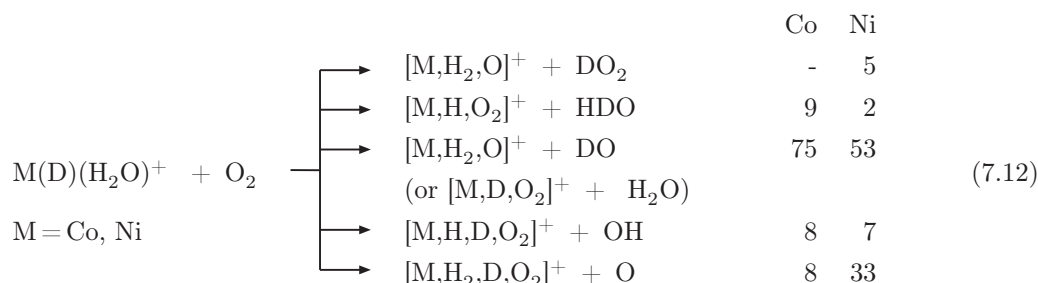
In the reactions of  $\text{O}_2$  with the metal(III)-hydride complexes  $\text{M}(\text{H})(\text{OH})^+$ ,  $\text{M} = \text{Fe}$  and  $\text{Co}$ , Equation 7.7, except for the formation of  $\text{HO}_2$  all other processes reported for  $\text{Ni}(\text{H})(\text{OH})^+/\text{O}_2$  reactants. Although the experiments of  $\text{M}(\text{H})(^{16}\text{OH})^+$  with  $^{18}\text{O}_2$  (Equation 7.9) demonstrate that activation of the O–O bond occurs, as indicated by the formations of  $\text{H}_2^{18}\text{O}$  and  $\text{H}^{18}\text{O}$ , respectively, the competitive productions of  $^{16}\text{O}$  and  $^{18}\text{O}$  from the iron and cobalt couples indicate a more complex reaction scenario. Further, the expulsion of  $\text{H}^{16}\text{O}$  from  $\text{Fe}(\text{H})(^{16}\text{OH})^+/\text{O}_2$  points to a ligand replacement of the hydroxyl group in competition with a combined insertion of  $\text{O}_2$  in the Fe–H and activation of the O–O bond in analogy to Schemes 7.3 and 7.4.

**The  $\text{MH}^+/\text{O}_2$  and  $\text{M}(\text{H})(\text{H}_2\text{O})^+/\text{O}_2$  systems** The diatomic  $\text{M}^{\text{II}}$  hydrides  $\text{MH}^+$  bring about only sluggish ion-molecule reactions with dioxygen, with  $k_{\text{rel},\text{O}_2} < 1\%$ . Two of the products formed in Equation 7.10 demonstrate O–O bond activation, most likely proceeding through an insertion of  $\text{O}_2$  in the metal-deuterium bond.

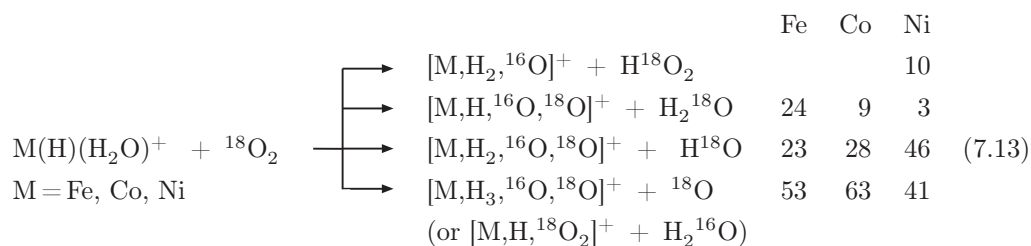
The conclusion, however, that transition-metal hydrides carrying a formal oxidation state +2 are, in general, of low reactivity towards molecular oxygen is not warranted. For example, in the thermal reactions of  $\text{O}_2$  with the solvated  $\text{M}^{\text{II}}$ -hydride complexes  $\text{M}(\text{H})(\text{H}_2\text{O})^+$  ( $\text{M} = \text{Fe}, \text{Co}, \text{Ni}$ ), O–O bond activation accounts for  $>90\%$  of the total reaction, and insertion of  $\text{O}_2$  in the M–H bond is operative (Equation 7.11). However, with respect to the



efficiencies of the reactions, there is quite some variation with 60 % for the nickel, 16 % for the cobalt, and only 4 % for the iron complex of  $M(H)(H_2O)^+$ , respectively. Compared to the  $NiBr^+/C_3H_8$  couple, the efficiencies are quite low (3.1 % for the  $Ni(H)(H_2O)^+/O_2$  system and below 1 % for the  $Fe(H)(H_2O)^+/O_2$  and  $Co(H)(H_2O)^+/O_2$  couples). However, it should be noted that gas-phase reactions with small reactants are in general associated with lower efficiencies compared to reactants with a larger number of atoms. For the latter, increased possibilities to distribute the energy gained by adduct formation over the available degrees of freedom causes an enhanced life-time of the encounter complex and a thus smaller rate for back dissociation.



Labeling experiments were conducted for a few selected systems (Equations 7.12 and 7.13). While some atom scrambling for the  $Ni(H_2O)^+/O_2$  couple is observed, the majority of the processes are highly specific. This holds true also for the productions of HO and atomic oxygen from the iron and cobalt complexes, as indicated by the specific formations of  $H^{18}O$  and  $^{18}O$  in the reactions of the metal hydrides with  $^{18}O_2$  and the absence of signals due to the losses of  $H^{16}O$  and  $^{16}O$  (Equation 7.13). However, for the Fe and Co complexes



some remarkable differences exist. For example, although the water loss channel cannot be analyzed quantitatively due to an overlap of the isobaric  $H_2^{16}O/^{18}O$  and  $H_2O/DO$  molecules, respectively, a comparison of the data given in Equations 7.11-7.13 suggests that for these two systems much of the water eliminated results from displacement of the already present water ligand by the incoming  $O_2$  molecule.

Finally, in view of the formal relationship of the group 10 metal-hydride complexes (see section 6.1.2), the generation of  $Pd(H)(OH)^+$  and  $Pt(H)(OH)^+$  by ESI has also been tried.



However, while all attempts failed to generate these isomers, the production of diatomic  $PdH^+$  and  $PtH^+$  was successful and the reactions with  $O_2$  have been examined (Equation 7.14). In a moderately efficient process ( $k_{rel, O_2} = 8\%$ ),  $PdH^+$  brings about H atom abstraction;  $PtH^+$  does not react with  $O_2$  under thermal conditions.



## 8 Conclusions and outlook

This Thesis reports some selected examples from the manifold of charged nickel species that are accessible in the gas phase. A combination of mass spectrometry together with isotopic labeling and quantum-chemical calculations is employed to unravel mechanistic details of the reactions of nickel-containing cations with small alkanes and molecular oxygen.

It is shown that nickel-containing dimers  $\text{NiM}'^+$  occupy a prominent position in a series of dimeric  $3d$  metal cations. In contrast to the majority of these species, *e.g.*  $\text{V}_2^+$ ,  $\text{Fe}_2^+$ ,  $\text{Co}_2^+$ ,  $\text{FeCo}^+$ , or  $\text{FeCu}^+$ , which display a much lower reactivity compared to the respective atomic  $\text{M}^+$ , the combination of two metal atoms in  $\text{NiM}^+$  leads to an enhancement in reactivity such that  $\text{Ni}_2^+$ ,  $\text{NiCu}^+$ , and  $\text{NiAl}^+$  are capable of ethane activation. Further, labeling studies reveal differences in the mechanistic details for the  $3d$  metal dimers  $\text{Ni}_2^+$  and  $\text{NiCu}^+$  compared to  $\text{NiAl}^+$ , where the latter is a combination of nickel with the main group metal aluminium: Dehydrogenation of ethane by  $\text{NiAl}^+$  proceeds via a specific 1.2 elimination whereas complete equilibrations of the H atoms take place in the reactions of  $\text{Ni}_2^+$  and  $\text{NiCu}^+$ , respectively. In general, cationic transition-metal dimers are more inclined to specifically activate C–H bonds. However, experiments with labeled cyclohexane indicate that the activation of C–C bond is also involved in the course of dehydrogenation.

With respect to the role of formal oxidation states of mononuclear nickel complexes, the different reactivities of  $\text{Ni}^{\text{I}}$  complexes  $\text{NiL}^+$  ( $\text{L}$  = neutral, closed-shell ligands  $\text{H}_2\text{O}$  or  $\text{CO}$ ) compared to  $\text{Ni}^{\text{II}}$  complexes  $\text{NiX}^+$  ( $\text{X}$  = open-shell ligands) are clearly evident in the inertness of  $\text{Ni}(\text{CO})^+$  and  $\text{Ni}(\text{H}_2\text{O})^+$  on the one hand and the thermal activation, even of methane, by  $\text{NiH}^+$  and  $\text{NiF}^+$ . In the latter reaction, the formation of a high-valent insertion complex  $\text{Ni}(\text{X})(\text{CH}_3)(\text{H})^+$  is circumvented by a ligand switch according to a  $\sigma$ -complex-assisted metathesis ( $\sigma$ -CAM) reaction in which the nickel center remains in the oxidation state +2. In general, the  $\sigma$ -CAM-associated transition structures are favored in the low-spin singlet states, whereas all  $\text{NiX}^+$  complexes investigated in this Thesis possess high-spin triplet ground states; thus, crossings between these potential-energy surfaces according to a two-state reactivity scenario (Figure 6.1) enable the thermal activation of methane by  $\text{NiH}^+$ . Thus, while the thermal reactions of  $\text{MH}^+$  ( $\text{M} = \text{Ni}, \text{Pd}, \text{Pt}$ ) [63–65, 218, 303] with methane have many features in common, fundamental differences exist with regard to the details of the potential-energy surfaces and thus to the actual reaction mechanisms: The activation of methane in case of the  $\text{PdH}^+/\text{CH}_4$  couple can be fully explained without invoking a multistate pattern. As the excited states of  $\text{PdH}^+$  ( $^3\Delta$  and  $^3\Phi$ ) are  $>320 \text{ kJ mol}^{-1}$  higher

in energy than the  $^1\Sigma^+$  ground state, they are too high in energy to contribute to a TSR scenario; instead, the whole reaction proceeds on the singlet potential-energy surface in a spin-conserving manner. Finally, for the  $\text{PtH}^+/\text{CH}_4$  system, one encounters yet another electronic situation. Here, the  $^1\Sigma^+$  and  $^3\Delta$  states are practically isoenergetic [66, 68, 247] and spin-orbit coupling for heavy elements is generally rather efficient [48, 72, 304]; accordingly, a multitude of both single- and multistate routes are accessible in the course of the platinum-mediated  $\text{H}/\text{CH}_3$  ligand exchange. Obviously, for the three formally related group 10 metal-hydride cations in their thermal reaction with methane and with regard to the mechanistic details it seems appropriate to use the phrase *The Same and Not the Same* coined by Hoffmann in a different context [305].

As exemplified in the comparison of  $\text{NiH}^+$  and  $\text{NiF}^+$ , not only the metal but also the ligand can change the mechanistic details. Thermal activation of methane under the formation of the methyl complex  $\text{Ni}(\text{CH}_3)^+$  is observed for both  $\text{NiH}^+$  and  $\text{NiF}^+$  in the gas phase; however, subtle mechanistic differences are also encountered here. In contrast to  $\text{NiH}^+$ , a two state reactivity scenario is not involved in the reaction of  $\text{NiF}^+$  with  $\text{CH}_4$ . Opposite to  $\text{PdH}^+$ , however, it is the high spin state of  $\text{NiF}^+$  that accounts for bond activation. The  $\sigma$ -CAM TS which is usually more stable in the singlet state, is for the  $\text{NiF}^+/\text{CH}_4$  system with  $42\text{ kJ mol}^{-1}$  favored in the triplet state and, moreover, below the entrance channel of separated  $\text{NiF}^+/\text{CH}_4$ . For the  $\text{Ni}(\text{OH})^+/\text{CH}_4$  system, for which no reaction is observed experimentally, B3LYP calculations reveal a similar pattern with the  $\sigma$ -CAM  $^3\text{TS}$  being still  $25\text{ kJ mol}^{-1}$  lower in energy compared to  $\sigma$ -CAM  $^1\text{TS}$ . The picture is reversed again for reaction of  $\text{Ni}(\text{OH})^+$  with the higher homolog ethane with the corresponding singlet  $\sigma$ -CAM TS being lower in energy. As for the  $\text{NiX}^+/\text{CH}_4$  systems ( $\text{X} = \text{F}, \text{OH}$ ), a comparison of the  $\text{NiX}^+/\text{ethane}$  couples ( $\text{X} = \text{OH}, \text{Cl}, \text{Br}$ ) revealed that the energy splittings of the  $\sigma$ -CAM transition structures correlate to the Pauling electronegativities of O, Cl, and Br (3.5, 3.0, and 2.8, respectively): The singlet  $\sigma$ -CAM TS is  $17\text{ kJ mol}^{-1}$ ,  $36\text{ kJ mol}^{-1}$ , and  $42\text{ kJ mol}^{-1}$  more stable compared to the triplet state (for OH, Cl, and Br, respectively).

The gas-phase ion-molecule reactions of electrospray-ionization generated  $\text{NiX}^+$  cations ( $\text{X} = \text{F}, \text{Cl}, \text{Br}$ , and I) with a set of small alkanes  $\text{RH}$  ( $\text{R} = \text{H}, \text{C}_2\text{H}_5, \text{C}_3\text{H}_7, n\text{-C}_4\text{H}_9$ ) exhibit a superficially complex product spectrum. However, a qualitative analysis permits a few general trends to be extracted from the rich data basis. All reactions fall into two major categories, that is, metal-mediated bond activation which gives rise to the liberation of closed-shell neutral molecules (such as  $\text{HX}$ ,  $\text{H}_2$ ,  $\text{CH}_4$ ), and secondly, inner-sphere electron-transfer processes in the course of which the  $\text{NiX}^+$  core is converted to  $\text{RNiX}$  ( $\text{R} = \text{H}, \text{CH}_3$ ) and the alkane to a carbenium ion. Outer-sphere electron transfer resulting in the formation of hydrocarbon cation radicals has not been observed in the systems studied. Although a quantitative analysis is impossible due to the lack of sufficiently reliable thermochemical data, extensive labeling experiments and DFT calculations have helped to uncover several



interesting features which shed light on aspects related to the topics of regioselective C–H and C–C bond activation, kinetic isotope effects and H/D scrambling, just to mention a few. Similar, for most of the  $\text{Ni}^{\text{II}}$  complexes  $\text{NiX}^+$  investigated in this Thesis, the ligand X is involved in the reactions with small alkanes as revealed by labeling studies and B3LYP calculations. This is most evident in the complex reaction scheme of  $[\text{Ni,C,H}_3,\text{O}]^+$  with ethane: The results of the labeling studies are only explainable by a large extent of H/D exchange between the ligand and the substrate. Interestingly, scrambling processes are much less involved in the reaction with propane and are completely absent in the reaction with butane.

As demonstrated in this Thesis, a large variety of gas-phase species can be formed by electrospray ionization. For the  $[\text{Ni,H}_2,\text{O}]^+$  system, labeling and reactivity studies revealed that two structural isomers are formed in the gas phase upon variation of the ionization conditions in electrospray. While the distinct properties of highly reactive  $\text{Ni}^{\text{III}}$  complex  $\text{Ni}(\text{H})(\text{OH})^+$  and of the inert  $\text{Ni}(\text{H}_2\text{O})^+$  cation are easily identified by the completely different behavior in ion-molecule reactions, it is more difficult to differentiate between  $\text{Ni}(\text{OCH}_3)^+ / \text{Ni}(\text{H})(\text{CH}_2\text{O})^+ / \text{Ni}(\text{CH}_2\text{OH})^+$  isomers. A detailed analysis of labeling and theoretical studies turned out to be a proper means to shed some light on the structural properties of  $[\text{Ni,C,H}_3,\text{O}]^+$  which are, quite interestingly, in distinct contrast to the related  $[\text{Fe,C,H}_3,\text{O}]^+$  system.

Thermal activation of molecular oxygen via genuine insertion in a metal-hydride bond and dissociation of the resulting metal-hydroperoxide intermediate(s) are in general facile gas-phase processes for the late transition-metal cation complexes  $\text{M}(\text{H})(\text{OH})^+$ , with  $\text{M} = \text{Fe}, \text{Co}, \text{Ni}$ . In contrast, for the diatomic  $\text{MH}^+$  species, with  $\text{M} = \text{Fe}, \text{Co}, \text{Ni}, \text{Pd}, \text{and Pt}$ , the analogous reactions are rather inefficient, if they occur at all. However, the addition of an “inert”  $\text{H}_2\text{O}$  ligand to a metal(II) hydride, as in  $\text{M}(\text{H})(\text{H}_2\text{O})^+$  ( $\text{M} = \text{Fe}, \text{Co}, \text{Ni}$ ), recovers some of the reactivity.

Nickel is long known for its favorable catalytic activity in industry [207] and the importance of nickel in enzymatic catalysis is more and more recognized [32]. It is therefore of basic interest to uncover the intrinsic features of the catalysts’ active site in these processes. Although gas-phase studies as carried out in the frame of this Thesis can by no means account for the precise mechanisms of catalytic reactions, the trends observed by systematically changing the surroundings of the nickel center in the cationic complexes investigated provide a conceptual framework and allow insight into reactivity patterns. Furthermore, not only variations in terms of the oxidation state ( $\text{Ni}^{\text{I}}$ ,  $\text{Ni}^{\text{II}}$ , or  $\text{Ni}^{\text{III}}$ ), the nature of the ligands (closed-shell, open-shell, H-, C-, O-, or halide ligands), or the substrates (methane, higher alkanes, or molecular oxygen), but also the systematic comparison to related transition-metal complexes like the congeners iron and cobalt or the group 10 metal palladium and platinum are helpful in understanding the correlation between reactivity and the electronic

characteristics and structural properties. Possible extensions of this work might address the questions remaining in some of the respective topics. For example, computational studies are indicated to uncover the electronic structure origin(s) of the contrasting behavior of *e. g.*  $\text{Ni}_2^+$  and  $\text{FeNi}^+$  compared to  $\text{Fe}_2^+$ . Similarly, for the rather remarkable ion-molecule oxidation processes in the reaction of the transition-metal hydrides with  $\text{O}_2$ , high-level calculations are desirable which can also account for the crucial role of spin changes [69, 306] and which might be able to address the relationship of the gas-phase experiments to analogous reactions in the condensed phase [86–90, 92–97]. Further, comparative gas-phase studies on the ligand effects in nickel-mediated C–C bond coupling and (co)polymerization reactions via CO or  $\text{C}_2\text{H}_4$  insertion into Ni–H or Ni–C bonds are of interest. Olefin-polymerization catalysts are often based on nickel and palladium  $\alpha$ -diimine complexes [209, 307] or nickel compounds with P/O chelating ligands [308]; thus, it would be also intriguing to examine the differences and similarities of the metals in these important transformations. Beside these industrially relevant processes, gas-phase models of the active sites of nickel enzymes [31, 32] constitute a challenging target, *e. g.* dinuclear ureases with N/O coordinated nickel, sulfur-ligated enzymes like acetyl-CoA synthases and superoxide dismutases, as well as methyl-coenzyme M reductase (MCR) which catalyzes the key step in converting  $\text{CO}_2$  to methane. The active site of the latter enzyme contains the nickel porphinoid  $\text{F}_{430}$ . Recently, a formal  $\text{Ni}^{\text{III}}$   $\text{F}_{430}$ -hydride complex has been suggested to play a key role in the “reverse methanogenesis”, *i. e.* the anaerobic oxidation of methane catalyzed by enzymes closely resembling MCR [309]. Mass spectrometry cannot contribute only to the solutions of problems in homogeneous catalysis [47], but can also address questions in bio-catalysis by adequate, yet simple gas-phase models *e. g.* for carbonic anhydrase [310]. Further, mechanistic studies by means of mass spectrometry helped to develop the concept of TSR [56, 69–72, 311, 312] which accounts also for catalytic reactions of the oxidoreductase Cytochrome P450 [313–315].

## Appendix



## A.1 Reactions of nickel dimers $\text{NiM}^{'+}$ with background oxygen

The reaction channels in the reactions of  $\text{NiM}^+$  with ethane, propane, butane (Table 4.5 on page 47), and cyclohexane (Table 4.1 on page 40 and Table 4.2 on page 41) are confined to dehydrogenation. In some cases, however,  $\text{Ni}^+$  is formed which has also been observed in reactions with linear nitriles [184] and  $\text{N}_2\text{O}$  [316]. The formation of  $\text{Ni}^+$  can be rationalized by a reaction with residual traces of oxygen present in the high vacuum system, reaction A.1. The exothermicity of this process has been demonstrated previously [317]; furthermore, the extent of  $\text{Ni}^+$  production varies largely from day to day, supporting the origin of  $\text{Ni}^+$  according to reaction A.1. Thus, the formation of  $\text{Ni}^+$  from electronically excited  $\text{Ni}_2^+$  as suggested before [316] is expected to be irrelevant in this study.



## A.2 Determination of branching ratios

The branching ratios of the reactions with  $c\text{-C}_6\text{H}_6\text{D}_6$  are given by the respective intensities of the signals in the broad-band spectra. Due to consecutive reactions, they depend upon the reaction time  $t$  and are extrapolated to  $t=0$  (see for example Figure A.1, the linear extrapolations result in 50 %  $3\text{H}_2$ , 28 %  $3\text{D}_3$ , 3 %  $2\text{H}_3$ , and 19 %  $2\text{D}_3$  elimination). This

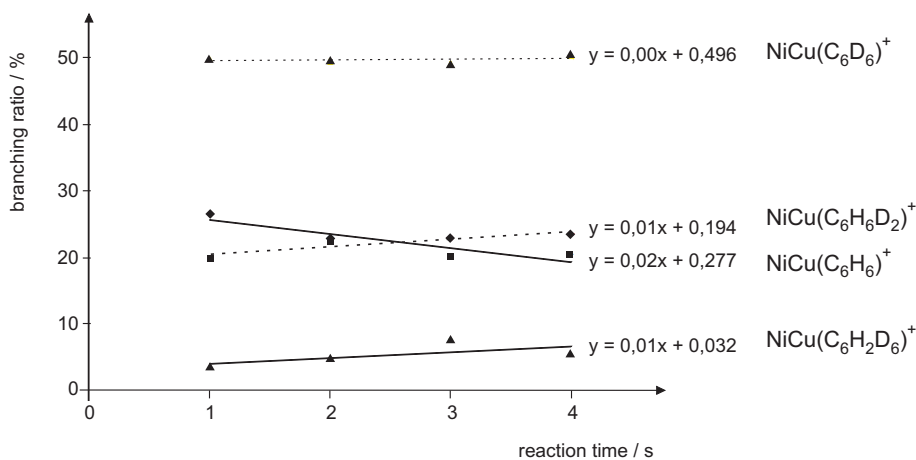


Figure A.1 – Extrapolation of the branching ratios to  $t=0$  for the elimination of  $3\text{H}_2$ ,  $2\text{H}_2$ ,  $3\text{D}_2$ , and  $2\text{D}_2$  by  $\text{NiCu}^+$ .

is sensible, provided that isobaric interferences of  $2\text{H}_2$  vs  $\text{D}_2$  elimination can be excluded. However, if more than one reaction channel from Equation 4.1 is observed for the  $\text{MM}^{'+}$

cations *and* if dehydrogenation proceeds from both side of the carbon ring which is indicated in coupled expulsions of hydrogen and deuterium atoms, the results are ambiguous. This is true for  $\text{NiMn}^+$ ,  $\text{Ni}_2^+$ ,  $\text{NiTi}^+$ , and  $\text{Ti}_2^+$ ; double dehydrogenation concomitant to triple dehydrogenation is observed and isobaric interference, *e. g.* loss of  $3\text{H}_2$  *vs*  $[\text{H}_2, \text{D}_2]$  elimination, complicate the determination of the H/D ratio of the respective dehydrogenation channel. Notwithstanding, a separation of these two reaction channels is possible due to the high

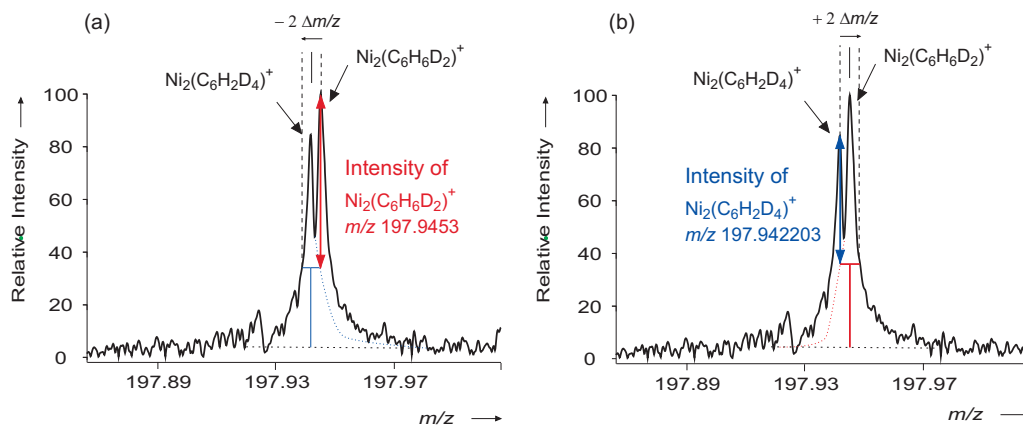


Figure A.2 – High resolution spectrum at the  $m/z$  region of both  $\text{Ni}(\text{C}_6\text{H}_6\text{D}_2)^+$  and  $\text{Ni}(\text{C}_6\text{H}_2\text{D}_4)^+$ . (a) Determination of the intensity for  $\text{Ni}(\text{C}_6\text{H}_6\text{D}_2)^+$ , red double-headed arrow. (b) Determination of the intensity for  $\text{Ni}(\text{C}_6\text{H}_2\text{D}_4)^+$ , blue double-headed arrow.

resolving power of the ICR instrument as exemplified in Figure A.2. Here, the signal for  $[\text{H}_4, \text{D}_2]$  loss as well as the elimination of  $2\text{D}_2$  are clearly distinguishable but partly overlapped. In this case, the intensities are diminished by the relative peak height of the other signal, respectively (Figure A.2). If there is only one signal displayed in the spectra, *e. g.* the loss of  $3\text{H}_2$  from [*all-cis*-1,2,3,4,5,6- $\text{D}_6$ ]-cyclohexane by  $\text{Ni}_2^+$  (Figure A.3), the elimination of  $[\text{H}_2, \text{D}_2]$  might be superimposed by the former signal. Thus, the signal intensity at the position of the expected  $m/z$  value has been taken as upper limit for  $[\text{H}_2, \text{D}_2]$  loss (Figure A.3). Also for  $\text{NiCo}^+$ ,  $\text{NiCu}^+$ , and  $\text{CuCo}^+$ , double and triple dehydrogenation is observed, but here bond activation takes place face-selectively from one side of the carbon ring. This conclusion is justified because although  $[\text{H}_4, \text{D}_2]$  might be superimposed by  $2\text{D}_2$  losses, the associated BR is assumed to be zero because the elimination of  $\text{H}_2\text{D}_4$  is neither observed (Table 4.3). Thus, the intensities in these cases are evaluated by broad-band spectra record and extrapolation to  $t = 0$ , as exemplified in Figure A.1, and no upper limit is given for the loss of  $[\text{H}_4, \text{D}_2]$ .

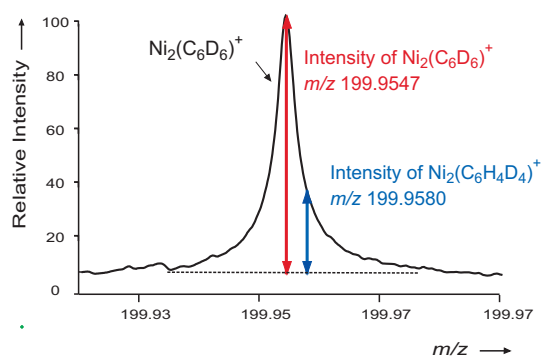


Figure A.3 – High resolution spectrum at the  $m/z$  region of  $\text{Ni}(\text{C}_6\text{D}_6)^+$  and  $\text{Ni}(\text{C}_6\text{H}_4\text{D}_4)^+$ .

### A.3 Solutions used for ESI

All the mononuclear metal complexes investigated by ESI in the frame of this Thesis were formed from millimolar solutions of the respective halides in different solvents. In the experiments with the nickel complexes, the ions containing the most abundant  $^{58}\text{Ni}$  isotope have been isolated by the first quadrupole of the VG BioQ for investigations. In most of the cases, the reactions have also been conducted with the complexes of the less abundant  $^{60}\text{Ni}$  isotope. The solvents employed for ESI to generate the respective ions for reactivity studies are listed in the following:

1.  $\text{NiH}^+$  and  $\text{NiX}^+$  ( $\text{X} = \text{F}, \text{Br}, \text{I}$ ):  $\text{NiX}_2$  ( $\text{X} = \text{F}, \text{Br}, \text{I}$ ) in methanol.
2.  $\text{NiF}^+$ :  $\text{NiF}_2$  in  $\text{CD}_3\text{OD}$  to avoid isobaric overlap with  $^{60}\text{Ni}(\text{OH})^+$ .
3.  $\text{NiCl}^+$ :  $\text{NiCl}_2$  in water to avoid isobaric overlap with isobaric  $^{60}\text{Ni}(\text{H})(\text{CH}_3\text{OH})^+$ .
4.  $\text{MD}^+$  ( $\text{M} = \text{Fe}, \text{Co}, \text{Ni}$ ):  $\text{MI}_2$  in  $\text{CD}_3\text{OH}$ .
5.  $\text{M}(\text{H})(\text{H}_2\text{O})^+$  and  $\text{M}(\text{H})(\text{OH})^+$  ( $\text{M} = \text{Fe}, \text{Co}, \text{Ni}$ ):  $\text{MX}_2$  in a mixed, ca. 1:3 methanol/water solution ( $\text{X} = \text{I}$  for iron and cobalt,  $\text{X} = \text{Cl}, \text{Br}$ , or  $\text{I}$ , for nickel).
6.  $\text{M}(\text{D})(\text{H}_2\text{O})^+$  and  $\text{M}(\text{D})(\text{OH})^+$  ( $\text{M} = \text{Fe}, \text{Co}, \text{Ni}$ ):  $\text{NiX}_2$  in a mixed, ca. 1:3  $\text{CD}_3\text{OH}/\text{H}_2\text{O}$  solution ( $\text{X} = \text{I}$  for iron and cobalt,  $\text{X} = \text{Cl}, \text{Br}$ , or  $\text{I}$ , for nickel).
7.  $\text{M}(\text{H})(\text{D}_2\text{O})^+$  and  $\text{M}(\text{H})(\text{OD})^+$  ( $\text{M} = \text{Fe}, \text{Co}, \text{Ni}$ ):  $\text{NiX}_2$  in a mixed, ca. 1:3  $\text{CH}_3\text{OD}/\text{D}_2\text{O}$  solution ( $\text{X} = \text{I}$  for iron and cobalt,  $\text{X} = \text{Cl}, \text{Br}$ , or  $\text{I}$ , for nickel).
8.  $\text{Ni}(\text{H})(^{13}\text{CO})^+$ :  $\text{NiI}_2$  in a mixed, ca. 1:4  $^{13}\text{CH}_3\text{OH}/\text{H}_2\text{O}$  solution.
9.  $\text{PdH}^+$ :  $\text{PdBr}_2$  in methanol. The ions containing palladium were readily identified by their characteristic isotope pattern. Experiments with  $\text{PdH}^+$  were conducted by

mass selection of the isotopomer involving the most abundant  $^{106}\text{Pd}$  isotope without isobaric interferences by other isotope compositions.

10.  $\text{PdD}^+$ :  $\text{PdBr}_2$  in  $\text{CD}_3\text{OH}$ . To avoid isobaric overlap, for the experiments with  $\text{PdD}^+$  the less abundant isotope  $^{105}\text{Pd}$  was employed.
11.  $\text{PtH}^+$ :  $\text{H}_2\text{PtCl}_6$  in methanol.

#### A.4 Synthesis of [*all-cis*-1,2,3,4,5,6- $\text{D}_6$ ]-cyclohexane

For the synthesis of [*all-cis*-1,2,3,4,5,6- $\text{D}_6$ ]-cyclohexane (**1**), [ $\text{D}_6$ ]benzene (Aldrich, 99.5 % atom % D) has been hydrogenated using ( $\eta^3$ -2-propenyl)tris(trimethyl phosphite)cobalt ( $(\eta^3\text{-C}_3\text{H}_5)\text{Co}\{\text{P}(\text{OCH}_3)_3\}_3$ ) which is known to bring about stereoselective all-cis hydrogenation of arenes [318, 319]. It has been synthesized in the group of Prof. Roesky at the Free University of Berlin in three steps by starting from  $\text{CoCl}_2$  and  $\text{P}(\text{OCH}_3)_3$  and following literature procedures [320, 321]. For the hydrogenation, a 2.5:1 mixture of  $\text{C}_6\text{D}_6$  and catalyst [322] was reacted at room temperature for 5 days under slightly elevated hydrogen-atmosphere pressure ( $p_{\text{H}_2} = 3\text{--}4$  bar). The crude reaction product was purified by vacuum distillation. Finally, the sample of **1**, which still contained a spurious amount of solvent as well as  $\text{C}_6\text{D}_6$ , was purified by preparative gas chromatography (CP-WAX 51,  $90^\circ\text{C}$ ).

A simple and convenient mode to determine the atom % D of **1** is the reaction with  $\text{Ti}^+$  [186]. The exclusive reaction products correspond to  $\text{Ti}(\text{C}_6\text{H}_6)^+$  and  $\text{Ti}(\text{C}_6\text{D}_6)^+$  revealed the face-selective dehydrogenation and is at the same time a measure of the purity of **1**. A quantitative analysis of the peak height of the signal for  $\text{Ti}(\text{C}_6\text{D}_6)^+$  in comparison to the signal of  $\text{Ti}(\text{C}_6\text{HD}_5)^+$  together with the corrections for the  $^{13}\text{C}$  isotopes reveals that **1** contains 99.4 % atom D. Within experimental error this figure corresponds to the isotopomeric purity of [ $\text{D}_6$ ]benzene (99.5 % D) which was used as a precursor for **1**. The same results have been obtained already the reactivity study described in reference [186]; in analogy, it is taken for granted that the isotopomeric purity of [ $\text{D}_6$ ]benzene is completely conserved in the hydrogenation.



## A.5 Relevant bond length of B3LYP-calculated geometries

Table A.1 – Relevant bond lengths (in Å) of the B3LYP-calculated geometries of the species involved in the reaction:  $\text{NiH}^+ + \text{CH}_4 \rightarrow \text{Ni}(\text{CH}_3)^+ + \text{H}_2$  (see Figure 6.1).

		Bond				
		Ni–H(1)	Ni–H(2)	Ni–C	C–H(2)	H(1)–H(2)
$\text{NiH}^+ / (\text{CH}_4)$	$^3\Delta$	1.481			1.090	
	$^1\Sigma^+$	1.415			1.090	
$\text{Ni}(\text{H})(\text{CH}_4)^+$ ( <b>3a</b> )	$^3A$	1.485	1.987	2.307	1.115	2.915
	$^1A$	1.411	1.849	2.101	1.123	2.292
TS <b>3a/4a</b>	$^3A$	1.633	1.575	2.117	1.543	1.042
	$^1A$	1.489	1.513	1.928	1.501	0.998
$\text{Ni}(\text{CH}_3)(\text{H}_2)^+$ ( <b>4a</b> )	$^3A$	1.932	1.936	1.921	3.838	0.769
	$^1A$	1.596	1.596	1.847	2.583	0.823
$\text{Ni}(\text{CH}_3)^+ / \text{H}_2$	$^3A$			1.936		0.744
	$^1A$			1.856		0.744

Table A.2 – Relevant bond lengths (in Å) of the B3LYP-calculated geometries of the species involved in the reaction:  $\text{PdH}^+ + \text{CH}_4 \rightarrow \text{Pd}(\text{CH}_3)^+ + \text{H}_2$  (see Figure 6.3).

	Bond						
	Pd–H(1)	Pd–H(2)	Pd–H(3)	Pd–C	C–H(2)	C–H(3)	H(1)–H(2)
PdH <sup>+</sup> /(CH <sub>4</sub> )	1.477				1.090		
Pd(H)(CH <sub>4</sub> ) <sup>+</sup> ( <b>3b</b> )	1.480	1.946	2.167	2.342	1.134	1.108	2.305
TS <b>3b/4b</b>	1.592	1.653		2.143	1.550		1.017
Pd(CH <sub>3</sub> )(H <sub>2</sub> ) <sup>+</sup> ( <b>4b</b> )	1.731	1.732		2.015	2.685		0.838
TS <b>3b/5b</b>	1.499	1.531		2.106	1.170		1.840
Pd(H)(CH <sub>3</sub> )(H) <sup>+</sup> ( <b>5b</b> )	1.505	1.505		2.040	2.427		1.794
TS <b>5b/4b</b>	1.527	1.527		2.035	2.474		1.391
Pd(CH <sub>3</sub> ) <sup>+</sup> /H <sub>2</sub>				1.999			0.744

Table A.3 – Relevant bond lengths (in Å) of the B3LYP-calculated geometries of the species involved in the reactions of  $\text{NiCl}^+ + \text{C}_2\text{H}_6$  (see Figure 6.9).

	Bond	Ni–Cl	Ni–C(1)	Ni–C(2)	Ni–H(1)	Ni–H(2)
$\text{NiCl}^+/\text{C}_2\text{H}_6$	$^3\Delta$	2.064				
	$^1\Sigma$	2.032				
$\text{Ni}(\text{Cl})(\text{C}_2\text{H}_6)^+$ ( <b>17a</b> )	$^3\text{A}$	2.050	2.374		1.948	
	$^1\text{A}$	2.044	2.113		1.653	
TS <b>17a/18a</b>	$^3\text{A}$	2.248	2.090		1.821	
	$^1\text{A}$	2.121	1.977		1.614	
$\text{Ni}(\text{C}_2\text{H}_5)(\text{HCl})^+$ ( <b>18a</b> )	$^3\text{A}$	2.414	1.934	2.823		3.055
	$^1\text{A}$	2.223	1.876	2.129		1.660
TS <b>18a/19a</b>	$^3\text{A}$	2.348	2.160	2.175		1.543
	$^1\text{A}$	2.261	2.011	2.124		1.411
$\text{Ni}(\text{H})(\text{C}_2\text{H}_4)(\text{HCl})^+$ ( <b>19a</b> )	$^3\text{A}$	2.414	2.339	2.304		1.514
	$^1\text{A}$	2.294	2.042	2.039		1.405
TS <b>19a/20a</b>	$^3\text{A}$	2.295	2.271	2.288	1.886	1.600
	$^1\text{A}$	2.137	2.130	2.130	1.629	1.528
$\text{Ni}(\text{Cl})(\text{C}_2\text{H}_4)(\text{H}_2)^+$	$^3\text{A}$	2.078	2.256	2.278	1.883	1.894
	$^1\text{A}$	2.063	2.191	2.195	1.604	1.604
$\text{Ni}(\text{Cl})(\text{C}_2\text{H}_4)^+/\text{H}_2$	$^3\text{A}$	2.089	2.261	2.261		
	$^1\text{A}$	2.035	2.041	2.041		
	Bond	Cl–H(1)	C(1)–H(1)	C(2)–H(2)	H(1)–H(2)	
$\text{NiCl}^+/\text{C}_2\text{H}_6$	$^3\Delta$		1.092			
	$^1\Sigma$		1.092			
$\text{Ni}(\text{Cl})(\text{C}_2\text{H}_6)^+$ ( <b>17a</b> )	$^3\text{A}$	3.478	1.125			
	$^1\text{A}$	2.693	1.175			
TS <b>17a/18a</b>	$^3\text{A}$	1.495	1.725			
	$^1\text{A}$	1.656	1.456			
$\text{Ni}(\text{C}_2\text{H}_5)(\text{HCl})^+$ ( <b>18a</b> )	$^3\text{A}$	1.301		1.092		
	$^1\text{A}$	1.304		1.178		
TS <b>18a/19a</b>	$^3\text{A}$	1.301		1.739		
	$^1\text{A}$	1.303		1.910		
$\text{Ni}(\text{H})(\text{C}_2\text{H}_4)(\text{HCl})^+$ ( <b>19a</b> )	$^3\text{A}$	1.010				
	$^1\text{A}$	1.301				
TS <b>19a/20a</b>	$^3\text{A}$	1.450			1.276	
	$^1\text{A}$	1.743			0.932	
$\text{Ni}(\text{Cl})(\text{C}_2\text{H}_4)(\text{H}_2)^+$ ( <b>20a</b> )	$^3\text{A}$	3.010			0.771	
	$^1\text{A}$	2.720			0.820	
$\text{Ni}(\text{Cl})(\text{C}_2\text{H}_4)^+/\text{H}_2$	$^3\text{A}$				0.744	
	$^1\text{A}$				0.744	

Table A.4 – Relevant bond lengths (in Å) of the B3LYP-calculated geometries of the species involved in the reactions of  $\text{NiBr}^+ + \text{C}_2\text{H}_6$  (see Figure 6.10).

	Bond	Ni–Br	Ni–C(1)	Ni–C(2)	Ni–H(1)	Ni–H(2)
$\text{NiBr}^+/\text{C}_2\text{H}_6$	$^3\Delta$	2.204				
	$^1\Sigma$	2.160				
$\text{Ni}(\text{Br})(\text{C}_2\text{H}_6)^+$ ( <b>17b</b> )	$^3\text{A}$	2.197	2.383		1.949	
	$^1\text{A}$	2.172	2.128		1.661	
TS <b>17b/18b</b>	$^3\text{A}$	2.369	2.075		1.794	
	$^1\text{A}$	2.256	1.968		1.611	
$\text{Ni}(\text{C}_2\text{H}_5)(\text{HBr})^+$ ( <b>18b</b> )	$^3\text{A}$	2.503	1.934	2.751		2.617
	$^1\text{A}$	2.330	1.874	2.135		1.671
TS <b>18b/19b</b>	$^3\text{A}$	2.455	2.157	2.176		1.545
	$^1\text{A}$	2.367	2.019	2.132		1.410
$\text{Ni}(\text{H})(\text{C}_2\text{H}_4)(\text{HBr})^+$ ( <b>19b</b> )	$^3\text{A}$	2.551	2.323	2.323		1.522
	$^1\text{A}$	2.403	2.051	2.045		1.405
TS <b>19b/20b</b>	$^3\text{A}$	2.438	2.279	2.289	1.941	1.577
	$^1\text{A}$	2.301	2.110	2.110	1.485	1.661
$\text{Ni}(\text{Br})(\text{C}_2\text{H}_4)(\text{H}_2)^+$ ( <b>20b</b> )	$^3\text{A}$	2.208	2.254	2.280	1.876	1.889
	$^1\text{A}$	2.197	2.192	2.192	1.604	1.603
$\text{Ni}(\text{Br})(\text{C}_2\text{H}_4)^+/\text{H}_2$	$^3\text{A}$	2.193	2.181	2.314		
	$^1\text{A}$	2.172	2.034	2.035		
	Bond	Br–H(1)	C(1)–H(1)	C(2)–H(2)	H(1)–H(2)	
$\text{NiBr}^+/\text{C}_2\text{H}_6$	$^3\Delta$		1.092			
	$^1\Sigma$		1.092			
$\text{Ni}(\text{Br})(\text{C}_2\text{H}_6)^+$ ( <b>17b</b> )	$^3\text{A}$	3.624	1.125			
	$^1\text{A}$	2.953	1.175			
TS <b>17b/18b</b>	$^3\text{A}$	1.626	1.725			
	$^1\text{A}$	1.748	1.456			
$\text{Ni}(\text{C}_2\text{H}_5)(\text{HBr})^+$ ( <b>18b</b> )	$^3\text{A}$	1.435		1.105		
	$^1\text{A}$	1.437		1.175		
TS <b>18b/19b</b>	$^3\text{A}$	1.435		1.749		
	$^1\text{A}$	1.437		1.931		
$\text{Ni}(\text{H})(\text{C}_2\text{H}_4)(\text{HBr})^+$ ( <b>19b</b> )	$^3\text{A}$	1.434				
	$^1\text{A}$	1.435				
TS <b>19b/20b</b>	$^3\text{A}$	1.552			1.402	
	$^1\text{A}$	1.730			1.031	
$\text{Ni}(\text{Br})(\text{C}_2\text{H}_4)(\text{H}_2)^+$ ( <b>20b</b> )	$^3\text{A}$	3.163			0.772	
	$^1\text{A}$	2.858			0.820	
$\text{Ni}(\text{Br})(\text{C}_2\text{H}_4)^+/\text{H}_2$	$^3\text{A}$				0.744	
	$^1\text{A}$				0.744	

Table A.5 – Relevant bond lengths (in Å) of the B3LYP-calculated geometries of the species involved in the reaction:  $\text{NiF}^+ + \text{CH}_4 \rightarrow \text{Ni}(\text{CH}_3)^+ + \text{HF}$  (see Figure 6.11).

		Bond				
		Ni–F	Ni–H(1)	Ni–C	C–H(1)	H(1)–F
$\text{NiF}^+ / (\text{CH}_4)$	$^3\Pi$	1.700			1.090	
	$^1\Sigma$	1.708			1.090	
$\text{Ni}(\text{F})(\text{CH}_4)^+$ ( <b>15a</b> )	$^3A$	1.702	1.917	2.186	1.122	3.491
	$^1A$	1.673	1.897	2.135	1.121	2.605
TS <b>15a/16a</b>	$^3A$	1.869	1.804	2.070	1.380	1.253
	$^1A$	1.762	1.734	1.984	1.315	1.316
$\text{Ni}(\text{CH}_3)(\text{HF})^+$ ( <b>16a</b> )	$^3A$	2.110	2.949	1.915	4.850	0.938
	$^1A$	1.971	2.699	1.851	3.478	0.939
$\text{Ni}(\text{CH}_3)^+ / \text{HF}$	$^3A$			1.936		0.925
	$^1A$			1.856		0.925
TS <b>15a/23a</b>	$^1A$	1.673	1.416	1.919	2.030	2.200
$\text{Ni}(\text{F})(\text{CH}_3)(\text{H})^+$ ( <b>23a</b> )	$^1A$	1.672	1.414	1.911	2.152	2.195
TS <b>23a/16a</b>	$^1A$	1.724	1.458	1.881	2.351	1.500

Table A.6 – Relevant bond lengths (in Å) of the B3LYP-calculated geometries of the species involved in the reaction:  $\text{Ni}(\text{OH})^+ + \text{CH}_4 \rightarrow \text{Ni}(\text{CH}_3)^+ + \text{H}_2\text{O}$  (see Figure 6.12).

		Bond				
		Ni–OH	Ni–H(1)	Ni–C	C–H(1)	H(1)–OH
$\text{Ni}(\text{OH})^+ / (\text{CH}_4)$	$^3A''$	1.711			1.090	
	$^1A'$	1.705			1.090	
$\text{Ni}(\text{OH})(\text{CH}_4)^+$ ( <b>15b</b> )	$^3A$	1.704	1.929	2.185	1.118	3.495
	$^1A$	1.698	1.829	2.136	1.127	2.794
TS <b>15b/16b</b>	$^3A$	1.854	1.783	2.100	1.360	1.357
	$^1A$	1.762	1.690	2.002	1.303	1.418
$\text{Ni}(\text{CH}_3)(\text{H}_2\text{O})^+$ ( <b>16b</b> )	$^3A$	1.997	2.680	1.922	4.291	0.969
	$^1A$	1.878	2.531	1.841	3.439	0.969
$\text{Ni}(\text{CH}_3)^+ / \text{H}_2\text{O}$	$^1A$			1.856		0.963
	$^3A$			1.936		0.963
TS <b>15b/23b</b>	$^1A$	1.687	1.419	1.906	1.897	2.322
$\text{Ni}(\text{OH})(\text{CH}_3)(\text{H})^+$ ( <b>23b</b> )	$^1A$	1.684	1.414	1.885	2.276	2.278
TS <b>23b/16b</b>	$^1A$	1.720	1.446	1.868	2.432	1.632

Table A.7 – Relevant bond lengths (in Å) of the B3LYP-calculated geometries of the species involved in the reactions of  $\text{Ni}(\text{OH})^+ + \text{C}_2\text{H}_6$  (see Figure 6.13).

	Bond	Ni–O	Ni–C(1)	Ni–C(2)	Ni–H(1)	Ni–H(2)
$\text{Ni}(\text{OH})^+/\text{C}_2\text{H}_6$	$^3A''$	1.711				
	$^1A'$	1.705				
$\text{Ni}(\text{OH})(\text{C}_2\text{H}_6)^+$ ( <b>17c</b> )	$^3A$	1.705	2.417		2.002	
	$^1A$	1.701	2.140		1.685	
TS <b>17c/18c</b>	$^3A$	1.870	2.116		1.782	
	$^1A$	1.773	1.893		1.609	
$\text{Ni}(\text{C}_2\text{H}_5)(\text{H}_2\text{O})^+$ ( <b>18c</b> )	$^3A$	2.000	1.932	2.865	2.682	3.133
	$^1A$	1.899	1.874	2.118	2.568	1.646
TS <b>18c/19c</b>	$^3A$	1.977	2.122	2.151		1.554
	$^1A$	1.916	2.016	2.122		1.411
$\text{Ni}(\text{H})(\text{C}_2\text{H}_4)(\text{H}_2\text{O})^+$ ( <b>19c</b> )	$^3A$	2.005	2.332	2.289		1.519
	$^1A$	1.940	2.046	2.046		1.407
TS <b>19c/20c</b>	$^3A$	1.875	2.233	2.221	1.786	1.750
	$^1A$	1.787	2.152	2.154	1.634	1.591
$\text{Ni}(\text{OH})(\text{C}_2\text{H}_4)(\text{H}_2)^+$ ( <b>20c</b> )	$^3A$	1.722	2.223	2.268	1.893	1.910
	$^1A$	1.705	2.189	2.191	1.622	1.622
$\text{Ni}(\text{OH})(\text{C}_2\text{H}_4)^+/\text{H}_2$	$^3A$	1.710	2.254	2.193		
	$^1A$	1.695	2.043	2.046		
TS <b>17c/21c</b>	$^1A$	1.694	1.922	2.205	1.424	1.797
$\text{Ni}(\text{OH})(\text{C}_2\text{H}_5)(\text{H})^+$ ( <b>21c</b> )	$^1A$	1.689	1.901	2.192	1.416	2.193
	Bond	HO–H(1)	C(1)–H(1)	C(2)–H(2)	H(1)–H(2)	
$\text{Ni}(\text{OH})^+/\text{C}_2\text{H}_6$	$^3\Delta$	1.092				
	$^1\Sigma$	1.092				
$\text{Ni}(\text{OH})(\text{C}_2\text{H}_6)^+$ ( <b>17c</b> )	$^3A$	3.111	1.120			
	$^1A$	2.549	1.162			
TS <b>17c/18c</b>	$^3A$	1.323	1.423			
	$^1A$	1.500	1.338			
$\text{Ni}(\text{C}_2\text{H}_5)(\text{H}_2\text{O})^+$ ( <b>18c</b> )	$^3A$	0.968		3.133		
	$^1A$	0.967		1.180		
TS <b>18c/19c</b>	$^3A$	0.968		1.723		
	$^1A$	0.968		1.945		
$\text{Ni}(\text{H})(\text{C}_2\text{H}_4)(\text{H}_2\text{O})^+$ ( <b>19c</b> )	$^3A$	0.968				
	$^1A$	0.968				
TS <b>19c/20c</b>	$^3A$	1.368			0.947	
	$^1A$	1.594			0.878	
$\text{Ni}(\text{OH})(\text{C}_2\text{H}_4)(\text{H}_2)^+$ ( <b>20c</b> )	$^3A$	2.677			0.768	
	$^1A$	2.512			0.814	
$\text{Ni}(\text{OH})(\text{C}_2\text{H}_4)^+/\text{H}_2$	$^3A$				0.744	
	$^1A$				0.744	
TS <b>17c/21c</b>	$^1A$	2.252	1.842			
$\text{Ni}(\text{OH})(\text{C}_2\text{H}_5)(\text{H})^+$ ( <b>21c</b> )	$^1A$	2.193	2.405			
	$^1A$	2.193	2.405			

Table A.8 – Relevant bond lengths (in Å) of the B3LYP-calculated geometries of  $[\text{Ni,C,H}_3,\text{O}]^+$  species (see Figure 6.14).

		Bond					
		Ni–C	Ni–O	Ni–H(1)	C–O	C–H(1)	O–H(1)
Ni(H)(CH <sub>2</sub> O) <sup>+</sup>	<sup>3</sup> A	3.016	1.951	1.493	1.224	3.886	3.116
( <b>43</b> )	<sup>1</sup> A	2.846	1.810	1.418	1.228	2.980	2.448
TS <b>43/44a</b>	<sup>3</sup> A	2.245	1.853	1.579	1.286	1.778	2.368
TS <b>43/44b</b>	<sup>1</sup> A	2.301	1.809	1.455	1.269	1.951	2.257
Ni(OCH <sub>3</sub> ) <sup>+</sup> ( <b>44a</b> )	<sup>3</sup> A		1.701	3.199	1.412	1.092	
	<sup>1</sup> A		1.704	3.189	1.388	1.189	
Ni(OCH <sub>3</sub> ) <sup>+</sup> ( <b>44b</b> )	<sup>1</sup> A		1.734	1.678	1.355	1.236	
Ni(CH <sub>2</sub> OH) <sup>+</sup> ( <b>45</b> )	<sup>3</sup> A	1.968	2.633	3.144	1.362		0.971
TS <b>45/46</b>	<sup>3</sup> A	2.649	1.949	2.642	1.410		0.970
Ni(OHCH <sub>2</sub> ) <sup>+</sup> ( <b>46</b> )	<sup>3</sup> A	2.993	1.956	2.599	1.405		0.968
TS <b>46/47</b>	<sup>3</sup> A		2.882	2.353	1.284		0.994
Ni(HOCH <sub>2</sub> ) <sup>+</sup> ( <b>47</b> )	<sup>3</sup> A	3.933	3.073	1.556	1.217		1.538
TS <b>47/43</b>	<sup>3</sup> A		2.990	1.481	1.212		1.958
Ni(CH <sub>2</sub> OH) <sup>+</sup> ( <b>48</b> )	<sup>1</sup> A	1.853	1.896	2.493	1.402		0.974
TS <b>48/43</b>	<sup>1</sup> A	2.049	1.817	1.475	1.309	2.114	1.452

Table A.9 – Relevant bond lengths (in Å) of the B3LYP-calculated geometries of the species involved in the reactions of  $[\text{Ni}, \text{C}, \text{H}_3, \text{O}]^+ + \text{C}_2\text{H}_6$  (see Figures 6.16, 6.17, and 6.18).

	Bond	Ni–O	Ni–C(1)	Ni–C(2)	Ni–C(3)	Ni–H(1)
$\text{Ni}(\text{OCH}_3)(\text{C}_2\text{H}_6)^+$	$^3A$	1.683	3.067	2.164	3.514	3.465
(17d)	$^1A$	1.775	2.133	2.179	2.181	1.629
TS 17d/17e	$^3A$	1.903	2.321	2.253	2.384	1.580
	$^1A$	1.883	2.450	2.258	2.124	1.446
$\text{Ni}(\text{H})(\text{CH}_2\text{O})(\text{C}_2\text{H}_6)^+$	$^3A$	1.997	2.971	2.340	2.535	1.512
(17e)	$^1A$	1.856	2.858	2.141	2.301	1.428
$\text{Ni}(\text{CH}_2\text{OH})(\text{C}_2\text{H}_6)^+$	$^3A$	2.344	1.948	2.282	3.451	2.900
(17f)						
$\text{Ni}(\text{OHCH}_2)(\text{C}_2\text{H}_6)^+$	$^3A$	1.943	2.966	2.139	3.320	2.580
(17g)						
$\text{Ni}(\eta^2\text{CH}_2\text{OH})(\text{C}_2\text{H}_6)^+$	$^1A$	1.902	1.859	2.135	3.305	2.485
(17f)						
TS 17f/17g	$^3A$	1.940	2.503	2.133	3.331	2.625
TS 17g/17e	$^3A$	1.962	3.049	2.210	3.394	1.698
TS 17f/17e	$^1A$	1.839	2.036	2.135	3.201	1.471
TS 17e/18e	$^3A$	1.940		2.147	2.359	1.628
	$^1A$	1.907		1.973	2.189	1.490
$\text{Ni}(\text{C}_2\text{H}_5)(\text{OCH}_2)(\text{H}_2)^+$	$^3A$	1.981		1.972	2.869	1.934
(18e)	$^1A$	1.867		1.916	2.820	1.629
	Bond		Ni–O	Ni–C(1)	Ni–C(2)	Ni–C(3)
TS 17d/18d	$^3A$		1.841		2.104	2.257
	$^1A$		1.777		1.979	2.135
TS 17f/18d	$^3A$		1.979	2.312	2.050	3.224
TS 17f/18d	$^1A$		1.977	1.896	1.914	2.151
$\text{Ni}(\text{C}_2\text{H}_5)(\text{CH}_3\text{OH})^+$	$^3A$		1.969		1.931	2.867
(18d)	$^1A$		1.882		1.873	2.119
TS 18d/19d	$^3A$		1.950		2.118	2.151
	$^1A$		1.895		2.023	2.128
$\text{Ni}(\text{H})(\text{C}_2\text{H}_4)(\text{CH}_3\text{OH})^+$	$^3A$		1.996		2.257	2.245
(19d)	$^1A$		1.918		2.052	2.050
TS 19d/20d	$^3A$		1.874		2.212	2.230
	$^1A$		1.787		2.152	2.154
$\text{Ni}(\text{OCH}_3)(\text{C}_2\text{H}_4)(\text{H}_2)^+$	$^3A$		1.712		2.244	2.205
(20d)	$^1A$		1.704		2.186	2.188
TS 19d/20e	$^3A$		2.111	2.487	2.180	2.195
	$^1A$		1.991	1.968	2.081	2.143
$\text{Ni}(\text{CH}_2\text{OH})(\text{C}_2\text{H}_4)(\text{H}_2)^+$	$^3A$		2.836	2.131	2.152	2.174
(20e)	$^1A$		2.795	1.913	2.100	2.093

Table A.9 – (cont.) Relevant bond lengths (in Å) of the B3LYP-calculated geometries of the species involved in the reactions of  $[\text{Ni,C,H}_3,\text{O}]^+ + \text{C}_2\text{H}_6$  (see Figures 6.16, 6.17, and 6.18).

	Bond				
	Ni–H(2)	C(1)–H(1)	C(2)–H(2)	H(1)–H(2)	O–H(2)
<hr/>					
Ni(OCH <sub>3</sub> )(C <sub>2</sub> H <sub>6</sub> ) <sup>+</sup> ( <b>17d</b> )					
<sup>3</sup> A	1.877	1.094	1.126		3.412
<sup>1</sup> A	1.752	1.251	1.142		2.503
TS <b>17d/17e</b>					
<sup>3</sup> A	1.915	1.993	1.124		
<sup>1</sup> A	1.646	2.212	1.167		
Ni(H)(CH <sub>2</sub> O)(C <sub>2</sub> H <sub>6</sub> ) <sup>+</sup> ( <b>17e</b> )					
<sup>3</sup> A	1.973		1.119	2.664	
<sup>1</sup> A	1.653		1.160	1.912	
	Ni–H(2)	O–H(1)	C(2)–H(2)	C(1)–H(2)	H(1)–H(2)
<hr/>					
Ni(CH <sub>2</sub> OH)(C <sub>2</sub> H <sub>6</sub> ) <sup>+</sup> ( <b>17f</b> )					
<sup>3</sup> A	1.895	0.969	1.122	3.539	
Ni(OHCH <sub>2</sub> )(C <sub>2</sub> H <sub>6</sub> ) <sup>+</sup> ( <b>17g</b> )					
<sup>3</sup> A	1.807	0.968	1.131	4.559	
Ni( $\eta^2$ CH <sub>2</sub> OH)(C <sub>2</sub> H <sub>6</sub> ) <sup>+</sup> ( <b>17f</b> )					
<sup>1</sup> A	1.697	0.973	1.145	2.873	
TS <b>17f/17g</b>					
<sup>3</sup> A	1.801	0.970	1.130		
TS <b>17g/17e</b>					
<sup>3</sup> A	1.827	1.342	1.130		
TS <b>17f/17e</b>					
<sup>1</sup> A	1.785	1.460	1.134		
TS <b>17e/18e</b>					
<sup>3</sup> A	1.597		1.541		1.035
<sup>1</sup> A	1.501		1.492		1.094
Ni(C <sub>2</sub> H <sub>5</sub> )(OCH <sub>2</sub> )(H <sub>2</sub> ) <sup>+</sup> ( <b>18e</b> )					
<sup>3</sup> A	1.904		3.020		0.766
<sup>1</sup> A	1.628		2.556		0.803



Table A.9 – (cont.) Relevant bond lengths (in Å) of the B3LYP-calculated geometries of the species involved in the reactions of  $[\text{Ni}, \text{C}, \text{H}_3, \text{O}]^+ + \text{C}_2\text{H}_6$  (see Figures 6.16, 6.17, and 6.18).

	Bond				
	Ni–H(2)	O–H(2)	C(1)-H(2)	C(2)–H(2)	
TS 17d/18d					
<sup>3</sup> A	1.790	1.287		1.449	
<sup>1</sup> A	1.613	1.458		1.354	
TS 17f/18d					
<sup>3</sup> A	1.565		1.531	1.464	
TS 17f/18d					
<sup>1</sup> A	1.448		1.776	1.922	
	Ni–H(3)	C(3)–H(3)			
TS 18d/19d					
<sup>3</sup> A	1.555	1.718			
<sup>1</sup> A	1.412	1.965			
Ni(H)(C <sub>2</sub> H <sub>4</sub> )(CH <sub>3</sub> OH) <sup>+</sup> (19d)					
<sup>3</sup> A	1.996	2.659			
<sup>1</sup> A	1.408	2.489			
	Ni–H(2)	Ni–H(3)	O–H(2)	C(1)–H(2)	H(2)–H(3)
TS 19d/20d					
<sup>3</sup> A	1.786	1.739	1.333		0.963
<sup>1</sup> A	1.634	1.591	1.524		0.889
Ni(OCH <sub>3</sub> )(C <sub>2</sub> H <sub>4</sub> )(H <sub>2</sub> ) <sup>+</sup> (20d)					
<sup>3</sup> A	1.872	1.897	2.718		0.769
<sup>1</sup> A	1.638	1.638	2.628		0.806
TS 19d/20e					
<sup>3</sup> A	1.780	1.647		1.493	0.990
<sup>1</sup> A	1.501	1.471		1.510	1.195
Ni(CH <sub>2</sub> OH)(C <sub>2</sub> H <sub>4</sub> )(H <sub>2</sub> ) <sup>+</sup> (20e)					
<sup>3</sup> A	1.828	1.819		2.794	0.779
<sup>1</sup> A	1.729	1.742		2.628	0.785

## A.6 ESI source spectra of Fe, Co, and Ni halides

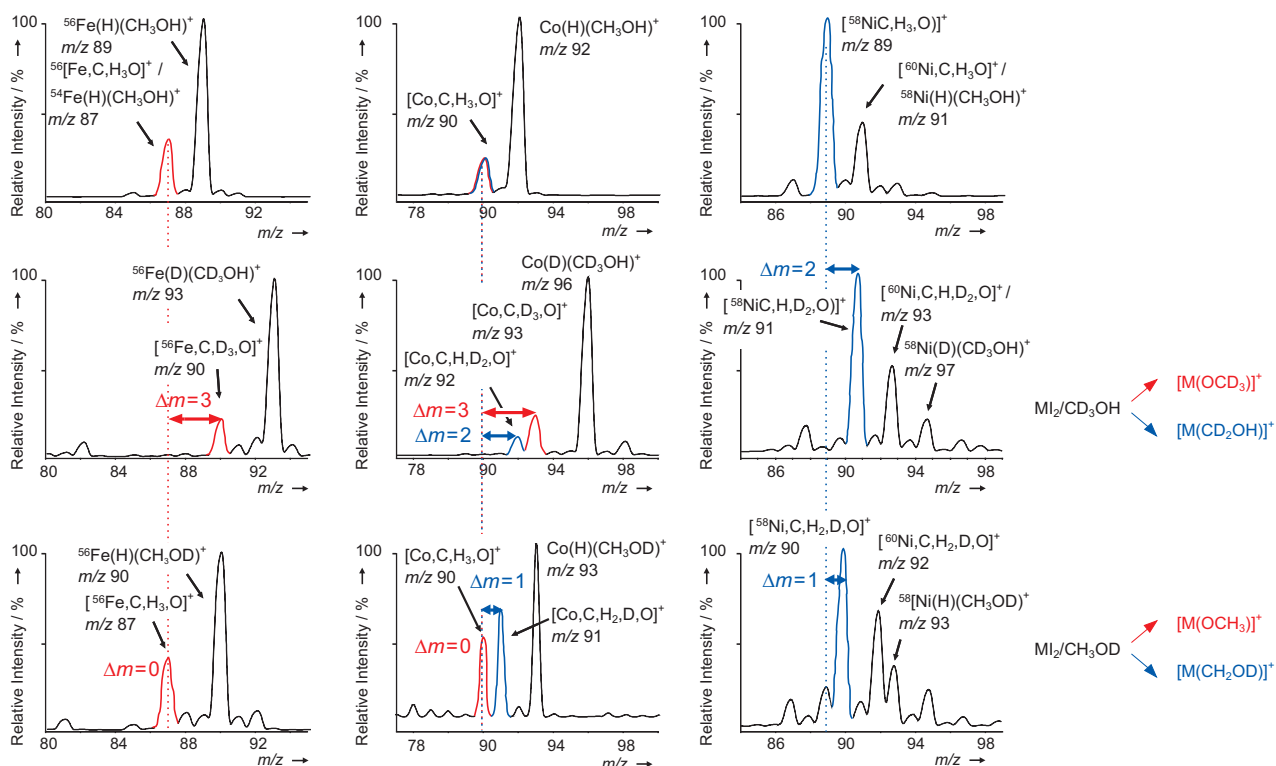


Figure A.4 – Source spectra of Fe, Co, and Ni halides  $MX_2$  in  $CH_3OH$ ,  $CD_3OH$ , and  $CH_3OD$ , respectively.

## References

- [1] Bradshaw, A. M.; Hamacher, T. In *Kernfusion: Eine nachhaltige Energiequelle der Zukunft*; zur Hausen, H., Ed.; Deutsche Akademie der Naturforscher Leopoldina e. V.: Halle (Saale), Germany, 2004.
- [2] Shilov, A. E.; Shul'pin, G. B. *Chem. Rev.* **1997**, *97*, 2879.
- [3] Lin, M.; Hogan, T.; Sen, A. *J. Am. Chem. Soc.* **1997**, *119*, 6048.
- [4] Sen, A. *Acc. Chem. Res.* **1998**, *31*, 550.
- [5] Periana, R. A.; Taube, D. J.; Gamble, S.; Taube, H.; Sato, T.; Fuji, H. *Science* **1998**, *280*, 560.
- [6] Muehlhofer, M.; Strassner, T.; Herrmann, W. A. *Angew. Chem. Int. Ed.* **2002**, *14*, 1745.
- [7] Periana, R. A.; Mironov, O.; Bhalla, D. J. T. G.; Jones, C. *Science* **2003**, *30*, 814.
- [8] Jones, C.; Taube, D.; Ziatdinov, V. R.; Periana, R. A.; Nielsen, R. J.; Oxgaard, J.; Goddard, W. A., III, *Angew. Chem. Int. Ed.* **2004**, *119*, 4626.
- [9] Olah, G. A.; Goeppert, A.; Prakash, G. K. S. *Beyond Oil and Gas: The Methanol Economy*; Wiley VCH: Weinheim, Germany, 2006.
- [10] Sabatier, P.; Senderens, J. P. *C. R. Acad. Sci. Paris* **1902**, *134*, 514.
- [11] Dry, M. E. *Appl. Catal. A Gen.* **2004**, *276*, 1.
- [12] Hindermann, J. P.; Hutchings, G. J.; Kiennemann, A. *Catal. Rev. Sci. Eng.* **1993**, *35*, 1.
- [13] Ziegler, K.; Gellert, H. G.; Holzkamp, E.; Wilke, G. *Brennstoff Chem.* **1954**, *321*, 35.
- [14] Wilke, G. *Angew. Chem. Int. Ed.* **1988**, *27*, 185.
- [15] Elschenbroich, C. *Organometallchemie*; B.G. Teubner Verlag: Wiesbaden, Germany, 2003; Vol. 4.
- [16] Tamaru, Y. *Modern Organonickel Chemistry*; Wiley-VCH: Weinheim, Germany, 2005.

- [17] Tamao, K.; Sumitani, K.; Kumada, M. *J. Am. Chem. Soc.* **1972**, *93*, 4374.
- [18] Corriu, R. J. P.; Masse, J. P. *J. Chem. Soc., Chem. Commun.* **1972**, 144.
- [19] Heimbach, P. *Angew. Chem. Int. Ed.* **1973**, *12*, 975.
- [20] Montgomery, J. *Acc. Chem. Res.* **2000**, *33*, 467.
- [21] Ikeda, S.-I. *Acc. Chem. Res.* **2000**, *33*, 511.
- [22] Moslin, R. M.; Miller-Moslin, K.; Jamison, T. F. *Chem. Commun.* **2007**, 4441.
- [23] Li, J.; Jia, G.; Lin, Z. *Organometallics* **2008**, *27*, 3892.
- [24] Bell, A. T. *Catal. Rev. Sci. Eng.* **1981**, *23*, 203.
- [25] Anderson, R. B. *The Fischer Tropsch Synthesis*; Academic Press: London, UK, 1984.
- [26] Maitlis, P. M. *Pure Appl. Chem.* **1989**, *61*, 1747.
- [27] Britovsek, G. J. P.; Gibson, V. C.; McTavish, S. J.; Solan, G. A.; White, A. J. P.; Williams, D. J.; Kimberley, B. S.; Maddox, P. J. *Chem. Commun.* **1998**, 849.
- [28] Dieck, H. A.; Heck, F. R. *J. Organomet. Chem.* **1975**, *93*, 259.
- [29] Liégault, B.; Renaud, J.-L.; Bruneau, C. *Chem. Soc. Rev.* **2008**, *37*, 290.
- [30] An entire issue was devoted to nickel catalysis: Jamison, T. F., *Tetrahedron* **2006**, *62*, 7499.
- [31] Kaim, W.; Schwederski, B. *Bioanorganische Chemie*; Teubner Verlag: Wiesbaden, Germany, 2005.
- [32] Sigel, A.; Sigel, H.; Sigel, R. K. O. *Nickel and its Surprising Impact in Nature*; John Wiley & Sons: West Sussex, UK, 2007; Vol. 2.
- [33] Eller, K.; Schwarz, H. *Chem. Rev.* **1991**, *91*, 1121.
- [34] Schröder, D.; Heinemann, C.; Koch, W.; Schwarz, H. *Pure Appl. Chem.* **1997**, *69*, 273.
- [35] Bondybey, V. E.; Beyer, M. K. *J. Phys. Chem. A* **2001**, *105*, 951.
- [36] Böhme, D. K.; Schwarz, H. *Angew. Chem. Int. Ed.* **2005**, *44*, 2336.
- [37] Koszinowski, K.; Schröder, D.; Schwarz, H. *J. Am. Chem. Soc.* **2003**, *125*, 3676.
- [38] Koszinowski, K.; Schröder, D.; Schwarz, H. *Organometallics* **2004**, *23*, 1132.

- [39] Koszinowski, K.; Schröder, D.; Schwarz, H. *Angew. Chem. Int. Ed.* **2004**, *121*, 43.
- [40] Schwarz, H. *Leopoldina Jahrbuch* **2004**, *49*, 397.
- [41] Schwarz, H. *Acc. Chem. Res.* **1989**, *22*, 283.
- [42] Armentrout, P. B.; Beauchamp, J. L. *Acc. Chem. Res.* **1989**, *22*, 315.
- [43] Armentrout, P. B. *Science* **2001**, *251*, 175.
- [44] Weisshaar, J. C. *Acc. Chem. Res.* **1993**, *26*, 213.
- [45] Schröder, D.; Schwarz, H. *Angew. Chem., Int. Ed. Engl.* **1995**, *34*, 1973.
- [46] Schwarz, H.; Schröder, D. *Pure Appl. Chem.* **2000**, *72*, 2319.
- [47] Chen, P. *Angew. Chem. Int. Ed.* **2003**, *42*, 2832.
- [48] Schwarz, H. *Angew. Chem. Int. Ed.* **2003**, *42*, 4442.
- [49] Plattner, D. A. *Top. Curr. Chem.* **2003**, *225*, 153.
- [50] Armentrout, P. B. *Acc. Chem. Res.* **1995**, *28*, 430.
- [51] Tjelta, B. L.; Armentrout, P. B. *J. Am. Chem. Soc.* **1996**, *118*, 9652.
- [52] Hall, C.; Perutz, R. N. *Chem. Rev.* **1996**, *96*, 3125.
- [53] Irion, M. P.; Selinger, A. *Ber. Bunsen-Ges.* **1989**, *93*, 1408.
- [54] Buckner, S. W.; McMahon, T. J.; Byrd, G. D.; Freiser, B. S. *Inorg. Chem.* **1989**, *28*, 3511.
- [55] Perry, J. K.; Ohanessian, G.; Goddard, W. A., III, *Organometallics* **1994**, *13*, 1870.
- [56] Shaik, S.; Danovich, D.; Fiedler, A.; Schröder, D.; Schwarz, H. *Helv. Chim. Acta* **1995**, *78*, 1393.
- [57] Schröder, D.; Schwarz, H.; Shaik, S. In *Structure and Bonding*; Meunier, B., Ed.; Springer: Berlin, Germany, 2000.
- [58] Ryan, M. F.; Fiedler, A.; Schröder, D.; Schwarz, H. *J. Am. Chem. Soc.* **1995**, *117*, 2033.
- [59] Shiota, Y.; Yoshizawa, K. *J. Am. Chem. Soc.* **2000**, *122*, 12317.
- [60] Schröder, D.; Holthausen, M. C.; Schwarz, H. *J. Phys. Chem. B* **2004**, *108*, 14407.

- [61] Stöckigt, D.; Schwarz, H. *Liebigs Ann.* **1995**, 429.
- [62] Brönstrup, M.; Schröder, D.; Schwarz, H. *Can. J. Chem.* **1999**, 77, 774.
- [63] Carlin, T. J.; Sallans, L.; Cassady, C. J.; Jacobsen, D. B.; Freiser, B. S. *J. Am. Chem. Soc.* **1983**, 105, 6320.
- [64] Halle, L. F.; Klein, F. S.; Beauchamp, J. L. *J. Am. Chem. Soc.* **1984**, 106, 2543.
- [65] Zhang, X. G.; Bowers, M. T. *J. Phys. Chem. A* **2004**, 108, 9755.
- [66] Ohanessian, G.; Goddard III, W. A. *Acc. Chem. Res.* **1990**, 23, 386.
- [67] Schilling, J. B.; Goddard III, W. A.; Beauchamp, J. L. *J. Am. Chem. Soc.* **1986**, 108, 582.
- [68] Schilling, J. B.; Goddard III, W. A.; Beauchamp, J. L. *J. Am. Chem. Soc.* **1987**, 109, 5565.
- [69] Schwarz, H. *Int. J. Mass Spectrom.* **2004**, 237, 75.
- [70] Schröder, D.; Shaik, S.; Schwarz, H. *Acc. Chem. Res.* **2000**, 33, 139.
- [71] Poli, R.; Harvey, J. N. *Chem. Soc. Rev.* **2003**, 32, 1.
- [72] Mercero, J. M.; Matxain, J. M.; Lopez, X.; York, D. M.; Largo, A.; Eriksson, L. A.; Ugalde, J. M. *Int. J. Mass Spectrom.* **2005**, 240, 37.
- [73] Liu, F.; Zhang, X. G.; Armentrout, P. B. *Phys. Chem. Chem. Phys.* **2005**, 7, 1054.
- [74] Armentrout, P. B.; Kickel, B. L. In *Organometallic Ion Chemistry*; Freiser, B. S., Ed.; Kluwer: Dordrecht, Holland, 1996.
- [75] Diefenbach, M.; Brönstrup, M.; Aschi, M.; Schröder, D.; Schwarz, H. *J. Am. Chem. Soc.* **1999**, 121, 10614.
- [76] Halle, L. F.; Armentrout, P. B.; Beauchamp, J. L. *Organometallics* **1982**, 1, 963.
- [77] Mandich, M. L.; Steigerwald, M. L.; Reents, W. D. *J. Am. Chem. Soc.* **1986**, 108, 6197.
- [78] Schröder, D.; Hrušák, J.; Schwarz, H. *Ber. Bunsen-Ges. Phys. Chem.* **1993**, 97, 1085.
- [79] Mazurek, U.; Schröder, D.; Schwarz, H. *Collect. Czech. Chem. Commun.* **1998**, 63, 1498.
- [80] Elstner, E. F. *Der Sauerstoff: Biochemie, Biologie, Medizin*; Wissenschaftsverlag: Mannheim, Germany, 1990.

- [81] Sawyer, D. T. *Oxygen Chemistry*; Oxford University Press: New York, 1991.
- [82] Fiedler, A.; Schröder, D.; Shaik, S.; Schwarz, H. *J. Am. Chem. Soc.* **1994**, *116*, 10734.
- [83] Ryan, M. F.; Stoeckigt, D.; Schwarz, H. *J. Am. Chem. Soc.* **1994**, *116*, 9565.
- [84] Lippard, S. J.; Berg, J. M. *Principles of Bioinorganic Chemistry*; University Science Book: Mill Valley, USA, 1994.
- [85] Lippard, S. J.; Berg, J. M. In *Oxygenase and Model Systems*; Fumabiki, T., Ed.; Kluwer: Boston, USA, 1997.
- [86] Stahl, S. S. *Angew. Chem. Int. Ed.* **2004**, *43*, 3400.
- [87] Hosokawa, T.; Musabashi, S. I. *Acc. Chem. Res.* **1990**, *23*, 49.
- [88] Denney, M. C.; Smythe, N. A.; Cetto, K. L.; Kemp, R. A.; Goldberg, K. I. *J. Am. Chem. Soc.* **2006**, *128*, 2508.
- [89] Konnick, M. M.; Gandhi, B. A.; Guzei, I. A.; Stahl, S. S. *Angew. Chem. Int. Ed.* **2006**, *45*, 2904.
- [90] Gligorich, K. M.; Sigman, M. S. *Angew. Chem. Int. Ed.* **2006**, *45*, 6612.
- [91] Konnick, M. M.; Stahl, S. S. *J. Am. Chem. Soc.* **2008**, *130*, 5753.
- [92] Privalov, T.; Linde, C.; Zetterberg, K.; Moberg, C. *Organometallics* **2005**, *24*, 885.
- [93] Keith, J. M.; Nielsen, R. J.; Oxgaard, J.; Goddard, W. A., III, *J. Am. Chem. Soc.* **2005**, *127*, 13172.
- [94] Keith, J. M.; Muller, R. P.; Kemp, R. A.; Goldberg, K. I.; Goddard, W. A., III, *Inorg. Chem.* **2006**, *45*, 9631.
- [95] Chowdhury, S.; Rivalta, I.; Russo, N.; Sicilia, E. *Chem. Phys. Lett.* **2007**, *443*, 183.
- [96] Popp, B. V.; Stahl, S. S. *J. Am. Chem. Soc.* **2007**, *129*, 4410.
- [97] Keith, J. M.; Goddard, W. A., III; Oxgaard, J. *J. Am. Chem. Soc.* **2007**, *129*, 10361.
- [98] Bayston, J. H.; Beale, R. N.; King, N. K.; Winfield, M. E. *Aust. J. Chem.* **1963**, *16*, 954.
- [99] Bayston, J. H.; Winfield, M. E. *J. Catal.* **1964**, *3*, 123.
- [100] Roberts, H. L.; Symes, W. R. *J. Chem. Soc. A* **1968**, 1450.

- [101] Johnston, L. E.; Page, J. A. *Can. J. Chem.* **1969**, *47*, 4241.
- [102] Gillard, R. D.; Heaton, B. T.; Vaughan, D. H. *J. Chem. Soc. A* **1970**, 3126.
- [103] Endicott, J. F.; Wong, C. L.; Inour, T.; Natarajan, P. *Inorg. Chem.* **1979**, *18*, 450.
- [104] Atley, M. T.; Preece, M.; Strukul, G.; James, B. R. *Can. J. Chem.* **1983**, *61*, 1332.
- [105] Bakac, A. *J. Am. Chem. Soc.* **1997**, *119*, 10726.
- [106] Wick, D. D.; Goldberg, K. I. *J. Am. Chem. Soc.* **1999**, *121*, 119900.
- [107] Thyagaran, S.; Incarvito, C. D.; Rheingold, A. L.; Theopold, K. H. *Chem. Commun.* **2001**, 2198.
- [108] Squires, R. R. *Chem. Rev.* **1969**, *87*, 623.
- [109] Hop, C. E. C. A.; McMahon, T. B. *J. Am. Chem. Soc.* **1992**, *114*, 1237.
- [110] Schröder, D.; Schwarz, H. *Angew. Chem., Int. Ed. Engl.* **1993**, *32*, 1420.
- [111] Boissel, P.; Marty, P.; Klotz, A.; de Parseval, P.; Candret, B.; Serra, G. *Chem. Phys. Lett.* **1995**, *242*, 157.
- [112] Fiedler, A.; Kretzschmar, I.; Schröder, D.; Schwarz, H. *J. Am. Chem. Soc.* **1996**, *118*, 5047.
- [113] Pavlov, M.; Blomberg, M. R. A.; Siegbahn, P. E. M.; Wesendrup, R.; Heinemann, C.; Schwarz, H. *J. Phys. Chem. A* **1997**, *101*, 1567.
- [114] Schröder, D.; Schwarz, H. In *Essays in Contemporary Chemistry: From Molecular Structure towards Biology*; Quinkert, G., Kisakürek, M. V., Eds.; Wiley-VCH: Weinheim, Germany, 2001.
- [115] Brönstrup, M.; Schröder, D.; Kretzschmar, I.; Schwarz, H.; Harvey, J. N. *J. Am. Chem. Soc.* **2001**, *123*, 142.
- [116] Koyanagi, G. K.; Böhme, D. K.; Kretzschmar, I.; Schröder, D.; Schwarz, H. *J. Phys. Chem. A* **2001**, *105*, 4259.
- [117] Engeser, M.; Weiske, T.; Schröder, D.; Schwarz, H. *J. Phys. Chem. A* **2003**, *107*, 2855.
- [118] Socacin, L. D.; Hagen, J.; Bernhardt, T. M.; Wöste, L.; Heiz, U.; Häkkinen, H.; Landmann, U. *J. Am. Chem. Soc.* **2003**, *125*, 10437.
- [119] Koszinowski, K.; Schröder, D.; Schwarz, H. *Chem. Phys. Chem.* **2003**, *4*, 1233.



- [120] Koszinowski, K.; Schröder, D.; Schwarz, H. *J. Phys. Chem. A* **2003**, *107*, 4999.
- [121] Kimble, M. L.; Castleman, A. W., Jr.; Mitrić, R.; Bürgel, C.; Bonačić-Koutecký, V. *J. Am. Chem. Soc.* **2004**, *126*, 2526.
- [122] Xia, F.; Cao, Z. *J. Phys. Chem. A* **2006**, *110*, 10078.
- [123] Eller, K.; Schwarz, H. *Int. J. Mass Spectrom. Ion Phys.* **1989**, *93*, 243.
- [124] Eller, K.; Schwarz, H. *J. Am. Chem. Soc.* **1990**, *112*, 621.
- [125] Maruyama, S.; Anderson, L. R.; Smalley, R. E. *Rev. Sci. Instr.* **1990**, *61*, 3686.
- [126] Berg, C.; Schindler, T.; Kantlehner, M.; Niedner-Schatteburg, G.; Bondybey, V. E. *Chem. Phys.* **2000**, *262*, 143.
- [127] Forbes, R. A.; Laucien, F. H.; Wronka, J. *Int. J. Mass Spectrom. Ion Phys.* **1988**, *83*, 23.
- [128] Strutt, J. W. (Lord Rayleigh), *Philos. Mag.* **1882**, *14*, 184.
- [129] Zeleny, J. *Phys. Rev.* **1917**, *10*, 1.
- [130] Evans, C. A, Jr.; Hendricks, C. D. *Rev. Sci. Instr.* **1972**, *43*, 1527.
- [131] Simons, D. S.; Colby, B. N.; Evans, C. A., Jr, *Int. J. Mass Spectrom. Ion Phys.* **1974**, *15*, 291.
- [132] Dole, M.; Mack, L. L.; Hines, R. L.; Mobley, R. C.; Ferguson, L. D.; Alice, M. B. *J. Chem. Phys.* **1968**, *49*, 2240.
- [133] Taylor, G. I. *Proc. R. Soc. London Ser. A* **1964**, *280*, 383.
- [134] van Berkel, G. J. In *Electrospray-Ionization Mass Spectrometry*; Cole, R. B., Ed.; Wiley: New York, USA, 1997.
- [135] Enke, C. G. *Anal. Chem.* **1997**, *69*, 4885.
- [136] Cech, N. B.; Enke, C. G. *Mass Spectrom. Rev.* **2001**, *20*, 362.
- [137] Bruins, A. P.; Covey, T. R.; Henion, J. D.; Budde, W. L. *Anal. Chem.* **1987**, *59*, 2647.
- [138] Covey, T. R.; Bonner, R. F.; Shushan, B. I.; Henion, J. D. *Rap. Commun. Mass Spectrom.* **1988**, *2*, 249.
- [139] Covey, T. R.; Bruins, A. P.; Henion, J. D. *Org. Mass Spectrom.* **1988**, *23*, 178.

- [140] Kebarle, P.; Tang, L. *Anal. Chem.* **1993**, *65*, 972A.
- [141] Cole, R. B. *J. Mass Spectrom.* **2000**, *35*, 763.
- [142] Schmelzeisen-Redeker, G.; Buttering, L.; Röllgen, F. W. *Int. J. Mass Spectrom. Ion Phys.* **1989**, *90*, 139.
- [143] Iribane, J. V.; Thomson, B. A. *J. Phys. Chem.* **1976**, *64*, 2287.
- [144] Thompson, B. A.; Iribane, J. V. *J. Phys. Chem.* **1979**, *71*, 4451.
- [145] Gross, J. *Mass Spectrometry: A Textbook*; Springer-Verlag: Berlin, Germany, 2004.
- [146] Holmes, J. L. *Org. Mass Spectrom.* **1985**, *20*, 169.
- [147] Kim, M. S. *Int. J. Mass Spectrom.* **1983**, *50*, 189.
- [148] Dunbar, R. C. *Mass Spectrom. Rev.* **1992**, *11*, 309.
- [149] Stöckigt, D.; Hrušák, J.; Schwarz, H. *Int. J. Mass Spectrom. Ion Phys.* **1995**, *149/150*, 1.
- [150] Blum, O.; Milstein, D. *J. Am. Chem. Soc.* **1995**, *117*, 4582.
- [151] Versluis, L.; Ziegler, T. *J. Am. Chem. Soc.* **1990**, *112*, 6763.
- [152] Langevin, M. P. *Ann. Chim. Phys.* **1905**, *5*, 245.
- [153] Su, T.; Bowers, M. *Int. J. Mass Spectrom. Ion Phys.* **1973**, *12*, 347.
- [154] Su, T.; Chesnavich, W. J. *J. Chem. Phys.* **1982**, *76*, 5183.
- [155] Su, T. *J. Chem. Phys.* **1988**, *89*, 5355.
- [156] Nakao, F. *Vacuum* **1975**, *25*, 431.
- [157] Bartmess, J. E.; Georgiadis, R. M. *Vacuum* **1983**, *33*, 149.
- [158] Schröder, D.; Schwarz, H.; Clemmer, D. E.; Chen, Y. M.; Armentrout, P. B.; Baranov, V. I.; Böhme, D. K. *Int. J. Mass Spectrom. Ion Phys.* **2002**, *161*, 175.
- [159] Anslyn, E. V.; Dougherty, D. A. *Modern Physical Organic Chemistry*; University Science Book: Sausalito, CA (USA), 2006.
- [160] Hehre, W. J.; Radom, L.; v R Schleyer, P.; Pople, J. A. *Ab initio Molecular Orbital Theory*; Wiley: New York, USA, 1986.

- [161] Truhlar, D. G.; Morokuma, K. *Transition State Modeling for Catalysis*; Oxford University Press: Dallas, USA, 1999.
- [162] Koch, W.; Holthausen, M. C. *A Chemist's Guide to Density Functional Theory*; Wiley-VCH: Weinheim, Germany, 2000.
- [163] Lowe, J. P. *Quantum Chemistry*, 2nd ed.; Academic Press: San Diego, USA, 1993.
- [164] Hohenberg, P.; Kohn, W. *Phys. Rev.* **1964**, *136*, B864.
- [165] Vosko, S. H.; Wilk, L.; Nusair, M. *Can. J. Chem.* **1980**, *58*, 1200.
- [166] Becke, A. D. *Phys. Rev. A* **1988**, *33*, 3098.
- [167] Perdew, J. P. *Phys. Rev. B* **1986**, *33*, 8822.
- [168] Perdew, J. P. *Phys. Rev. B* **1988**, *34*, 7064.
- [169] Lee, C.; Yang, W.; Parr, R. G. *Phys. Rev. B* **1988**, *37*, 785.
- [170] Lynch, B. J.; Fast, P. L.; Harris, M.; Truhlar, D. G. *Theor. Chem. Acc.* **2000**, *104*, 4811.
- [171] Zhao, Y.; Gonz  les-Garc  a, N.; Truhlar, D. G. *Theor. Chem. Acc.* **2005**, *109*, 2012.
- [172] Zhao, Y.; Truhlar, D. G. *Acc. Chem. Res.* **2008**, *41*, 157.
- [173] Zhao, Y.; Truhlar, D. G. *Theor. Chem. Acc.* **2008**, *120*, 215.
- [174] Becke, A. D. *J. Chem. Phys.* **1993**, *98*, 5648.
- [175] Frisch, M. J. et al. *Gaussian 03, Revision C.02*, Gaussian, Inc., Wallingford, CT, 2004.
- [176] Schaefer, A.; Huber, C.; Ahlrichs, R. *J. Chem. Phys.* **1994**, *100*, 5829.
- [177] The basis sets and ECPs correspond to Revision: Fri Jun 27, 1997, of the Stuttgart/Dresden groups.
- [178] Andrae, D.; Haeussermann, U.; Dolg, M.; Stoll, H.; Preuss, H. *Theor. Chem. Acc.* **1990**, *77*, 123.
- [179] Person, K. A.; Figgen, D.; Dolg, M.; Stoll, H. *J. Chem. Phys.* **2007**, *126*, 124101.
- [180] Holthausen, M. C.; Fiedler, A.; Schwarz, H.; Koch, W. *Angew. Chem. Int. Ed.* **1995**, *34*, 2282.
- [181] Fukui, K. *J. Phys. Chem.* **1970**, *74*, 4161.

- [182] Fukui, K. *Acc. Chem. Res.* **1981**, *14*, 363.
- [183] Gonzalez, C.; Schlegel, H. B. *J. Phys. Chem.* **1990**, *94*, 5523.
- [184] Schlangen, M. *Diploma thesis*, TU Berlin, 2004.
- [185] Schlangen, M.; Schröder, D.; Schwarz, H. *Helv. Chim. Acta* **2005**, *88*, 1405.
- [186] Seemeyer, K.; Schröder, D.; Kempf, M.; Lettau, O.; Müller, J.; Schwarz, H. *Organometallics* **1995**, *14*, 4465.
- [187] Tews, E. C.; Freiser, B. S. *J. Am. Chem. Soc.* **1987**, *109*, 4433.
- [188] Prüsse, T.; Fiedler, A.; Schwarz, H. *Helv. Chim. Acta* **1991**, *74*, 1127.
- [189] Seemeyer, K.; Prüsse, T.; Schwarz, H. *Helv. Chim. Acta* **1993**, *76*, 1632.
- [190] Hoshino, K.; Kurikawa, T.; Takeda, H.; Nakajima, A.; Kaya, K. *J. Phys. Chem.* **1995**, *99*, 3053.
- [191] Kurikawa, T.; Takeda, H.; Nakajima, A.; Kaya, K. *Z. Phys. D* **1997**, *40*, 65.
- [192] Weis, P.; Kemper, P. R.; Bowers, M. T. *J. Phys. Chem. A* **1997**, *101*, 8207.
- [193] Kurikawa, T.; Takeda, H.; Hirano, M.; Judai, K.; Arita, T.; Nagao, S.; Nakajima, A.; Kaya, K. *Organometallics* **1999**, *18*, 1430.
- [194] Georgiadis, R.; Fisher, E. R.; Armentrout, P. B. *J. Am. Chem. Soc.* **1989**, *111*, 4251.
- [195] Armentrout, P. B.; Tjelta, B. L. *Organometallics* **1997**, *16*, 5372.
- [196] Carpenter, C. J.; van Koppen, P. A. M.; Bowers, M. T. *J. Am. Chem. Soc.* **1995**, *117*, 10976.
- [197] Khan, F. A.; Steele, D. L.; Armentrout, P. B. *J. Phys. Chem.* **1995**, *99*, 7819.
- [198] Schröder, D.; Eller, C.; Prüsse, T.; Schwarz, H. *Organometallics* **1991**, *10*, 2052.
- [199] Schröder, D.; Schwarz, H. *J. Organomet. Chem.* **1995**, *504*, 123.
- [200] Tjelta, B. L.; Armentrout, P. B. *J. Am. Chem. Soc.* **1995**, *117*, 5531.
- [201] Schröder, D.; Bärsch, S.; Schwarz, H. *Chem. Phys. Lett.* **1999**, *309*, 407.
- [202] Montag, M.; Schwartsburd, L.; Cohen, R.; Leitun, G.; Ben-David, Y.; Martin, J. M. L.; Milstein, D. *Angew. Chem. Int. Ed.* **2007**, *46*, 1901.
- [203] Freas, R. B.; Ridge, D. B. *J. Am. Chem. Soc.* **1984**, *106*, 825.

- [204] Rivalta, I.; Russo, N.; Sicilia, E. *J. Comp. Chem.* **2006**, *27*, 147.
- [205] Reppe, W. *Liebigs Ann.* **1953**, *582*, 1.
- [206] Klabunde, U.; Tulip, T. H.; Ittel, D. C. R. S. D. *J. Organomet. Chem.* **1987**, *334*, 141.
- [207] Keim, W. *Angew. Chem., Int. Ed. Engl.* **1990**, *29*, 235.
- [208] Sen, A. *Acc. Chem. Res.* **1993**, *26*, 303.
- [209] Ittel, S. D.; Johnson, L. K.; Brookhart, M. *Chem. Rev.* **2000**, *100*, 1169.
- [210] Ragsdale, S. W.; Wood, H. G. *J. Biol. Chem.* **1985**, *260*, 3970.
- [211] Raybuck, S. A.; Bastian, N. R.; Zydowsky, L. D.; Kobayashi, K.; Floss, H. G.; Orme-Johnson, W. H.; Walsh, C. T. *J. Am. Chem. Soc.* **1987**, *109*, 3171.
- [212] Stavropoulos, P.; Muetterties, M. C.; Carrie, M.; Holm, R. H. *J. Am. Chem. Soc.* **1991**, *113*, 8485.
- [213] Sellmann, D.; Häussinger, K.; Knoch, F.; Moll, M. *J. Am. Chem. Soc.* **1996**, *118*, 5368.
- [214] Ragsdale, S. W. *J. Inorg. Biochem.* **2007**, *101*, 1657.
- [215] Schröder, D.; Wesendrup, R.; Hertwig, R. H.; Dargel, T. K.; Grauel, H.; Koch, W.; Bender, B. R.; Schwarz, H. *Organometallics* **2000**, *19*, 2608.
- [216] Schröder, D.; Roithová, J. *Angew. Chem. Int. Ed.* **2006**, *45*, 5707.
- [217] Trage, C.; Schröder, D.; Schwarz, H. *Organometallics* **2003**, *22*, 693.
- [218] Schröder, D.; Schwarz, H. *Can. J. Chem.* **2005**, *83*, 1936.
- [219] Mandich, M. L.; Halle, L. F.; Beauchamp, J. L. *J. Am. Chem. Soc.* **1984**, *106*, 4403.
- [220] Tolbert, M. A.; Mandich, M. L.; Halle, H. F.; Beauchamp, J. L. *J. Am. Chem. Soc.* **1986**, *108*, 5675.
- [221] Schwarz, J.; Heinemann, C.; Schröder, D.; Schwarz, H.; Hrušák, J. *Angew. Chem. Int. Ed.* **1996**, *79*, 1.
- [222] Chen, Y. M.; Sievers, M. R.; Armentrout, P. B. *Int. J. Mass Spectrom. Ion Phys.* **1997**, *167/168*, 195.
- [223] Schwarz, J.; Schröder, D.; Schwarz, H.; Heinemann, C.; Hrušák, J. *Angew. Chem. Int. Ed.* **1996**, *79*, 1110.

- [224] Dyker, G. In *Transition Metals for Organic Synthesis*; Beller, M., Bolm, C., Eds.; Wiley-VCH: Weinheim, Germany, 1998.
- [225] Stahl, S. S.; Labinger, J. A.; Bercaw, J. E. *Angew. Chem. Int. Ed.* **1998**, *110*, 2298.
- [226] An, Z.; Pan, X.; Liu, X.; Han, X. *J. Am. Chem. Soc.* **2006**, *128*, 16028.
- [227] Niu, S.; Strout, D. L.; Zarić, S.; Bayse, C. A.; Hall, M. B. *ACS Symp. Ser.* **1998**, *721*, 138.
- [228] Niu, S.; Hall, M. B. *Chem. Rev.* **2000**, *100*, 353.
- [229] Sakaki, S. *Top. Organomet. Chem.* **2005**, *12*, 31.
- [230] Perutz, R. N.; Sabo-Etienne, S. *Angew. Chem. Int. Ed.* **2007**, *46*, 2667.
- [231] Canty, A. J.; Traill, P. R.; Colton, R.; Thomas, I. M. *Inorg. Chim. Acta* **1993**, *210*, 91.
- [232] Allison, J.; Ridge, D. P. *J. Am. Chem. Soc.* **1979**, *101*, 4998.
- [233] Eller, K.; Schwarz, H. *Organometallics* **1989**, *8*, 1820.
- [234] Trage, C.; Diefenbach, M.; Schröder, D.; Schwarz, H. *Chem. Eur. J.* **2006**, *12*, 2454.
- [235] Crabtree, R. H. *The Organometallic Chemistry of the Transition Metals*; Wiley: New York, USA, 2001.
- [236] Coulson, C. A. *Rev. Mod. Phys.* **1960**, *32*, 170.
- [237] Hoffmann, R. *Angew. Chem. Int. Ed.* **1982**, *21*, 711.
- [238] Hoffmann, R. *Am. Sci.* **2003**, *91*, 9.
- [239] Hoffmann, R.; Shaik, S.; Hiberty, P. C. *Acc. Chem. Res.* **2003**, *36*, 750.
- [240] Frenking, G.; Shaik, S. *J. Comp. Chem.* **2007**, *28*, 1.
- [241] Shaik, S. *New J. Chem.* **2007**, *31*, 2015.
- [242] Frenking, G.; Krapp, A. *J. Comp. Chem.* **2007**, *28*, 15.
- [243] Heiberg, H.; Gropen, O.; Swang, O. *Int. J. Quantum Chem.* **2003**, *92*, 391.
- [244] Armélin, M. *Diploma thesis*, TU Berlin, 2007.
- [245] Armélin, M.; Schlangen, M.; Schwarz, H. *Chem. Eur. J.* **2008**, *14*, 5229.
- [246] Ohanessian, G.; Brusich, M. J.; Goddard III, W. A. *J. Am. Chem. Soc.* **1990**, *112*, 7179.

- [247] Zhang, X. G.; Liyanage, R.; Armentrout, P. B. *J. Am. Chem. Soc.* **2001**, *123*, 5563.
- [248] Fiedler, A.; Schröder, D.; Zummack, W.; Schwarz, H. *Inorg. Chim. Acta* **1997**, *259*, 227.
- [249] Skupińska, J. *Chem. Rev.* **1991**, *91*, 613.
- [250] <http://webook.nist.gov/chemistry>.
- [251] Halle, L. F.; Houriet, R.; Kappes, M. M.; Staley, R. H.; Beauchamp, J. L. *J. Am. Chem. Soc.* **1982**, *104*, 6293.
- [252] Blanksby, S. J.; Ellison, G. B. *Acc. Chem. Res.* **2003**, *36*, 255.
- [253] Jagoda-Cwiklik, B.; Jungwirth, P.; Rulišek, L.; Milko, P.; Roithová, J.; Lemaire, J.; Maitre, P.; Ortega, J. M.; Schröder, D. *Chem. Phys. Chem.* **2007**, *8*, 1629.
- [254] Hildenbrand, D. L.; Lau, K. H. *J. Phys. Chem. A* **2006**, *110*, 11886.
- [255] Schröder, D.; Hrušák, J.; Schwarz, H. *Helv. Chim. Acta* **1992**, *75*, 2215.
- [256] Mazurek, U.; Schröder, D.; Schwarz, H. *Eur. J. Inorg. Chem.* **2002**, 1622.
- [257] Mazurek, U.; Schwarz, H. *Inorg. Chem.* **2000**, *39*, 5586.
- [258] Schlangen, M.; Schröder, D.; Schwarz, H. *Chem. Eur. J.* **2007**, *13*, 6810.
- [259] Giese, B. *Angew. Chem., Int. Ed. Engl.* **1977**, *16*, 125.
- [260] Feyel, S.; Schröder, D.; Schwarz, H. *J. Phys. Chem. A* **2006**, *110*, 2647.
- [261] Morton, T. H. *Tetrahedron* **1982**, *38*, 3195.
- [262] Heinrich, N.; Schwarz, H. In *Ion and Cluster Ion Spectroscopy and Structure*; Maier, J. P., Ed.; Elsevier: Amsterdam, Holland, 1989.
- [263] Bowen, R. D. *Acc. Chem. Res.* **1991**, *24*, 364.
- [264] Cassady, C. J.; Freiser, B. S. *J. Am. Chem. Soc.* **1985**, *107*, 1566.
- [265] Schröder, D.; Weiske, T.; Schwarz, H. *Int. J. Mass Spectrom.* **2002**, *219*, 729.
- [266] Schröder, D.; Semialjac, M.; Schwarz, H. *Int. J. Mass Spectrom.* **2004**, *233*, 103.
- [267] Bouchoux, G.; Leblanc, D.; Salpin, J. Y. *Int. J. Mass Spectrom.* **1996**, *153*, 37.
- [268] Schröder, D.; Engeser, M.; Brönstrup, M.; Daniel, C.; Spandl, J.; Hartl, H. *Int. J. Mass Spectrom.* **2003**, *228*, 743.

- [269] Schröder, D.; Engeser, M.; Schwarz, H.; Rosenthal, E.; Döbler, E. C. E.; Sauer, J. *Inorg. Chem.* **2006**, *45*, 6235.
- [270] Gruene, P.; Trage, C.; Schröder, D.; Schwarz, H. *Eur. J. Inorg. Chem.* **2006**, *2006*, 4546.
- [271] Levsen, K. *Fundamental Aspects of Organic Mass Spectrometry*; VCH: Weinheim, Germany, 1978.
- [272] McLafferty, F. W.; Wachs, T.; Lifshitz, C.; Innorta, G.; Irving, P. *J. Am. Chem. Soc.* **1970**, *92*, 6867.
- [273] Chupka, W. A. *J. Chem. Phys.* **1959**, *30*, 191.
- [274] Lifshitz, C. *Eur. J. Mass Spectrom.* **2002**, *8*, 85.
- [275] Lifshitz, C.; Long, F. A. *J. Chem. Phys.* **1964**, *41*, 2468.
- [276] Schlangen, M.; Schröder, D.; Schwarz, H. *Helv. Chim. Acta* **2007**, *90*, 847.
- [277] Schröder, D.; Schwarz, H. *Angew. Chem. Int. Ed.* **1990**, *29*, 910.
- [278] Schröder, D.; Zummack, W.; Schwarz, H. *Organometallics* **1993**, *12*, 1079.
- [279] Schwarz, H. *Top. Curr. Chem.* **1981**, *97*, 1.
- [280] Schulze, C.; Schwarz, H. *Organometallics* **1990**, *9*, 2034.
- [281] Jackson, T. C.; Jacobson, D. B.; Freiser, B. S. *J. Am. Chem. Soc.* **1984**, *106*, 1252.
- [282] Tolbert, M. A.; Beauchamp, J. L. *J. Am. Chem. Soc.* **1984**, *106*, 8117.
- [283] Sunderlin, L. S.; Armentrout, P. B. *Organometallics* **1990**, *9*, 1248.
- [284] Engeser, M.; Schlangen, M.; Schröder, D.; Schwarz, H. *Organometallics* **2003**, *22*, 3933.
- [285] Irigoras, A.; Elizalde, O.; Silanes, I.; Fowler, J. E.; Ugalde, J. M. *J. Am. Chem. Soc.* **2000**, *122*, 114.
- [286] Schröder, D.; Fiedler, A.; Hrušák, J.; Schwarz, H. *J. Am. Chem. Soc.* **1992**, *114*, 1215.
- [287] Aguirre, F.; Husband, J.; Thompson, C. J.; Stringer, K. L.; Metz, R. B. *J. Chem. Phys.* **2002**, *116*, 4071.
- [288] Shiota, S.; Yoshizawa, K. *J. Chem. Phys.* **2003**, *118*, 5872.



- [289] Schröder, D.; Schwarz, H. *Angew. Chem. Int. Ed.* **1993**, *32*, 1420.
- [290] Stahl, S. S.; Lippard, S. J. In *Dioxygen and alkane activation by iron-containing enzymes*; Ferreira, G. C., Moura, J. J. G., Franco, R., Eds.; Wiley-VCH: Weinheim, Germany, 1999; p 303.
- [291] Costas, M.; Mehn, M. P.; Jensen, M. P.; Que, L., Jr., *Chem. Rev.* **2004**, *104*, 939.
- [292] Nam, W. *Acc. Chem. Res.* **2007**, *40*, 522.
- [293] Nakagawa, K.; Konaka, R.; Nakata, T. *J. Organomet. Chem.* **1962**, *27*, 1597.
- [294] Christoskova, S. G.; Danova, N.; Georgieva, M.; Argirov, O. K.; Mehndzhiev, D. *Appl. Catal. A* **1995**, *128*, 219.
- [295] Herzberg, G. *Molecular Spectra and Molecular Structure*; Krieger: Malabar, USA, 1991; Vol. 3.
- [296] Schalley, C. A.; Wesendrup, R.; Schröder, D.; Schwarz, H. *Organometallics* **1996**, *15*, 678.
- [297] Bärsch, S.; Schröder, D.; Schwarz, H. *Helv. Chim. Acta* **2000**, *83*, 827.
- [298] Walling, C. *Acc. Chem. Res.* **1998**, *31*, 155.
- [299] MacFaul, P. A.; Wayner, D. D. M.; Ingold, K. U. *Acc. Chem. Res.* **1998**, *31*, 159.
- [300] Goldstein, S.; Meyerstein, D. *Acc. Chem. Res.* **1999**, *32*, 547.
- [301] Schröder, D.; Schalley, C. A.; Goldberg, N.; Hrušák, J.; Schwarz, H. *Chem. Eur. J.* **1996**, *2*, 1235.
- [302] Schalley, C. A.; Harvey, J. N.; Schröder, D.; Schwarz, H. *J. Phys. Chem. A* **1998**, *102*, 1021.
- [303] Schlangen, M.; Schröder, D.; Schwarz, H. *Angew. Chem. Int. Ed.* **2007**, *46*, 1641.
- [304] Pyykkö, P. *Chem. Rev.* **1988**, *88*, 563.
- [305] Hoffmann, R. *The Same and Not the Same*; Columbia University Press: New York, 1995.
- [306] Milburn, R. K.; Baranov, V. I.; Hopkinson, A. C.; Böhme, D. K. *J. Phys. Chem. A* **1999**, *103*, 6373.
- [307] Johnson, L. K.; Killian, M. C.; Brookhart, M. *J. Am. Chem. Soc.* **1995**, *117*, 6414.

- [308] Kuhn, P.; Sémeril, D.; Matt, D.; Chetcuti, M. J.; Lutz, P. *Dalton Trans.* **2007**, 515.
- [309] Harmer, J.; Finazzo, C.; Piskorski, R.; Ebner, S.; Duin, E. C.; Goenrich, M.; Thauer, R. K.; Reiher, M.; Schweiger, A.; Hinderberger, D.; Jaun, B. *J. Am. Chem. Soc.* **2008**, *130*, 10907.
- [310] Schröder, D.; Schwarz, H.; Schenk, S.; Anders, E. *Angew. Chem. Int. Ed.* **2003**, *42*, 5087.
- [311] Shaik, S.; Filatov, M.; Schröder, D.; Schwarz, H. *Chem. Eur. J.* **1998**, *4*, 193.
- [312] Shaik, S.; de Visser, S. P.; Ogliaro, F.; Schwarz, H.; Schröder, D. *Curr. Opin. Chem. Biol.* **2002**, *6*, 556.
- [313] Hirao, H.; Kumar, D.; Thiel, W.; Shaik, S. *J. Am. Chem. Soc.* **2005**, *127*, 13007.
- [314] Schoneboom, J. C.; Neese, F.; Thiel, W. *J. Am. Chem. Soc.* **2005**, *126*, 4017.
- [315] Shaik, S.; Hirao, H.; Kumar, D. *Acc. Chem. Res.* **2007**, *40*, 532.
- [316] Koszinowski, K.; Schlangen, M.; Schröder, D.; Schwarz, H. *Eur. J. Inorg. Chem.* **2005**, 2464.
- [317] Vardhan, D.; Liyanage, R.; Armentrout, P. B. *J. Chem. Phys.* **2003**, *119*, 4166.
- [318] Muettertides, E. L.; Hirsekorn, F. J. *J. Am. Chem. Soc.* **1974**, *96*, 4063.
- [319] Muettertides, E. L.; Rakowski, M. C.; Hirsekorn, F. J.; Larson, W. D.; Basus, V. J.; Arnet, F. A. *J. Am. Chem. Soc.* **1975**, *97*, 1266.
- [320] Muettertides, E. L.; Hirsekorn, F. J. *J. Am. Chem. Soc.* **1974**, *96*, 7920.
- [321] Rakowski, M. C.; Hirsekorn, F. J.; Stuhl, L. S.; Muettertides, E. L. *Inorg. Chem.* **1976**, *15*, 2379.
- [322] Bleeker, J. R.; Muettertides, E. L. *J. Am. Chem. Soc.* **1981**, *103*, 556.

## Publication list

1. "Alkane oxidation by  $\text{VO}_2^+$  in the gas phase: A unique dependence of reactivity on the chain length", M. Engeser, M. Schlangen, D. Schröder, H. Schwarz, *Organometallics* **2003**, *22*, 3933.
2. "C–H and N–H activation by gaseous  $\text{Rh}_2^+$  and  $\text{PtRh}^+$  cluster ions", K. Koszinowski, M. Schlangen, D. Schröder, H. Schwarz, *Int. J. Mass Spectrom.* **2004**, *237*, 19.
3. "Formation, structure and reactivity of gaseous  $\text{Ni}_2\text{O}_2^+$ ", K. Koszinowski, M. Schlangen, D. Schröder, H. Schwarz, *Eur. J. Inorg. Chem.* **2005** *12*, 2464.
4. "Gas-phase reactions of homo- and heteronuclear clusters  $\text{MM}'^+$  ( $\text{MM}' = \text{Fe, Co, Ni}$ ) with linear alkane nitriles", M. Schlangen, D. Schröder, H. Schwarz, *Hel. Chim. Acta* **2005**, *88*, 1405.
5. "C–H bond activation of methane with gaseous  $(\text{CH}_3)\text{Pt}(\text{L})^+$  complexes ( $\text{L} = \text{pyridine, bipyridine, and phenanthroline}$ )", B. Butschke, M. Schlangen, H. Schwarz, D. Schröder, *Z. Naturforsch.* **2007**, *62b*, 309.
6. "Pronounced ligand effects and the role of formal oxidation states in the nickel-mediated thermal activation of methane", M. Schlangen, D. Schröder, H. Schwarz, *Angew. Chem.* **2007**, *119*, 1667; *Angew. Chem. Int. Ed.* **2007**, *46*, 1641.
7. "Specific processes and scrambling in the dehydrogenation of ethane and the degenerate hydrogen exchange in the gas-phase ion chemistry of the  $[\text{Ni,C,H}_3,\text{O}]^+/\text{C}_2\text{H}_6$  couple", M. Schlangen, D. Schröder, H. Schwarz, *Hel. Chim. Acta* **2007**, *90*, 847.
8. "Thermal activation of methane by 'bare' group 10 metal-hydride cations  $\text{MH}^+$  ( $\text{M} = \text{Ni, Pd, and Pt}$ ): The same and not the same", M. Schlangen, H. Schwarz, *Angew. Chem.* **2007**, *119*, 5771; *Angew. Chem. Int. Ed.* **2007**, *46*, 5614.
9. "Ligand and substrate effects in the gas-phase reactions of  $\text{NiX}^+/\text{RH}$  couples ( $\text{X} = \text{F, Cl, Br, I}$ ;  $\text{R} = \text{CH}_3, \text{C}_2\text{H}_5, \text{C}_3\text{H}_7, n\text{-C}_4\text{H}_9$ )", M. Schlangen, D. Schröder, H. Schwarz, *Chem. Eur. J.* **2007**, *13*, 6810.
10. "Gas-phase C–H and N–H bond activation by a high valent nitrido-iron dication and  $\langle\text{NH}\rangle$ -transfer to activated olefins", M. Schlangen, J. Neugebauer, M. Reiher,

D. Schröder, J. Pitarch Lopez, M. Haryono, F.W. Heinemann, A. Grohmann, H. Schwarz, *J. Am. Chem. Soc.* **2008**, *130*, 4285.

11. "Insertion of molecular oxygen in transition-metal hydride bonds, oxygen-bond activation, and unimolecular dissociation of metal hydroperoxide intermediates", M. Schlangen, H. Schwarz, *Helv. Chim. Acta* **2008**, *91*, 379.
12. "On the mechanisms of degenerate ligand exchange in  $M(\text{CH}_3)^+/\text{CH}_4$  couples ( $M = \text{Fe}, \text{Co}, \text{Ni}, \text{Ru}, \text{Rh}, \text{Pd}, \text{Os}, \text{Ir}, \text{Pt}$ ) as explored by mass spectrometric and computational studies: oxidative addition/reductive elimination versus  $\sigma$ -complex-assisted metathesis", M. Armélin, M. Schlangen, H. Schwarz, *Chem. Eur. J.* **2008**, *14*, 5229.
13. "Room-temperature nitrile-alkyne metathesis reactions of a high-valent iron-nitrido dication in the gas phase", J. Boyd, M. Schlangen, A. Grohmann, H. Schwarz, *Helv. Chim. Acta* **2008**, *91*, 1430.
14. "Competitive intramolecular aryl- and alkyl-C-H bond activation and ligand evaporation from gaseous bisimino  $\text{Pt}(\text{L})(\text{CH}_3)((\text{CH}_3)_2\text{S})^+$  complexes ( $\text{L} = \text{C}_6\text{H}_5\text{N}=\text{C}(\text{CH}_3)-\text{C}(\text{CH}_3)=\text{NC}_6\text{H}_5$ )", B. Butschke, M. Schlangen, D. Schröder, H. Schwarz, *Helv. Chim. Acta*, in press.
15. "'Roll-over' cyclometalation of 2,2'-bipyridine platinum(II) complexes in the gas phase: A combined experimental/computational study", B. Butschke, M. Schlangen, D. Schröder, H. Schwarz, *Chem. Eur. J.*, submitted.
16. "Platinum(II)-mediated dehydrosulfurization and oxidative carbon-carbon coupling in the gas-phase decomposition of thioethers", B. Butschke, M. Schlangen, D. Schröder, H. Schwarz, *Int. J. Mass Spectrom.*, submitted.

## Curriculum Vitae

Name	Maria Schlangen
Geburtsdatum	27.02.1968
Staatsangehörigkeit	deutsch
Familienstand	ledig
ab 12/2007	Wissenschaftliche Mitarbeiterin im Leitungsbereich des Massenspektrometrie-Laboratoriums der TU Berlin.
ab 09/2004	Anfertigung der Dissertation “Nickel-mediated bond activation of small alkanes and of molecular oxygen - Ligand effects and the role of the metal’s formal oxidation state” unter Anleitung von Prof. Dr. Drs. h.c. Helmut Schwarz, TU Berlin.
02/2004 - 08/2004	Diplomarbeit zum Thema “Bindungsaktivierung durch kationische Metallcluster” unter Anleitung von Prof. Dr. Drs. h.c. Helmut Schwarz, TU Berlin.
10/2000 - 08/2004	Studium der Chemie (Diplom) an der TU Berlin.
10/1999 - 09/2000	Studium der Chemie (Diplom) an der Universität Köln.
03/1999	Examen für MTA/L.
04/1996 - 03/1999	Ausbildung zur MTA/L an der Lehranstalt für Medizinisch-Technische-LaboratoriumsassistentInnen der Medizinischen Hochschule Hannover.
10/1992 - 03/1993	Diplomarbeit zum Thema “Auswirkungen der Arbeitszeitverkürzung auf individuelle und gesellschaftliche Zusammenhänge” unter Anleitung von Prof. Dr. Gert Schäfer, Fachrichtung Politische Wissenschaft, Universität Hannover.
10/1987 - 03/1993	Studium der Sozialwissenschaften (Diplom) an der Universität Hannover
05/1987	Abitur
09/1978 - 05/1987	Besuch des Kreisgymnasiums St. Ursula in Haselünne, Emsland.